A Systematic X-ray Study of Supernova Remnants in the Large Magellanic Cloud

Kentaro Someya

Department of Physics, Tokyo Institute of Technology

Abstract

We present a systematic study of supernova remnants (SNRs) in the Large Magellanic Cloud (LMC) using the data obtained by the X-ray *Suzaku*, *XMM-Newton*, and *Chandra* satellites. SNRs play a key role in the nucleosynthesis of heavy elements, composition and condition of the interstellar medium, and the chemical evolution of the Universe. Because SNRs are composed of hot plasmas with temperature of million degree, they predominantly emit soft X-rays with occasional contribution from pulsar. However, a systematic X-ray study of the Galactic SNRs was not easy due to the large interstellar absorption and the ambiguity of the distance estimation. Thus we focused on the SNRs in the LMC. They are located effectively at the same distance ($\sim$ 50 kpc) and the interstellar absorption toward the LMC is known to be rather small. Among the 54 SNRs known in the LMC, a total of 44 SNRs were found to be observed at least one of the three satellites mentioned above and the data were available in the archive focusing on the thermal X-ray emission from the SNRs. We found that the X-ray emission from the SNRs can be reproduced by a model of one or two temperature plasma in non-equilibrium ionization with variable abundance. A total of 25 SNRs could be reproduced with the single-temperature plasma model and 6 SNRs with the two-temperature model. Systematic analysis for such a large number of SNRs was done for the first time.

From the systematic analysis, we could obtain new results on (1) an evolutionary phase of the SNRs, (2) origin of the apparent correlation between radii and plasma densities of the SNRs, and (3) surrounding environment of the two main types of supernova (SN) explosion (type Ia and core-collapse: CC SN). (1) We discovered that most SNRs we studied were in the Sedov phase (i.e. adiabatic expansion phase), because the large plasma masses (> 20 $M_\odot$), metal abundance ratios close to the LMC average (Russell & Dopita, 1992), young dynamical ages, and so on are all consistent with the prediction of a Sedov phase. In addition, we found that the derived emission measure had the excellent correlation with the Sedov model, as a function of the plasma density, coincides nicely. Futhermore, the plasma temperature also showed a relatively good correlation with the Sedov model. (2) the derived plasma density appears to decrease with a radius. We confirmed this apparent relation discovered by McKee & Ostriker (1977), which is one of the open questions. We succeeded to identify the origin of the correlation. Duration of the Sedov phase, which is determined by the transition to the radiative cooling phase, depends on the local gas density. This dependence was found to create the apparent correlation. We also found that the plasma temperature in the Sedov phase appeared to concentrate looks like $\sim$0.4 keV. This is because the radius dependence and the density dependence of the plasma temperature may be canceled out if we assume the empirical correlation between the radius and plasma density of the SNRs. (3) We compared the ionization and the dynamical ages for different types of SNRs. The ionization age for Type Ia SNRs were compatible to the dynamical age within a factor of three, while those for several CC SNRs remain small compared to their dynamical ages. From these results, we concluded that CC SNRs exploded in a preexisting low-density cavity, while Type Ia SNRs in a relatively uniform medium.

Contents

1 Introduction **1**

2 Review of Supernova Remnants **3**
2.1 Supernovae (SNe) . . . 3
2.1.1 Classication of SNe . . . 4
2.1.2 Multiwavelength SNR . . . 6
2.2 Nucleosynthesis . . . 9
2.3 Shock Wave . . . 11
2.3.1 Condition of Discontinuity . . . 11
2.3.2 The Shock Adiabatic . . . 13
2.4 SNR Evolution . . . 15
2.4.1 Free Expansion Phase . . . 15
2.4.2 Adiabatic Phase (Sedov Phase) . . . 15
2.4.3 Radiative Cooling Phase . . . 16
2.5 Characteristic Timescale . . . 17
2.5.1 Ionization and Recombination . . . 17
2.5.2 Collisional Ionization Equilibrium . . . 18
2.5.3 Thermal Equilibrium . . . 18
2.6 Radiation Process . . . 20
2.6.1 Line Emission . . . 20
2.6.2 Continuum Emission . . . 21
2.6.3 Synchrotron Radiation . . . 22
2.7 Particle Acceleration by a Pulsar and its Wind Nebula . . . 23
2.8 Spectral Model . . . 24
2.8.1 Optically Thin Thermal Plasma in Non-Ionization equilibrium: VNEI Model . . . 24
2.8.2 Interstellar Absorption: PHABS and VPHABS Model . . . 27

3 The Large Magellanic Cloud **29**
3.1 *Einstein* Observation . . . 30
3.1.1 Plasma density-Radius Relation, Luminosities, and Thermal Energies 30
3.1.2 Σ-D Relation . . . 32
3.1.3 N-D Relation . . . 32
3.2 *ROSAT*'s Observation: Morphologies . . . 34
3.3 *ASCA* Observation . . . 35
3.3.1 SNR Spectra . . . 36
3.3.2 Metal Abundances . . . 36

3.3.3 Cavity Explosion . . . 38

4 The Synoptic X-ray Analysis of SNRs in the LMC 41
4.1 Samples and Their Properties . . . 41
4.1.1 Samples . . . 41
4.1.2 Their Properties . . . 41
4.2 Observation & Data Reduction . . . 44
4.2.1 *Suzaku* data set . . . 46
4.2.2 *XMM-Newton* data set . . . 47
4.2.3 *Chandra* data set . . . 47
4.3 Spectral Analysis . . . 48
4.3.1 Source Extraction . . . 48
4.3.2 Spectral Model . . . 48
4.3.3 Basic Concepts for Spectral Modeling . . . 49
4.3.4 "$1kT1nt$" and "$1kT1nt$ + Power law (1) (2)" . . . 53
4.3.5 "$2kT1nt$–$2kT2nt$" . . . 62
4.3.6 Systematic Error of Observed Fluxes . . . 67

5 Discussion 69
5.1 Summary of the Observational Results . . . 69
5.2 Metal Abunadnce Ratios . . . 69
5.3 Plasma Densities, Thermal energies and Masses . . . 71
5.3.1 Comparison of the Plasma Densities with the Sedov Model and the Ambient Medium . . . 74
5.4 Dynamical Age vs. Cooling Timescale . . . 74
5.4.1 Comparison of the Dynamical Age with the Characteristic Age . . . 76
5.5 Spectral Parameters in the Sedov Phase . . . 76
5.6 Comparison of the Derived Spectral Parameters with the Sedov Model; Emission Measure & Temperature . . . 77
5.6.1 Emission Measure . . . 77
5.6.2 Temperature . . . 78
5.7 Apparent Relations - Plasma Density-Radius Relation - . . . 80
5.8 Apparent Relations - Temperature Distribution - . . . 82
5.9 Ionization Age vs. Dynamical Age . . . 83
5.9.1 Cavity Explosion . . . 84

6 Summary & Conclusion 85

A Instruments 87
A.1 The *Suzaku* Stellite . . . 87
A.1.1 X-ray Telescopes (XRTs) . . . 88
A.1.2 X-ray Imaging Spectrometer (XIS) . . . 96
A.2 *XMM-Newton* Satellite . . . 104
A.2.1 X-ray Telescopes . . . 105
A.2.2 European Photon Imaging Camera (EPIC) . . . 108
A.2.3 EPIC Background . . . 112
A.3 The *Chandra* Satellite . . . 115
A.3.1 High Resolution Mirror Assembly (HRMA) . . . 116

A.3.2 Advanced CCD Imaging Spectrometer (ACIS) 118

B Selected Regions **121**
B.1 Notes on Individual Objects 121

C Individual Analysis **133**
C.1 The Hard Diffuse Emission from J0543.1-6858 (DEM L299) 133
C.2 J0505.7-6753 (DEM L71) 134

D Systematic Errors of Spectral Modeling **137**
D.1 Spectral Modeling 137
D.1.1 χ^2_ν of $\leq$2.00 137
D.1.2 χ^2_ν of $\leq$1.75 141
D.1.3 χ^2_ν of $\leq$1.25 145
D.2 Comparison 149
D.2.1 Ne/O 149
D.2.2 Mg/O 150
D.2.3 Si/O 151
D.2.4 S/O 152
D.2.5 Fe/O 153
D.2.6 Plasma Densities 154
D.2.7 Thermal Energies 155
D.2.8 Plasma Masses 156
D.2.9 Dynamical Age vs. Cooling Timescale 157
D.2.10 Temperature vs. Emission Measure 158
D.2.11 Emission Measure 159
D.2.12 Temperature 160
D.2.13 Plasma Density-Radius Relation & Temperature Distribution . . . 161
D.2.14 Cavity Explosion 162

E Analysis of N23 **163**
E.1 Overview of N23 163
E.2 Observation & Data Reduction 163
E.3 Spectral Analysis 165
E.3.1 Extraction of Source and Background Photons 165
E.3.2 Spectral Models 165
E.4 Discussion 167
E.4.1 Densities, total energy, and swept up mass 167
E.4.2 SNR phase 169
E.4.3 Abundance 171
E.5 Summary 171

F Notes on Individual Objects **173**

List of Figures

2.1 Left: Schematic light curves for Types Ia, Ib, II-L, II-P, and SN 1987A SNe. Right: Spectra of SNe, showing early-time distinctions between the four major types and subtypes (a: Type Ia; SN 1987N, b: Type II; SN 1987A, c: Type Ic; SN 1987M, and d: Type Ib; SN 1987L). These figures were taken from Filippenko (1997). 4

2.2 *Chandra* and *XMM-Newton* (bottom images) images of SNRs. From left to right, top to bottom: Cas A, G292.2-1.8, E0102-7219, DEM L71, SN 1006, and RCW 86. This picture was adopted from Vink (2004). 7

2.3 The radio (top left), Infrared (top right), optical (bottom left), and X-ray (bottom right) images of Cassiopeia A. 8

2.4 Onion-like structure in massive star just prior to core collapse. 10

2.5 A schematic view of the coordinate system around the shock front. 12

2.6 The electron and proton temperature ratio as a function of the shock velocity (Rakowski, 2005). 20

2.7 The convolved VNEI model (a: 0.2 keV, b: 0.5 keV, and c: 1.0 keV) in the XSPEC library. The black, red, green are represented with the ionization parameter of 10^{10} cm^{-3} s, 10^{11} cm^{-3} s, and 10^{12} cm^{-3} s, respectively. 25

2.8 The 90 % confidence contour plotted for line ratios from the measured OVII and OVIII. This picture was taken by Flanagan et al. (2004). The red, green, and blue lines are represented with the line ratios for OVII/OVIII, OVII Lyα/OVIII, and OVIII Lyβ/OVIII Lyα, respectively. 26

2.9 The PHABS model. The black, red, and green solid lines are represented with the hydrogen column density for 10^{22} cm^{-2}, 10^{21} cm^{-2}, and 5×10^{20} cm^{-2}, respectively. 27

3.1 Optical images of the two magellanic clouds (top), LMC (left below) and SMC (right below). These images were taken by Anglo-Australian Observatory. 29

3.2 HI column density map of the "bridge" and the "Magellanic System". This figure were taken from Putman et al. (2003). 30

3.3 The plasma density (top), the thermal energy (bottom left), and the X-ray luminosity (bottom right) as a function of SNR diameter. These samples were observed in the LMC. The upper line in the plasma density-radius relation is represented with a temperature limit (0.2 keV; based on the Sedov model) which can be observed in the X-ray band, while the lower line is the detection limit of *Einstein* satellite. These figures were taken from Long (1983). 31

3.4 Σ-D relation. These samples were observed in the LMC, SMC, and Galaxy. This figure was taken from Berkhuijsen (1986). 33

3.5 The cumulative number-diameter relation. These samples were observed in the LMC. This figure was taken from Long (1983). 34

3.6 The X-ray images of DEM L71 (shell; top left), N63A (diffuse face; top middle), N206 (centrally brightened; top right), N23 (peaked emission; bottom left), and DEM L238 (Irregular; bottom right) observed by *ROSAT*. These figures were taken from Williams et al. (1999). 35

3.7 The schematic stages of their evolution in a cloudy medium. Striping regions are those from which Xray emission is expected, while solid regions indicate dense material, from which optical emission may be observed. The relative darkness of the shading indicates areas of higher (darker) and lower (lighter) density. This figure was taken from Williams et al. (1999). 36

3.8 *ASCA* X-ray spectra of three LMC SNRs: 0509-67.5, 0519-69.0, and N103B. The lower panel shows the residuals from the best-fit model. These figures were taken from Hughes et al. (1995). 37

3.9 Mean metalicity (relative to cosmic value) vs. radius (left), dymical age derived from the Sedov solution (middle), and swept-up mass (right), provided by Hughes et al. (1998). The difference symbol types refer to the different remnants. Error bars represent the rms scatter in the individual fitted abundances of the various elemental species considered. Results plotted are the average of the values obtained under the two different model assumptions about the timescale of electron-ion temperature equilibrium. The only significant correlations are between metalicity and either radius or age. 37

3.10 Average chemical abundances of the LMC relative to the cosmic value plotted as a function of elemental species by Hughes et al. (1998). The gas-phase abundances of the LMC derived from optical and UV studies of HII regions are shown as the crosses (Dufour, 1984). More recent results from Russell & Dopita (1992), whose as the circle, are based on the detailed modeling of optical/UV spectra from HII regions, SNRs, and supergiant stars. 38

3.11 Remnant age determined from the fitted ionization age vs. the dynamical age derived from the Sedov model. The different symbol types refer to the different remnants (circle, cross, square, star, triangle, plus sign, and diamond correspond to N23, N49, N63A, DEM 71, N132D, 0453-68.5, and N49B, respectively). Error bars include only the statistical uncertainty from fits for the ionization age. Data points with dotted error bars (at the 90 % confidence level) are from the results assuming full electron-ion temperature equilibration at the SNR shock front, while the solid error bars refer to results using Coulomb equilibration timescales. This figure was taken by Hughes et al. (1998). 38

4.1 The optical R-band image for the Large Magellanic Cloud. The cyan, green, and yellow diamond points are represented with SNRs observed by *Suzaku*, *XMM-Newton*, and *Chandra*, respectively. The red diamond points, on the other hand, are represented without any X-ray observations. The coordinate is represented with the equatorial coordinate system for the epoch 2000. 42

4.2 Comparison with the previous results; Left: Temperature (keV), Right: Ionization parameter ($\log(\mathrm{cm}^{-3}\,\mathrm{s})$. The horizontal and vertical axises are represented with the our and previous results, respectively. The black, red, green, and blue data points are represented with APEC, MEKAL, NEI, and PSHOCK models in the XSPEC library, respectively. Plasmas in collisional ionization equilibrium ($\sim 12\ \log(\mathrm{cm}^{-3}\,\mathrm{s})$) have relatively large uncertainties. The several error bars were not presented in the previous results. . . 54

4.3 The data and the best-fit spectra. SNR names are on the top of each panel. The black, red and green crosses show the data points from the MOS1, MOS2 and pn in *XMM-Newton*, respectively. The black cross shows the data points from the ACIS in *Chandra*. The lower panel shows the residuals from the best-fit model. 55

4.3 The data and the best-fit spectra. SNR names are on the top of each panel. The black and red crosses show the data points from the FI and BI CCDs in *Suzaku*, respectively. The black, red and green crosses show the data points from the MOS1, MOS2 and pn in *XMM-Newton*, respectively. The black cross shows the data points from the ACIS in *Chandra*. The lower panel shows the residuals from the best-fit model. 56

4.3 The data and the best-fit spectra. SNR names are on the top of each panel. The black and red crosses show the data points from the FI and BI CCDs in *Suzaku*, respectively. The black, red and green crosses show the data points from the MOS1, MOS2 and pn in *XMM-Newton*, respectively. The lower panel shows the residuals from the best-fit model. 57

4.4 Comparison with the previous results for the non-thermal components; Left: photon-index, Right: normalization. The labels in these figures are represented with each SNR. 58

4.5 The data and the best-fit spectra. SNR names are on the top of each panel. The black and red crosses show the data points from the FI and BI CCDs in *Suzaku*, respectively. The black, red and green crosses show the data points from the MOS1, MOS2 and pn in *XMM-Newton*, respectively. The lower panel shows the residuals from the best-fit model. The orange and green solid histogram are represented with the non-thermal and thermal component, respectively. 59

4.6 The data and the best-fit spectra. SNR names are on the top of each panel. The black, red and green crosses show the data points from the MOS1, MOS2 and pn in *XMM-Newton*, respectively. The black cross shows the data points from the ACIS in *Chandra*. The lower panel shows the residuals from the best-fit model. The green solid histogram are represented with the thermal component, respectively. The orange solid histogram are represented with the high energy component. 60

4.7 Comparison with the previous results of temperatures and ionization parameters. The horizontal and vertical axises are represented with the our and previous results, respectively. The green and blue data points are represented with NEI and PSHOCK models in the XSPEC library, respectively. The filled boxes and open circles are represented with the first and second VNEI components, respectively. Plasmas in collisional ionization equilibrium (~ 12 $\log(\mathrm{cm}^{-3}\,\mathrm{s})$) have relatively large uncertainties. 62

4.8 The data and the best-fit spectra. SNR names are on the top of each panel. The black and red crosses show the data points from the FI and BI CCDs in *Suzaku*, respectively. The black, red, and green crosses show the data points from the MOS1, MOS2 and pn in *XMM-Newton*, respectively. The black cross shows the data points from the ACIS in *Chandra*. In two components VNEI model, the green and blue solid histograms show the cool and hot component, respectively. The lower panel shows the residuals from the best-fit model. 64

4.9 The observed flux (previous results; vertical axis)-flux (our results; horizontal axis) relation. 67

5.1 The derived metal abundance ratios (top left for Ne/O, top right for Mg/O, middle left for Si/O, middle right for S/O, and bottom Fe/O). The derived abundance ratios are compared to the LMC average (Russell & Dopita 1992; black dotted line and Hughes et al. 1998; red dotted line). The ratios are all relative to solar (Anders & Grevesse, 1989) and normalized to oxygen. Since the Si metal abundance has the large uncertainty (Russell & Dopita, 1992), we did not include the result in the figure. The numbers from left to right in the horizon axis indicate relative number of the SNRs from top to bottom in table 4.1. 70

5.2 Evolutions of (a) a plasma density, (b) a thermal energy, and (c) a plasma mass as a function of SNR radius. The red, orange, magenta, green, and blue data points represent with the plasma densities of $n_\mathrm{e} \geq 4.0$, $4.0 > n_\mathrm{e} \geq 2.0$, $2.0 > n_\mathrm{e} \geq 0.4$, $0.4 > n_\mathrm{e} \geq 0.2$, and $0.2 > n_\mathrm{e}$ cm^{-3}, respectively. The filled boxes and open circles also represent the first and second VNEI components, respectively. 71

5.2 Continue. 72

5.3 The ratio between the derived and simulated (based on the Sedov model) plasma density as a function of SNR radius (left), and the derived plasma density histogram (right). 73

5.4 The dynamical age vs. cooling timescale between 2,000–500,000 yr. The blue, green, sky blue, magenta, yellow, orange, and red data points are represented with the temperature of $0.08 < kT_\mathrm{e} \leq 0.2$, $0.2 < kT_\mathrm{e} \leq 0.4$, $0.4 < kT_\mathrm{e} \leq 0.6$, $0.6 < kT_\mathrm{e} \leq 0.8$, $0.8 < kT_\mathrm{e} \leq 1.0$, $1.0 < kT_\mathrm{e} \leq 1.2$, $1.2 \leq kT_\mathrm{e}$, respectively. The filled boxes and open circles are also represented with the first and second VNEI components, respectively. The dotted line indicates $\pm 3 \times t_\mathrm{sedov}$ (t_cool). 75

5.5 The relations between the observed parameters; (a) kT_e-EM relation, (b) EM-R relation, and (c) kT_e-R relation. The red, magenta, green, blue and sky blue solid lines are represented with the simulated spectral parameters in the Sedov phase with the ambient densities of 1 ($n_e = 4$), 0.5 ($n_e = 2$), 0.1 ($n_e = 0.4$), 0.05 ($n_e = 0.2$), and 0.01 ($n_e = 0.04$) cm^{-3}, respectively. The red, orange, magenta, green, and blue data points are represented with the plasma densities of $n_e \geq 4$, $4 > n_e \geq 2$, $2 > n_e \geq 0.4$, $0.4 > n_e \geq 0.2$, and $0.2 > n_e$ cm^{-3}, respectively. The filled boxes and open circles are also represented with the first and second VNEI components, respectively. . . . 78

5.5 Continue. 79

5.6 The ratio between the derived and simulated (based on the Sedov model) plasma temperature as a function of SNR radius. The red, orange, magenta, green, and blue data points are represented with the plasma densities of $n_e \geq 4$, $4 > n_e \geq 2$, $2 > n_e \geq 0.4$, $0.4 > n_e \geq 0.2$, and $0.2 > n_e$ cm^{-3}, respectively. The filled boxes and open circles are also represented with the first and second VNEI components, respectively. 80

5.7 The plasma density-radius relation. The red (1.4 $M_\odot$), green (10 $M_\odot$) and blue (20 $M_\odot$) solid lines are represented with at the end of the free expansion phase. The purple (10^{51} erg) and sky blue (10^{51} erg) are also represented with at the beginning of the radiative cooling phase. The filled boxes and open circles are represented with the first and second VNEI components, respectively. The solid black line is represented with the best-fit model. . . 81

5.8 The temperature histogram. The bin size is 0.1 keV. The black solid line is represented with the GAUSSIAN model with the central temperature of 0.42 ± 0.23 keV at the 68 % confidence level. 83

5.9 SNR age determined from the derived ionization parameter vs. the dynamical age derived from the Sedov model. The blue, green, and red data points are represented with CC, Type Ia, and unknown SNe, respectively. The filled boxes and open circles are represented with the first and second VNEI components, respectively. 84

A.1 The *Suzaku* orbit. This figure was taken by the *Suzaku* technical description. 87

A.2 Left: Schematic picture of the *Suzaku* satellite. Right: A side view of the instruments and telescopes on *Suzaku* (Mitsuda et al., 2007). 88

A.3 Left: The Encircled Energy Function (EEF) showing the fractional energy within a given radius for one quadrant of the XRT-I telescopes on *Suzaku* at 4.5 and 8.0 keV (Serlemitsos et al., 2007). Right: XIS effective area of one XRT + XIS system, for the FI and BI CCDs. no contamination. . . . 89

A.4 Layout of the XRTs on the *Suzaku* spacecraft (Serlemitsos et al., 2007). . . 89

A.5 A *Suzaku* X-ray Telescope Serlemitsos et al. (2007). 91

A.6 A thermal shield. This picture was adapted from Serlemitsos et al. (2007). 92

A.7 Top to bottom; Image, Point-Spread Function (PSF), and EEF of the four XRT-I modules in the focal plane Serlemitsos et al. (2007). All the images are binned with 2×2 pixels followed by being smoothed with a Gaussian with a sigma of 3 pixels, where the pixel size is 24 μm. The EEF is normalized to unity at the edge of the CCD chips (a square of 17'.8 on a side). With this normalization, the HPD of the XRT-I0 thorough I3 is 1'.8, 2'.3, 2'.0 and 2'.0, respectively. 93

A.8 Locations of the optical axis of each XRT-I module in the focal plane determined from the observations of the Crab Nebula in 2005 August-Septermber. This figure implies that the image on each XIS detector becomes brightest when a target star is placed at the position of the corresponding cross. The dotted circles are drawn every 30" in radius from the XIS-default position. This figure was adapted from Serlemitsos et al. (2007). 94

A.9 Vignetting of the four XRT-I modules using the data of the Crab Nebula taken during 2005 August 22–27 in the two energy bands 3–6 keV and 8–10 keV. The model curves are calculated with the ray-tracing simulator with the spectral parameters of $N_{\rm H} = 0.33 \times 10^{22}$ cm^{-2}, photon index = 2.09, and the normalization = 9.845 photons cm^{-2} s^{-1} keV^{-1} at 1 keV. Note that the abrupt drop of the model curves at ∼8' is due to the source approaching the detector edge. The excess of the data points of XIS1 is probably due to insufficient calibration of the BI CCD. This figure was adapted from Serlemitsos et al. (2007). 94

A.10 Focal plane images formed by stray light (Serlemitsos et al., 2007). The left and middle panels show simulated images of a monochromatic point-like source of 4.51 keV locating at (DETX, DETY) = (-20', 0') in the cases of without and with the pre-collimator, respectively. The radial dark lanes are the shades of the alignment bars. The right panels is the in-flight stray image of the Crab Nebula in the 2.5–5.5 keV band located at the same off-axis angle. The unit of the color scale of this panel is counts per 16 pixels over the entire exposure time of ∼8.4 ks. the counting rate from the whole image is 0.78±0.01 c s^{-1} including background. Note that the intensity of the Crab Nebula measured with XIS3 at the XIS-default position is 458±3 c s^{-1} in the same 2.5–5.5 keV band. All the images are binned with 4×4 pixels followed by being smoothed with a Gaussian with a sigma of 2 pixels, where the pixel size is 24 μm. 95

A.11 Angular responses of the XRT-I at 1.5 (left) and 4.5 keV (right) up to 2 degrees (see *Suzaku* technical description). The effective area is normalized at on-axis. The integration ares is corresponding to the detector size of XIS (17'.8×17'.8). The three solid lines in the plots correspond to different parameters of ray-tracing program while the crosses are the normalized effective area using the Crab pointings. 95

A.12 The XIS detector before installation onto *Suzaku*. This picture was adapted from Koyama et al. (2007). 96

A.13 Left: The XIS background rate for each of the four XIS detectors, with prominent fluorescent lines marked. These spectra are based on ∼110–160 ksec of observations towards the dark Earth. These spectra dose not included Cosmic X-ray background (CXB). Right: The XIS background rate for each of the four XIS detectors, showing only energies between 0.1–2.0 keV. Below 0.3 keV the background rate for the FI chips cannot be determined due to their low effective area. 100
A.14 Definition of GRADE of CCD events. 102
A.15 Left: The time history of the contamination of all four XIS detectors, measured at the center of the OBF. Right: The radial profile of the contamination of the BI chip. 103
A.16 Sketch of the *XMM-Newton* payload. The mirror modules, two of which are equipped with Reflecting Grazing Arrays, are visible at the lower left. At the right end of the assembly, the focal X-ray instruments are shown: The EPIC MOS cameras with their radiators (black:green horns), the radiator of the EPIC pn camera (violet) and those of the (light blue) RGS detectors (in pink). The OM telescope is obscured by lower mirror module. 104
A.17 The light path in *XMM-Newton*'s XRT with the pn camera in focus. 106
A.18 The light path in *XMM-Newton*'s XRT with the MOS camera and RGA. . 106
A.19 On-axis images of the MOS1, MOS2 and on XRTs (left to right). The images are 110 arcsec wide and a logarithmic scale has been used to visualize the wings of the point spread function. 107
A.20 Left: Radial counts distribution for the on-axis PSF of the MOS1 XRT in the 0.75–2.25 keV energy range. The solid line indicates the best-fit King profile. Right: The encircled energy function as a function of angular radius (an-axis) at different energies. The curve are calculated assuming a fraction encircled energy of 100 % at a radial distance of 5 arcmin. 107
A.21 Left: The net effective area of all *XMM-Newton* XRT, combined with the response characteristics of the focal detectors. Right: Vignetting function as a function of off-axis angle at several different energies (based on simulations). 108
A.22 The effect of straylight in pn image of GRS 1758-258. 109
A.23 A rough sketch of the field of view of the two types of EPIC cameras (MOS, left; pn, right). The shaded circle depicts a 30 arcmin diameter area which is equivalent with the XRT field of view. 109
A.24 Left: The EPIC MOS energy resolution (FWHM) as a function of energy. The solid curve is a best-fit $E^{0.5}$ function to ground calibration data between 0.1–12.0 keV. Below around 0.6 keV (shown by the dotted region), surface charge loss effects distort the main photopeak significantly from a Gaussian from and, hence the effective energy resolution The measured in-flight FWHM of the Al Kα (1.487 keV) and Mn Kα (5.893 keV) lines are also plotted. Right: The EPIC pn energy resolution (FWHM) as a function of energy. Curve are given for single and double events (fill frame mode) at the focus position node. 110
A.25 Left: Quantum efficiency of the EPIC MOS camera as a function of photon energy, Right: Quantum efficiency of the EPIC pn camera as a function of photon energy. 111

A.26 Event patterns recognized by the MOS (pn) detector. The red pixel is the centre pixel, its signal is above threshold and is the largest signal in the 3×3 inner matrix. The green pixels have signals above threshold. The white pixels have signal below threshold. The crosses indicates pixels no considered. 112
A.27 An example of light curve from a MOS1 observation badly affected by proton flares. 113
A.28 MOS1 (left) and pn (right) background spectrum from a blank sky region. In the left figure, the prominent features around 1.5 and 1.7 keV are Al K and Si K fluorescence lines, respectively. On the other hands, the prominent features, in right figure, are identified as Al-K (1.5 keV), Cr-K (5.5 keV), Ni-K, Cu-K, Zn-K (8.0 keV) and Mo-K (17.5 keV), respectively. 114
A.29 The MOS (left) and pn (right) background image. The MOS image in the energy band centered on Si-K fluorescent line region. As the same, the pn image in the Cu-K fluorescent line energy region. 115
A.30 Left: The *Chandra* Observatory with certain subsystems labeled. LGA is an acronym for the Low Gain Antenna. Right: Major components of the telescope system. The grating assemblies are also shown. 116
A.31 Arrangement of the ACIS and the HRC in the focal plane. The view is along the axis of the telescope from the direction of the mirrors. For reference, the two back-illuminated ACIS-S chips are shaded. Numbers indicate positions of chips I0–I3 and S0–S5. SIM motion can be used to place the aimpoint at any point on the vertical solid line. 116
A.32 The four nested HRMA mirror pairs and associated structures. 117
A.33 The HRMA effective area from the raytrace prediction as a function of energy. The raytrace includes the effects of molecular contamination of variable thickness on the mirrors. The dotted line (tp emphasize that these measurements were taken simultaneously) with error bars shows the data taken with a solid state detector (SSD) with a C-K continuum source. Data obtained from spectral line sources with a flow proportional counter (FPC) are shown as diamonds; obtained with a solid state detector (SSD) are shown as triangles. All the line measurements are circled for clarity. The dashed (green) line shows the absolute HRMA effective area with the X-Ray Calibration Facility (XRCF) empirical correction. 118
A.34 A schematic drawing of the ACIS focal plane; insight to the terminology is given in the lower left. Note the nominal aimpoints: on S3 (the '+') and on I3 (the 'x'). It is standard practice to add an offset to all observations on S3 to move the source away from the node 0–1 boundary. Note the differences in the orientation of the I and S chips, important when using Sub array. Note also the (Y, Z) coordinate system and the target offset convention as well as the SIM motion (+/- Z). The view is along the optical axis, from the source toward the detectors, (-X). The numerous ways to refer to a particular CCD are indicated: chip letter+number, chip serial number, and ACIS chip number. The node numbering scheme is illustrated lower center. 119
A.35 The ACIS pre-launch energy resolution as a function of energy. 120

B.1 The *XMM-Newton* X-ray SNR image; J0449.3-6920 (right) and J0450.2-6922 (left; B0450-69270). 121
B.1 The *XMM-Newton* X-ray SNR image; J0518.7-6939 (N120). 122
B.1 The *XMM-Newton* X-ray SNR image; J0450.4-7050 (B0450-709). 122
B.1 The *XMM-Newton* X-ray SNR image; J0453.2-6655 (N4). 122
B.1 The *XMM-Newton* X-ray SNR image; J0453.6-6829 (B0453-685). 122
B.1 The *Chandra* X-ray SNR image; J0453.9-7000 (B0454-7005). 123
B.1 The *Chandra* X-ray SNR image; J0454.6-6713 (N9). 123
B.1 The *XMM-Newton* X-ray SNR image; J0454.8-6626 (N11L). 123
B.1 The *XMM-Newton* X-ray SNR image; J0455.6-6839 (N86). 123
B.1 The *Chandra* X-ray SNR image; J0459.9-7008 (N186D). 124
B.1 The *Suzaku* X-ray SNR image; J0505.7-6753 (DEM L71; top) and J0505.9-6802 (N23; bottom). 124
B.1 The *XMM-Newton* X-ray SNR image; J0506.1-6541. 124
B.1 The *Suzaku* X-ray SNR image; J0509.0-6844 (N103B). 124
B.1 The *Suzaku* X-ray SNR image; J0509.5-6731 (B0509-67.5). 125
B.1 The *XMM-Newton* X-ray SNR image; J0519.6-6902 (B0519-690). 125
B.1 The *XMM-Newton* X-ray SNR image; J0519.7-6926 (B0520-694). 125
B.1 The *Suzaku* X-ray SNR image; J0523.1-6753 (N44). 125
B.1 The *Suzaku* X-ray SNR image; J0525.1-6938 (N132D). 126
B.1 The *XMM-Newton* X-ray SNR image; J0525.4-6559 (N49B). 126
B.1 The *XMM-Newton* X-ray SNR image; J0526.0-6605 (N49). 126
B.1 The *XMM-Newton* X-ray SNR image; J0527.6-6912 (B0528-692) 126
B.1 The *XMM-Newton* X-ray SNR image; J0529.9-6701 (DEM L214). 127
B.1 The *Suzaku* X-ray SNR image; J0531.9-7100 (N206). 127
B.1 The *XMM-Newton* X-ray SNR image; J0532.5-6732 (B0532-675). 127
B.1 The *Suzaku* X-ray SNR image; J0534.0-6955 (B0534-699). 127
B.1 The *XMM-Newton* X-ray SNR image; J0534.3-7033 (DEM L238). 128
B.1 The *Suzaku* X-ray SNR image; J0535.5-6916 (SNR 1987A). 128
B.1 The *XMM-Newton* X-ray SNR image; J0535.7-6602 (N63A). 128
B.1 The *XMM-Newton* X-ray SNR image; J0535.8-6918 (Honeycomb). 128
B.1 The *XMM-Newton* X-ray SNR image; J0536.1-6735 (DEM L241). 129
B.1 The *XMM-Newton* X-ray SNR image; J0536.1-7039 (DEM L249). 129
B.1 The *Suzaku* X-ray SNR image; J0536.2-6912 (30 Dor C). 129
B.1 The *XMM-Newton* X-ray SNR image; J0537.4-6628 (DEM L256). 129
B.1 The *XMM-Newton* X-ray SNR image; J0537.6-6920 (B0538-6922). 130
B.1 The *XMM-Newton* X-ray SNR image; J0537.8-6910 (N157B). 130
B.1 The *Chandra* X-ray SNR image; J0540.0-6944 (N159). 130
B.1 The *Suzaku* X-ray SNR image; J0540.2-6920 (B0540-693). 130
B.1 The *XMM-Newton* X-ray SNR image; J0543.1-6858 (DEM L299). 131
B.1 The *XMM-Newton* X-ray SNR image; J0547.0-6943 (DEM L316B; right and DEM L316A; left). 131
B.1 The *Suzaku* X-ray SNR image; J0547.8-7025 (B0548-704). 131
B.1 The *Chandra* X-ray SNR image; J0550.5-6823. 131

C.1 The J0543.1-6858 (DEM L299) images in the 0.5–2.0 (left) and 2.0–10.0 keV (right). The white solid and dotted circles are represented with the source and background regions. The sky blue solid circle is also represented with the source region of the hard diffuse emission (source A). 133

C.2 The black, red and green crosses show the data points from the MOS1, MOS2 and pn, respectively. The green and orange solid histograms show the thermal and non-thermal components, respectively. The lower panel shows the residuals from the best-fit model. 134

C.3 Left: J050550.3-675017 image in the 2.0-10.0 keV. The source and background regions of this point source are represented with the solid circle and annulus, respectively. The dotted circle is also represented with the source region observed by *Suzaku*. The lower right in this figure is the expanded figure around this point source. Right: The upper panel shows the background-subtracted ACIS spectrum of J050550.3-675017. The lower panel shows the residuals to the fit. 135

C.4 The data and the best-fit spectra. SNR names are on the top of each panel. The black and red crosses show the data points from the FI and BI CCDs in *Suzaku*, respectively. In two components VNEI model, the green and blue solid histograms show the cool and hot component, respectively. The lower panel shows the residuals from the best-fit model. The black solid histogram shows the non-thermal component. 135

D.1 The data and the best-fit spectra. SNR names are on the top of each panel. The black and red crosses show the data points from the FI and BI CCDs in *Suzaku*, respectively. The black, red and green crosses show the data points from the MOS1, MOS2 and pn in *XMM-Newton*. The orange solid histogram is represented with the non-thermal component. The green and blue solid histograms are represented with the thermal components. The lower panel shows the residuals from the best-fit model. The adopted threshold is the χ^2_ν of ≤ 2.00. 138

D.2 The data and the best-fit spectra. SNR names are on the top of each panel. The black and red crosses show the data points from the FI and BI CCDs in *Suzaku*, respectively. The black, red and green crosses show the data points from the MOS1, MOS2 and pn in *XMM-Newton*. The orange solid histogram is represented with the non-thermal component. The green and blue solid histograms are represented with the thermal components. The lower panel shows the residuals from the best-fit model. The adopted threshold is the χ^2_ν of ≤ 1.75. 142

D.3 The data and the best-fit spectra. SNR names are on the top of each panel. The black and red crosses show the data points from the FI and BI CCDs in *Suzaku*, respectively. The black, red and green crosses show the data points from the MOS1, MOS2 and pn in *XMM-Newton*. The orange solid histogram is represented with the non-thermal component. The green and blue solid histograms are represented with the thermal components. The lower panel shows the residuals from the best-fit model. The adopted threshold is the χ^2_ν of ≤ 1.25. 146

D.4 The derived metal abundance ratios (Ne/O). The derived abundance ratios are compared to the LMC average (Russell & Dopita 1992; black dotted line and Hughes et al. 1998; red dotted line). The ratios are all relative to solar (Anders & Grevesse, 1989) and normalized to oxygen. The numbers from left to right in the horizon axis are represented with SNRs from top to bottom in table 4.1. The adopted thresholds are the χ^2_ν of < 1.50 (top), 2.00 (middle left), 1.75 (middle right), and 1.25 (bottom). 149

D.5 The derived metal abundance ratios (Mg/O). The derived abundance ratios are compared to the LMC average (Russell & Dopita 1992; black dotted line and Hughes et al. 1998; red dotted line). The ratios are all relative to solar (Anders & Grevesse, 1989) and normalized to oxygen. The numbers from left to right in the horizon axis are represented with SNRs from top to bottom in table 4.1. The adopted thresholds are the χ^2_ν of < 1.50 (top), 2.00 (middle left), 1.75 (middle right), and 1.25 (bottom). 150

D.6 The derived metal abundance ratios (Si/O). The derived abundance ratios are compared to the LMC average (Russell & Dopita 1992; black dotted line and Hughes et al. 1998; red dotted line). The ratios are all relative to solar (Anders & Grevesse, 1989) and normalized to oxygen. Since the Si metal abundance has the large uncertainty (Russell & Dopita, 1992), we dose not represent that. The numbers from left to right in the horizon axis are represented with SNRs from top to bottom in table 4.1. The adopted thresholds are the χ^2_ν of < 1.50 (top), 2.00 (middle left), 1.75 (middle right), and 1.25 (bottom). 151

D.7 The derived metal abundance ratios (S/O). The derived abundance ratios are compared to the LMC average (Russell & Dopita 1992; black dotted line and Hughes et al. 1998; red dotted line). The ratios are all relative to solar (Anders & Grevesse, 1989) and normalized to oxygen. The numbers from left to right in the horizon axis are represented with SNRs from top to bottom in table 4.1. The adopted thresholds are the χ^2_ν of < 1.50 (top), 2.00 (middle left), 1.75 (middle right), and 1.25 (bottom). 152

D.8 The derived metal abundance ratios (Fe/O). The derived abundance ratios are compared to the LMC average (Russell & Dopita 1992; black dotted line and Hughes et al. 1998; red dotted line). The ratios are all relative to solar (Anders & Grevesse, 1989) and normalized to oxygen. The numbers from left to right in the horizon axis are represented with SNRs from top to bottom in table 4.1. The adopted thresholds are the χ^2_ν of < 1.50 (top), 2.00 (middle left), 1.75 (middle right), and 1.25 (bottom). 153

D.9 Evolutions of the plasma density as a function of SNR radius. The red, orange, magenta, green, and blue data points are represented with the plasma densities of $n_\mathrm{e} \geq 4.0$, $4.0 > n_\mathrm{e} \geq 2.0$, $2.0 > n_\mathrm{e} \geq 0.4$, $0.4 > n_\mathrm{e} \geq 0.2$, and $0.2 > n_\mathrm{e}$ cm^{-3}, respectively. The filled boxes and open circles are also represented with the first and second vnei components, respectively. The adopted thresholds are the χ^2_ν of < 1.50 (top), 2.00 (middle left), 1.75 (middle right), and 1.25 (bottom). 154

D.10 Evolutions of the thermal energy as a function of SNR radius. The red, orange, magenta, green, and blue data points are represented with the plasma densities of $n_e \geq 4.0$, $4.0 > n_e \geq 2.0$, $2.0 > n_e \geq 0.4$, $0.4 > n_e \geq 0.2$, and $0.2 > n_e$ cm^{-3}, respectively. The filled boxes and open circles are also represented with the first and second vnei components, respectively. The adopted thresholds are the χ^2_ν of < 1.50 (top), 2.00 (middle left), 1.75 (middle right), and 1.25 (bottom). 155

D.11 Evolutions of the plasma mass as a function of SNR radius. The red, orange, magenta, green, and blue data points are represented with the plasma densities of $n_e \geq 4.0$, $4.0 > n_e \geq 2.0$, $2.0 > n_e \geq 0.4$, $0.4 > n_e \geq 0.2$, and $0.2 > n_e$ cm^{-3}, respectively. The filled boxes and open circles are also represented with the first and second vnei components, respectively. The adopted thresholds are the χ^2_ν of < 1.50 (top), 2.00 (middle left), 1.75 (middle right), and 1.25 (bottom). 156

D.12 The dynamical age vs. cooling timescale between 2,000–500,000 yr. The blue, green, sky blue, magenta, yellow, orange, and red data points are represented with the temperature of $0.2 \geq kT_e > 0.08$, $0.4 \geq kT_e > 0.2$, $0.6 \geq kT_e > 0.4$, $0.8 \geq kT_e > 0.6$, $1.0 \geq kT_e > 0.8$, $1.2 \geq kT_e > 1.0$, and $kT_e > 1.2$ keV respectively. The filled boxes and open circles are also represented with the first and second VNEI components, respectively. The dotted line indicates $\pm 3 \times t_{\rm sedov}$ ($t_{\rm cool}$).The adopted thresholds are the χ^2_ν of < 1.50 (top), 2.00 (middle left), 1.75 (middle right), and 1.25 (bottom). 157

D.13 The relations between the observed parameters; kT_e-EM relation.The red, green, and sky blue solid lines are represented with the simulated spectral parameters in the Sedov phase with the ambient densities of 1 ($n_e = 4$), 0.1 ($n_e = 0.4$), and 0.01 ($n_e = 0.04$) cm^{-3}, respectively. The red, orange, magenta, green, and blue data points are represented with the plasma densities of $n_e \geq 4$, $4 > n_e \geq 2$, $2 > n_e \geq 0.4$, $0.4 > n_e \geq 0.2$, and $0.2 > n_e$ cm^{-3}, respectively. The filled boxes and open circles are also represented with the first and second VNEI components, respectively. The adopted thresholds are the χ^2_ν of < 1.50 (top), 2.00 (middle left), 1.75 (middle right), and 1.25 (bottom). 158

D.14 The relations between the observed parameters; EM-R relation. The red, magenta, green, blue and sky blue solid lines are represented with the simulated spectral parameters in the Sedov phase with the ambient densities of 1 ($n_e = 4$), 0.5 ($n_e = 2$), 0.1 ($n_e = 0.4$), 0.05 ($n_e = 0.2$), and 0.01 ($n_e = 0.04$) cm^{-3}, respectively. The red, orange, magenta, green, and blue data points are represented with the plasma densities of $n_e \geq 4$, $4 > n_e \geq 2$, $2 > n_e \geq 0.4$, $0.4 > n_e \geq 0.2$, and $0.2 > n_e$ cm^{-3}, respectively. The filled boxes and open circles are also represented with the first and second VNEI components, respectively. The adopted thresholds are the χ^2_ν of < 1.50 (top), 2.00 (middle left), 1.75 (middle right), and 1.25 (bottom). 159

D.15 The relations between the observed parameters; $kT_{\rm e}$-R relation.The red, green, and sky blue solid lines are represented with the simulated spectral parameters in the Sedov phase with the ambient densities of 1 ($n_{\rm e}$ = 4), 0.1 ($n_{\rm e}$ = 0.4), and 0.01 ($n_{\rm e}$ = 0.04) cm^{-3}, respectively. The red, orange, magenta, green, and blue data points are represented with the plasma densities of $n_{\rm e} \geq 4$, $4 > n_{\rm e} \geq 2$, $2 > n_{\rm e} \geq 0.4$, $0.4 > n_{\rm e} \geq 0.2$, and $0.2 > n_{\rm e}$ cm^{-3}, respectively. The filled boxes and open circles are also represented with the first and second VNEI components, respectively. The adopted thresholds are the χ^2_ν of < 1.50 (top), 2.00 (middle left), 1.75 (middle right), and 1.25 (bottom). 160

D.16 SNR age determined from the derived ionization parameter vs. the dynamical age derived from the Sedov model. The blue, green, and red data points are represented with CC, Type Ia, and unknown SNe, respectively. The filled boxes and open circles are represented with the first and second VNEI components, respectively. The adopted thresholds are the χ^2_ν of $<$ 1.50 (top), 2.00 (middle left), 1.75 (middle right), and 1.25 (bottom). . . . 162

E.1 Suzaku XIS X-ray image of the N23 in the bands 0.2–2 keV. Another nearby SNR, DEM L71, is also shown. The images from all the four XIS modules are combined. The green circles with a radius of 3.'3 are integration regions of the source photons from N23. The background photons were extracted from annular region which was removed the source and a center regions. The calibration sources at the corners are masked. 164

E.2 The data and the best-fit '$2kT1nt$' model of N23. in the 0.45–2.0 keV band. The black and red crosses show the data point from the FI and BI CCDs, respectively. The solid histograms with the same color are the best-fit model. The blue and green broken histograms show the components with $kT_{\rm e}$=0.57 and 0.22 keV, respectively. The lower panel shows the residuals from the best-fit model. 167

E.3 Smoothed *Chandra* image of N23 (a) in the 0.2–0.8 keV and (b) in the 1.5–2.0 keV band. The contours overlaid with labels of 1.0, 5.0, 15.0 (left) and 0.1, 0.5, 1.0 counts pixel^{-1} 168

E.4 Elemental abundance as derived from fits to the XIS data. The derived N23 abundance value is the square. The ratios are all relative to solar (Andres & Grevesse 1989). The silicon abundance in Russell & Dopita's work is highly uncertain as indicated by our use of a large error bar for this species. Dashed line represents the abundance in these SNRs are same to the LMC average. 171

List of Tables

2.1 Predicted mss of heavy elements nucleosynthesized by Type II and Ia. . . . 11
2.2 K-shell emission line energies for H-like and He-like ions. 21
2.3 The solar and LMC abundances for the major elements. 28

4.1 The X-ray Properties for SNRs in the LMC. 43
4.2 The observation logs for SNRs in the LMC. 45
4.3 The χ^2 $(d.o.f./\chi^2_\nu)$ for all models*. 51
4.4 The Best-Fit Parameters of the Thermal Component with "$1kT1nt$" and/or "$1kT1nt$ + Power law (1) (2)".* 52
4.5 The Best-Fit Parameters of the Non-Thermal Component with "$1kT1nt$ + Power law (1)".* 59
4.6 The Best-Fit Parameters of the Thermal Component with "$1kT1nt$".* . . . 60
4.7 The Best-Fit Parameters of the Non-Thermal Component with "$1kT1nt$+ Power law (2)".* 61
4.8 The Best-Fit Parameters of the Thermal Component with "$2kT1nt$–$2kT2nt$" and/or "$2kT1nt$–$2kT2nt$ + Power law (1) (2)".* 63
4.9 The derived metal abundance for SNRs in the LMC*. 66

A.1 Telescope dimensions and design parameters of XRT-I, compared with *ASCA* XRT. 90
A.2 Design parameters for pre-colimator. 91
A.3 Major XIS Background Emission Lines. 100
A.4 Parameters used in GTI selection of *Suzaku* 103
A.5 Basic performance of the EPIC detectors 105
A.6 The on-axis in orbit and on ground 1.5 keV HEW of the different XRT. . . 108
A.7 *Chandra* HRMA characteristics 117

C.1 The best-fit parameters of the entire remnant and the source A.* 134

D.1 The χ^2 $(d.o.f./\chi^2_\nu)$ for all models*. 139
D.2 The Best-Fit Parameters of the Thermal Component.* 140
D.3 The χ^2 $(d.o.f./\chi^2_\nu)$ for all models*. 143
D.4 The Best-Fit Parameters of the Thermal Component.* 144
D.5 The χ^2 $(d.o.f./\chi^2_\nu)$ for all models*. 147
D.6 The Best-Fit Parameters of the Thermal Component.* 148
D.7 Plasma density-radius relations and temperature distributions. 161

E.1 observation log. 164

E.2 Best-fit parameters for N23. 166
E.3 Input and derived properties for N23. 169
E.4 The characteristic ages for N23. 170

Chapter 1

Introduction

Supernovae (SNe) are explosion of stars at the end of their life. They are extremely luminous and sometimes outshine a whole galaxy. Because of the extremely large energy (10^{51} erg), a bright nebula is left behind the explosion, which is sustained over tens of thousands of years. It is called a SuperNova Remnant (SNR). SNRs are one of the targets of intense studies in X-ray astronomy. They are a key to understand the evolution of stars, nucleosynthesis of heavy elements, composition and conditions of interstellar medium, chemical evolution of the universe, and so on. Such information will be a basis to understand a galactic chemical evolution and a star formation history.

About 270 SNRs are known in the Milky Way Galaxy. They are mostly located near the galactic plane and suffer from large interstellar extinction. Therefore, they are not necessarily adequate for the systematic studies. Those in the Large Magellanic Cloud (LMC), on the other hand, are rather suited for the systematic studies because of its well-determined and uniform distance ($\sim$50 kpc; Feast 1999) and small interstellar absorption. These advantages mean that accurate plasma parameters can be estimated for the SNRs. Thus, systematic X-ray studies of SNRs in the LMC were tried with the launch of major X-ray observatories (e.g. Long 1983; Berkhuijsen 1986; Berkhuijsen 1987; Berkhuijsen 1988; Hughes et al. 1998; Williams et al. 1999). In spite of many observations, however, comprehensive understanding of the SNRs is still remained in a primitive stage. This is mostly due to the limitation of the X-ray telescopes. The past X-ray observations (e.g. *Einstein* and *ROSAT* satellites), for example, could obtain an X-ray flux and image, but little spectral information due to the lack of the energy resolution of the detectors. Because of this, even basic plasma parameters (e.g. temperature) could not be derived. The situation is drastically changed in early 1990s after the launch of the *ASCA* satellite, which utilized an X-ray CCD camera for the first time to archive good energy resolution. However, data statistics were rather poor and the resolution was still not enough especially below 1 keV. Furthermore, number of SNRs observed was also small (7 SNRs; Hughes et al. 1998). The energy resolution in this energy band is important to study the natures of the plasma in detail, because the X-ray emission from most SNRs is dominated below $\sim$ 2 keV. Currently, there are several X-ray observatories working on orbit with the good spectroscopic capability in this energy band and the large effective area, such as *Suzaku*, *XMM-Newton* and *Chandra*. Since the observation data with these satellites are accumulating now, a systematic study of SNRs in the LMC has finally become possible through the re-analysis of the good quality of data in archives.

This thesis focuses on the study of thermal X-ray emission from the SNRs utilizing

the advanced performances of *Suzaku*, *XMM-Newton*, and *Chandra* than previous X-ray observatories. In this thesis, we try to answer the following basic questions, which are essential to understand the nature and evolution of SNR comprehensively.

(1) Determination of evolutionary phase of the SNRs.
To determine evolutionary phase of the SNRs is important to estimate plasma parameters, such as mass, temperature, age, and so on. Thus, we discuss their evolutionary phase based on the various observed parameters.

(2) Empirical relations among the parameters.
It is known that the observed plasma density appears to decrease with a radius. Though this relation was discovered by McKee & Ostriker (1977), it remained one of the open questions for decades. We try to give a possible explanation to this relation. In general, this is related to the problem (1). Thus, it is important to identify their evolutionary phase. In addition, the plasma temperature distribution is closely related with this relation. We also discuss the plasma temperature distribution.

(3) a surrounding environment for both types of the SN explosions (Type Ia and CC).
Hughes et al. (1998) suggested that CC SNe exploded within a preexisting low-density cavity. We re-examine this topic with much larger numbers of samples.

In Chapter 2, we review the current understanding of the physical processes in the SNR. In Chapter 3, we also review the past results of systematic studies of SNRs in the LMC. In Chapter 4, we give results of the systematic studies of SNRs in the LMC. Combing all the works, we discuss and summarize their indications in Chapter 5 and 6. In this systematic study, several SNRs were found to stay possibly in the radiative cooling phase. Of these SNRs, we analyzed J0505.9-6802 (N23) in detail. Results of the analyses is presented in appendix § E.

Chapter 2

Review of Supernova Remnants

2.1 Supernovae (SNe)

Bright stellar outbursts are called "novae". "Supernovae" (SNe) were first recognized as an extremely bright class of novae clearly distinguished from the ordinary ones by Baade & Zwicky (1934). Nova results from the explosion at the surface of a mass accreting white dwarf, while SNe is originated from the explosion collapsing the entire star. A SN is believed to be the final stage of the evolution of a star. Since the brightness of SNe is comparable to that of a whole galaxy, SN explosion therefore is one of the most energetic stellar events. The kinetic energy reaches typically $\sim 10^{51}$ erg. SNe trigger the star formation through compression of the surrounding medium by the shock wave generated by the explosion. SNe also synthesize heavy elements, and release them into the interstellar space. SNe therefor play an important role in the cycle of matters. To study SNe and their remnants (SNRs) is one of the most interesting topics in astrophysics. In spite of the intense research by many people in recent years, the basic nature, e.g. the explosion mechanism, evolution of the remnants and the progenitor stars are not well understood.

At least 5 SN events occurred in our galaxy in the last 1000 years were recorded in our history. They are SN 1006, SN 1054 (Crab), SN 1181 (3C58), SN 1572 (Tycho), and SN 1604 (Kepler). For example, the last one was discovered on October 9, 1604. On February 23, 1987, a supernova (SN 1987A) appeared in the LMC. SN 1987A was so close that the progenitor star (B3 supergiant) could be identified in the archive data. This SN was the first one whose characteristics of the progenitor just before the explosion was known. An exciting discovery was the detection of neutrinos at the exacted time of the explosion. This was a remarkable confirmation of the theory on a process occurring in the core of a collapsing star. Information on the frequency of SNe is also important for many fields in astrophysics. The SN rate in galaxies largely affects the structure, kinematics, and composition of the interstellar medium (ISM). Especially, the evolution of elliptical galaxies may depend critically on the SN rate in them. SNe and their remnants also contribute to the cosmic-ray flux, and the SN rate is related to the birth rate of pulsars, X-ray binaries, and possibly black holes. A few tens of SNe are discovered in the galaxies other than the milky Way. From such studies, the galactic SN rate is believed to be a few per one century. While, in the Galaxy, about a half dozen galactic SNe have been recorded in history in the past 10 centuries. An apparently young supernova remnant Cassiopeia A (Cas A) is believed to be about $\sim$300 yr old. Such SNRs are all located

within about 5 kpc from the Sun, which covers only 15 % for the Galactic disk. This implies that ∼40 SNRs with ages younger than 1000 years would exist in the Galactic disk.

2.1.1 Classication of SNe

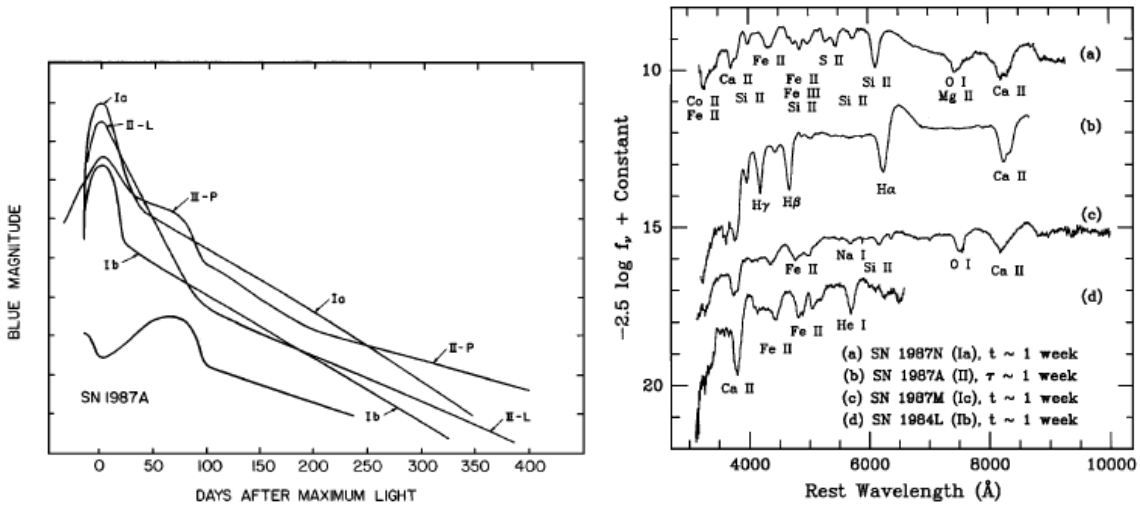

Figure 2.1: Left: Schematic light curves for Types Ia, Ib, II-L, II-P, and SN 1987A SNe. Right: Spectra of SNe, showing early-time distinctions between the four major types and subtypes (a: Type Ia; SN 1987N, b: Type II; SN 1987A, c: Type Ic; SN 1987M, and d: Type Ib; SN 1987L). These figures were taken from Filippenko (1997).

SNe are essentially classified into a core-collapsed (CC; Type II and Type Ib/Ic) by massive stars and a thermonuclear runaway of white dwarfs (Type Ia). They play an important role for the chemical evolution of galaxies through the production of heavy elements, such as O group for CC and Fe group for Type Ia. Thus, studying SNRs is also important to understand the chemical evolution of galaxies. In this subsection, we summarize the detailed classification and the nature of SNe referring to the research history.

Historically astronomers recognized two types of SNe which were distinguished by their optical spectra. The basic classification scheme currently adopted is therefore also based on their optical spectra as shown in figure 2.1 (right; Filippenko 1997). A basic criterion of the classification is the presence (SN II: Type II supernova) or the absence (SN I: Type I supernova) of H lines in the spectrum near the maximum light (figure 2.1 left; Filippenko 1997). This is a fundamental criterion, not only because one or two high-quality spectra suffice for their classification, but because it is of clear-cut physical importance as well. Stars that have shed their outer hydrogen in the end of its evolution are pre-SN I stars, while stars that have retained them until the explosion are pre-SN II stars. The distribution for SN II events observed in distant galaxies (relatively young galaxies) supports this classification scheme. SNe II also occur in the arms of spiral galaxies where the stellar population is relatively old. In contrast, the SN I events occur in all types of galaxies, and show no preference for spiral arms. This suggests that the

progenitor stars for SNe I (especially SNe Ia) are billions of years old, and consequently not very massive. Subclasses for SNe I are difined by the presence or the absence of Si and He lines, while subclasses of SNe II are difined by the light curves. The light curves also have important informations. SNe I and II also display different light curves and luminosities at the maximum light. SN Ia events display similar light curves, and the intensity rises quickly to the maximum, reaching a luminosity of more than 10^9 $L_\odot$ in about two weeks. An initial rapid decay is followed by a long slow decline in the light curve. The luminosity falls exponentially with the characteristic time scale of ∼55 days until the SNe dade out to become invisible. On the other hand, SN II events show at least two distinct light curves. One subclass of SNe II has a 'plateau' in the post-maximum phase (SNe II-P), which sustains a nearly constant luminosity for about 50 days. The other subclass sometimes show a plateau, whose brightness decline linearly after the maximum (SNe II-L).

Type Ia Supernovae (SNe Ia)

Hoyle & Fowler (1960) pointed out that SNe I resulted from an explosion following the ignition of the nuclear fuel under conditions of the extreme degeneracy in an evolved star. Arnett (1969) presented the hydrostatic and hydrodynamic calculations for the evolution of the ignited core. An explosive instability due to the ignition of C+C develops at a center density of $\sim 2 \times 10^{19}$ $\mathrm{g\,cm^{-3}}$, and leads to a supersonic burning ("detonation wave"). The shock wave toward the surface of the star reaches up to ~ 20000 $\mathrm{km\,s^{-1}}$. The star is totally disrupted, and no condensed remnant is left behind. The nuclear reactions produce a large amount ^{56}Ni, which becomes main constituent of the exploded star. Finally, significant amount Fe is produced by the following nuclear decays, $^{56}\mathrm{Ni} \rightarrow {}^{56}\mathrm{Co} \rightarrow {}^{56}\mathrm{Fe}$. However, the amount Fe predicted by this model was several times larger than those actually observed. To solve this problem, Nomoto et al. (1984) proposed "deflagration" instead of "detonation". They proposed the carbon deflagration models in accreting C+O white dwarfs. According to this model, the relatively rapid accretion onto the surface of the white dwarfs leads to the ignition of the core. Subsequent propagation of the convective carbon burning front ("deflagration wave") and associated explosive nucleosyntheses were calculated for several cases of mixing length in the convection theory. The deflagration wave synthesizes ^{56}Ni of 0.5–0.6 $M_\odot$ in the inner layer of the stars; this amount is sufficient to explain the light curve of SNe I by the radioactive decays of ^{56}Ni and ^{60}Co. In the outer layers, substantial amount of intermediate mass elements, Ca, Ar, S, Si, Mg, and O are synthesized in the decaying deflagration wave; this is consistent with the spectra of SNe I near the maximum light. As a result, a star is disrupted completely, leaving no compact star remnant behind. Thus, since the carbon deflagration model can account for many observed features for SNe Ia, it is considered to be a standard model for SNe I. Although SNe I is divided into a few subclasses, "Classical" SNe I is now referred to as SNe Ia which is one of the major classes.

Core-Collapsed Supernovae (SNe II and Ib/Ic)

A final stage of evolution of a star more massive than 10 $M_\odot$ is different from that for a lighter star. It consumes nuclear fuel very quickly. When its fuel is exhausted, the end is marked by a great catastrophe (e.g. SN II or Ib/Ic explosion). The core of the star collapse suddenly to release a large amount of the gravitational energy, which in turn

leads to the explosion of the star. Among the SNe I, two other subclasses SNe Ib/Ic, which are fainter than the SN Ia, are caused by this mechanism. SN Ib events occur in spiral galaxies and star forming regions. The clearest difference from SNe Ia is in the spectra at the late phase of >250 days. Fe lines dominate the spectra for SNe Ia, while O lines dominate the spectra for SNe Ib. The progenitors for SNe Ib are thought to be massive stars that have lost their envelope (hydrogen). Wolf-Rayet stars, for example, are possible progenitors since they have shed their outer hydrogen envelope in their massive stellar wind. The SN Ib events which show the weak evidence of He, are inferred as SNe Ic.

At the beginning of their evolution, hydrogen in the core is converted to helium . When helium is exhausted, the core of the star contracts. It contracts until the temperature becomes high enough to ignite helium into carbon, oxygen, and so on. At the same time, the pressure increases in the layer for hydrogen surrounding the core. This results in an ignition of nuclear burning in this outer layer, creating s shell of the helium surrounding the core of heavier elements. At the end, the star is stratified like "onion" layers. The central core is accumulates Fe, which is the end point of the fusion process because Fe can no longer generate nuclear energy. It is sustained by the degenerate pressure of electrons, and is at the Chandrasekhar limit. The mass of the core, however, is continuously increasing as the adjacent layer of Si, which burns into Fe. The core is compressed more, and the internal temperature increases to $\simeq 10^{10}$ K. This causes the decomposition of ^{56}Fe,

$$^{56}\mathrm{Fe} \rightarrow 13^{4}\mathrm{He} + 4\mathrm{n} - 124.4 \text{ MeV}. \tag{2.1}$$

As a result, the energy is absorbed, reducing the pressure and causing the core to shrink. Free protons are created which combine with electrons to make neutrons. Core-supporting electrons disappear in this process to cause further drop in pressure. The process runs away, and the gravity overwhelms the electron pressure. The gravitational collapse proceeds, and finally leads to a heavier homogeneous neutron matter which is supported by the nuclear force. The energy explosively released by the falling matter creates a shock wave. This shock propagates outward until it reaches the outermost layer of a star. The shock wave leads to an explosive nuclear fusion, and ejects the nuclear fused material outwards. Therefore, the abundances created by CC (Type II or Ia/Ic) are affected by the envelope, which depends on the mass of the collapsing star.

We can observe the expanding hot material in such remnants. A rapidly-cooling hot neutron star may be left at the center and, if the neutron star is spinning rapidly, it will become observable later as a pulsar at the remnant center. Total energy generated by the collapse and subsequent nuclear reaction are to be $\sim 10^{53}$ erg. Of this amount of energy, almost all is carried away by neutrinos, because of their low reaction cross section, can escape easily from the collapsing star, and are extremely difficult to be detected. The light from the supernova itself carries only $\sim 10^{49}$ erg. On the other hand, the kinetic energy of the expanding matter is typically to be $\sim 10^{51}$ erg. Finally, we present SNR images for each SN type in figure 2.2. Cas A, G292.2-1.8, and E0102-7219 are to be CC SNe, while DEM L71, SN 1006, and RCW 86 are believed to be Type Ia SNe.

2.1.2 Multiwavelength SNR

In this subsection, we brief explain emissions from SNRs over multiwavelength. Cassiopeia A is relatively young SNR in our Galaxy. Thus, Cassiopeia A is one of the good targets

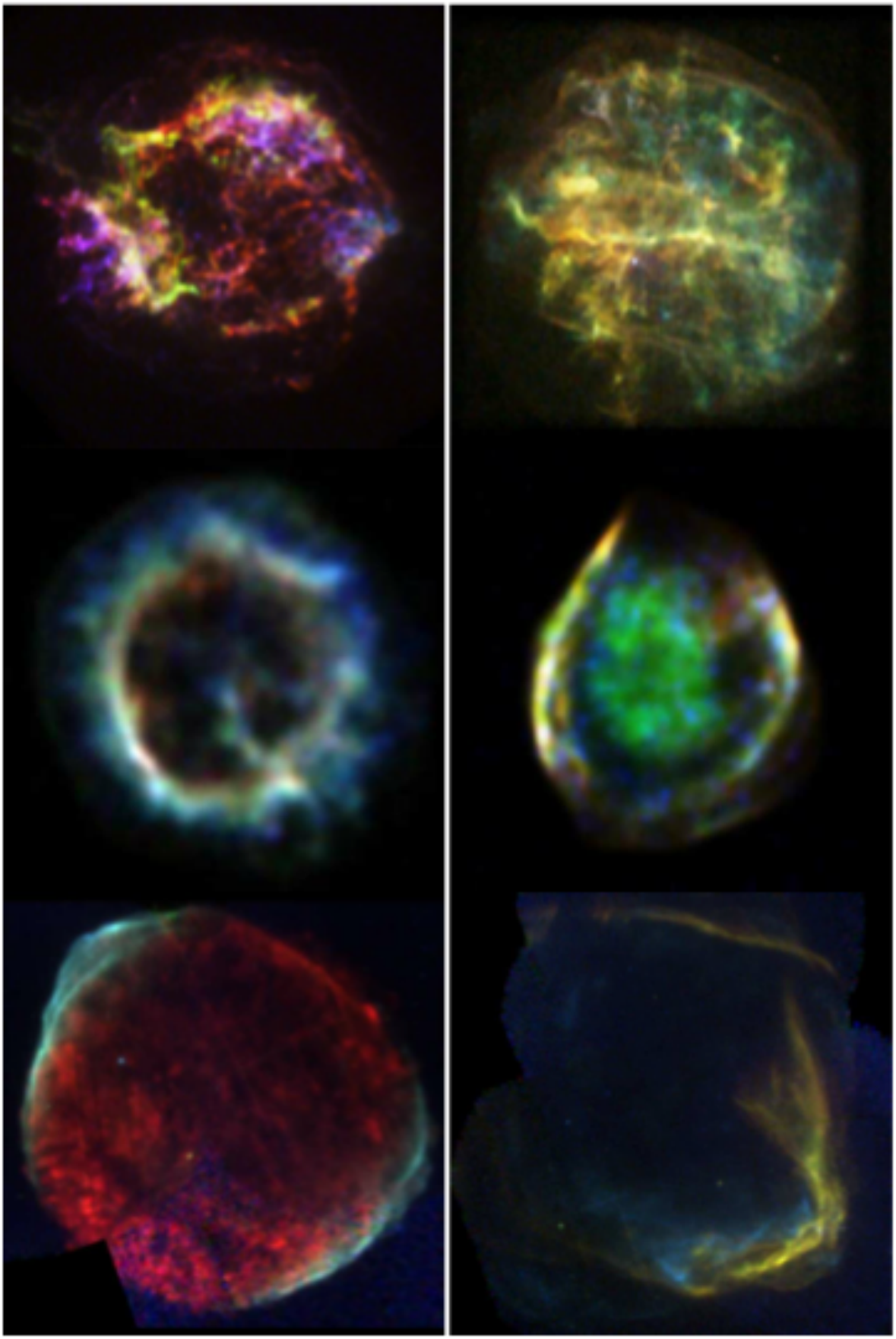

Figure 2.2: *Chandra* and *XMM-Newton* (bottom images) images of SNRs. From left to right, top to bottom: Cas A, G292.2-1.8, E0102-7219, DEM L71, SN 1006, and RCW 86. This picture was adopted from Vink (2004).

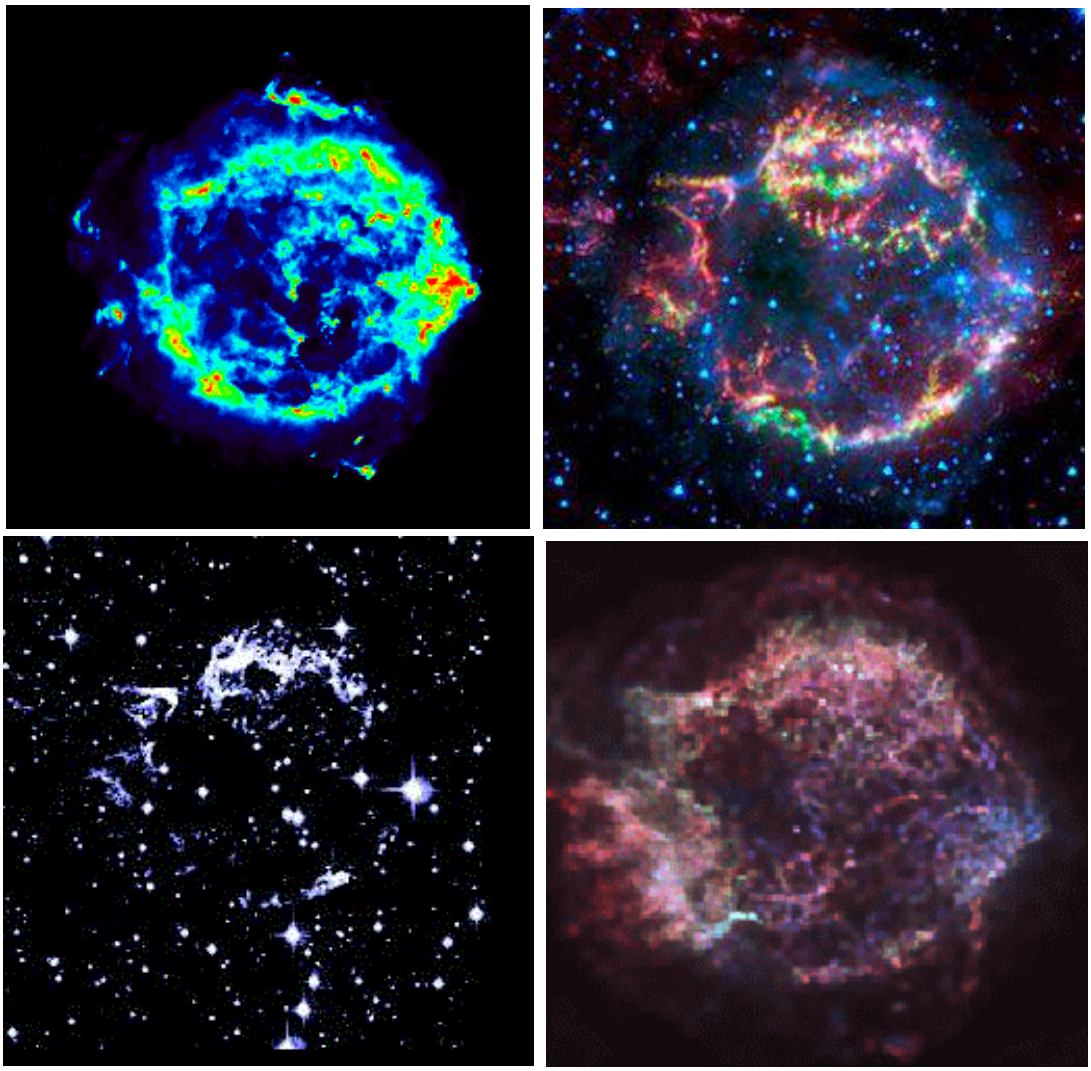

Figure 2.3: The radio (top left), Infrared (top right), optical (bottom left), and X-ray (bottom right) images of Cassiopeia A.

to study phenomena over multiwavelength. In figure 2.3 we present the multiwavelength images of Cassiopeia A. [1]

The radio image of Cassiopeia A was obtained at a wavelength of ∼21 cm with the Very Large Array interferometer in New Mexico. This image reveals a complex structure in the emission shell, due in part to the variable density of the surrounding interstellar medium. The radio emission is primarily associated with synchrotron radiation, the result of fast-moving electrons immersed in a magnetic field.

The Near/Mid-Infrared image Cassiopeia A was obtained from the Spizer Space Telescope. In this image 3.6 microns is shown as blue, 4.5 microns as green and 8.0 microns as red. As the star's layers whiz outward, they are ramming, one by one, into a shock wave from the explosion and heating up. Material that hit the shock wave sooner has had more time to heat up to temperatures that radiate X-ray and visible light. Material that

[1] http://coolcosmos.ipac.caltech.edu/cosmic_classroom/multiwavelength_astronomy/multiwavelength_museum/casA.html

is just now hitting the shock wave is cooler and glowing with infrared light. Consequently, previous X-ray and visible-light observations identified hot, deep-layer material that had been flung out quickly, but not the cooler missing chunks that lagged behind. Spiter's infrared detectors were able to find the missing chunks – gas and dust consisting of the middle-layer elements neon, oxygen and aluminum.

Unlike many astronomical phenomena, SNRs are often unimpressive at visible-light wavelengths. This image barely reveal the expanding spherical gas shell, a remnant of the original SN explosion, with the most prominent emission seen to the north.

The X-ray image was the first science image obtained and released by the *Chandra* X-ray Observatory. The colors denote different X-ray energies, with red corresponding the lowest energies and blue corresponding the highest. The small greenish-white clumps, most notable to the southeast (lower left) , are enhanced in silicon and sulfur. The reddish filaments in the outer shell to the southeast are enhanced in iron. These elements are remnants from deep within the progenitor star that exploded and produced this SNR.

2.2 Nucleosynthesis

Heavy elements are synthesized through a thermonuclear fusion and a supernova explosion, and are distributed in the universe. In this section, we briefly explain their nucleosynthesis. Stars stay in hydrostatic equilibrium archived by the balance between the thermal pressure and the gravity. When a star is formed through gravitational contraction, and the central temperature exceeds the some critical value, a thermonuclear fusion reaction will start. First, when the central temperature reaches $\sim 10^7$ K, hydrogen is ignited through the following process called a p-p chain:

$$\begin{aligned} \mathrm{p} + \mathrm{p} &\rightarrow {}^2\mathrm{H} + \mathrm{e}^+ + \nu_\mathrm{e} + 1.44 \text{ MeV} \\ {}^2\mathrm{H} + \mathrm{p} &\rightarrow {}^3\mathrm{He} + \gamma + 5.49 \text{ MeV} \\ {}^3\mathrm{He} +^3 \mathrm{He} &\rightarrow {}^4\mathrm{He} + 2\mathrm{p} + 12.86 \text{ MeV}. \end{aligned}$$

When the central temperature reaches $\sim 2\times10^7$ K, hydrogen burning proceeds dominantly through the CNO cycle defined below:

$$\begin{aligned} \mathrm{p} +^{12} \mathrm{C} &\rightarrow {}^{13}\mathrm{N} + \gamma + 1.95 \text{ MeV} \\ {}^{13}\mathrm{N} &\rightarrow {}^{13}\mathrm{C} + \mathrm{e}^+ + \nu_\mathrm{e} + 1.37 \text{ MeV} \\ p +^{13} \mathrm{C} &\rightarrow {}^{14}\mathrm{N} + \gamma + 7.54 \text{ MeV} \\ p +^{14} \mathrm{N} &\rightarrow {}^{15}\mathrm{O} + \gamma + 7.35 \text{ MeV} \\ {}^{15}\mathrm{O} &\rightarrow {}^{15}\mathrm{N} + \mathrm{e}^+ + \nu_\mathrm{e} + 1.86 \text{ MeV} \\ p +^{15} \mathrm{N} &\rightarrow {}^{12}\mathrm{C} +^4 \mathrm{He} + 4.96 \text{ MeV}. \end{aligned}$$

Helium is synthesized from hydrogen in both processes. The p-p chain is the dominant process in the sun. Stars spend most of the their lifetime in the hydrogen burning stage. Therefore, they are called main-squence stars. When hydrogen at the core is exhausted, the pressure to be balanced with gravity is no longer maintained. The core begins to contract to raise the temperature and pressure which becomes high enough to ignite helium, and carbon and oxygen are synthesized by the helium burning. This process proceeds quickly in stars whose mass is larger than $\sim$2 $\mathrm{M}_\odot$. If the stellar mass exceeds $\sim$

8 $M_\odot$, carbon burning takes place, and O+Ne+Mg core is produced. If the mass is larger than ∼10 $M_\odot$, Si is synthesized by O burning, and Fe is synthesized by Si burning. As a result, stars have an onion-like structure at the final stage of their evolution as shown in figure 2.4. Such massive stars become core-collapse SNe. The elements synthesized by an

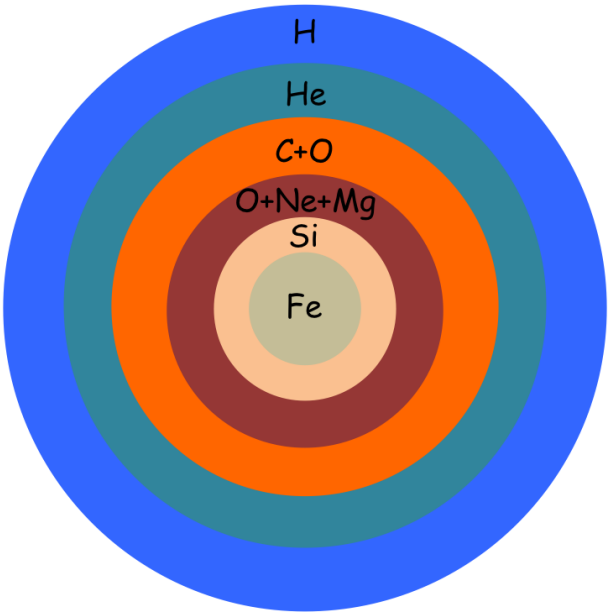

Figure 2.4: Onion-like structure in massive star just prior to core collapse.

explosive nuclear fusion depend on the temperature and the density. Since the explosive nucleosynthesis must take place quickly before the temperature decreases, it requires higher temperature than the stellar nucleosynthesis. When the maximum temperature reaches $\sim 2 \times 10^9$ K, explosive carbon burning begins:

$$^{12}\mathrm{C} +^{12} \mathrm{C} \rightarrow^{4} \mathrm{He} +^{20} \mathrm{Ne},$$

and explosive Ne burning begins, at the same temperature. Main reactions for the Ne burning are described in the following processes:

$$^{20}\mathrm{Ne} + \gamma \rightarrow {}^{4}\mathrm{He} +^{26} \mathrm{O}$$
$$^{20}\mathrm{Ne} +^{4} \mathrm{He} \rightarrow \gamma +^{24} \mathrm{Mg}$$
$$^{24}\mathrm{Mg} +^{4} \mathrm{He} \rightarrow \gamma +^{28} \mathrm{Si}.$$

If the maximum temperature reaches $\sim$ 3–4$\times 10^9$ K, the explosive O burning begins:

$$^{16}\mathrm{O} +^{16} \mathrm{O} \rightarrow {}^{4}\mathrm{He} +^{28} \mathrm{Si}$$
$$^{16}\mathrm{O} +^{16} \mathrm{O} \rightarrow \gamma +^{32} \mathrm{S}.$$

Furthermore, ^{36}Ar and ^{40}Ca are synthesized by the reaction between ^{32}Si and ^{4}He. If the temperature exceeds $\sim 4 \times 10^9$ K, the explosive Si burning begins. Si and S absorb the He nucleus, and synthesize heavy elements, such as Cr, Fe, Ni, and Z. A large amount of ^{56}Ni is synthesized in the Si burning process. Heavier elements than Ni are synthesized by SNe. Mass of the various elements synthesized in SNe is predicted by Iwamoto et al. (1999) and Nomoto et al. (1997), which is listed in table 2.1.

Table 2.1: Predicted mss of heavy elements nucleosynthesized by Type II and Ia.

Species	Mass $M_\odot$				
	SN II 13 $M_\odot$	SN II 15 $M_\odot$	SN II 20 $M_\odot$	SN II 25 $M_\odot$	W7
C	2.7×10^{-3}	8.3×10^{-2}	1.1×10^{-1}	1.5×10^{-1}	4.8×10^{-2}
N	5.8×10^{-8}	5.4×10^{-3}	2.7×10^{-3}	9.5×10^{-3}	1.2×10^{-6}
Ne	2.3×10^{-2}	3.3×10^{-1}	1.5	3.0	1.4×10^{-1}
Mg	1.2×10^{-2}	3.6×10^{-2}	2.6×10^{-1}	2.3×10^{-1}	8.6×10^{-3}
Si	7.0×10^{-2}	7.9×10^{-2}	1.8×10^{-1}	1.2×10^{-1}	1.6×10^{-1}
S	1.7×10^{-2}	3.2×10^{-2}	1.0×10^{-1}	4.1×10^{-2}	8.7×10^{-2}
Ar	2.9×10^{-3}	6.3×10^{-3}	2.4×10^{-2}	7.4×10^{-3}	1.6×10^{-2}
Ca	2.7×10^{-3}	5.4×10^{-3}	3.5×10^{-3}	6.2×10^{-3}	1.2×10^{-2}
Fe	1.6×10^{-1}	1.5×10^{-1}	7.9×10^{-2}	5.8×10^{-2}	7.5×10^{-1}
Ni	1.1×10^{-2}	1.2×10^{-2}	6.8×10^{-3}	2.2×10^{-3}	1.3×10^{-1}

2.3 Shock Wave

A supernova explosion produces ejecta whose speed far exceeds the sound speed. When the ejecta collide with surrounding medium, a "shock" wave is produced and propagates in the interstellar medium. In this section, we summarize basic physics related to the shock wave. When the velocity of fluid exceeds a sound speed of ambient medium, physical quantities may change discontinuously at the shock front. This is because the information cannot propagate faster than the sound velocity. If it is the case, the discontinuity of the physical quantities can steadily exist, and propagate at supersonic speed in the surrounding medium. This is called a "shock wave". The sound velocity is given by

$$v_{\rm s} = \sqrt{\frac{\gamma p}{\rho}}, \tag{2.2}$$

where γ, p, and ρ are the heat capacity ratio, the pressure, and the density, respectively. Assuming an adiabatic condition ($p\rho^{-\gamma} = const$), that is $p \propto \rho^{\gamma}$, the sound velocity is also given by

$$v_{\rm s} \propto \sqrt{\gamma\rho^{\gamma-1}}. \tag{2.3}$$

Therefore, the sound velocity is a function of the density.

2.3.1 Condition of Discontinuity

Discontinuity in a gas flow can occur at one or more surface. The physical quantities change discontinuously across such a surface, which is called a "surface of discontinuity". Certain boundary conditions must be satisfied across the surface of discontinuity. To formulate these conditions, we consider a surface element, and use a coordinate system fixed to the element. The coordinate system is shown in figure 2.5. The boundary conditions for the surface of the discontinuity are as follows. The continuity for the mass flux is given by

$$\rho_1 v_{1\rm x} - \rho_2 v_{2\rm x} = 0, \tag{2.4}$$

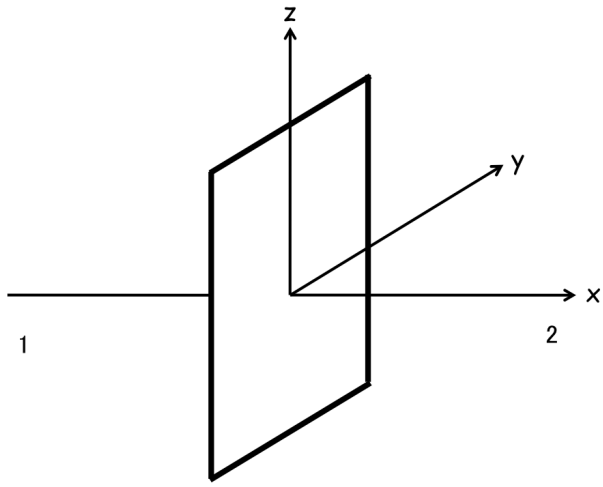

Figure 2.5: A schematic view of the coordinate system around the shock front.

where ρ_i and $v_{\rm ix}$ are a density and an X-ray component of velocity in the region "i", respectively. The continuity of the energy flux is also given by

$$\rho_1 v_{1\rm x}(\frac{1}{2}v_{1\rm x}^2 + \omega_1) - \rho_2 v_{2\rm x}(\frac{1}{2}v_{2\rm x}^2 + \omega_2) = 0, \tag{2.5}$$

where $\omega = \epsilon + pV$ is an enthalpy per unit mass (ϵ: an internal energy, V: a volume, and p: a pressure). The continuity of the momentum flux is given by

$$p_1 + \rho_1 v_{1\rm x}^2 - p_2 - \rho_2 v_{2\rm x}^2 = 0 \tag{2.6}$$
$$\rho_1 v_{1\rm x} v_{1\rm y} - \rho_2 v_{2\rm x} v_{2\rm y} = 0 \tag{2.7}$$
$$\rho_1 v_{1\rm x} v_{1\rm z} - \rho_2 v_{2\rm x} v_{2\rm z} = 0, \tag{2.8}$$

where $v_{\rm iy}$ and $v_{\rm iz}$ are velocities in the region "i" along the y- and z-axis, respectively. From these equations, we can immediately deduce the possibility of two types for the surface of the discontinuity. In the first type, there is no mass flux through the surface. This means that

$$\rho_1 v_{1\rm x} = \rho_2 v_{2\rm x} = 0 \rightarrow v_{1\rm x} = v_{2\rm x} = 0 \tag{2.9}$$
$$p_1 = p_2, \tag{2.10}$$

where $v_{\rm y}$ and $v_{\rm z}$ may be discontinuous by any amount from equation 2.7 and 2.8. We call this a "tangential discontinuity". In the second type, the mass flux is not zero, and $v_{1\rm x}$ and $v_{2\rm x}$ are therefore also not zero. Equations equation 2.4–2.8 can be reduced to the followings:

$$v_{1\rm y} - v_{2\rm y} = v_{1\rm z} - v_{2\rm z} = 0 \tag{2.11}$$
$$\rho_1 v_{1\rm x} - \rho_2 v_{2\rm x} = 0 \tag{2.12}$$
$$\frac{1}{2}v_{1\rm x}^2 + \omega_1 - \frac{1}{2}v_{2\rm x}^2 - \omega_2 = 0. \tag{2.13}$$

Discontinuity like this is called a "shock wave", or simply a "shock".

2.3.2 The Shock Adiabatic

Details of the shock wave are described in this subsection. For this purpose, we first rewrite the conditions for the shock wave. We have seen in the previous section that the tangential component of the gas velocity ($v_{\rm y}$ and $v_{\rm z}$) is continuous in this type of discontinuity ("shock wave"). We can therefore take a coordinate system in which the tangential component of the gas velocity ($v_{\rm y}$ and $v_{\rm z}$) becomes zero in both region (1 and 2). Then, we can write $v_{\rm x}$ simply as v. We rewrite the conditions for the shock as follows:

$$\rho_1 v_1 = \rho_2 v_2 \equiv j \tag{2.14}$$

$$p_1 + \rho_1 v_1^2 = p_2 + \rho_2 v_2^2 \tag{2.15}$$

$$\frac{1}{2} v_2^1 + w_1 = \frac{1}{2} v_2^2 + w_2. \tag{2.16}$$

Here we define the specific volume (volume per mass unit) as $V_1 = \frac{1}{\rho_1}$ and $V_2 = \frac{1}{\rho_2}$. Using the specific volume, we can rewite equation 2.14 as

$$v_1 = jV_1 \text{ and } \mathrm{v}_2 = \mathrm{jV}_2. \tag{2.17}$$

From equations 2.15 and 2.17, we obtain the relation among the density, the pressure, and the shock velocity, as follows,

$$j^2 = \frac{p_2 - p_1}{V_1 - V_2}. \tag{2.18}$$

Moreover, we can obtain the following equation from equations 2.15 and 2.18:

$$v_1 - v_2 = \sqrt{(p_2 - p_2)(V_1 - V2)}. \tag{2.19}$$

We eliminate v from equations 2.14, 2.15 and 2.16, and obtain:

$$\omega_1 - \omega_2 + \frac{1}{2}(V_1 + V_2)(p_2 - p_1) = 0. \tag{2.20}$$

Substituting $\omega = pV + \epsilon$, we also obtain:

$$\epsilon_1 - \epsilon_2 + \frac{1}{2}(V_1 - V_2)(p_1 + p_2) = 0. \tag{2.21}$$

These relations combine the thermodynamical quantities in the two regions separated by the surface of the discontinuity. When p_1 and V_1 are given, equations 2.20 and 2.21 give the relation between p_2 and V_2. This relation is called the "shock adiabatic" or the "*Rankine- Hugoniot* adiabatic". If we assume the ideal gas, the equation of the state is $pV = \frac{RT}{\mu}$, where $R = 8.314 \times 10^7$ erg K^{-1}, μ is the mean atomic weight of the gas. The entropy is given by $\omega = \gamma/(\gamma - 1)pV$. Substituting them into equations 2.20 and 2.21, we can obtain the ratios for densities and temperatures before and after the shock as follows:

$$\frac{\rho_1}{\rho_2} = \frac{V_2}{V_1} = \frac{(\gamma+1)p_1 + (\gamma-1)p_2}{(\gamma-1)p_1 + (\gamma+1)p_2} \tag{2.22}$$

$$\frac{T_1}{T_2} = \frac{p_2}{p_1}\frac{(\gamma+1)p_1 + (\gamma-1)p_2}{(\gamma-1)p_1 + (\gamma+1)p_2}. \tag{2.23}$$

For the velocities of the gas, we also obtain:

$$v_1^2 = \frac{1}{2}V_1[(\gamma-1)p_1 + (\gamma+1)p_2] \tag{2.24}$$

$$v_2^2 = \frac{1}{2}\frac{V_1[(\gamma+1)p_1 + (\gamma-1)p_2]^2}{(\gamma-1)p_1 + (\gamma+1)p_2}. \tag{2.25}$$

Assuming a strong shock ($\frac{p_2}{p_1} \gg 1$), equations 2.22 and 2.23 can be reduced to:

$$\frac{\rho_1}{\rho_2} \sim \frac{\gamma-1}{\gamma+1} \tag{2.26}$$

$$\frac{T_1}{T_2} \sim \frac{(\gamma-1)p_2}{(\gamma+1)p_1}. \tag{2.27}$$

From equation 2.24, the velocities are also given as:

$$v_2^2 = \frac{1}{2}(\gamma+1)p_2V_1 \tag{2.28}$$

$$v_1^2 = \frac{1}{2}\frac{(\gamma-1)^2p_2V_1}{\gamma+1}. \tag{2.29}$$

From equation 2.19, the pressure after the shock is

$$p_2 \sim \frac{\gamma+1}{2}\rho_1(v_1-v_2)^2. \tag{2.30}$$

Here, v_p is a post-shock velocity, and $v_s \equiv v_1$ is a shock velocity at the rest frame of the upstream. From equations 2.24, 2.25 and 2.30, the post-shock velocity v_p and the post-shock pressure $v_p = v_2$ are

$$v_p = \frac{2v_2}{\gamma+1} \tag{2.31}$$

$$p_p = \frac{2\rho_1 v_s^2}{\gamma+1}. \tag{2.32}$$

Using the equation of state, we can derive the relation between the post-shock temperature and velocity:

$$kT_p = \frac{p_p\mu}{\rho_2} = \frac{2(\gamma-1)(\gamma+1)^2}{\mu}m_{\rm H}v_s^2, \tag{2.33}$$

where $m_{\rm H}$ is the hydrogen mass, and μ is the mean atomic weight. Assuming the solar composition, the mean atomic weight is estimated to be ~ 0.6. If we assume monatomic gas ($\gamma = \frac{5}{3}$), the density ratio is derived from equation 2.26 as follows:

$$\frac{\rho_1}{\rho_2} = \frac{1}{4}. \tag{2.34}$$

In addition, from equation 2.33, the post-shock temperature for monoatomic gas is also derived as:

$$kT_p = \frac{3}{16}\mu m_{\rm H}v_s^2. \tag{2.35}$$

Equations 2.34 and 2.35 can be used to estimate a plasma density and temperature from the X-ray observation.

2.4 SNR Evolution

An evolution of SNRs are essential for understanding the nucleosynthesis, nature and surrounding environment for SNRs. In this section, we explain the evolution for SNRs. The evolution for SNRs is divided into the following 4 steps: free expansion phase, adiabatic expansion phase (Sedov phase), radiative cooling phase and disappearance phase. Let us assume that the explosion occurs a spherical symmetrically in a uniform medium. We summarize the evolution in this section.

2.4.1 Free Expansion Phase

Free expansion phase is the initial phase of the SNR evolution. In this phase, the shock expand without any deceleration unless a swept-up ISM mass is much bigger an ejecta mass. The initial phase for the SNR evolution therefore is characterized by the free expansion ejecta. The average velocity for the ejecta ($v_{\rm free}$) with the energy conservation low is given by

$$v_{\rm free} = \sqrt{\frac{2E_0}{M_0}} = 3.2 \times 10^8 \left(\frac{E_0}{10^{51}\ {\rm erg}}\right)^{0.5} \left(\frac{M_0}{10\ {\rm M}_\odot}\right)^{-0.5}\ [{\rm cm\,s^{-1}}], \tag{2.36}$$

where E_0, M_0 and $\rm M_\odot$ are the initial explosion energy, the ejecta, and the mass of Sun ($\rm M_\odot = 1.9884\times10^{30}$ kg), respectively. Since the velocity is much larger than the sound speed to a surrounding medium, a shock wave (the blast wave shock) precede. The blast wave shock expands without any deceleration, and the time dependence for the radius $R(t)$ is given simply by

$$R(t) \propto t. \tag{2.37}$$

The blast-wave push the surrounding medium outward, then the ejecta is retarded by the reaction. The deceleration is caused by the occurrence of a shock in the ejecta, which is called "reverse shock". At the end of this phase, the swept-up ISM mass by the blast wave shock ($M_{\rm swept}$) becomes comparable to that of the ejecta mass. The radius and the age for SNR at this stage are given by

$$R_{\rm free} = \left(\frac{3M_0}{4\pi\rho_0}\right)^{\frac{1}{3}} = 4.6 \left(\frac{M_0}{10\ {\rm M}_\odot}\right)^{\frac{1}{3}} \left(\frac{n_0}{1\ {\rm cm^{-3}}}\right)^{-\frac{1}{3}}\ [{\rm pc}], \tag{2.38}$$

and

$$t_{\rm free} \simeq \frac{\sqrt{2}R_{\rm free}}{v_{\rm free}} = 6.3 \times 10^{10} \left(\frac{E_0}{10^{51}\ {\rm erg}}\right)^{-\frac{1}{2}} \left(\frac{M_0}{10\ {\rm M}_\odot}\right)^{\frac{5}{6}} \left(\frac{n_0}{1\ {\rm cm^{-3}}}\right)^{\frac{1}{3}}\ [{\rm s}], \tag{2.39}$$

where ρ_0 [$\rm g\,cm^{-3}$] and n_0 [$\rm cm^{-3}$] are an ambient density. The free expansion phase continues ~1000 yr from the expansion, and the radius becomes ~5 pc, assuming a typically explosion.

2.4.2 Adiabatic Phase (Sedov Phase)

The next phase of the SNR evolution is called an adiabatic phase (Sedov phase). When the swept-up ambient mass becomes larger than the ejecta mass, the SNR evolution moves

into Sedov phase. Then, the radiative cooling is still negligible. The evolution can be explained as the result for the similarly solution at a point explosion (Sedov, 1959). The condition can be characterized by using only the expansion energy (E_0), the ambient density (ρ_0) and the age ($t_{\rm sedov}$). Thus, we can defined a non-dimensional parameter ξ as

$$\xi = R_{\rm sedov}\left(\frac{E_0 t^2}{\rho_0}\right)^{-\frac{1}{5}}. \tag{2.40}$$

In the case of that the ambient density has the radius dependence with $\rho_0(r) = Ar^{-m}$, such as massive star, which make a density profile with $\propto r^2$ by a stellar wind (Dwarkadas, 2005). Then, equation 2.40 is rewritten by

$$\xi = R_{\rm sedov}\left(\frac{E_0 t^2}{\rho_0}\right)^{-\frac{1}{5-m}} t^{-\frac{2}{5-m}}. \tag{2.41}$$

Then, the radius for the expanding shell $R_{\rm sedov}$ is also given by

$$R_{\rm sedov} = \xi_0\left(\frac{E_0}{A}\right)^{\frac{1}{5-m}} t^{\frac{2}{5-m}}, \tag{2.42}$$

where ξ_0 can be determined from the energy conservation law. The shock velocity is decelerated in nearly uniform density with $m < 3$, and is accelerated in high density gradient with $m > 3$. In this study, we utilize the density profile with $m = 0$. Using $\xi_0 = 1.17$ for an ideal gas ($\gamma = \frac{5}{3}$; Landau & Lifshitz 1959), and $m = 0$ which means an uniform ambient density, the radius ($R_{\rm sedov}$), the temperature ($T_{\rm sedov}$), and the velocity of the shock ($v_{\rm sedov}$) are described as

$$R_{\rm sedov} = 12.5\left(\frac{E_0}{10^{51}\ {\rm erg}}\right)^{\frac{1}{5}}\left(\frac{n_0}{1\ {\rm cm}^{-3}}\right)^{-\frac{1}{5}}\left(\frac{t_{\rm sedov}}{10^4\ {\rm yr}}\right)\ [{\rm pc}], \tag{2.43}$$

$$T_{\rm sedov} = 0.29\left(\frac{E_0}{10^{51}\ {\rm erg}}\right)^{\frac{2}{5}}\left(\frac{n_0}{1\ {\rm cm}^{-3}}\right)^{-\frac{2}{5}}\left(\frac{t_{\rm sedov}}{10^4\ {\rm yr}}\right)^{-\frac{6}{5}}\ [{\rm keV}], \tag{2.44}$$

$$v_{\rm sedov} = \frac{dR_{\rm sedov}}{dt} = 490\left(\frac{E_0}{10^{51}\ {\rm erg}}\right)^{\frac{1}{5}}\left(\frac{n_0}{1\ {\rm cm}^{-3}}\right)^{-\frac{1}{5}}\left(\frac{t_{\rm sedov}}{10^4\ {\rm yr}}\right)^{-\frac{3}{5}}\ [{\rm km\,s^{-1}}]. \tag{2.45}$$

Until the end of this stage, about 70% of the initial explosion energy is converted into thermal energy of the swept-up ambient medium (Chevalier, 1974). These equations are utilized to estimate the age, and so on through the X-ray observation.

2.4.3 Radiative Cooling Phase

The remnant continues to expand adiabatically until radiative losses can be neglected. At this moment, the shock velocity is decelerated down to ~ 200 km s^{-1}. According to Falle (1981) and Falle (1988), the age ($t_{\rm cool}$), radius ($R_{\rm cool}$), and expansion velocity at the begging in this stage are given by

$$t_{\rm cool} = 2.7\times 10^4\left(\frac{E_0}{10^{51}\ {\rm erg}}\right)^{0.34}\left(\frac{n_0}{1\ cm^{-3}}\right)^{-0.52}\ {\rm yr}, \tag{2.46}$$

$$R_{\rm cool} = 20 \left(\frac{E_0}{10^{51}}\right)^{0.295} \left(\frac{n_0}{1\ cm^{-3}}\right)^{-0.409}\ {\rm pc}, \tag{2.47}$$

$$V_{\rm cool} = 277 \left(\frac{E_0}{10^{51}}\right)^{0.0554} \left(\frac{n_0}{1\ cm^{-3}}\right)^{-0.111}\ {\rm km\,s^{-1}}. \tag{2.48}$$

At this point, the swept-up ambient medium is compressed into a thin shell, which is to be a dense layer. However, the SNR interior still expands adiabatically. The interior pressure pushed the thin shell through the ambient medium, like a snowplow would. The last stage is called the momentum conserving snowplow phase, after which SNR merge completely with the surrounding medium, leaving behind a cavity with a high temperature than the surrounding medium. This merging takes place $\sim 750,000$ yr after the supernova explosion.

2.5 Characteristic Timescale

After the shock has passed, the ions in the plasma are almost instantaneously heated to the shock temperature about 10^7–10^9 K. However, the heating mechanism for the electrons dose not understand . This question has been open for many years. One is to assume that the electrons are heated by Coulomb collisions. In this process, the electron temperature is determined by the mass ratio of electron and ion just after the shock heating, and gradually increase by Coulomb collisions. In the other process, the electron temperature instantaneously increases by plasma instabilities. In this section, we explain the former process. Since the electron temperature is heated by the Coulomb collisions, there is a timescale for thermal equilibrium between ions and electrons. Similarly, there is a timescale for ionization equilibrium. We summarize the variable timescales in this section.

2.5.1 Ionization and Recombination

Physical processes changing the ionization states are as follows. There are three processes; an electric impact ionization, a photo ionization, and an auto-ionization. In general, a photo ionization effect is negligible due to weak relative to the electron impact ionization in thin thermal plasma. In addition, there are three recombination process; a three-body recombination, a radiative recombination, a dielectric recombination. Each process is inverse that of the previous ionization process.

From the point of view of collisional atomic process for thermal emission, a plasma condition can be classified into the following three states by the relation between the thermal energy and the energy distributed in the ionization state.

1 Ionization equilibrium; it is balanced between the ionization rate and the recombination rare.

2 Ionizing; the plasma is under-ionization with much thermal energy. The ionization rate exceeds the recombination rate. This condition can be found in X-ray spectra of SNRs.

3 Recombining; this condition is that the thermal energy is lower compared with the energy distributed in ionization state. The plasma is dominated by recombination process.

In order to express the plasma condition, we define an characteristic ionization temperature, $T_{\rm Z}$ as follows. When the ion fractions of an element at a given $T_{\rm e}$ are approximated by those collisional ionization equilibrium (CIE) at an electron temperature $T'_{\rm e}$, then we put $T_{\rm Z} = T'_{\rm e}$. According to this definition, the above three state are written as follows,

1 $T_{\rm Z} = T_{\rm e}$: ionization equilibrium

2 $T_{\rm Z} < T_{\rm e}$: ionizing

3 $T_{\rm Z} > T_{\rm e}$: recombining

2.5.2 Collisional Ionization Equilibrium

A characteristic timescale for a plasma to reach an ionization equilibrium is derived. On the element of the atomic number Z, the ionization rate equation is given by,

$$\frac{df_{\rm Z}}{d(n_{\rm e}t)} = S_{\rm Z-1}f_{\rm Z-1} - (S_{\rm Z} + \alpha_{\rm Z})f_{\rm Z} + \alpha_{\rm Z+1}f_{\rm Z+1} \tag{2.49}$$

$$\sum_{\rm z=0}^{\rm Z} f_{\rm Z} = 1, \tag{2.50}$$

where $f_{\rm Z}$ is an ionic fraction of the element which is ionized z-1 times. $S_{\rm Z}$ and $\alpha_{\rm Z}$ are the ionization and recombination rate coefficients from the z-th ion, respectively. The characteristic timescale ($t_{\rm ion}$) to reach an ionization equilibrium can be derived from the solution for the rate equation. At the zero-th order estimation, the timescale is given by

$$n_{\rm e}t_{\rm ion} \simeq \sum_{\rm z=0}^{\rm Z}(S_{\rm Z} + \alpha_{\rm Z})^{-1} \tag{2.51}$$

$$\simeq [min(S_{\rm Z} + \alpha_{\rm Z})]^{-1} \tag{2.52}$$

$$\simeq 10^{12}\ {\rm cm}^{-3}\,{\rm s} \tag{2.53}$$

(Masai, 1994). This value is nearly independent for Z or $T_{\rm e}$. For example, assuming the electron density of 1 cm^{-3}, the ionization age ($t_{\rm iont}$) is estimated to be $\sim 3 \times 10^4$ yr. Therefore, most SNRs would be still in non-ionization equilibrium.

2.5.3 Thermal Equilibrium

A characteristic timescale for a plasma to reach a thermal equipartition between electrons and ions is estimated through Coulomb collisions. A timescale to reach the equipartition through Coulomb collisions between the same spices (Spitzer, 1962) is given by

$$t_{\rm c} = \frac{m^{\frac{1}{2}}(3kT)^{\frac{3}{2}}}{0.714 \times 8\pi n{\rm e}^4{\rm Z_e}^4 \ln\Lambda}, \tag{2.54}$$

where m, T, $\mathrm{Z_e}$ and n are a mass, a temperature, a charge, and a number density of a particle. $\ln\Lambda$ is the Coulomb logarithm, which is ∼30 in the X-ray band. Therefore, assuming that the density and temperature of an electron are equal to those of ion, the ratio of the timescale for each species to reach the thermal equilibrium is given by

$$\frac{t_{\mathrm{c(i-i)}}}{t_{\mathrm{c(e-e)}}} = \left(\frac{m_{\mathrm{i}}}{m_{\mathrm{e}}}\right)^{\frac{1}{2}} \mathrm{Z}^{-4} \sim 43\mathrm{A}^{\frac{1}{2}}\mathrm{Z}^{-4}, \tag{2.55}$$

where A is a mass number of an ion. A timescale (t_{eq}) to reach the thermal equipartition between different species is given by

$$\frac{dT}{dt} = \frac{T_{\mathrm{f}} - T}{t_{\mathrm{eq}}}, \tag{2.56}$$

where T and T_{f} are the temperature of a given particle and field particles (here, the quantities suffixed f are physical quantities of the field particles). From this equation, the timescale is given by

$$t_{\mathrm{eq}} = \frac{3mm_{\mathrm{f}}k^{\frac{3}{2}}}{8(2\pm)^{\frac{1}{2}}n_{\mathrm{f}}\mathrm{Z}^2\mathrm{Z}_{\mathrm{f}}^2\mathrm{e}^4\ln\Lambda}\left(\frac{T}{m} + T_{\mathrm{f}} + \frac{T_{\mathrm{f}}}{m_{\mathrm{f}}}\right)^{\frac{3}{2}}. \tag{2.57}$$

Assuming that the given particle and the field particle are electron and ion, respectively, and $T \sim T_{\mathrm{f}}$ in the above equation, we can roughly compare each time scales for thermal equipartition.

$$t_{\mathrm{eq}} \sim \left(\frac{m_{\mathrm{i}}}{m_{\mathrm{e}}}\right)^{\frac{1}{2}} t_{\mathrm{c(i-i)}} \sim \frac{m_{\mathrm{i}}}{m_{\mathrm{e}}} t_{\mathrm{c(e-e)}}. \tag{2.58}$$

Thus, the electrons reach equilibrium first, followed by ions, and following finally by equipartition of all particles. Masai (1994) analytically estimated the equipartition process, and found the post-shock temperature T_{e} to be approximately

$$T_{\mathrm{e}} \sim 0.21 \times (\ln\Lambda)^{\frac{2}{5}}(n_{\mathrm{e}}t)^{\frac{2}{5}}T_{\mathrm{s}}^{\frac{2}{5}}\ \mathrm{K}, \tag{2.59}$$

where T_{s} is the shock temperature as follows,

$$kT_{\mathrm{s}} = \frac{3}{16}\mu m_{\mathrm{i}}V_{\mathrm{s}}^2, \tag{2.60}$$

where μ, m_{i}, and V_{s} are a mean atomic weight, a average ion mass, and a shock velocity, respectively. Masai (1994) shows the electron temperature increases to be $\sim 0.1T_{\mathrm{s}}$ and $0.3T_{\mathrm{s}}$ in $10^{-3}t_{\mathrm{Eeq}}$ and $10^{-2}t_{\mathrm{Eeq}}$, respectively, where t_{Eeq} is the equipartition time constant as follows,

$$t_{\mathrm{Eeq}} = \frac{3m_{\mathrm{p}}(kT_{\mathrm{s}})^{\frac{3}{2}}}{8(2\pi)^{\frac{1}{2}}n_{\mathrm{e}}m_{\mathrm{e}}^{\frac{1}{2}}\mathrm{e}^4\ln\Lambda}. \tag{2.61}$$

For example, assuming the electron density of 1 cm^{-3} and the post-shock temperature of 1 keV, the timescale for electron-electron collision is estimated to be $t_{\mathrm{Eeq}} \sim 4.7\times10^8$ sec ∼ 15 yr. Therefore, all observed SNRs are in thermal equilibrium between electrons. From the observation, the degree of thermal equilibrium between electrons and protons just behind the shock front seems to have an inverse relation for the shock velocity in figure 2.6 (Rakowski, 2005).

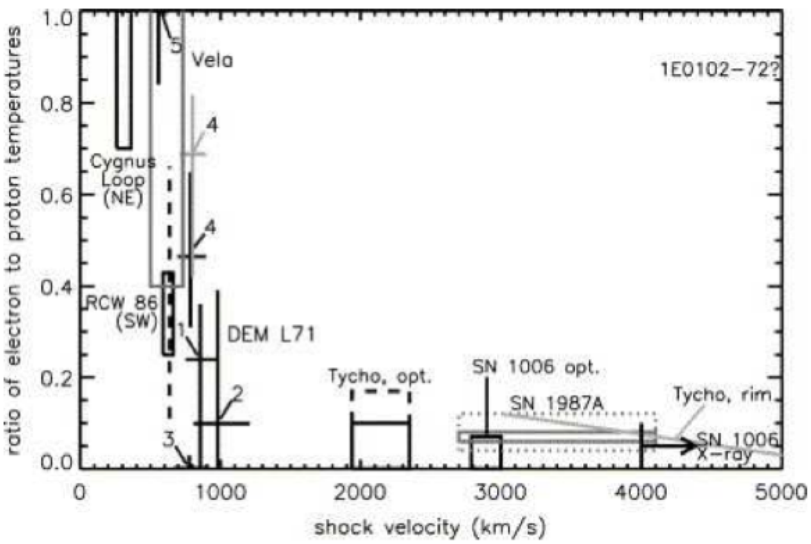

Figure 2.6: The electron and proton temperature ratio as a function of the shock velocity (Rakowski, 2005).

2.6 Radiation Process

There are some kinds of the X-ray emission from the phenomena accompanying the SN explosion. One is the thermal emission from the optically thin thermal plasma heated by the shock wave. Another is the X-ray emission from a central pulsar and/or its associated nebula. The X-ray emission from the pulsar is the non-thermal component from the magnetosphere, while the thermal component is from the hot surface and/or their ejecta. The X-ray emission from the nebula associated the pulsar is also the non-thermal emission. The other is non-thermal emission from the shell-like SNRs (SN 1006 and RX J1713.7-3946, etc). They are explained it to be X-ray synchrotron emission from relativistic electrons accelerated by the shock wave. We summarize X-ray radiation processes in this hot plasma, and the X-ray emission from relativistic electrons accelerated by the shock wave in this section.

2.6.1 Line Emission

The transitions between two discrete quantum levels often accompany a photon emission called line emission or bound-bound emission. In pure Coulomb cases for hydrogen atom or other hydrogen-like ions, such as HeII, OVIII, and SiXIV, a complete discussion of transition rate can be given by quantum theory. For the hydrogen atom, the energy for a photon absorbed or emitted in a transition between two discrete levels with a principal quantum number n and n' is given by

$$E_{\rm bb} = R_{\rm y}\left(\frac{1}{n^2} - \frac{1}{n'^2}\right), \tag{2.62}$$

where $R_{\rm y}$ is Rydberg constant (= 13.6 eV). For heavy elements, $E_{\rm bb}$ roughly become

$$E_{\rm bb} \sim {\rm Z}^2{\rm R_y}\left(\frac{1}{\rm n^2} - \frac{1}{\rm n'^2}\right), \tag{2.63}$$

where X is a mass number for an ion. These H-like transitions are called "Lyman series" discovered by Theodore Lyman. The transitions are named sequentially by Greek letters: transition of $1s$–$2p$ is Lyα (H-like Kα), $1s$–$3p$ is Lyβ (H-like Kβ), $1s$–$4p$ is Lyγ (H-like Kγ), and so on, where s and p mean azimuthal quantum numbers (l) are 0 and 1, respectively. If ions have more electrons, the transition process becomes relatively complicated. For example, He-like ions (which have two electrons) emit three most intense lines; resonance ($1{\rm s}^{21}{\rm S}_0$-$1s2p^1{\rm P}_1$), forbidden ($1s^{21}{\rm S}_0$-$1s2p^3{\rm S}_1$), and inter-combination ($1s^{21}{\rm S}_0$-$1s2p^3{\rm S}_{2,1}$) transition lines. The relative intensities for the these lines depend on the temperature because the collision excitation rates have not the same dependence with the temperatures among the three lines. The line energies for H- and He-like ions are listed in table 2.2.

Table 2.2: K-shell emission line energies for H-like and He-like ions.

Species	Line energy (eV)							
	H-like			He-like ions				
	Lyα	Lyβ	Lyγ	Kα(r)	Kα(f)	Kα(i)	Kβ	Kγ
C	367	436	459	308	299	204	355	371
N	500	593	625	431	420	426	498	522
O	654	774	817	574	561	569	666	698
Ne	1022	1211	1277	921	905	914	1073	1127
Mg	1472	1745	1840	1352	1330	1343	1579	1660
Si	2006	2377	2506	1865	1840	1854	2183	2294
S	2623	3107	3277	2461	2431	2447	2884	3033
Ar	3323	3936	4151	3140	3104	3124	3685	3875
Ca	4106	4864	5130	3908	3845	3892	4582	4918
Fe	6966	8266	8732	6702	6641	6670	7798	8217

Thin-thermal plasma are collisionally excited by free electrons. Since the lifetime for the excited states are much shorter than that of the collision between the electrons and the ions, we can assume that the rate of a photon emission is the same as that of the excitation. The line intensity is therefore proportional to $n_{\rm e}n_{\rm i}$, which determines the probability of collisions between electrons and ions. Relative abundances therefore are derived by comparing line intensities from different elements. If the plasma is dominated by the hydrogen, the intensity for the thermal bremsstrahlung is proportional to $n_{\rm e}n_{\rm H}$, and absolute abundances area also derived by comparing the intensities of the line and continuum.

2.6.2 Continuum Emission

There are three radiative processes for continuum emissions: a thermal bremsstrahlung, a radiative recombination, and a two-photon radiation. The thermal bremsstrahlung is

also called the free-free radiation. This radiation is due to the acceleration of electrons, which are distributed in Maxwellian at a temperature, in the Coulomb field of ions. The emissivity is given by

$$\epsilon_\nu^{ff} = 6.8 \times 10^{-38} Z^2 n_\mathrm{e} n_\mathrm{i} T_\mathrm{e}^{\frac{1}{2}} e^{\frac{h\nu}{kT_\mathrm{e}}} g_{ff} \ (\mathrm{erg}^{-1}\,\mathrm{cm}^{-3}\,\mathrm{Hz}^{-1}), \tag{2.64}$$

(Rybicki & Lightman, 1986) where n_e and n_i are an electron and ion density, respectively. Z is an atomic number of ion, and h and k are the Plank constant and Boltzman constant, respectively. g_{ff} is a velocity averaged Gaunt factor, which includes the calculative approximation, the quantum effect and so on. We can approximate g_{ff} as follows,

$$g_{ff} \simeq \begin{cases} 1 - 5(10^{-4} < \frac{h\nu}{kT_\mathrm{e}} < 1) \\ 1(\frac{h\nu}{kT_\mathrm{e}} \simeq 1). \end{cases}$$

g_{ff} value is therefore not so important for the spectral shape. Therefore, we can roughly estimate the spectral shape, the dependence of ϵ_ν^{ff} on $h\nu$,

$$\epsilon_\nu^{ff} \propto \begin{cases} 1(\frac{h\nu}{kT_\mathrm{e}} < 1) \\ e^{-\frac{h\nu}{kT_\mathrm{e}}}(\frac{h\nu}{kT_\mathrm{e}} > 1). \end{cases}$$

The spectral shape is therefore determined uniquely at a given electron temperature. Observed continuum flux almost depends on the electron temperature and $\int n_\mathrm{e} n_\mathrm{i} dV \simeq \int n_\mathrm{e}^2 dV$ called a volume emission measure. Radiative recombination is called the free-bound radiation. This process is dominant in the recombination condition ($T_\mathrm{e} < T_\mathrm{z}$). In the process, the energy with the radiative photon is roughly depended on the binding energy and the thermal energy. The two-photon radiation is the bound-bound radiation. In this process, the energy of photons is shared of the electron transition energy.

2.6.3 Synchrotron Radiation

Charged particles emit a synchrotron radiation by an interaction with a magnetic field. The power of the synchrotron radiation per unit frequency from a single electron of an energy E and a charge e is given by

$$P(\omega; E) = \frac{\sqrt{3}}{2\pi} \frac{e^3 B \sin\alpha}{m_\mathrm{e} c^2} F\left(\frac{\omega}{\omega_c}\right), \tag{2.65}$$

where α is the angle between the velocity of the electron and the magnetic field, $F(x)$ is a dimensionless function given by Rybicki & Lightman (1986) from which has a peak at $\frac{\omega}{\omega_c} \simeq 0.29$, and ω_c is the characteristic frequency described as

$$\omega_c = \frac{3}{2} \frac{eB \sin\alpha}{m_\mathrm{e} c} \gamma^2. \tag{2.66}$$

The typical energy of a synchrotron photon is given by

$$\epsilon = h\nu_\mathrm{synch} = 0.29 h\omega_c \sim 1.2 \left(\frac{B}{1\ \mu\mathrm{G}}\right) \left(\frac{E_\mathrm{e}}{100\ \mathrm{TeV}}\right)^2 \ \mathrm{keV}. \tag{2.67}$$

Electrons with the energy of ∼10 GeV in the $\sim \mu$G magnetic field radiate the synchrotron photon in the radio band. When electrons have the energy of ∼TeV, the photon energy becomes ∼keV. An integration of equation 2.65 over ω gives total emitted power of

$$P_{\rm synch} = \frac{4}{3}\sigma_{\rm T} c\beta^3\gamma^2 U_{\rm B}, \tag{2.68}$$

where $\sigma_{\rm T}$ is the Thomson cross section and $U_{\rm B}$ is the magnetic energy density ($=\frac{B^2}{8\pi}$).

In order to calculate the spectrum of the synchrotron radiation from a distribution of electrons, we assume an electron distribution with power-law expressed as

$$N_{\rm e} dE = CE^{-p} dE. \tag{2.69}$$

The total radiated power per unit volume per unit frequency is obtained by the integration of the single particle synchrotron radiation formula (equation 2.65) times the electron distribution (equation 2.65) over all energies. Therefore, the spectrum can be given by

$$P_{\rm tot}(\omega) = \int_0^{\rm inf} P(\omega; E) N_{\rm e}(E) dE \tag{2.70}$$

$$= \frac{\sqrt{3}}{2\pi}\frac{e^3 C}{m_{\rm e}c^2}\left(\frac{3ec}{(mc^2)^3}\right)^{(p-1)/2} \frac{\Gamma\left(\frac{p}{4}+\frac{10}{12}\right)\Gamma\left(\frac{p}{4}-\frac{1}{12}\right)}{P+1}(B\sin\alpha)^{\frac{(p+1)}{2}}\omega^{-\frac{(p-1)}{2}} \tag{2.71}$$

$$\propto B^{(p+1)/2}\omega^{-(p-1)/2}, \tag{2.72}$$

where $\Gamma(y)$ is the gamma function of an argument y. The spectral index of the synchrotron emission of electrons is related to the electron distribution index p by

$$s = \frac{p-1}{2}, \tag{2.73}$$

and the photon index Γ of a power low for the synchrotron spectrum, defined by $I(\epsilon) \propto \epsilon^{-\Gamma}$ is given by

$$\Gamma = \frac{p+1}{2}. \tag{2.74}$$

In the case that an electron spectral index p is 2, the photon index of the synchrotron emission becomes 1.5.

2.7 Particle Acceleration by a Pulsar and its Wind Nebula

A pulsar and/or its associated nebula are located in SNRs. It is possible that the X-ray emission from overall SNR are included both emissions from the non-thermal component from the pulsar (and/or its wind nebula) and the thermal component from their surface (and/or their ejecta). In this section, we therefore brief summarize the mechanism for the X-ray emission from the pulsar and its wind nebula. The mechanism for a particle acceleration by a rotating neutron star (pulsar) can be roughly following two cases. The first is related to a pair (electron-positron) creation plasma inside the light cylinder, where the rotation velocity is smaller than the light velocity, thus, the magnetic filed line from a neutron star may rotate. The other is a MHD acceleration outside the light cylinder.

The dipole magnetic filed B and vector potential A at a vector position of r from a neutron star with the magnetic moment μ are given by

$$B = \frac{3(r \cdot \mu)r - \mu}{r^5} \tag{2.75}$$

$$A = \frac{\mu \times r}{r^3}. \tag{2.76}$$

In the simplest case of a rigidly rotating and perfectly conductive neutron star, the scalar potential is given by

$$\phi = -\frac{(\Omega \times r) \cdot A}{c} = \frac{\Omega r \sin\theta A_\varphi}{c}, \tag{2.77}$$

where Ω and (r, θ, φ) are the angular velocity of the star and the spherical polar coordinates in the reference to the rotation axis, respectively. For an oblique rotator,

$$\phi = \frac{\mu\Omega}{cr}(\sin^2\theta\cos\alpha + \sin\theta\cos\theta\sin\varphi\sin\alpha), \tag{2.78}$$

where is the angle between the magnetic moment and the rotation axis. Due to the strong electric filed created, electrons and ions at the surface of the neutron star are strongly accelerated, and move along the strong magnetic field line toward the ambient space. Since the magnetic filed line is not straight but are curved, the electrons emit gamma rays. The high energy gamma rays are converted to electron-positron pairs. The pairs are then accelerated by the electric filed, and again radiate gamma rays. By repeating this cycle, large numbers of electrons and positrons are created. The particles created on the magnetic-field lines move along the lines out of the light cylinder. There are called the pulsar winds.

2.8 Spectral Model

Given an ionization parameter, a metal abundance, a temperature, and an emission measure, an expected emission spectrum can be calculated by summing spectral emissivities due to the variable radiative processes described so far. In this thesis, we adopted mainly optically thin thermal plasma model in non-ionization equilibrium in the XSPEC library (so-called VNEI model; Hamilton et al. 1983, Borkowski et al. 1994, Liedahl et al. 1995, Borkowski et al. 2001). A light from stars is absorbed by a gas and a dust in the interstellar medium because of the photo-electric absorption. We therefore adopted the interstellar absorption model in the XSPEC library (i.e. PHABS or VPHABS model). In this section, we explain theses models.

2.8.1 Optically Thin Thermal Plasma in Non-Ionization equilibrium: VNEI Model

For example, assuming the electron density of 1 cm^{-3}, the ionization age is estimated to be $\sim 3 \times 10^4$ yr. Most SNRs ($< 10^4$ yr) would be therefore still in non-ionization equilibrium. We therefore adopted optically thin thermal plasma model in non-equilibrium ionization in the XSPEC library (VNEI model). Figure 2.7 shows the convolved VNEI model

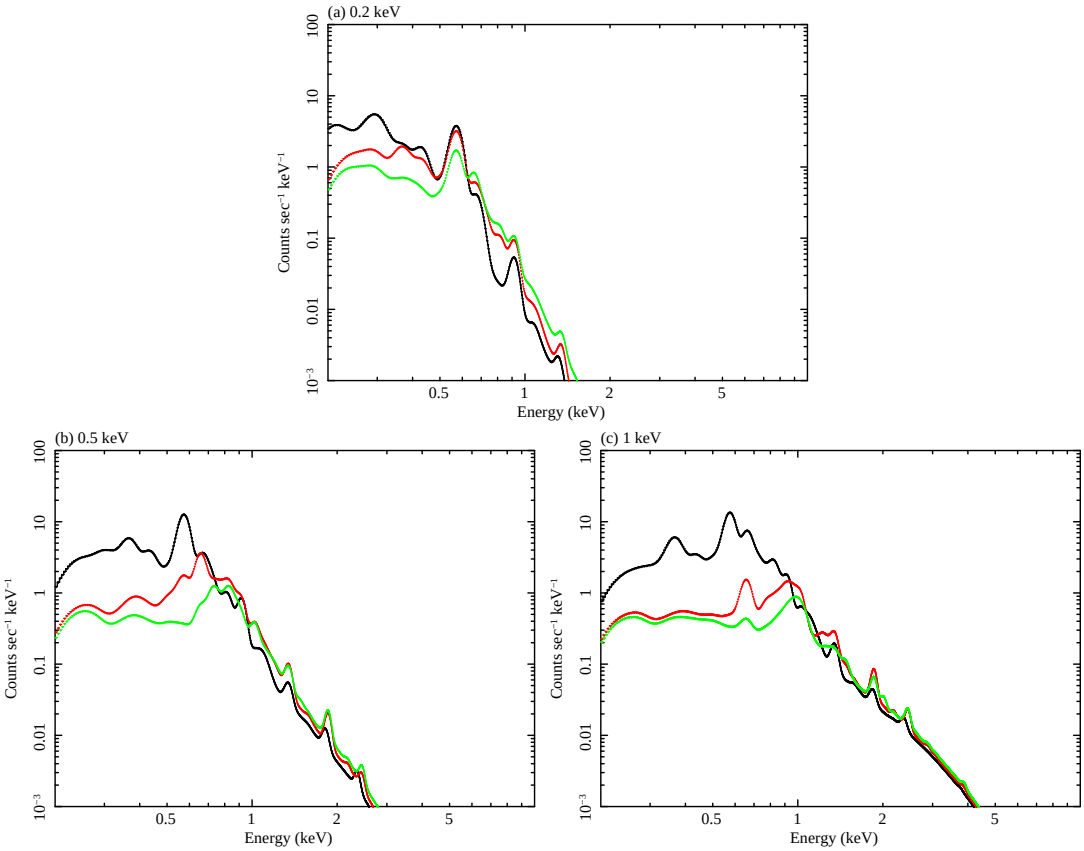

Figure 2.7: The convolved VNEI model (a: 0.2 keV, b: 0.5 keV, and c: 1.0 keV) in the XSPEC library. The black, red, green are represented with the ionization parameter of 10^{10} cm^{-3} s, 10^{11} cm^{-3} s, and 10^{12} cm^{-3} s, respectively.

for each temperature and ionization parameter. Since the spectra are significant differences for each plasma temperature and ionization parameter, we can derive the plasma temperature, the ionization parameter, the emission measure and the metal abundance through the spectral analysis in several independent processes. We explain how to derived these parameters as follows.

Through the spectral analysis, the electron temperature is mainly determined by the following two methods; (1): since the bremsstrahlung continuum shape is the simple function for an electron temperature ($\propto \sqrt{kT_{\rm e}}$), the electron temperature therefore can be determined with the continuum shape, (2): For example, the probability ratio for the collisional excitation between $n = 1 \rightarrow 2$ and $n = 1 \rightarrow 3$ in He-like ions only depends on the energy for a colliding electron. When the collisional excitation is the major process in a plasma, and a photo ionization can be ignored, the Kα/Kβ flux ratio directly reflects the transition probability ratio. The electron temperature therefore is also determined with these line ratios. The ionization parameter, for example, is also determined with the Kα flux ratio between He- and H-like ions. Figure 2.8 shows the line ratios from the measured OVII and OVIII. We found that the plasma temperature and the ionization parameter can be determined with such two line ratios. The volume emission measure (simply emission measure) is also one of the basic plasma parameters, and given by $EM = \int n_{\rm e} n_{\rm H} dV / 4\pi D^2$, where $n_{\rm e}$, $n_{\rm H}$, V, and D are an electron and hydrogen density,

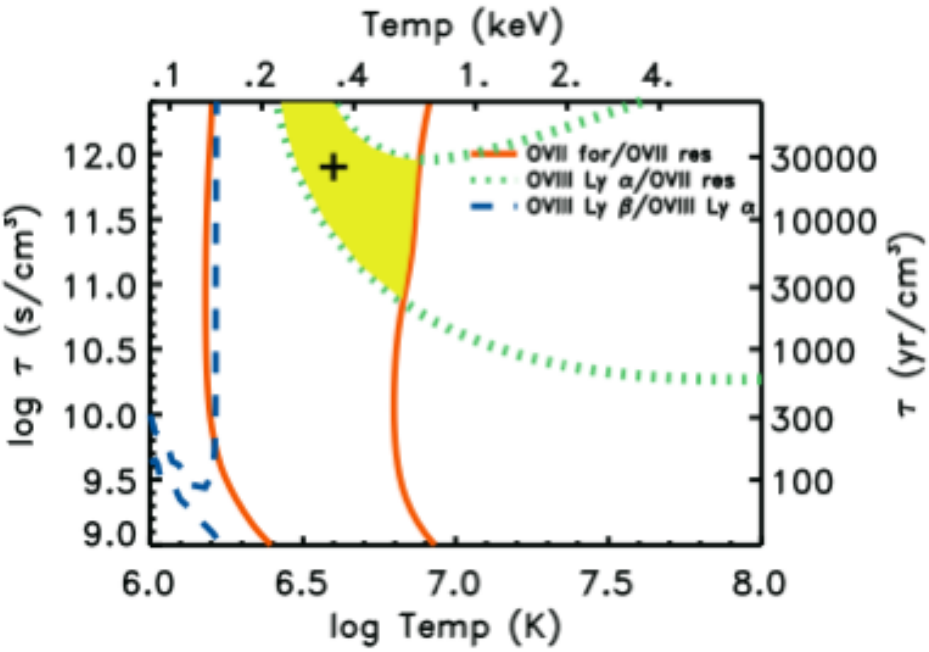

Figure 2.8: The 90 % confidence contour plotted for line ratios from the measured OVII and OVIII. This picture was taken by Flanagan et al. (2004). The red, green, and blue lines are represented with the line ratios for OVII/OVIII, OVII Lyα/OVIII, and OVIII Lyβ/OVIII Lyα, respectively.

a plasma volume and the distance to a source, respectively. When a plasma emissivity is determined, an emission measure is proportion to an observed flux. Finally, a metal abundance for an ion "i" is given by $n_{\rm i}/n_{\rm H}$, where $n_{\rm i}$ is the ion "i" density. The metal abundance is therefore determined the ratio of a line flux ($n_{\rm e}n_{\rm i}$) to an emission measure ($n_{\rm e}n_{\rm H}$). We therefore can derive the all plasma parameters through the spectral analysis.

2.8.2 Interstellar Absorption: PHABS and VPHABS Model

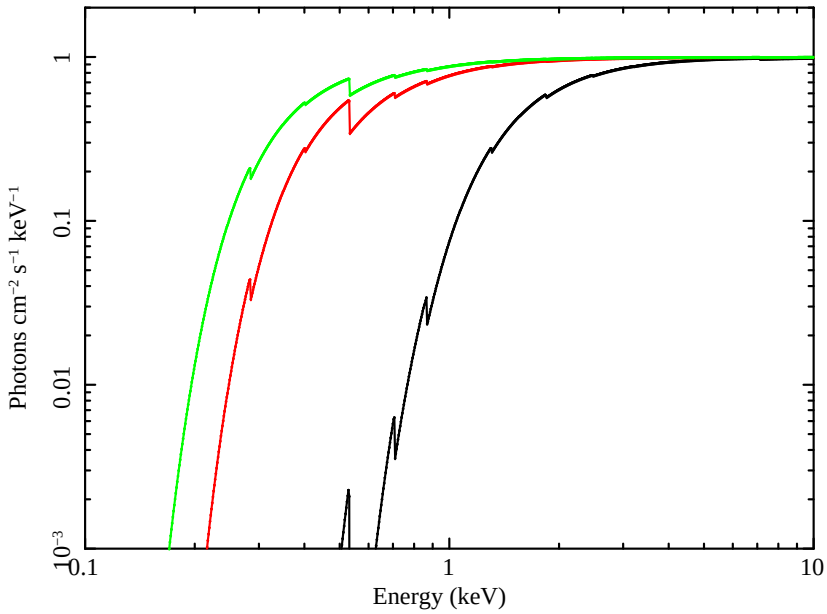

Figure 2.9: The PHABS model. The black, red, and green solid lines are represented with the hydrogen column density for 10^{22} cm^{-2}, 10^{21} cm^{-2}, and 5×10^{20} cm^{-2}, respectively.

A light from stars is absorbed by a gas and a dust in the interstellar medium because to the photo-electric absorption. In this process, a photon is absorbed by an atom and an electron, and is emitted with an energy given by the incident photon energy minus its binding energy. To have a difference binding energy for each metal, the photo-electric absorption is given by $\exp\{-(n_{\rm H}\sigma(E)_{\rm H} + n_{\rm C}\sigma(E)_{\rm C} + n_{\rm N}\sigma(E)_{\rm N} + n_{\rm O}\sigma(E)_{\rm O} + \cdots)\} = \exp\{-n_{\rm H}(\sigma(E)_{\rm H} + A_{\rm C}\sigma(E)_{\rm C} + A_{\rm N}\sigma(E)_{\rm N} + A_{\rm O}\sigma(E)_{\rm O} + \cdots)\}$, where $n_{\rm i}$, $A_{\rm i}$ and $\sigma(E)_{\rm i}$ are a column density, a metal abundance and a photo-electric cross section with an incident photon energy (E) for an ion-i, respectively. The emission from sources in the LMC is attenuated by the interstellar matter in our galaxy and the LMC. Since the metal abundances these two absorption components are significantly difference, we estimated these absorptions is followings to be. The abundances of the absorption matter in our galaxy assumed the solar abundance (Anders & Grevesse, 1989), and represented the hydrogen column density as $N_{\rm H}^{\rm G}$. The value of $N_{\rm H}^{\rm G}$ toward our observation has been already obtained from the Galactic HI survey. We fixed $N_{\rm H}^{\rm G}$ at this value, and used PHABS model in the xspec library to represent the absorption in our galaxy. On the other hand, the average metal abundances in the LMC have been measured by Russell & Dopita (1992) to be ∼0.3 solar. We therefore used the VPHANSE model in the xspec library to represent the absorption in the LMC, which is reflected these abundances. The solar and

Table 2.3: The solar and LMC abundances for the major elements.

	Our galaxy*	LMC*
H	1.00	1.00
He	9.77×10^{-2}	0.89
C	3.63×10^{-4}	0.30
N	1.12×10^{-4}	0.12
O	8.51×10^{-4}	0.26
Ne	1.23×10^{-4}	0.33
Mg	3.80×10^{-5}	0.78
Si	3.55×10^{-5}	1.82
S	1.62×10^{-5}	0.31
Ca	2.29×10^{-6}	0.34
Fe	4.68×10^{-5}	0.36
Ni	1.78×10^{-6}	0.62

* The solar abundances are normalized by the hydrogen, while the LMC abundances are normalized by the solar abundances.

LMC abundances for major elements are listed in table 2.3. Figure 2.9 shows the PHABS model for each the hydrogen column density. Because of the relatively high abundance for oxygen, there is the deep edge around ~ 0.5 keV. Since the hydrogen column density in our galaxy is roughly estimated to be $\sim 10^{20}$ cm^{-2}, a light from stars in the LMC is not absorbed almost in our galaxy.

Chapter 3

The Large Magellanic Cloud

Figure 3.1: Optical images of the two magellanic clouds (top), LMC (left below) and SMC (right below). These images were taken by Anglo-Australian Observatory.

The southern celestial sphere would be much more spectacular than the northern hemisphere. There are two bright and diffuse clouds in the southern celestial sphere. These clouds are called the Large and Small Magellanic Clouds (hereafter, the LMC and SMC), which are took by Magellan's voyage around the world. The LMC and SMC are one of the satellite galaxies of the Milky Way. In this chapter, we present a brief review on these clouds. Figure 3.1 shows the visible images of the LMC and SMC taken by the

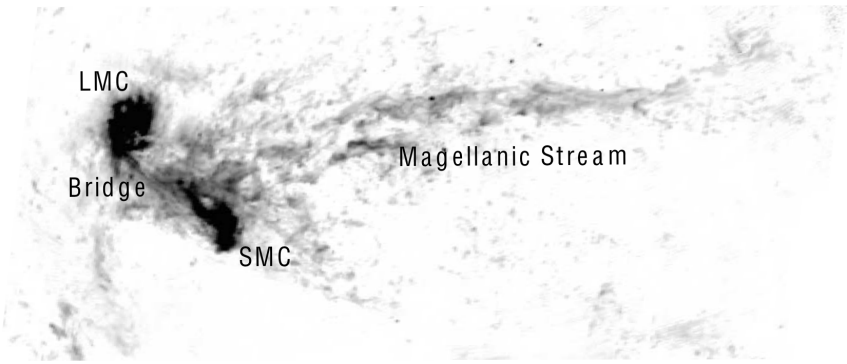

Figure 3.2: HI column density map of the "bridge" and the "Magellanic System". This figure were taken from Putman et al. (2003).

Anglo-Australian observatory. Both of them have bars seen in their optical images. The size of them are $\sim 3^\circ \times 1^\circ$ for the LMC and $\sim 2.5^\circ \times 1^\circ$ for the SMC. In particular, the distance to the LMC was measured to be $\sim$ 50 kpc with Cepheid variable stars (Feast, 1999). They are connected by the "bridge" of gases as shown in figure 3.2. It would be precise to say that these clouds are drowned in an immense gas cloud. This cloud is called the Magellanic Stream as shown in figure 3.2, and discovered about 25 years ago (Mathewson et al., 1974).

The LMC are suited for the systematic studies because of its well-determined and uniform distance ($\sim$ 50 kpc; Feast 1999) and small interstellar absorption. These advantage mean that accurate plasma parameters can be estimated for the SNRs. Thus, systematic studies of SNRs in the LMC were tried with the launch of major X-ray observatories. In the following section, we summarize the systematic X-ray observations of SNRs in the LMC.

3.1 *Einstein* Observation

In this section, we summarize the systematic X-ray observation by *Einstein* satellite (e.g Long 1983). Long (1983) reported a systematic study of 25 SNRs in the LMC. They discussed mainly a plasma density, thermal energy, and a luminosity as a function of SNR diameter in their paper. In their works, a plasma density-radius relation is one of the interesting topics.

3.1.1 Plasma density-Radius Relation, Luminosities, and Thermal Energies

Figure 3.3 shows the plasma density, the thermal energy, and the luminosity as a function of SNR diameter. The thermal energy appears to increase with a diameter. Long (1983) suggested that electron and proton temperatures are evolved into thermal equilibrium. In contrast, the plasma density and the X-ray luminosity appear to decrease with a diameter. These effects are one of the open questions.

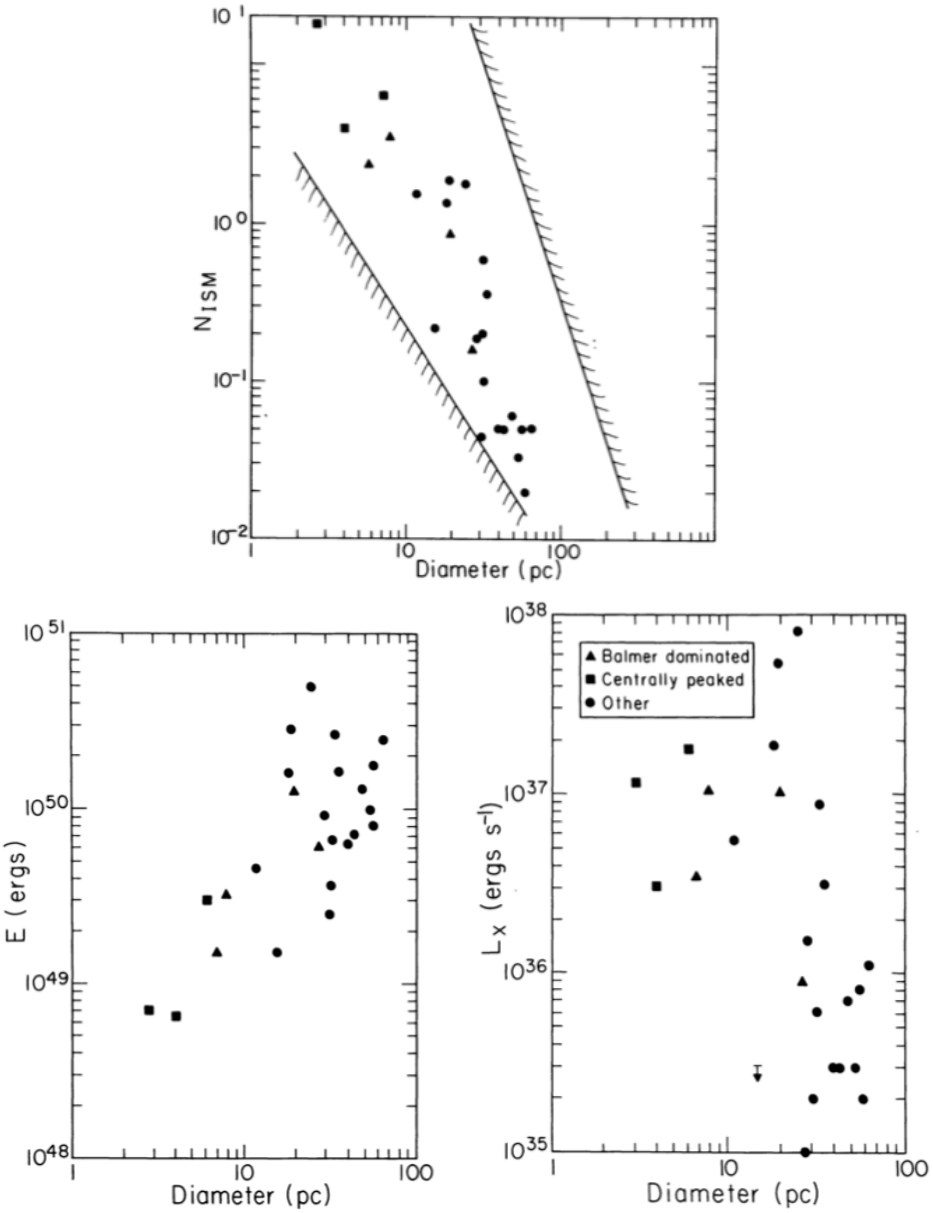

Figure 3.3: The plasma density (top), the thermal energy (bottom left), and the X-ray luminosity (bottom right) as a function of SNR diameter. These samples were observed in the LMC. The upper line in the plasma density-radius relation is represented with a temperature limit (0.2 keV; based on the Sedov model) which can be observed in the X-ray band, while the lower line is the detection limit of *Einstein* satellite. These figures were taken from Long (1983).

A plasma density is given by

$$n_{\rm e} \propto \Lambda^{-0.5} L_{\rm x}^{0.5} D^{-1.5}, \tag{3.1}$$

where Λ, $L_{\rm x}$, and D are a specific emissivity, a X-ray luminosity, and a SNR diameter, respectively. Assuming that Λ did not change greatly with a diameter, they discussed the plasma density-diameter relation. Since the plasma density decreases with a diameter as

shown in figure 3.3, the X-ray luminosity is also considered to be decreased with that.

However, it is considered that a plasma density in the Sedov phase has a constant in a time when we focus a SNR (Sedov, 1959). Thus, this is one of the open questions. Long (1983) believed to reflect their evolution. They explained the physical implication of this relation as follows: (1): cloudlet evaporation. McKee & Ostriker (1977) used this correlation to support a multiphase model of an ambient medium in which a tenuous gas is studded with dense cloudlets. But, an ambient medium (i.e. density) is significant difference for each progenitor type, and so on. It would be difficult to explain with such an ambient medium. (2) the X-ray emission from ejecta. The plasma density in ejecta would be proportion to $M_{\rm ejecta}/D^3$, which $M_{\rm ejecta}$ and D are an ejecta mass and a diameter, respectively. Long et al. (1982) argued that if the ejecta was a metal rich, the plasma density-diameter relation could be understood. However, this implication would be also difficult to explain this relation because most SNRs are believed to be in the Sedov phase. Like this, the plasma density-radius relation is not well understood observationally from past to present.

3.1.2 Σ-D Relation

The next topic is the X-ray surface brightness-diameter relation (Σ-D relation). We took this relation as an example of the systematic study with *Einstein* observation. Σ-D relation is utilized mainly to determine a distance to a SNR in the X-ray and radio observations. An X-ray surface brightness is defined as

$$\Sigma = \frac{L_{\rm x}}{\pi D^2}\ {\rm erg\,s^{-1}\,pc^{-2}}, \tag{3.2}$$

where D is a mean diameter observed in the X-ray. The observed Σ-D relation is shown in figure 3.4 (Berkhuijsen, 1986). Larger SNRs appear to have lower surface brightnesses. An X-ray luminosity is given by

$$L_{\rm x} \propto \Lambda n_{\rm e}^2 D^3, \tag{3.3}$$

where Λ, $n_{\rm e}$, and D are a specific emissivity, a plasma density, and a diameter, respectively. Assuming that the specific emissivity has a constant in a time, the X-ray surface brightness is proportion to $n_{\rm e}^2 R$. Since a plasma density in the Sedov phase has a constant in a time (Sedov, 1959), the X-ray surface brightness should increase with a diameter (i.e time). However, the observed X-ray surface brightness seems to decrease with a diameter.

Berkhuijsen (1986) estimated that the plasma density was proportion to $D^{-2.56}$. As a result, a surface brightness is also roughly proportion to $\sim D^5$, which is compatible with the observed Σ-D relation. In general terms, Σ-D relation is correlated with the plasma density-radius relation.

3.1.3 N-D Relation

The final topic is a number-diameter relation (N-D relation). We took this relation as an example of the systematic study with *Einstein* observation. If most of the SNR are expanding into an uniform density ISM, and have swept up enough ISM. Then, their time evolution resembles the Sedov expansion.

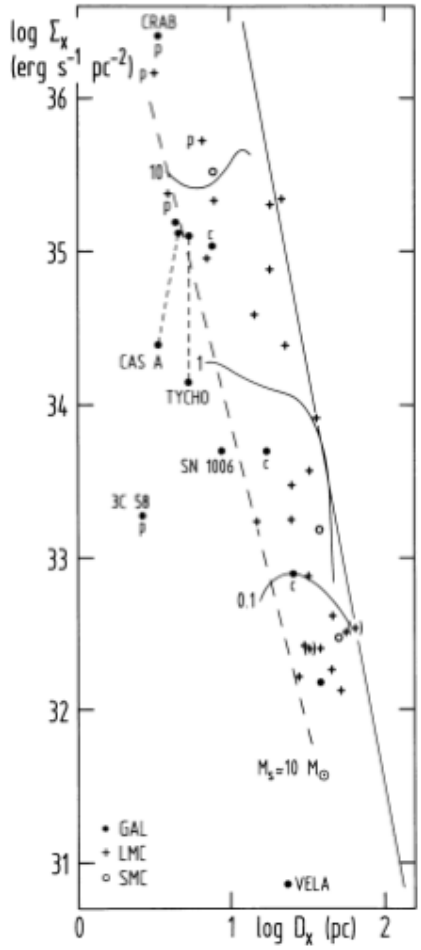

Figure 3.4: Σ-D relation. These samples were observed in the LMC, SMC, and Galaxy. This figure was taken from Berkhuijsen (1986).

The velocity in the Sedov phase is given by

$$v_{\rm Sedov} = \frac{dD}{dt} \propto D^{-\frac{3}{2}}, \tag{3.4}$$

where D is a diameter. We assumed that the initial expansion energy and ambient density had constant in a time. Under the assumption of a constant SN rate in the LMC over the past few kyr ($\frac{dN}{dt} = const$, where N is the cumulative number of SNRs whose diameter is smaller than D), the expected size distribution of SNRs in the Sedov phase is given by

$$\frac{dN}{dD} = \frac{dN}{dt}\frac{dt}{dD} \propto D^{\frac{3}{2}}. \tag{3.5}$$

Thus, the number of SNR with diameters less than D should increase as $D^{3/2}$. However, this is contrary to the observed uniform distribution in the nearby galaxies, such as the LMC, SMC, and M33 ($\frac{dN}{dr} \sim r^0$; e.g. Long 1983; Badenes et al. 2010). Figure 3.5 shows the number-diameter relation.

The observed number-diameter relationship is usually given by

$$N(< D) \propto D^{\alpha}. \tag{3.6}$$

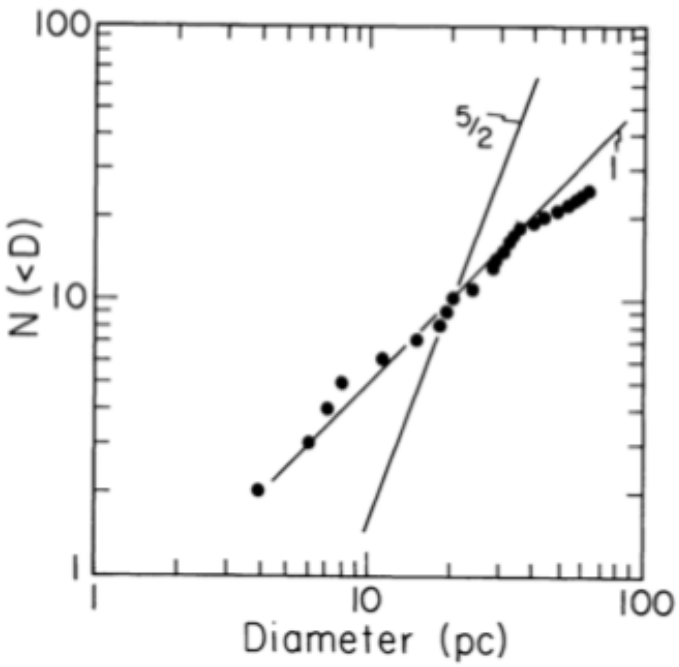

Figure 3.5: The cumulative number-diameter relation. These samples were observed in the LMC. This figure was taken from Long (1983).

Let us assume that the X-ray emission coefficient is constant in a time and that the expansion of SNR is nearly self-similar with the mass (M) evolving as D^{β}. Then, the plasma density is given by

$$n_{\rm e} \propto \frac{M}{D^3} \propto D^{\beta-3}. \tag{3.7}$$

In a self-similar expansion with a fixed total energy, the kinetic and thermal energies are separately conserved. Since the kinematic conservation low is give by $\mathrm{M}(dD/dt)^2 = const$, the equation between α and β is also given by

$$\beta = 2(1-\alpha) \tag{3.8}$$

(Itoh, 1984). Since the plasma density is roughly proportion to $\sim D^{-3}$ ($\beta = 0$), the cumulative number of SNRs is also roughly proportion to $\sim D^1$ ($\alpha = 1$), which is compatible with the previous observation (e.g. Long 1983; Badenes et al. 2010). In general terms, N-D relation is correlated with the plasma density-radius relation.

3.2 *ROSAT*'s Observation: Morphologies

Williams et al. (1999) analyzed archival *ROSAT* HRI or PSPC data of 31 SNRs. In this paper, they discussed the X-ray morphologies. They categorized the X-ray morphologies into the following 5 groups; shell: limb is near complete and is brighter than face, diffuse face: face as bright as shell; limb sometimes indistinct from face, centrally brightened: center of face notably brighter than limb, peaked emission: emission dominated by central

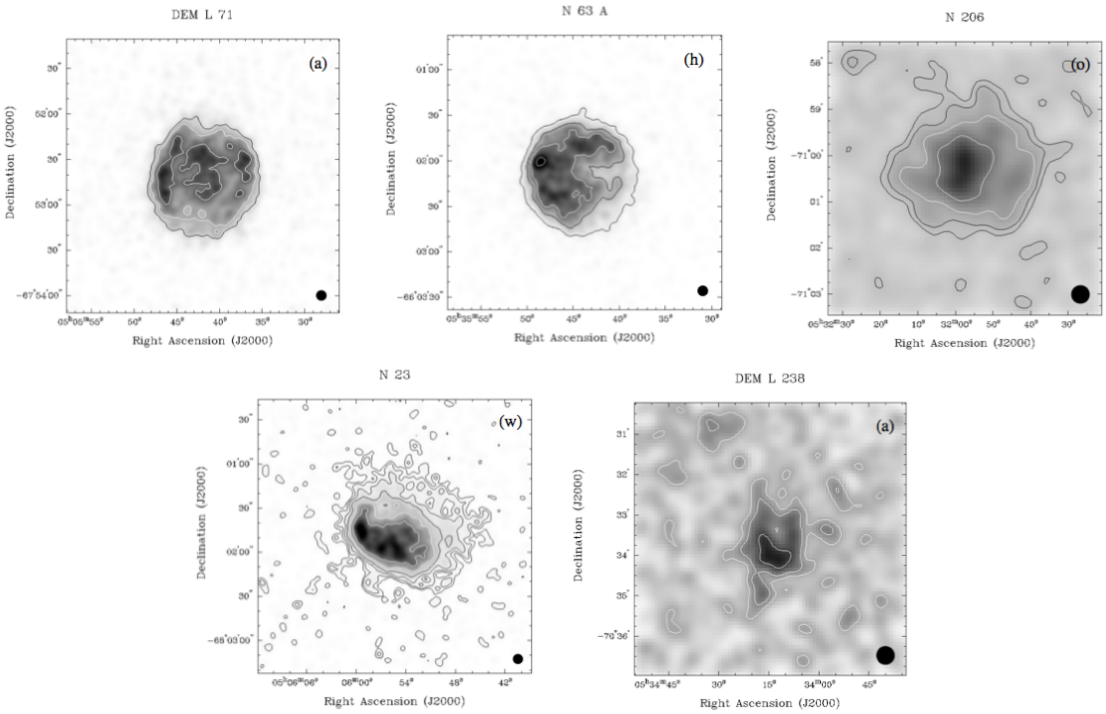

Figure 3.6: The X-ray images of DEM L71 (shell; top left), N63A (diffuse face; top middle), N206 (centrally brightened; top right), N23 (peaked emission; bottom left), and DEM L238 (Irregular; bottom right) observed by *ROSAT*. These figures were taken from Williams et al. (1999).

bright source of small diameter with respect to that of the entire SNR, and Irregular: incomplete or nonexistent shell, patchy emission. They also categorized the detailed X-ray morphologies as secondary X-ray features, though we did not explain in this section. Figure 3.6 shows the X-ray images of DEM L71 (shell), N63A (diffuse face), N206 (centrally brightened), N23 (peaked emission), and DEM L238 (Irregular) observed by *ROSAT*.

They discussed physical implications for these morphologies. The younger and smaller remnants seem to show a clear shell-type morphology. The reasonable explanation is that such remnants have an X-ray emission from a shock front. Then, cloudlets in an ambient medium would be left behind. These cloudlets which were head by the shock evaporate within SNR, and produce a bright X-ray emission near the cloudlets. They are called "diffuse face". When the interior cloudlets were prevalent, this process would cause an X-ray emission toward a center. The hot interior becomes dense enough of the emission to overwhelm that from the shock front itself. This may lead to the "central brightened" morphology. Figure 3.7 shows the schematic stages of their evolution.

3.3 *ASCA* Observation

The systematic spectral analysis of three young SNRs and seven middle-aged SNRs were performed with *ASCA* SIS instruments by Hughes et al. (1995), Hayashi (1997) (Ph.D thesis), and Hughes et al. (1998). They constructed self-consistent non-equilibrium ion-

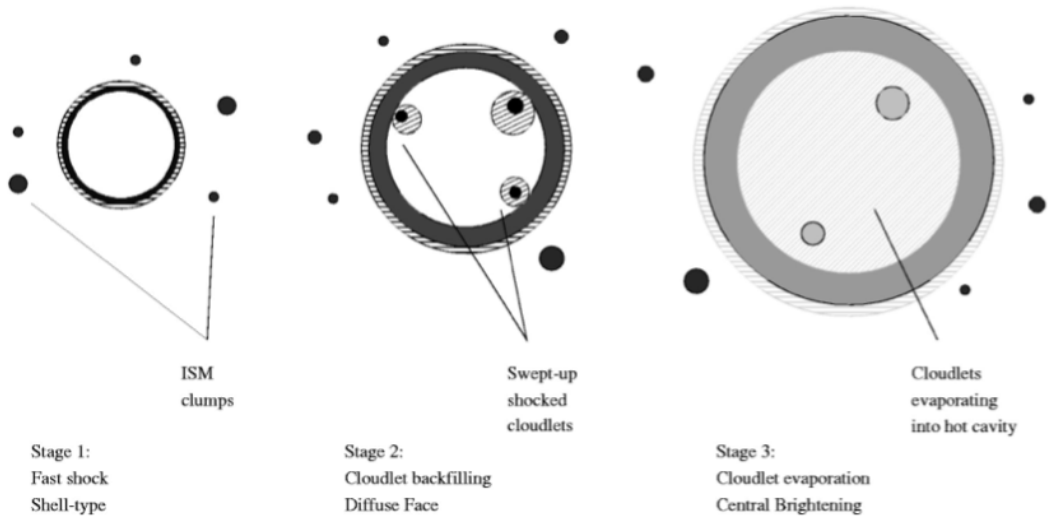

Figure 3.7: The schematic stages of their evolution in a cloudy medium. Striping regions are those from which Xray emission is expected, while solid regions indicate dense material, from which optical emission may be observed. The relative darkness of the shading indicates areas of higher (darker) and lower (lighter) density. This figure was taken from Williams et al. (1999).

ization SNR models assuming the Sedov solution for the dynamical evolution, and then applied the resulting spectral models to the data. The detailed spectral analysis of SNRs in the LMC were performed by them for the first time.

3.3.1 SNR Spectra

Figure 3.8 shows *ASCA* X-ray SNR spectra (0509-67.5, 0519-69.0, and N103B). Thanks to large energy range of the Solid-state Imaging Spectrometers (SIS) onboard *ASCA*, they presented these spectra over 0.3–10.0 keV band for the first time. They estimated many plasma parameters (temperature, metal abundances, ionization parameter, and so on) through the spectral analysis.

3.3.2 Metal Abundances

ASCA satellite revealed mean LMC "gas-phase" abundances for the first time. From the results of the middled-aged SNRs, they found a statistical evidence of an enrichment ambient medium by a supernova ejecta in the sense that smaller remnants show a somewhat higher metalicity than the larger one as shown in figure 3.9. However, the derived metal abundances were in general dominated by a swept-up ambient medium, and so these middle-aged SNRs could be used for the estimation of the mean LMC gas-phase abundances. The derived elements were less abundant than the solar values by a factor of two as shown in figure 3.10. Overall these results were consistent with the derived results from the optical or UV observations (Russell & Dopita, 1992). It was notable that this method for the abundance determination with the X-ray observations was entirely

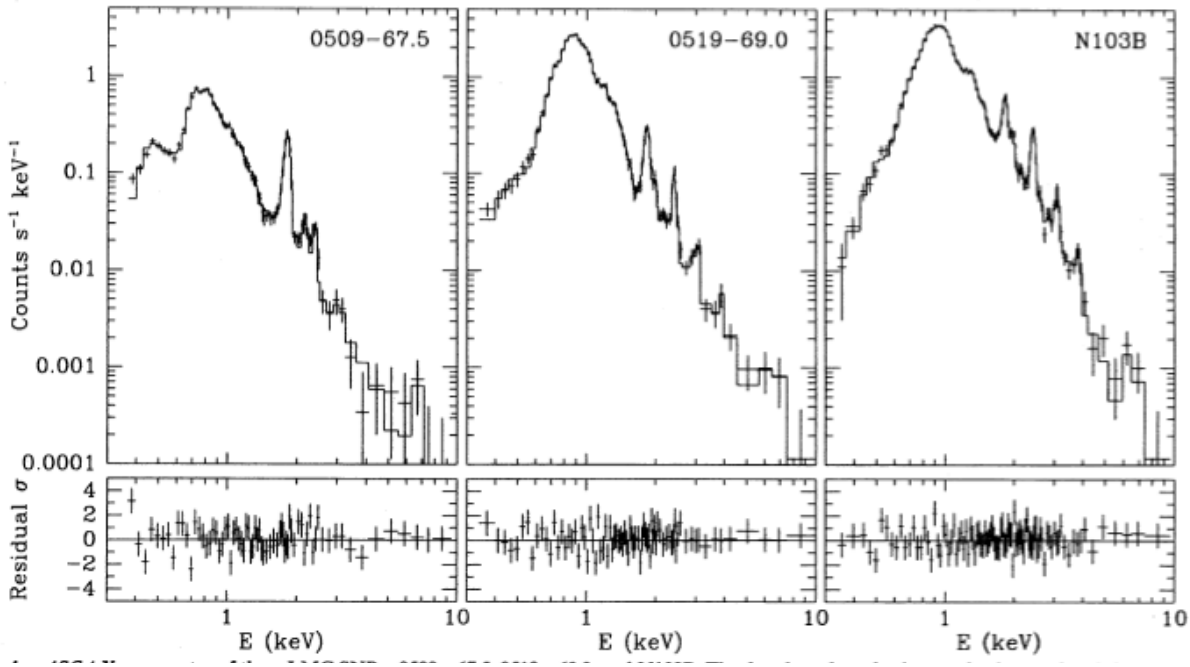

Figure 3.8: *ASCA* X-ray spectra of three LMC SNRs: 0509-67.5, 0519-69.0, and N103B. The lower panel shows the residuals from the best-fit model. These figures were taken from Hughes et al. (1995).

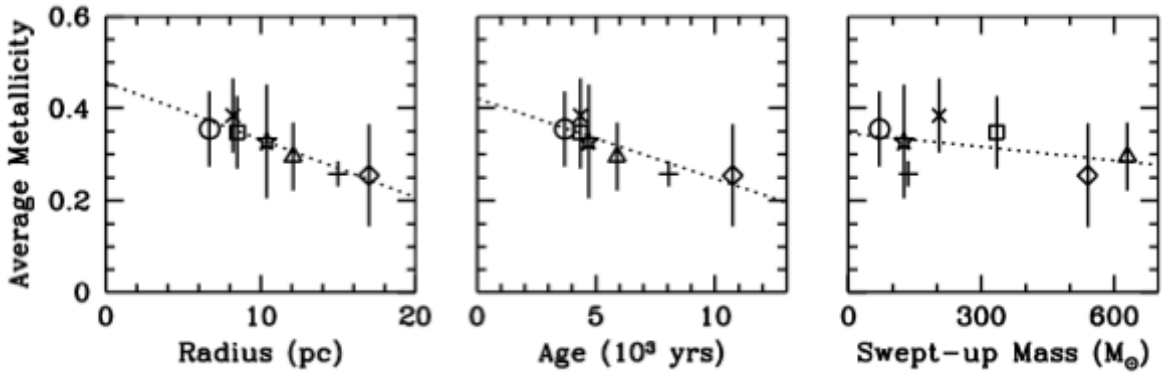

Figure 3.9: Mean metalicity (relative to cosmic value) vs. radius (left), dymical age derived from the Sedov solution (middle), and swept-up mass (right), provided by Hughes et al. (1998). The difference symbol types refer to the different remnants. Error bars represent the rms scatter in the individual fitted abundances of the various elemental species considered. Results plotted are the average of the values obtained under the two different model assumptions about the timescale of electron-ion temperature equilibrium. The only significant correlations are between metalicity and either radius or age.

independent compared with a previous methods using the UV or optical observations.

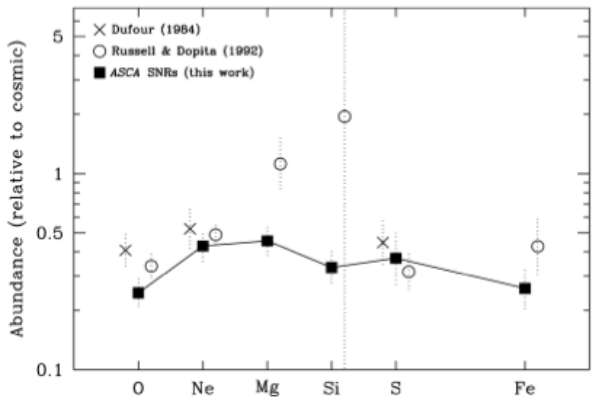

Figure 3.10: Average chemical abundances of the LMC relative to the cosmic value plotted as a function of elemental species by Hughes et al. (1998). The gas-phase abundances of the LMC derived from optical and UV studies of HII regions are shown as the crosses (Dufour, 1984). More recent results from Russell & Dopita (1992), whose as the circle, are based on the detailed modeling of optical/UV spectra from HII regions, SNRs, and supergiant stars.

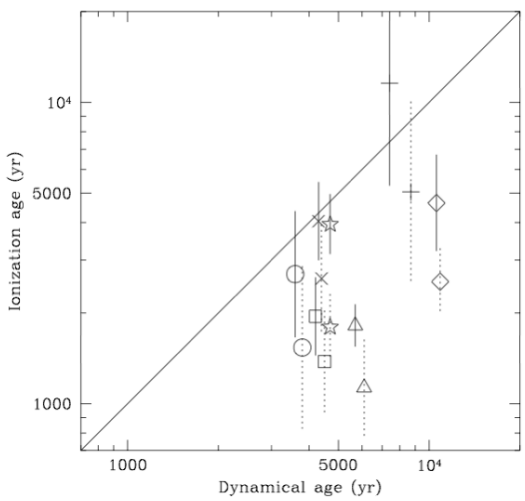

Figure 3.11: Remnant age determined from the fitted ionization age vs. the dynamical age derived from the Sedov model. The different symbol types refer to the different remnants (circle, cross, square, star, triangle, plus sign, and diamond correspond to N23, N49, N63A, DEM 71, N132D, 0453-68.5, and N49B, respectively). Error bars include only the statistical uncertainty from fits for the ionization age. Data points with dotted error bars (at the 90 % confidence level) are from the results assuming full electron-ion temperature equilibration at the SNR shock front, while the solid error bars refer to results using Coulomb equilibration timescales. This figure was taken by Hughes et al. (1998).

3.3.3 Cavity Explosion

Figure 3.11 shows the relation between fitted ionization ages and dynamical ages derived from the Sedov model. It was not coincidental that the several remnants were signifi-

cant differences between their ionization and dynamical ages. They explained for both discrepancies that such remnants exploded within preexisting low-density cavities in the ambient medium. The low interior density allows the blast wave to propagate rapidly to the cavity wall, where it then encounters a denser gas, begin to slow down, and emits the X-ray emission. This relation is one of the interesting topics.

Chapter 4

The Synoptic X-ray Analysis of SNRs in the LMC

4.1 Samples and Their Properties

In this section, we summarize our samples and their properties.

4.1.1 Samples

There are many catalogues for SNRs in the LMC over different wavelength from the radio to X-ray. Of these catalogues, one listed by Badenes et al. (2010) has the largest number of entries, which lists 54 confirmed SNRs. We therefore utilized this catalogue for the systematic study. In the X-ray band, we found 44 SNRs observed by *Suzaku*, *XMM-Newton* and *Chandra* with High Energy Astrophysics Archive Research Center (HEASARC)[1], though the detailed observations are explained in the later section. In figure 4.1 we present the optical R-band image (filter centered at 6571 Å with FWHM of 14 Å) for the LMC[2] (Bothun & Thompson 1988; Kennicutt et al. 1995; Parker et al. 1998). All SNRs belong to the LMC.

4.1.2 Their Properties

In this subsection, we summarize their properties, such as a name, a position, a size, and a SNe type.

Their Names, Positions, and Sizes

Their names and positions are listed in the second, third, forth, and fifth columns of table 4.1 (Badenes et al., 2010). Their sizes in the X-ray band are one of the natural properties to trace their evolution. We therefore decided to utilize previous results for their size estimations. The *Chandra* online catalogue[3] and *ROSAT* observations (Williams et al., 1999) are listed well about their sizes. Since they have superior angular resolutions (0".5; *Chandra* HRMA; Weisskopf et al. 2002, 5"–6"; *ROSAT* HRI; Aschenbach 1988),

[1] http://heasarc.gsfc.nasa.gov/
[2] http://dirty.as.arizona.edu/ kgordon/research/mc/mc.html
[3] http://hea-www.harvard.edu/ChandraSNR

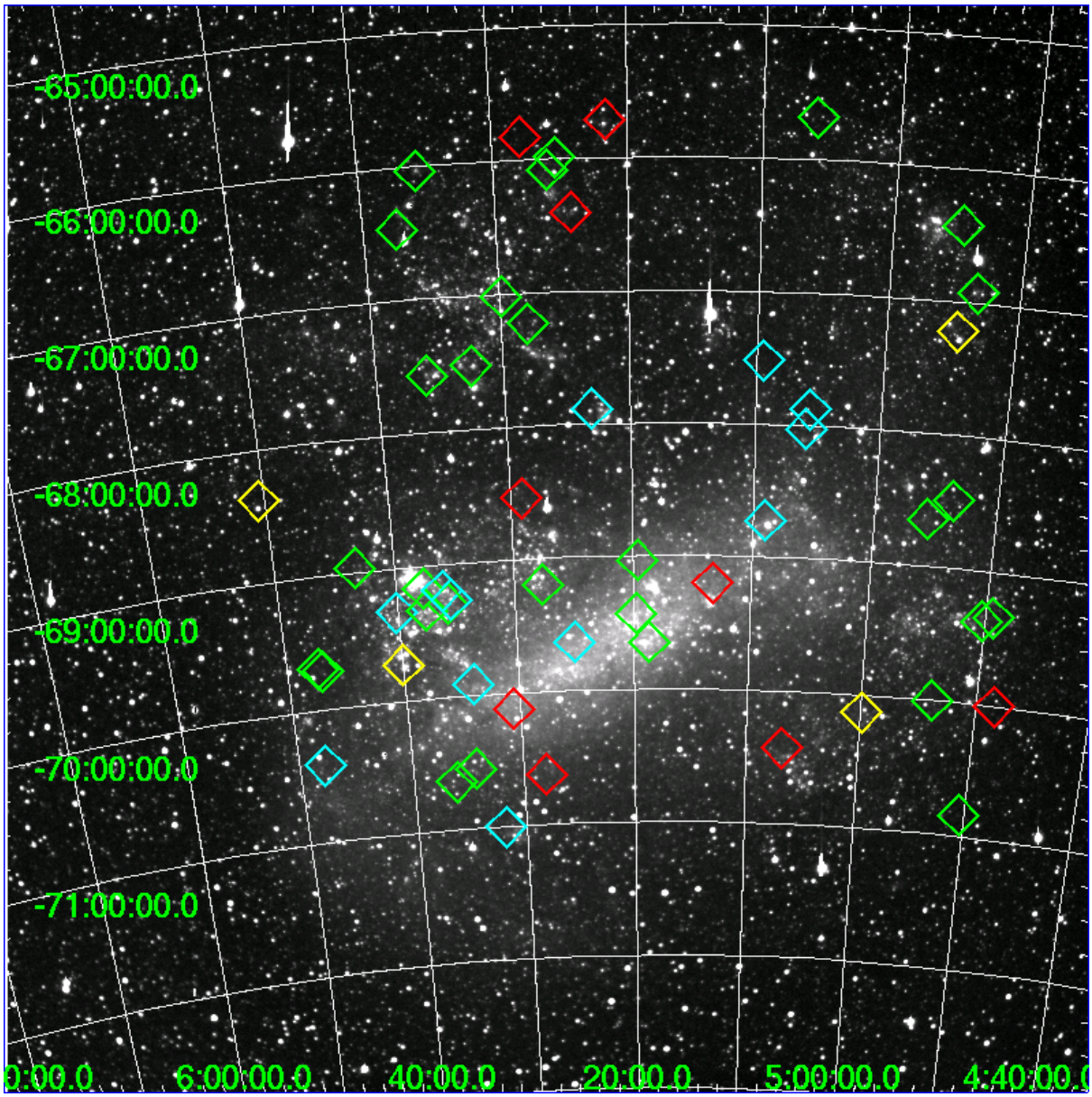

Figure 4.1: The optical R-band image for the Large Magellanic Cloud. The cyan, green, and yellow diamond points are represented with SNRs observed by *Suzaku*, *XMM-Newton*, and *Chandra*, respectively. The red diamond points, on the other hand, are represented without any X-ray observations. The coordinate is represented with the equatorial coordinate system for the epoch 2000.

Table 4.1: The X-ray Properties for SNRs in the LMC.

N	Name	Other name	Position (J2000)		The X-ray size	SNe type	Reference
		RA	Dec.	(arcmin)			
1	J0448.4-6660	-	04h48m22s	-69d59m52s	no observation		1
2	J0449.3-6920	-	04h49m20s	-69d20m20s	2.6×1.5	unknown	1, 4
3	J0450.2-6922	B0450-6927	04h50m15s	-69d22m12s	3.1	unknown	1
4	J0450.4-7050	B0450-709	04h50m27s	-70d50m15s	6.5×4.7	Ia (E)	1, 6, 31
5	J0453.2-6655	N4	04h53m14s	-66d55m13s	3.0×2.3 (T)	unknown	1, 3
6	J0453.6-6829	B0453-685	04h53m38s	-68d29m27s	2.0×1.9	CC (M, P)	1, 2, 6, 16, 30
7	J0453.9-7000	B0454-7005	04h53m52s	-70d00m13s	7.2	unknown	1
8	J0454.6-6713	N9	04h54m33s	-67d13m13s	3.6×2.4	Ia (A)	1, 2, 7
9	J0454.8-6626	N11L	04h54m49s	-66d25m32s	1.9×1.6	CC (E)	1, 3, 6
10	J0455.6-6839	N86	04h55m37s	-68d38m47s	6.1×2.8	Ia (E)	1, 3, 6
11	J0459.9-7008	N186D	04h59m55s	-70d07m52s	1.9×1.9	CC (E)	1, 2, 6
12	J0505.7-6753	DEM L71	05h05m42s	-67d52m39s	1.4×1.2	Ia (E, A, B. M)	1, 2, 6, 9, 10, 16
13	J0505.9-6802	N23	05h05m55s	-68d01m47s	1.6×1.6	CC (E, A, M)	1, 2, 6, 11, 12, 16
14	J0506.1-6541	-	05h06m05s	-65d41m08s	4.2×2.7	unknown	1, 4
15	J0506.8-7026	B0507-7029	05h06m50s	-70d25m53s	no observation		1
16	J0509.0-6844	N103B	05h08m59s	-68d43m35s	0.50×0.49	Ia (A, M) CC (E, A)	1, 2, 6, 13, 14, 15, 16
17	J0509.5-6731	B0509-67.5	05h09m31s	-67d31m17s	0.53×0.50	Ia (E, B, M)	1, 2, 6, 10, 16
18	J0513.2-6912	DEM L109	05h13m14s	-69d12m20s	no observation		1
19	J0518.7-6939	N120	05h18m41s	-69d39m12s	4.0×3.0	CC (E)	1, 3, 6
20	J0519.6-6902	B0519-690	05h19m35s	-69d02m09s	0.56×0.54	Ia (E, B, M)	1, 2, 6, 10, 16
21	J0519.7-6926	B0520-694	05h19m44s	-69d26m08s	2.6×2.2	Ia (E)	1, 3, 6
22	J0521.6-6543	-	05h21m39s	-65d43m07s	no observation		1
23	J0523.1-6753	N44	05h23m07s	-67d53m12s	4.3×4.0	unknown	1, 3
24	J0524.3-6624	DEM L175a	05h24m20s	-66d24m23s	no observation		1
25	J0525.1-6938	N132D	05h25m04s	-69d38m24s	2.1×1.6	CC (E, M, A)	1, 2, 6, 16, 29
26	J0525.4-6559	N49B	05h25m25s	-65d59m19s	2.6×2.6	CC (E, M, A)	1, 2, 6, 28
27	J0526.0-6605	N49	05h26m00s	-66d04m57s	1.4×1.4	CC (E, P, A)	1, 2, 6, 16, 26, 27
28	J0527.6-6912	B0528-692	05h27m39s	-69d12m04s	2.10×1.72 (T)	CC (E)	1, 3, 6
29	J0527.9-6550	DEM L204	05h27m54s	-65d49m38s	no observation		1
30	J0527.9-6714	B0528-6716	05h27m56s	-67d13m40s	no observation		1
31	J0528.1-7038	B0528-7038	05h28m02s	-70d37m40s	no observation		1
32	J0529.1-6833	DEM L203	05h29m05s	-68d32m30s	no observation		1
33	J0529.9-6701	DEM L214	05h29m51s	-67d01m05s	no detection		1
34	J0530.7-7008	DEM L218	05h30m40s	-70d07m30s	no observation		1
35	J0531.9-7100	N206	05h31m56s	-71d00m19s	2.8×2.6	CC (E, P, M)	1, 2, 6, 16, 25
36	J0532.5-6732	B0532-675	05h32m30s	-67d31m33s	2.54×1.30	unknown	1
37	J0534.0-6955	B0534-699	05h34m02s	-69d55m03s	2.2×2.0	CC (E, M) Ia (A)	1, 2, 6, 16, 17
38	J0534.3-7033	DEM L238	05h34m18s	-70d33m26s	3.0×2.2	Ia (E, A)	1, 2, 6, 22
39	J0535.5-6916	SNR 1987A	05h35m28s	-69d16m11s	<0.1	CC H)	1, 3
40	J0535.7-6602	N63A	05h35m44s	-66d02m14s	1.4×1.3	CC (E)	1, 2, 6
41	J0535.8-6918	Honeycomb	05h35m46s	-69d18m02s	1.6×0.8	CC (A)	1, 2, 24
42	J0536.1-6735	DEM L241	05h36m03s	-67d34m36s	6.0×3.0	CC (E, P, A)	1, 6, 23
43	J0536.1-7039	DEM L249	05h36m07s	-70d38m37s	2.64×1.00 (T)	Ia (E, A)	1, 3, 6, 22
44	J0536.2-6912	30 Dor C	05h36m09s	-69d11m53s	5.4 (T)	CC (E)	1, 6
45	J0537.4-6628	DEM L256	05h37m27s	-66d27m50s	3.2×1.6	unknown	1, 4
46	J0537.6-6920	B0538-6922	05h37m37s	-69d20m23s	no detection		1
47	J0537.8-6910	N157B	05h37m46s	-69d10m28s	2.0×2.0	CC (E, P, A)	1, 2, 6, 20, 21
48	J0540.0-6944	N159	05h39m59s	-69d44m02s	1 (T)	CC (E, A)	1, 2, 6, 19
49	J0540.2-6920	B0540-693	05h40m11s	-69d19m55s	1.2×1.1	CC (E, P)	1, 2, 6, 18
50	J0543.1-6858	DEM L299	05h43m08s	-68d58m18s	4 (T)	CC (E)	1, 3, 6
51	J0547.0-6943	DEM L316B	05h46m59s	-69d42m50s	3.3×2.1	CC (A)	1, 2, 8
52	J0547.4-6941	DEM L316A	05h47m22s	-69d41m26s	2.0×1.8	Ia (A)	1, 2, 8
53	J0547.8-7025	B0548-704	05h47m49s	-70d24m54s	1.9×1.7	Ia (A, B, M)	1, 2, 10, 16, 17
54	J0550.5-6823	-	05h50m30s	-68d22m40s	5.2×3.5	unknown	1, 2

Reference: (1) Badenes et al. (2010), (2) *Chandra* online catalogue, (3) Williams et al. (1999), (4) Klimek et al. (2010), (5) Bamba et al. (2006), (6) Chu & Kennicutt (1988), (7) Seward et al. (2006), (8) Williams & Chu (2005), (9) Hughes et al. (2003), (10) Tuohy et al. (1982), (11) Hughes et al. (2006), (12) Hayato et al. (2006), (13) Hughes et al. (1995), (14) Lewis et al. (2003), (15) van der Heyden et al. (2002), (16) Lopez et al. (2011), (17) Hendrick et al. (2003), (18) Seward et al. (1984), (19) Seward et al. (2010), (20) Marshall et al. (1998), (21) Chen et al. (2006), (22) Borkowski et al. (2006), (23) Bamba et al. (2006), (24) Dennerl et al. (2001), (25) Williams et al. (2006), (26) Rothschild et al. (1994), (27) Park et al. (2003), (28) Park et al. (2003), (29) Borkowski et al. (2007), (30) Gaensler et al. (2003), and (31) Williams et al. (2004).

it is suitable for our purpose. The sixth column in table 4.1 we present their sizes (≡ diameter) in unit of arcmin. Since the following SNRs had no any references above, we therefore utilized *XMM-Newton* observations; J0449.3-6920 (Klimek et al., 2010), J0506.1-6541 (Klimek et al., 2010), J0537.4-6628 (DEM L256; Klimek et al. 2010), J0450.4-7050 (B0450-709; Williams et al. 2004), J0536.1-6735 (DEM L241; Bamba et al. 2006). On the other hand, we estimated their radii for the several SNRs with the *Chandra* and *XMM-Newton* observations, which were listed in the sixth column of table 4.1 labeled "T".

Their SNe Types

Type Ia and CC SNRs have very different progenitors. Since both core-collapsed and Type Ia SNe release $\sim 10^{51}$ erg in kinetic energy, it is difficult to distinguish SNR from both types of explosion. For this reason, there are many methods to estimate the progenitor. (P): the presence of a pulsar and/or its wind nebula are identified clearly originated from a CC SN. (A): Type Ia and CC SNe are mainly produced Fe (e.g. Iwamoto et al. 1999) and O/Ne/Mg (e.g. Nomoto et al. 1997), respectively. In the X-ray observation, these elements are detected strongly if SNRs have enhanced metal abundances. (E): Chu & Kennicutt (1988) suggested a Population I environment based on its proximity to the HII region, the OB association, the high density of OB stars, and the CO molecular cloud. The Population I and the other (a Population II) environments are indicated to be CC and Type Ia SNe, respectively. (M): in the recent report, from a systematic X-ray study of ejecta morphologies based on SiXIII, Type Ia SNRs have high symmetry morphologies compared with those of CC SNRs (Lopez et al., 2011). Finally, (B): several SNRs originated from Type Ia SN have an optical spectrum which is dominated by the hydrogen emission (balmer series) with little or no emission from forbidden lines of OIII and SiII. The seventh column of table 4.1 shows the possible SN types and the estimated methods. However, several SNRs could not be revealed their SN types in previous observations. Such SNRs were also listed in the seventh column of table 4.1 labeled "unknown". Moreover, J0509.0-6844 (N103B) and J0534.0-6955 (B0534-699) have not concluded about their SN types in the previous observations.

4.2 Observation & Data Reduction

Our aim is to discuss SNRs mainly from the Sedov phase to the radiative cooling phase in our study. Of these evolutionary phases, it can be expected to have a low temperature plasma in collisional ionization equilibrium at the late stage. For example, several authors (e.g. van der Heyden et al. 2003; Borkowski et al. 2006; Someya et al. 2010) have been reported that SNRs with a low temperature plasma (∼0.2 keV) in collisional ionization equilibrium may be in the radiative cooling phase. Such plasma emits strongly from H- and He-like oxygen Kα emission lines. Since these emission lines appear in the 0.5–0.7 keV, it is important to have a high resolution spectroscopy and a large effective area in this energy band to determine mainly a low temperature plasma in collisional ionization equilibrium. XISs onboard *Suzaku* (Mitsuda et al. 2007; Koyama et al. 2007) have the best energy resolution in the 0.5–0.7 keV among the CCDs currently in orbit, and this satellite also has the comparatively larger effective area (Serlemitsos et al., 2007). Fortunately, since most SNRs observed by *Suzaku* have the longer exposure time compared with those observed by

Table 4.2: The observation logs for SNRs in the LMC.

Name	Other name	Obs ID	Obs day	Exp*	Count rates†		Satellite
					MOS/FI/ACIS	pn/BI	
			(yyyymmdd)	(ksec)	(cts s^{-1})	(cts s^{-1})	
J0448.4-6660	-			no observation			
J0449.3-6920	-	0205260101	20040224	5.6	0.007±0.002	0.030±0.005	Newton
J0450.2-6922	B0450-6927	0205260101	20040224	5.6	0.006±0.001	0.015±0.005	Newton
J0450.4-7050	B0450-709	0089210601	20011011	38.2	0.037±0.002	-	Newton
J0453.2-6655	N4	0503710101	20070720	14.9	0.052±0.002	0.026±0.008	Newton
J0453.6-6829	B0453-685	0062340101	20010329	5.7	0.76±0.01	3.03±0.03	Newton
J0453.9-7000	B0454-7005	0503680101	20080310	9.6	0.05±0.01	0.14±0.02	Newton
J0454.6-6713	N9	3847	20040206	66	0.16±0.02	-	Chandra
J0454.8-6626	N11L	0109260201	20010917	28.5	0.020±0.001	0.073±0.002	Newton
J0455.6-6839	N86	0062340101	20010329	3.4	-	0.11±0.01	Newton
J0459.9-7008	N186D	3355	20030101	37	0.031±0.003	-	Chandra
J0505.7-6753	DEM L71	100003010	20050816	7.1	1.04±0.01	2.37±0.02	Suzaku
J0505.9-6802	N23	100003010	20050816	7.1	0.56±0.01	1.26±0.02	Suzaku
J0506.1-6541	-	0205260201	20040116	9.1	0.0345±0.003	0.016±0.009	Newton
J0506.8-7026	B0507-7029			no observation			
J0509.0-6844	N103B	100013010	20050830	33	2.13±0.01	3.71±0.01	Suzaku
J0509.5-6731	B0509-67.5	501041010	20060818	38	0.296±0.002	0.552±0.0004	Suzaku
J0513.2-6912	DEM L109			no observation			
J0518.7-6939	N120	0089210701	20011011	31.3	0.55±0.02	0.52±0.02	Newton
J0519.6-6902	B0519-690	0113000501	20010917	27.2	1.935±0.007	7.11±0.004	Newton
J0519.7-6926	B0520-694	0204770101	20040117	15.5	0.142±0.002	0.55±0.01	Newton
J0521.6-6543	-			no observation			
J0523.1-6753	N44	803036010	20080409	30	1.7±0.3	2.7±0.2	Suzaku
J0524.3-6624	DEM L175a			no observation			
J0525.1-6938	N132D	105011010	20100827	29	5.85±0.01	10.72±0.02	Suzaku
J0525.4-6559	N49B	0111130301	20000708	6.8	2.44±0.01	-	Newton
J0526.0-6605	N49	0113000201	20010408	11.9	4.05±0.01	-	Newton
J0527.6-6912	B0528-692	065583010	20100430	33	-	0.042±0.004	Newton
J0527.9-6550	DEM L204			no observation			
J0527.9-6714	B0528-6716			no observation			
J0528.1-7038	B0528-7038			no observation			
J0529.1-6833	DEM L203			no observation			
J0529.9-6701	DEM L214	0402000601	20070128	no detection			Newton
J0530.7-7008	DEM L218			no observation			
J0531.9-7100	N206	803038010	20080428	49	0.021±0.002	0.040±0.001	Suzaku
J0532.5-6732	B0532-675	0400320101	20060828	14.2	0.113±0.004	0.43±0.01	Newton
J0534.0-6955	B0534-699	505064010	20100331	99	0.107±0.001	0.229±0.002	Suzaku
J0534.3-7033	DEM L238	0156560101	20030723	22.2	0.096±0.002	0.037±0.006	Newton
J0535.5-6916	SNR 1987A	500006010	20051103	26	2.47±0.04	4.26±0.05	Suzaku
J0535.7-6602	N63A	0109990101	20001125	7.5	12.99±0.03	48.02±0.09	Newton
J0535.8-6918	Honeycomb	0144530101	20030510	51	0.034±0.001	-	Newton
J0536.1-6735	DEM L241	0205380101	20041229	29.5	0.2585±0.0002	0.800±0.001	Newton
J0536.1-7039	DEM L249	0142660901	20031024	4.5	0.041±0.003	0.14±0.01	Newton
J0536.2-6912	30 Dor C	500006010	20051103	26	2.47±0.04	4.26±0.05	Suzaku
J0537.4-6628	DEM L256	0301410601	20051002	18.5	0.022±0.001	0.087±0.004	Newton
J0537.6-6920	B0538-6922	0113020201	20011119	no detection			Newton
J0537.8-6910	N157B	0113020201	20011119	36.3	8.29±0.04	-	Newton
J0540.0-6944	N159	3849	20031209	20.9	0.0260±0.0004	-	Chandra
J0540.2-6920	B0540-693	102023010	20080216	67	1.76±0.01	2.19±0.01	Suzaku
J0543.1-6858	DEM L299	0094410101	20011019	10.1	0.114±0.004	0.45±0.01	Newton
J0547.0-6943	DEM L316B	0201030101	20040105	9.6	0.094±0.002	0.022±0.007	Newton
J0547.4-6941	DEM L316A	0201030101	20040105	9.6	0.068±0.002	0.283±0.007	Newton
J0547.8-7025	B0548-704	505065010	20100701	103	0.045±0.002	0.133±0.002	Suzaku
J0550.5-6823	-	3850	20031002	68	0.127±0.005	-	Chandra

* Mean exposure times after the background flare subtraction.
† Count rates in the 0.5-10 keV band within a source region after the background subtraction.

the other satellites, such as *XMM-Newton* and *Chandra*. We therefore decided to utilize preferentially *Suzaku* data. On the other hand, for the data which were not observed by *Suzaku*, we utilized preferentially the data observed by *XMM-Newton*. *XMM-Newton* carries also CCDs (EPIC-MOS and -pn; Turner et al. 2001 and Strüder et al. 2001), which have the moderate energy resolution in the 0.5–0.7 keV. Finally, the others were utilized the data observed by *Chandra*, which carries CCDs (ACIS; Garmire et al. 2003) with the relatively low energy resolution in this energy band. In our study, we did not utilize the HRC and RGS data because of the narrow energy band and the relatively small effective area, which could not provided us with the X-ray image and spectrum simultaneously.

There are 54 confirmed SNRs in the LMC over difference wave length from the radio to X-ray (Badenes et al., 2010). In the X-ray band, we found 44 SNRs observed by *Suzaku*, *XMM-Newton*, and *Chandra* with HEASARC until 31 March, 2011: *Suzaku*: 12 SNRs, *XMM-Newton*: 28 SNRs, and *Chandra*: 4 SNRs. Of these SNRs, we could not analyze J0529.9-6701 (DEM L214) and J0537.6-6920 (B0538-6922), which have the very faint X-ray emission. In table 4.2 we present the observation logs.

4.2.1 *Suzaku* data set

Suzaku (Mitsuda et al., 2007) is carried with two kinds of the X-ray detectors: one is the Hard X-ray Detector (HXD; Takahashi et al. 2007; Kokubun et al. 2007), which is a non-imaging type detector, and is sensitive in the 10–600 keV. The other is the X-ray Imaging Spectrometer (XIS; Koyama et al. 2007), which is an X-ray CCD camera mounted on the focal plane of the X-ray telescope (XRT; Serlemitsos et al. 2007). In total, there are four modules of the XIS, three of which are Front-illuminated (FI) CCDs, which are hereafter referred to as XIS0, 2, and 3, and the other one is a Back-illuminated (BI) CCD, which is referred to as XIS1. Unfortunately, XIS2 suddenly was damaged on November 9, 2006. We therefore could not utilize the XIS2 data for 6 SNRs; J0523.1-6753 (N44), J0525.1-6938 (N132D), J0531.9-7100 (N206), J0534.0-6955 (B0534-699), J0540.2-6920 (B0540-693), and J0547.8-7025 (B0548-704). In addition, though 1/8 of XIS0 was damaged on June 23, 2009, the laced areas were very small, which had little problem for following SNRs; J0525.1-6938 (N132D), J0534.0-6955 (B0534-699), and J0547.8-7025 (B0548-704). These information were referred in JX-ISAS-SUZAKU-MEMO-2007-08 and -2010-01 [4]. The half-power diameter (HPD) of each telescope is $\sim 2'$ (Serlemitsos et al., 2007).

We utilized the data with the 5×5 and 3×3 editing mode with Revision 2 with the HEADAS 6.5.1 software package. In order to exclude high background events, we removed time intervals while the South Atlantic Anomaly (SAA) and the elevation angles from the night and day earth less than 5° and 20°, respectively. We also utilized only the event with a grade of 0, 2, 3, 4 and 6 in the following spectral analysis. We applied the charge-transfer inefficiency (CTI) correction with XISPI software and CTI parameter of 2007-05-30 for J0523.1-6753 (N44), J0535.5-6916 (SN 1987A; 30 Dor C) and J0540.2-6920 (B0540-693), and 2009-12-02 for J0525.1-6938 (N132D) and J0547.8-7025 (B0548-704). As for J0534.0-6955 (B0534-699) and J0531.9-7100 (N206), we applied CTI parameter of 2009-02-28 and 2008-01-31, respectively. Response matrix files (RMF) and ancillary response files (ARF) were made using XISRMFGEN and XISSIMARFGEN (Ishisaki et al.,

[4] http://www.astro.isas.ac.jp/suzaku/swg/suzakumemo/

2007) version 2007-09-22, respectively. The available data have no background flares.

4.2.2 *XMM-Newton* data set

XMM-Newton (Jansen et al., 2001) provides the following three type of science instruments; European Photon Imaging Camera (EPIC), Reflection Grating Spectrometers (RGS; den Herder et al. 2001) and Optical Monitor (OM; Mason et al. 2001). We concentrate on the MOS and pn data in this chapter. The three EPIC cameras; the two different types of CCD camera, MOS (Turner et al., 2001) and pn (Strüder et al., 2001) reside in the focal planes of the X-ray telescopes. The HEWs of the X-ray telescopes for MOS and pn are ∼13–15" (Jansen et al., 2001).

We began from a raw archive data (so-called Observation Data File: ODF), and screened them ourselves based on the current calibration data, by utilizing the *XMM-Newton* Science Analysis Software (SAS) version 10.0.0. In order to reject soft proton flares, we made a light curve and its count-rate histogram of each data set for each detector with >10 keV for MOS and 10.0–12.0 keV for pn, with 100 sec integration. Then, we fitted the histogram with a gaussian function, and discarded whose time bins which were deviated by more than 2σ from the mean rate. After this study, we made a light curve again. The prominent background events for all SNRs were excluded. In the following spectral analysis, we selected X-ray events with PATTERN=0–12, which were passed through the #XMMEA_EM filter for MOS data. As for pn data, the X-ray events with PATTERN=0–4 and FLAG=0 were extracted. #XMMEA_EM and FLAG=0 selections remove events from or adjacent to noisy pixel and known bright columns. We referred USERS GUIDE TO THE *XMM-Newton* SCIENCE ANALYSIS SYSTEM [5] due to the data reduction for *XMM-Newton* data. Response matrix files (RMF) and ancillary response files (ARF) were made using ARFGEN and RMFGEN, respectively. Finally, we utilized only the data operated by Full Frame Window Mode. Of these SNRs, since J0455.6-6839 (N86) and J0527.6-6912 (B0528-692) were out of the FOV of the MOS detector, we utilized only the pn data. On the other hand, since J0532.5-6732 (B0532-675) was in the lack of the MOS 1 detector, we therefore utilized only the pn and MOS 2 data. Count rates in table 4.2 are after the data screening above.

4.2.3 *Chandra* data set

Chandra (Weisskopf et al., 2002) carried the X-ray CCD cameras (ACIS-I; Garmire et al. 2003) on the focal plane of the X-ray telescopes (High Resolution Mirror Assembly: HRMA). The FWHM of HRMA is <0.5" (Garmire et al., 2003). We utilized *Chandra* ACIS archive data. The cleaned event file was taken from the public *Chandra* archive data[6]. We started our analysis from level 2 event files processed with calibration data files. The data reduction and analysis were performed with Chandra Interactive Analysis of Observations (CIAO) version 4.0. Response matrix files (RMF) and ancillary response files (ARF) were made with SPECEXTRACT in CIAO package.

[5] http://xmm.esa.int/external/xmm_user_support/documentation/sas_usg/USG/
[6] http://cda.harvard.edu/chaser/

4.3 Spectral Analysis

The spectra were fitted with XSPEC v11.3.2aj to apply a χ^2 minimization technique, and the errors for all spectral parameters quoted 90 % confidence level for one interesting parameter (i.e., $\Delta\chi^2 = 2.7$).

4.3.1 Source Extraction

A small structure in SNRs depends strongly on a surrounding environment, its explosion property, and so on. Since we want to discuss global SNR natures, the extracted region is selected to cover the entire SNR. In order to extract the source photons, we made the surface brightness for each SNR, and selected the region to cover the entire SNR by eye. On the other hand, the background region was taken from the nearby blank-sky region by eye. The background regions were constructed so as to exclude possible point source contamination. Moreover, the background events for *XMM-Newton* and *Chandra* were extracted the same chip as much as possible. Our SNR spectra were thermally in nature, and showed emission lines from highly ionized atoms. The background level in the most SNRs were relatively low (in the 0.5–2.0 keV >70 % of the total: source + background count rate), while the J0453.9-7000 (B0454-7005; 80 %) was the relatively large contribute of the background. The selected source and background regions were listed in appendix § B.

4.3.2 Spectral Model

The X-ray emission from a general SNR is known that the emission is well reproduced by the optically thin thermal emission model in non-equillibrium ionization. We therefore adopted non-equilibrium ionization VNEI model in the XSPEC library (Hamilton et al. 1983, Borkowski et al. 1994, Liedahl et al. 1995, Borkowski et al. 2001). From the spectral analysis, we can obtain a plasma temperature ($kT_{\rm e}$), a metal abundance ($A_{\rm i}$, where a metal abundance is relative to the solar abundance: Anders & Grevesse 1989), an ionization parameter ($n_{\rm e}t_{\rm ion}$, where $n_{\rm e}$ and $t_{\rm ion}$ are a plasma density and an elapsed time scale of the shock, respectively) and a normalization ($\frac{10^{-14}}{4\pi D^2}\int n_{\rm e}n_{\rm H}dV$, where D, $n_{\rm H}$, and dV are a distance to a source, a hydrogen number density, and a volume element of a plasma, respectively). The VNEI model gives as an average ionization parameter. Since this model is not considered shock propagation, we also adopted plane-parallel, non-equilibrium ionization VPSHOCK model in the XSPEC library, which integrates the emission with ionization parameters varying linearly from 0 to $n_{\rm e}t$ (Hughes et al., 2000). The obtained parameters are shared with VNEI model. On the other hand, we adopted collisional ionization equilibrium VAPEC (Smith et al., 2001) or MEKAL (e.g. Mewe et al. 1985; Mewe et al. 1986) model in the XSPEC library to compare with the previous results. These models are given the same parameters above other than the ionization parameter.

The emission from sources in the LMC is attenuated by the interstellar matter in our galaxy and the LMC. Since the metal abundances of these two absorption components are significantly different, we estimated these absorptions is as following to be. The abundances of the absorption matter in our galaxy assumed the solar abundance (Anders & Grevesse, 1989), and represented the hydrogen column density as $N_{\rm H}^{\rm G}$. The value of $N_{\rm H}^{\rm G}$ toward our observation has been already obtained from the Galactic HI survey

(Dickey & Lockman, 1990). We fixed $N_{\rm H}^{\rm G}$ at this value, and used PHABS model in the XSPEC library to represent the absorption in our galaxy. The absorptions in our galaxy toward SNR in the LMC are estimated to be $\sim$(5–9)$\times 10^{20}$ cm^{-2}. On the other hand, the average metal abundances in the LMC have been measured by Russell & Dopita (1992) to be $\sim$0.3 solar. We therefore used the VPHABS model in the XSPEC library to represent the absorption in the LMC, which is reflected these abundances. The hydrogen column density is represented as $N_{\rm H}^{\rm L}$, and set the value to vary.

4.3.3 Basic Concepts for Spectral Modeling

Thermal Components

In evaluating the spectra of SNRs in the LMC through the spectral fitting, we began with a single component VNEI model attenuated by an interstellar absorption. To reduce the number of model parameters as much as possible, we fixed the metal abundances at the LMC average (Russell & Dopita, 1992). However, many SNRs needed to vary the metal abundances because of the good photon statistics and the difference from the LMC average. Whether the metal abundances are constrained or not, we judge with the F-test. If the probability significantly was improvement, basically above $\sim 3\ \sigma$, the metal abundances were constrained. Then, the metal abundances of O, Ne, Mg, Si, and Fe (Fe-L complex) were constrained, in general. Since the majority of the X-ray emission from many SNRs is concerned below 2 keV, this study provides the valid assumption in our study. However, several SNRs with high temperature plasma emitted the strong line features from S, Ar, and Ca. Then, we also constrained the metal abundance for such SNRs. Since the spectral analysis, we fitted spectra in the 0.5–10 keV and/or 0.5–5 keV band, the C and N abundances were fixed at the LMC average (Russell & Bessell, 1989). In our study, several SNRs strong coupled the normalization with the metal abundances because of the poor photon statistics and/or the no continuum emission, though the spectra fittings were improved significantly. For such SNRs, we fixed the O abundance at the LMC average (Russell & Bessell, 1989). It is probably difficult to derive absolute metal abundances for such SNRs. Since we discuss only the relative abundances in the later sections, it is little important. We call this spectral modeling "$1kT1nt$". If "$1kT1nt$" has no longer an acceptable fit, we append an another VNEI model. Then, to reduce the model parameters as much as possible, we constrained either an ionization parameter or temperature common between the two VNEI model. We also call the former modeling "$2kT1nt$", and the latter modeling "$1kT2nt$". If these models have no longer still an acceptable fit, we constrain the ionization parameter and temperature between the two VNEI components to vary independently. We call this model "$2kT2nt$". Finally, we appended an another VNEI model with "$2kT2nt$". Then, we constrained the ionization parameter and the temperature among the three VNEI components to vary independently. We call this model "$3kT3nt$". Through the spectral analysis, we contained the metal abundances common between the two and three component VNEI models. In this study, we decided to increase the model parameters until the χ^2_ν of $\leq$1.5 by considering systematic errors. The systematic error of the spectral modelings is summarized in appendix § D. In table 4.3 we give the χ^2 ($d.o.f./\chi^2_\nu$) for each model. The adopted models are represented with in bold type.

Non-Thermal Components

It has already reported that 5 SNRs (J0536.1-6735: DEM L241, J0536.2-6912: 30 Dor C, J0537.8-6910: N157B, and J0540.2-6920: B0540-693) have a strong non-thermal emission from electrons accelerated by a shock and/or a pulsar (its wind nebula). The previous results are summarized in appendix § F. For these SNRs, we appended POWER LAW model in the XSPEC library with "$1kT1nt$–$3kT3nt$". We call these models "$1kT1nt$–$3kT3nt$ + Power law (1)". On the other hand, it is found that 4 SNRs (J0540.0-6944: N159, J0453.9-7000: B0454-7005, J0543.1-6858: DEM L299, and J0505.7-6753: DEM L71) have a high energy component, though these SNRs have not been reported to have a non-thermal component. We therefore doubted several cases for such SNRs; (i) a contamination from prominent point-like sources and (ii) a non-thermal emission. We therefore decided to utilize the same model above. We also call these models "$1kT1nt$–$3kT3nt$ + Power law (2)". The detailed spectral analysis of J0505.7-6753 (DEM L71) is summarized in appendix § C.2. For these SNRs, we judged with "$1kT1nt$ + Power law (1) (2)" whether the metal abundances were constrained or not. We also present showed "$1kT1nt$–$3kT3nt$ + Power law (1) (2)" as "$1kT1nt$–$3kT3nt$". In table 4.3 we give the χ^2 ($d.o.f.$) for each model. The adopted models are represented with in bold type in table 4.3.

Notes

In the spectral analysis, we utilized the energy range in the 0.5–10 keV band in general. For several SNRs, on the other hand, we ignored the energy range of $\geq$5 keV, which have remarkable noisy events to exceed roughly 1 σ because of poor photon statistics and fluctuations of the non-X-ray background. Since the majority of the X-ray emission from many SNRs is concentrated below 2 keV, this is little important in our study. In this study, we have no longer acceptable fits (the χ^2_ν of >1.5) until "$3kT3nt$" for the following 8 SNRs; J0454.6-6713 (N9), J0505.7-6753 (DEM L71), J0525.1-6938 (N132D), J0526.0-6605 (N49), J0534.3-7033 (DEM L238), J0536.1-6735 (DEM L241), J0535.7-6602 (N63A) and J0536.1-7039 (DEM L249). We therefore did not utilize these SNRs for discussion in the later sections. These SNRs would be needed to analyze in detail. The detailed spectral analysis of J0505.7-6753 (DEM L71) is summarized in appendix § C.2. Moreover, we could not utilize for the following SNRs to depend on the spectral modeling strongly; J0509.0-6844 (N103B; Lewis et al. 2003; van der Heyden et al. 2002), J0509.5-6731 (B0509-67.5; Kosenko et al. 2008), J0519.6-6902 (B0519-690; Kosenko et al. 2010).

Table 4.3: The χ^2 $(d.o.f./\chi^2_\nu)$ for all models*.

Name	Other name	$1kT1nt$	$2kT1nt$	$1kT2nt$	$2kT2nt$	$3kT3nt$
			χ^2 $(d.o.f/\chi^2_\nu)$			
J0449.3-6920	-	**5.7 (20/0.29)**	-	-	-	-
J0450.2-6922	B0450-6927	**17.8 (24/0.74)**	-	-	-	-
J0450.4-7050	B0450-709	**43.7 (53/0.82)**	-	-	-	-
J0453.2-6655	N4	**93.6 (95/0.99)**	-	-	-	-
J0453.6-6829	B0453-685	**224.0 (167/1.34)**	-	-	-	-
J0453.9-7000	B0454-7005	**67.9 (50/1.36)**	-	-	-	-
J0454.6-6713	N9	100.3 (30/3.34)	68.7 (28/2.45)	73.4 (28/2.62)	68.6 (27/2.54)	54.3 (24/2.26)
J0454.8-6626	N11L	**114.1 (108/1.06)**	-	-	-	-
J0455.6-6839	N86	**18.7 (17/1.10)**	-	-	-	-
J0459.9-7008	N186D	**12.5 (10/1.25)**	-	-	-	-
J0505.7-6753	DEM L71	554.3 (125/4.43)	191.2 (123/1.55)	276.4 (123/2.25)	189.4 (122/1.55)	187.7 (119/1.58)
J0505.9-6802	N23	163.1 (107/1.52)	**109.7 (105/1.05)**	120.5 (105/1.15)	-	-
J0506.1-6541	-	**47.5 (48/0.99)**	-	-	-	-
J0509.0-6844	N103B	-	-	-	-	-
J0509.5-6731	B0509-67.5	-	-	-	-	-
J0518.7-6939	N120	**100.7 (77/1.31)**	-	-	-	-
J0519.6-6902	B0519-690	-	-	-	-	-
J0519.7-6926	B0520-694	**133.0 (122/1.09)**	-	-	-	-
J0523.1-6753	N44	**36.2 (44/0.82)**	-	-	-	-
J0525.1-6938	N132D	12425.7 (1066/11.7)	7204.2 (1064/6.8)	5569.7 (1064/5.2)	5010.4 (1063/4.7)	4185.5 (1060/4.0)
J0525.4-6559	N49B	**213.7 (156/1.37)**	-	-	-	-
J0526.0-6605	N49	1669.3 (260/6.42)	674.7 (258/2.62)	813.6 (258/3.15)	535.1 (257/2.08)	394.1 (254/1.55)
J0527.6-6912	B0528-692	**36.3 (38/0.96)**	-	-	-	-
J0531.9-7100	N206	**69.2 (83/0.83)**	-	-	-	-
J0532.5-6732	B0532-675	**81.9 (76/1.08)**	-	-	-	-
J0534.0-6955	B0534-699	429.2 (190/2.26)	**280.8 (188/1.49)**	304.0 (188/1.62)	-	-
J0534.3-7033	DEM L238	284.1 (82/3.47)	160.0 (80/2.00)	172.5 (80/2.16)	160.0 (79/2.03)	153.0 (76/2.01)
J0535.5-6916	SNR 1987A	455.3 (225/2.03)	**218.9 (223/0.98)**	304.0 (188/1.62)		-
J0535.7-6602	N63A	9088.3 (712/12.8)	3176.0 (710/4.5)	2417.1 (710/3.4)	3305.5 (709/4.6)	2297.692 (706/3.3)
J0535.8-6918	Honeycomb	**126.5 (95/1.33)**	-	-	-	-
J0536.1-6735	DEM L241	450.4 (181/2.49)	443.3 (179/2.48)	412.6 (179/2.31)	418.6 (178/2.35)	457.6 (175/2.62)
J0536.1-7039	DEM L249	31.6 (19/1.66)	28.8 (17/1.69)	28.8 (17/1.69)	28.3 (16/1.77)	27.7 (13/2.13)
J0536.2-6912	30 DorC	**100.8 (69/1.46)**	-	-	-	-
J0537.4-6628	DEM L256	83.0 (49/1.69)	74.3 (47/1.58)	**69.8 (47/1.49)**	-	-
J0537.8-6910	N157B	**469.2 (486/0.97)**	-	-	-	-
J0540.0-6944	N159	**91.6 (77/1.19)**	-	-	-	-
J0540.2-6920	B0540-693	**526.6 (512/1.03)**	-	-	-	-
J0543.1-6858	DEM L299	**184.3 (134/1.38)**	-	-	-	-
J0547.0-6943	DEM L316B	107.8 (66/1.63)	**60.4 (64/0.94)**	100.1 (64/1.56)	-	-
J0547.4-6941	DEM L316A	**89.1 (72/1.24)**	-	-	-	-
J0547.8-7025	B0548-704	304.4 (202/1.51)	**267.3 (200/1.34)**	273.1 (200/1.37)	-	-
J0550.5-6823	-	**29.3 (25/1.17)**	-	-	-	-

* The adopted models were represented with in bold type.

Table 4.4: The Best-Fit Parameters of the Thermal Component with "$1kT1nt$" and/or "$1kT1nt$ + Power law (1) (2)".*

Name	Other Name	$N_{\rm H}^{\rm G}$ (10^{20} cm^{-2})	$N_{\rm H}^{\rm L}$ (10^{21} cm^{-2})	$kT_{\rm e}$ (keV)	$\log(n_{\rm e}t)$	$EM^{\dagger}$ (cm^{-3})	Flux (erg cm^{-2} s^{-1})	$\chi^2/d.o.f.$
J0449.3-6920	-	7.65 (fixed)	$8.22^{+3.42}_{-6.31}$	$0.20^{+0.15}_{-0.05}$	$13.62^{+0.08}_{-5.62}$	$< 3.90 \times 10^{59}$	3.75×10^{-14}	10.2/20
J0450.2-6922	B0450-6927	7.91 (fixed)	<10.2	$0.32^{+0.56}_{-0.24}$	$8.00^{+2.72}_{-0.00}$	$0.21^{+8.17}_{-0.18} \times 10^{58}$	2.66×10^{-14}	17.8/24
J0450.4-7050	B0450-709	9.00 (fixed)	$1.76^{+1.81}_{-1.28}$	$0.42^{+0.14}_{-0.12}$	$10.69^{+0.26}_{-0.22}$	$0.94^{+1.73}_{-0.44} \times 10^{58}$	2.13×10^{-13}	43.7/53
J0453.2-6655	N4	4.69 (fixed)	<2.82	$0.43^{+0.08}_{-0.10}$	$10.64^{+0.38}_{-0.24}$	$< 4.56 \times 10^{58}$	3.32×10^{-13}	93.6/95
J0453.6-6829	B0453-685	6.40 (fixed)	$1.12^{+0.64}_{-0.62}$	$0.43^{+0.07}_{-0.06}$	$10.56^{+0.11}_{-0.10}$	$2.57^{+0.67}_{-0.96} \times 10^{59}$	5.00×10^{-12}	224.0/167
J0453.9-7000	B0454-7005	8.99 (fixed)	$4.22^{+1.81}_{-2.11}$	$0.18^{+0.07}_{-0.10}$	$11.53^{+2.17}_{-1.06}$	$1.23^{+0.56}_{-0.26} \times 10^{59}$	4.71×10^{-13}	67.9/50
J0454.8-6626	N11L	4.15 (fixed)	<1.97	$0.67^{+0.20}_{-0.24}$	$10.20^{+0.29}_{-0.17}$	$3.24^{+6.14}_{-0.51} \times 10^{57}$	2.67×10^{-13}	114.1/108
J0455.6-6839	N86	6.83 (fixed)	$15.2^{+3.46}_{-2.56}$	$0.11^{+0.04}_{-0.03}$	$10.08^{+0.52}_{-0.33}$	$< 2.30 \times 10^{63}$	4.52×10^{-13}	18.7/17
J0459.9-7008	N186D	8.82 (fixed)	$4.63^{+3.22}_{-1.41}$	$0.36^{+0.33}_{-0.19}$	$10.13^{+1.14}_{-0.21}$	$< 3.17 \times 10^{59}$	1.37×10^{-13}	12.5/10
J0506.1-6541	-	4.61 (fixed)	$4.02^{+0.11}_{-0.12}$	0.17 ± 0.02	$12.94^{+0.76}_{-1.43}$	$1.46^{+1.24}_{-0.69} \times 10^{59}$	2.11×10^{-13}	47.5/48
J0518.7-6939	N120	6.64 (fixed)	<2.16	$0.56^{+0.10}_{-0.15}$	$10.46^{+0.26}_{-0.16}$	$1.17^{+2.41}_{-0.34} \times 10^{58}$	3.39×10^{-13}	100.7/77
J0519.7-6926	B0520-694	6.44 (fixed)	$0.09^{+0.09}_{-0.08}$	$0.42^{+0.08}_{-0.07}$	$10.66^{+0.08}_{-0.18}$	$5.98^{+5.06}_{-2.59} \times 10^{58}$	8.88×10^{-13}	133.0/122
J0523.1-6753	N44	6.13 (fixed)	<4.37	$0.39^{+0.05}_{-0.03}$	$13.37^{+0.33}_{-2.00}$	$3.14^{+3.57}_{-1.39} \times 10^{58}$	3.26×10^{-13}	36.2/44
J0525.4-6559	N49B	5.53 (fixed)	$3.69^{+0.32}_{-0.36}$	0.50 ± 0.03	$10.51^{+0.05}_{-0.04}$	$1.24^{+0.23}_{-0.20} \times 10^{60}$	1.40×10^{-11}	213.7/165
J0527.6-6912	B0528-692	6.20 (fixed)	$11.4^{+3.83}_{-3.57}$	$0.17^{+0.04}_{-0.05}$	$9.32^{+0.66}_{-0.34}$	$0.43^{+3.15}_{-0.30} \times 10^{60}$	2.03×10^{-13}	36.3/38
J0531.9-7100	N206	7.13 (fixed)	<1.38	0.37 ± 0.05	$11.84^{+1.86}_{-0.31}$	$7.02^{+4.19}_{-2.60} \times 10^{58}$	7.93×10^{-13}	69.2/83
J0532.5-6732	B0532-675	5.96 (fixed)	$2.30^{+1.53}_{-1.05}$	$0.49^{+0.26}_{-0.15}$	$10.48^{+0.30}_{-0.21}$	$< 1.94 \times 10^{59}$	9.07×10^{-13}	81.9/76
J0535.8-6918	Honeycomb	6.39 (fixed)	<0.89	0.28 ± 0.02	$13.33^{+0.37}_{-1.18}$	$0.25^{+2.46}_{-0.05} \times 10^{59}$	2.26×10^{-13}	126.5/95
J0536.2-6912	30 Dor C	6.36 (fixed)	$13.5^{+2.3}_{-1.7}$	$0.95^{+1.08}_{-0.27}$	$11.19^{+1.38}_{-0.30}$	$0.88^{+1.16}_{-0.66} \times 10^{58}$	1.68×10^{-12}	100.8/69
J0537.8-6910	N157B	6.43 (fixed)	$7.61^{+0.61}_{-0.64}$	$0.69^{+0.30}_{-0.26}$	$10.25^{+0.38}_{-0.24}$	$4.04^{+2.43}_{-1.39} \times 10^{58}$	8.13×10^{-12}	469.2/486
J0540.0-6944	N159	6.88 (fixed)	$1.40^{+0.82}_{-0.41}$	0.64 ± 0.04	$12.99^{+0.71}_{-1.12}$	$3.33^{+0.50}_{-0.72} \times 10^{57}$	9.23×10^{-13}	91.6/77
J0540.2-6920	B0540-693	6.65 (fixed)	$8.36^{+0.47}_{-0.40}$	$0.33^{+0.03}_{-0.02}$	$11.00^{+0.20}_{-0.37}$	$3.72^{+2.54}_{-0.82} \times 10^{59}$	3.83×10^{-11}	586.4/516
J0543.1-6858	DEM L299	6.54 (fixed)	$8.30^{+0.63}_{-0.49}$	$0.18^{+0.01}_{-0.06}$	$11.41^{+0.25}_{-0.23}$	$1.07^{+0.42}_{-0.27} \times 10^{60}$	7.87×10^{-13}	184.3/134
J0547.4-6941	DEM L316A	7.02 (fixed)	$3.61^{+1.48}_{-1.09}$	0.78 ± 0.05	$11.69^{+0.54}_{-0.32}$	$2.68^{+0.97}_{-0.67} \times 10^{59}$	5.14×10^{-13}	89.1/72
J0550.5-6823	-	6.18 (fixed)	<5.80	$0.38^{+0.30}_{-0.16}$	$10.99^{+0.78}_{-0.32}$	$< 2.21 \times 10^{59}$	4.33×10^{-13}	19.3/25

* The errors in the parentheses represent the 90 % confidence intervals.

† Emission measure $EM = \int n_{\rm e} n_{\rm H} dV$, where $n_{\rm e}$ and V are the electron density and the plasma volume. The distance to SNRs in the LMC is assumed to be 50 kpc (Feast, 1999).

4.3.4 "$1kT1nt$" and "$1kT1nt$ + Power law (1) (2)"

In this section, we present SNRs reproduced with "$1kT1nt$" or "$1kT1nt$ + Power law (1) (2)". In our study, 25 SNRs were adopted with "$1kT1nt$" or "$1kT1nt$ + Power law (1) (2)". We could reproduce with the very simple model for many SNRs.

The Detailed Spectral Analysis with "$1kT1nt$"

Here, we present SNRs reproduced with "$1kT1nt$". Through the spectral analysis with "$1kT1nt$–$3kT3nt$" or "$1kT1nt$–$3kT3nt$ + Power law (1)(2)", we adopted "$1kT1nt$" for the following 22 SNRs for discussion in the later sections; J0449.3-6920, J0450.2-6922 (B0450-6927), J0450.4-7050 (B0450-709), J0453.2-6655 (N4), J0453.6-6829 (B0453-685), J0453.9-7000 (B0454-7005), J0454.8-6626 (N11L), J0455.6-6839 (N86), J0459.9-7008 (N186D), J0506.1-6541, J0518.7-6939 (N120), J0519.7-6926 (B0520-694), J0523.1-6753 (N44), J0525.4-6559 (N49B), J0527.6-6912 (B0528-692), J0531.9-7100 (N206), J0532.5-6732 (B0532-675), J0535.8-6918 (Honeycomb), J0547.4-6941 (DEM L316A), and J0550.5-6823.

Of these SNRs, we found that 8 SNRs (J0449.3-6920, J0450.2-6922: B0450-6927, J0450.4-7050: B0450-709, J0453.9-7000: B0454-7005, J0455.6-6839: N86, J0459.9-7008: N186D, J0506.1-6541, and J0527.6-6912: B0528-692) were not needed to constrain the metal abundance statistically in our study. On the other hand, we constrained only the Ne, Mg, and Fe metal abundances for J0523.1-6753 (N44) to couple the normalization with the Si metal abundance. Then, the Si metal abundance was fixed at the LMC average (Russell & Dopita, 1992). If the Si metal abundance was constrained, for example, the emission measure had the large uncertainty of $< 9.71 \times 10^{63}$ cm^{-3}. The derived metal abundances were listed in table 4.9. The derived best-fit parameters were listed in table 4.4. In figure 4.3 we present the best-fit spectra.

The Comparison with the Previous Results

In the previous observations, the several SNRs were reproduced with a single component APEC, MEKAL, or PSHOCK model attenuated by an interstellar absorption. If we adopted the same model for such SNRs, the derived results were compatible with the previous observations. Then, the same metal abundances were constrained with the our best-fit model. The comparison with the previous results are shown in figure 4.2. It is found that the temperature and ionization parameter for most SNRs are consistent with the previous results within ∼20 % and ∼10 % at the 90 % confidence level, respectively. The previous results are listed in appendix § F.

The temperature of J0518.7-6939 (N120) derived by us was to be $0.56^{+0.10}_{-0.15}$ keV. This was relatively different from the previous results (0.31 ± 0.06 keV; Reyes-Iturbide et al. 2008). We therefore fitted this remnant with their model (a single temperature component MEKAL model attenuated by an interstellar absorption fixed the metal abundances at the LMC average; Russell & Bessell 1989). Then, we obtained the temperature of $0.24^{+0.02}_{-0.01}$ keV, which was consistent with their results at the 90 % confidence level. However, since this model provided no longer an acceptable fit with the χ^2 ($d.o.f.$) of 197.3 (83), we adopted our best-fit model.

Of these SNRs, we performed the detailed spectroscopy in the following SNRs for the first time; J0450.2-6922 (B0450-6927), J0454.8-6626 (N11L), J0459.9-7008 (N186D),

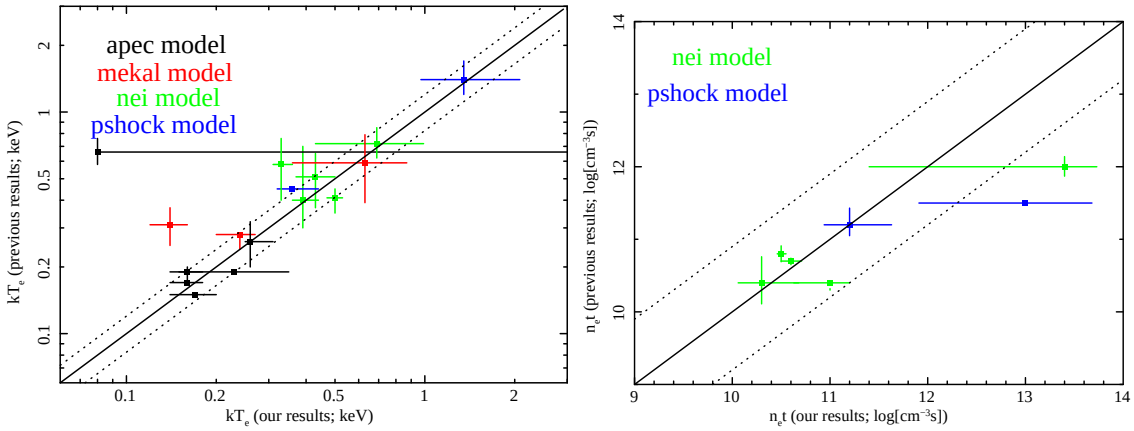

Figure 4.2: Comparison with the previous results; Left: Temperature (keV), Right: Ionization parameter (log(cm^{-3} s). The horizontal and vertical axises are represented with the our and previous results, respectively. The black, red, green, and blue data points are represented with APEC, MEKAL, NEI, and PSHOCK models in the XSPEC library, respectively. Plasmas in collisional ionization equilibrium ($\sim$ 12 log(cm^{-3} s)) have relatively large uncertainties. The several error bars were not presented in the previous results.

J0519.7-6926 (B0520-694), J0527.6-6912 (B0528-692), J0532.5-6732 (B0532-675), and J0550.5-6823. We derived an absorbed flux which was converted to an estimated *ROSAT* PSPC count rate using the PIMMS tool from HEASARC. The *ROSAT* PSPC count rates for J0454.8-6626 (N11L), J0519.7-6926 (B0520-694), J0527.6-6912 (B0528-692), and J0532.5-6732 (B0532-675) were estimated to be 2.74×10^{-2} counts s^{-1}, 1.13×10^{-1} counts s^{-2}, 4.37×10^{-2} counts s^{-1}, and 6.67×10^{-2} counts s^{-1}, respectively. We fitted these SNRs with a single component APEC model attenuated by an interstellar absorption again to calculate the absorbed flux from the *ROSAT* PSPC count rate with the PIMMS tool. These models provided acceptable fits with χ^2_ν of <1.3. Then, we calculated the absorbed flux with the best-fit parameters. The absorbed flux in the 0.5–10.0 keV for J0454.8-6626 (N11L), J0519.7-6926 (B0520-694), J0527.6-6912 (B0528-692), and J0532.5-6732 (B0532-675) were estimated to be 3.13×10^{-13} erg s^{-1} cm^{-2}, 1.25×10^{-12} erg s^{-1} cm^{-2}, 4.26×10^{-13} erg s^{-1} cm^{-2}, and 6.87×10^{-13} erg s^{-1} cm^{-2}, respectively, which were compatible with the our results within $\sim$50 %. The absorbed flux in the 0.5–10.0 keV for J0459.9- 7008 (N186D) and J0550.5-6823 were estimated to be 2.03×10^{-13} erg s^{-1} cm^{-2} and 3.98×10^{-13} erg s^{-1} cm^{-2} with the *Chandra* online catalogue, respectively. These results were compatible with our results within $\sim$30 %. J0450.2-6922 (B0450-6927) had no any references.

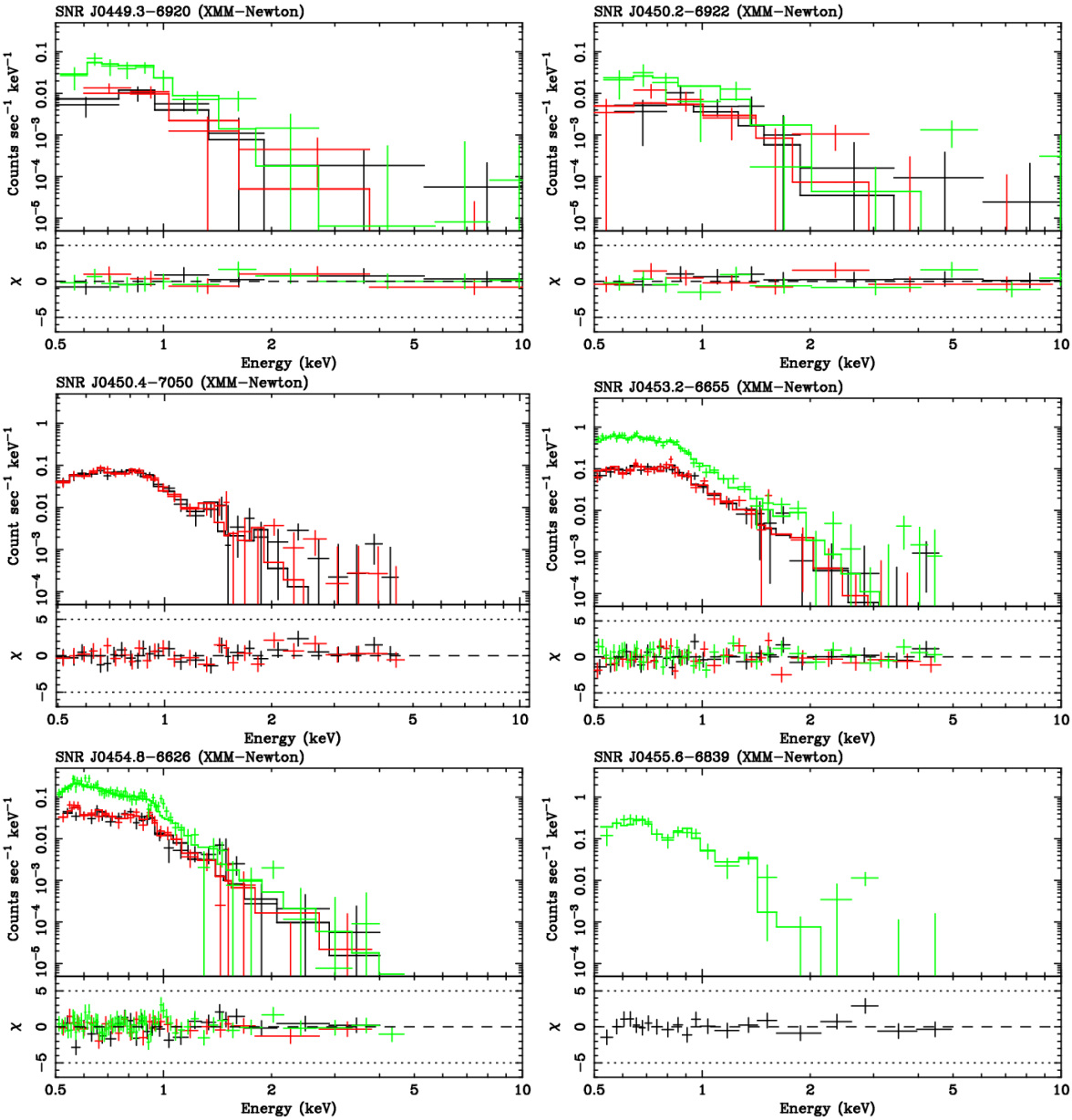

Figure 4.3: The data and the best-fit spectra. SNR names are on the top of each panel. The black, red and green crosses show the data points from the MOS1, MOS2 and pn in *XMM-Newton*, respectively. The black cross shows the data points from the ACIS in *Chandra*. The lower panel shows the residuals from the best-fit model.

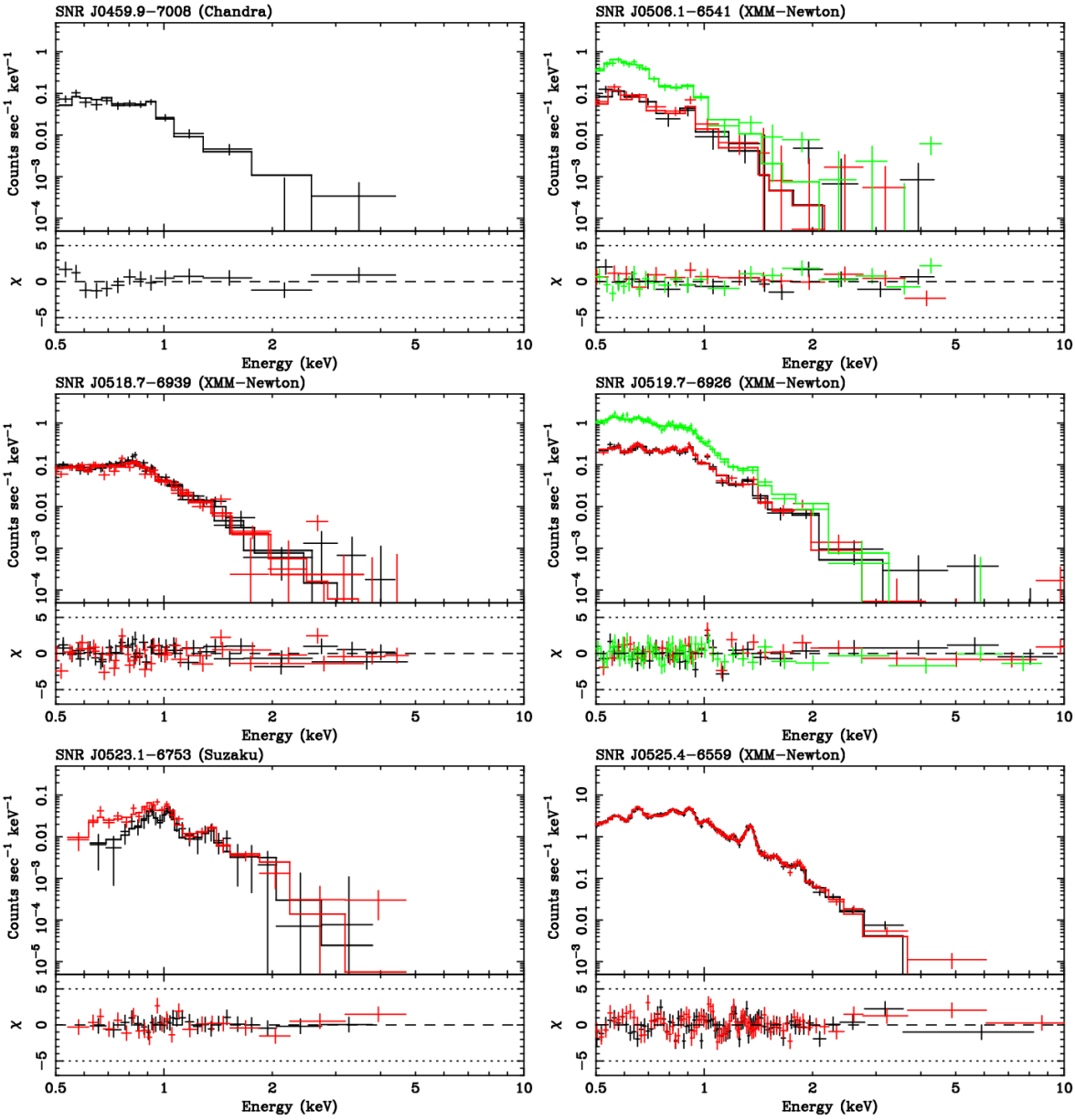

Figure 4.3: The data and the best-fit spectra. SNR names are on the top of each panel. The black and red crosses show the data points from the FI and BI CCDs in *Suzaku*, respectively. The black, red and green crosses show the data points from the MOS1, MOS2 and pn in *XMM-Newton*, respectively. The black cross shows the data points from the ACIS in *Chandra*. The lower panel shows the residuals from the best-fit model.

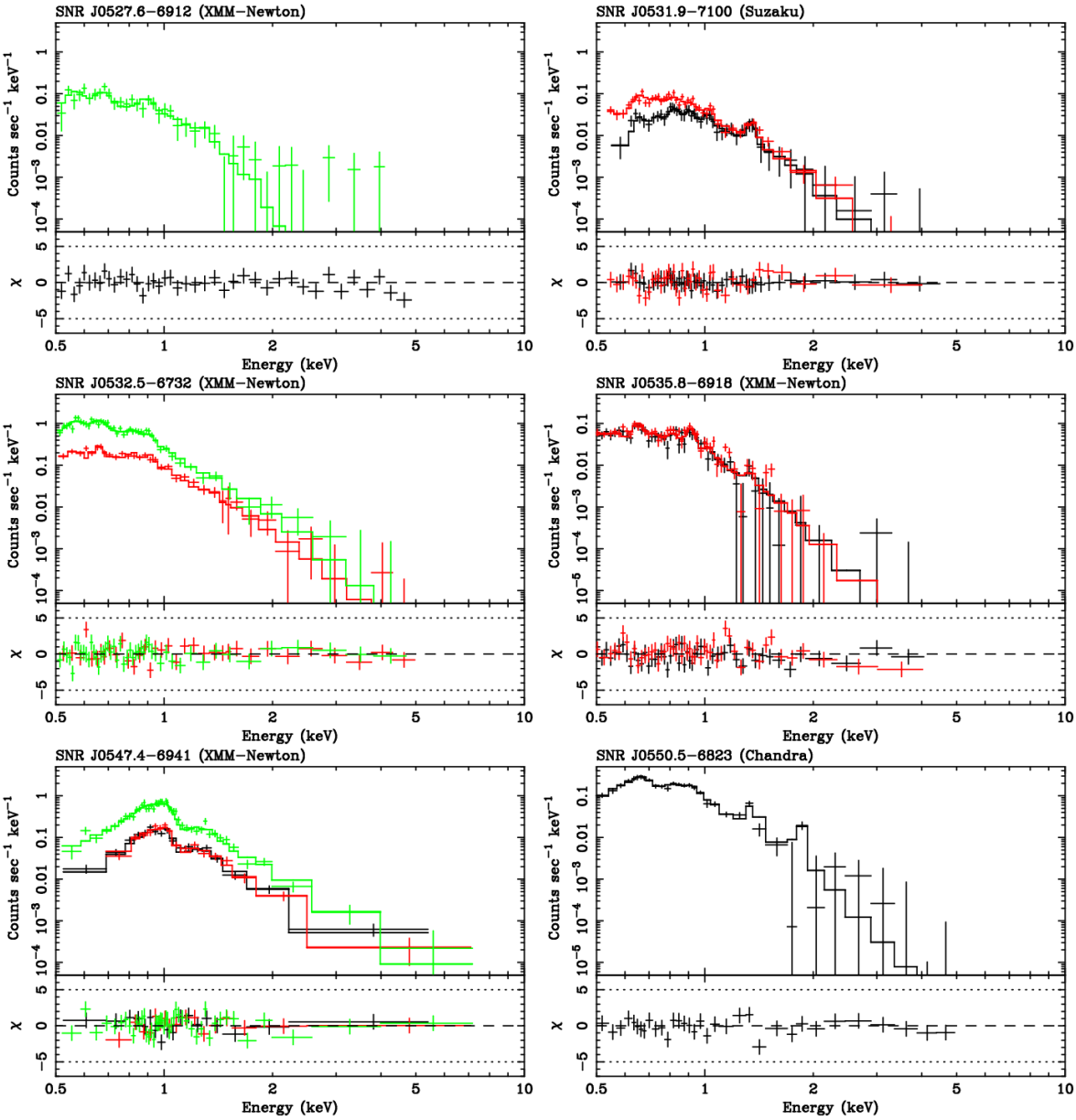

Figure 4.3: The data and the best-fit spectra. SNR names are on the top of each panel. The black and red crosses show the data points from the FI and BI CCDs in *Suzaku*, respectively. The black, red and green crosses show the data points from the MOS1, MOS2 and pn in *XMM-Newton*, respectively. The lower panel shows the residuals from the best-fit model.

The Detailed Spectral Analysis with "$1kT1nt$ + Power law (1)"

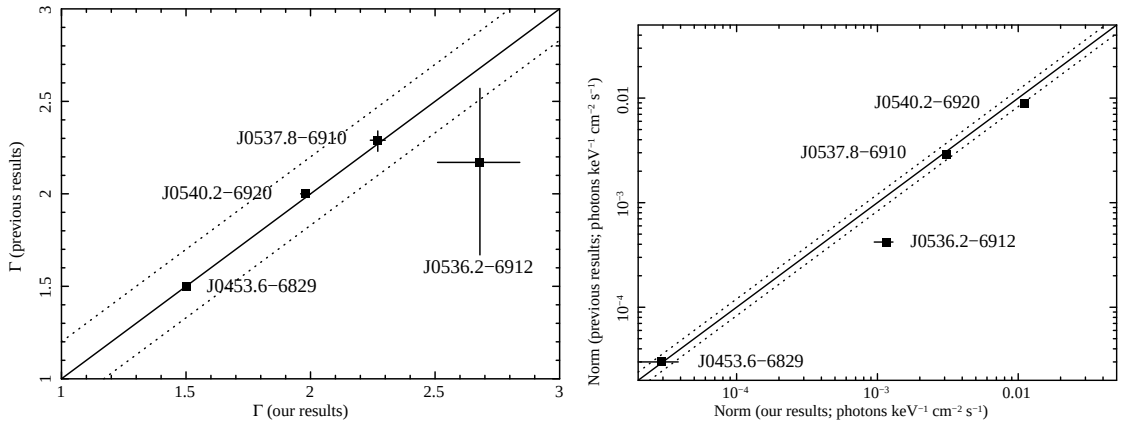

Figure 4.4: Comparison with the previous results for the non-thermal components; Left: photon-index, Right: normalization. The labels in these figures are represented with each SNR.

Here, we present SNRs reproduced with "$1kT1nt$ + Power law (1)". Through the spectral analysis with "$1kT1nt$–$3kT3nt$" or "$1kT1nt$–$3kT3nt$+ Power law (1)(2)", we adopted "$1kT1nt$ + Power law (1)" for the following 4 SNRs; J0453.6-6829 (B0453-685), J0536.2-6912 (30 Dor C), J0537.8-6910 (N157B) and J0540.2-6920 (B0540-693). These SNRs have been reported to have a strong non-thermal component based on electrons accelerated by a shock and/or a pulsar (its wind nebula). The previous results are summarized in appendix § F.

As for J0453.6-6829 (B0453-685), we fixed the photon index at 1.5 (Gaensler et al., 2003) because of the poor photon statistics. In table 4.5 we present the best-fit parameters for the non-thermal component. The comparison for the non-thermal component with the previous results are shown in figure 4.4. Note that we present a part in J0536.2-6912 (30 Dor C; Yamaguchi et al. 2009). It is found that the photon index and the normalization are consistent with the previous results within ∼20 % (except J0536.2-6912: 30 Dor C) at the 90 % confidence level. On the other hand, in the spectral analysis for the thermal component, we fixed the the metal abundances at the LMC average (Russell & Dopita, 1992), since the non-thermal emission from J0536.2-6912 (30 Dor C) and J0540.2-6920 (B0540-693) covered their thermal emission. Thus, the derived metal abundances for J0537.8-6910 (N157B) were listed in table 4.9. The derived best-fit parameters for the thermal component were listed in table 4.4. In figure 4.5 we present the best-fit spectra.

The Comparison with the Previous Results

In the previous observations, the several SNRs were reproduced with a single component APEC and PSHOCK model attenuated by an interstellar absorption. If we adopted the same model for such SNRs, the derived results were compatible with the previous observations. Then, the same metal abundances were constrained with the our best-fit model. The comparison with the previous results are shown in figure 4.2. It is found that the temperature and ionization parameter for all SNRs are consistent with the previous results within ∼20 % and ∼10 % at the 90 % confidence level, respectively. The previous

Table 4.5: The Best-Fit Parameters of the Non-Thermal Component with "$1kT1nt$ + Power law (1)".*

Name	Other name	Γ	Norm†
J0453.6-6829	B0453-685	1.50 (fixed)	$2.95^{+0.90}_{-0.89} \times 10^{-5}$
J0536.2-6912	30 Dor C	$2.68^{+0.16}_{-0.17}$	$1.16^{+0.13}_{-0.21} \times 10^{-3}$
J0537.8-6910	N157B	2.27±0.03	$3.12^{+0.17}_{-0.13} \times 10^{-3}$
J0540.2-6920	B0540-693	1.98±0.02	$(1.11\pm0.03) \times 10^{-2}$

* The errors in the parentheses represent 90 % confidence level.
† The normalization at 1 keV in unit of photons $\mathrm{keV^{-1}\,cm^{-2}\,s^{-1}}$.

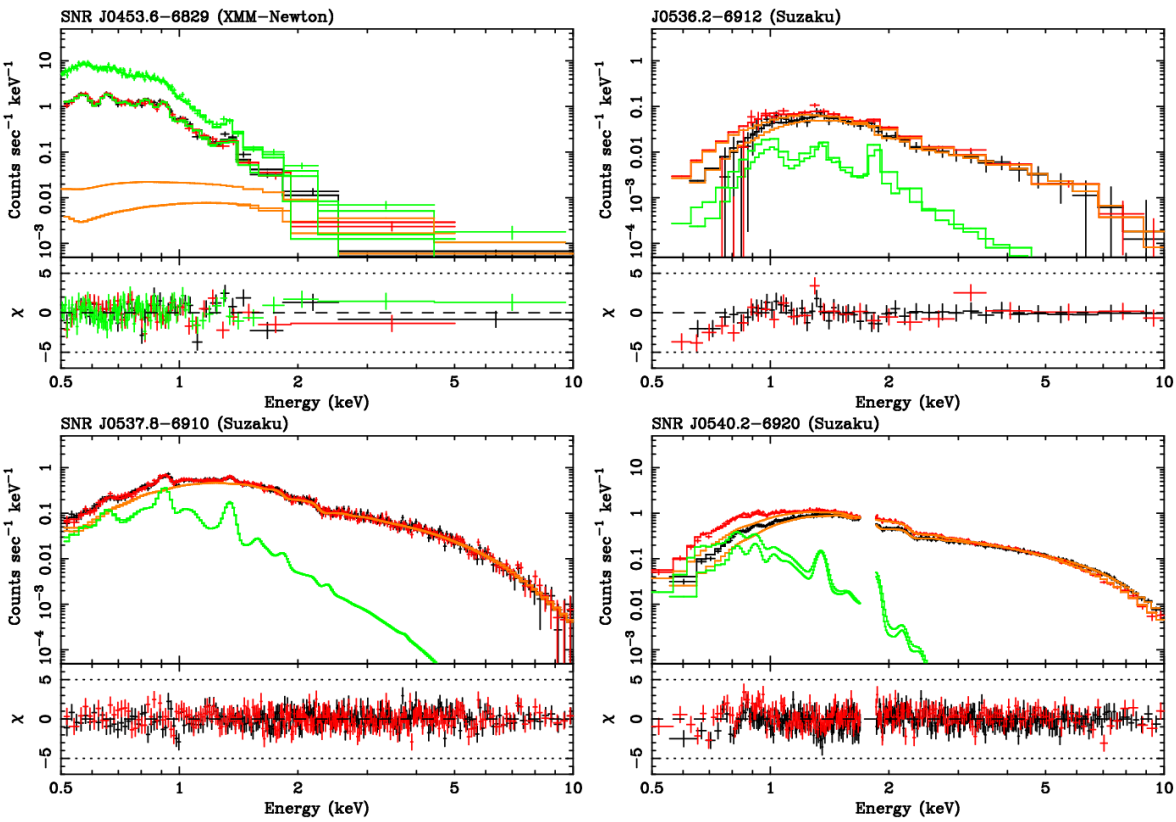

Figure 4.5: The data and the best-fit spectra. SNR names are on the top of each panel. The black and red crosses show the data points from the FI and BI CCDs in *Suzaku*, respectively. The black, red and green crosses show the data points from the MOS1, MOS2 and pn in *XMM-Newton*, respectively. The lower panel shows the residuals from the best-fit model. The orange and green solid histogram are represented with the non-thermal and thermal component, respectively.

results are listed in appendix § F. Note that we presented a part in J0536.2-6912 (30 Dor C) and J0540.2-6920 (B0540-693).

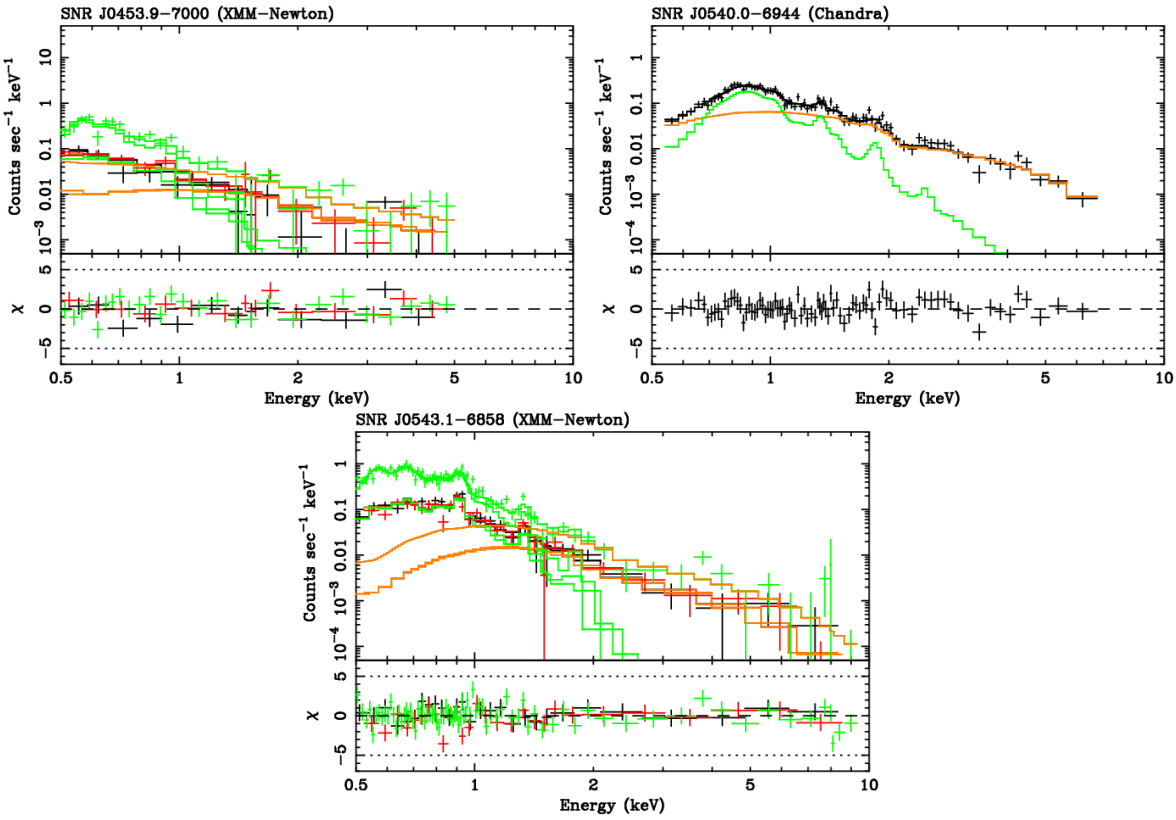

Figure 4.6: The data and the best-fit spectra. SNR names are on the top of each panel. The black, red and green crosses show the data points from the MOS1, MOS2 and pn in *XMM-Newton*, respectively. The black cross shows the data points from the ACIS in *Chandra*. The lower panel shows the residuals from the best-fit model. The green solid histogram are represented with the thermal component, respectively. The orange solid histogram are represented with the high energy component.

The Detailed Spectral Analysis with "$1kT1nt$ + Power law (2)"

Here, we present SNRs reproduced with "$1kT1nt$ + Power law (2)". Through the spectral analysis with "$1kT1nt$–$3kT3nt$" or "$1kT1nt$–$3kT3nt$ + Power law (1)(2)" for the following 3 SNRs for discussion in the later sections; J0453.9-7000 (B0454-7005), J0540.0-6944 (N159) and J0543.1-6858 (DEM L299).

Table 4.6: The Best-Fit Parameters of the Thermal Component with "$1kT1nt$".*

Name	Other Name	$kT_{\rm e}$ (keV)	$\log(n_{\rm e}t)$ (cm^{-3} s)	$\chi^2/d.o.f.$
J0453.9-7000	B0454-7005	$3.67^{+5.48}_{-2.59}$	$9.68^{+0.13}_{-0.09}$	79.7/52
J0543.1-6858	DEM L299	$1.35^{+0.68}_{-0.33}$	$9.86^{+0.05}_{-0.04}$	261.6/136

* The errors in the parentheses represent the 90 % confidence intervals.

J0453.9-7000 (B0454-7005) and J0543.1-6858 (DEM L299) have a high temperature

Table 4.7: The Best-Fit Parameters of the Non-Thermal Component with "$1kT1nt$+ Power law (2)".*

Name	Other Name	Γ	Norm†
J0453.9-7000	B0454-7005	$1.45^{+1.05}_{-0.67}$	$3.63^{+0.20}_{-0.17} \times 10^{-5}$
J0543.1-6858	DEM L299	$2.33^{+0.84}_{-0.47}$	$1.19^{+0.90}_{-0.52} \times 10^{-4}$

* The errors in the parentheses represent the 90 % confidence intervals.
† The normalization at 1 keV in unit of photons $\mathrm{keV^{-1}\,cm^{-2}\,s^{-1}}$.

plasma of > 1 keV with "$1kT1nt$", though these SNRs have the large diameters (>60 pc). The best-fit parameters with "$1kT1nt$" were listed in table 4.6. We therefore doubted that these SNRs have a high energy component, for example, a non-thermal emission based on electrons accelerated by a shock, pulsar, and its wind nebula or a contamination from point-like sources.

Of these SNRs, J0540.0-6944 (N159) was included the X-ray emission from the bright X-ray source LMC X-1, we therefore a single component POWER LAW model with "$1kT1nt$". After this study, our result was compatible with the previous observation (Seward et al. 2010). The comparison with the previous result is shown in figure 4.2.

It was found that there were many stars in the source region for J0453.9-7000 (B0454-7005) with the SIMBAD database. Moreover, the X-ray image for this remnant in figure B.1 shows point-like sources. Since it was difficult to exclude only the point-like source from this image, we therefore decided to adopt "$1kT1nt$ + Power law (2)" for this remnant. On the other hand, we could not find the prominent point sources in the source region for J0543.1-6858 (DEM L299) with the SIMBAD database. The hard X-ray image for this remnant in figure B.1 seems to have the faint extended emission (sky blue region). Though we analyzed this faint extended emission (source A), the hard component could not be explained in appendix § C.1. This hard component may be due to cumulated point-like sources as shown. We therefore also decided to adopt "$1kT1nt$ + Power law (2)" for this remnant.

We found that J0453.9-7000 (B0454-7005) and J0543.1-6858 (DEM L299) were not needed to constrain the metal abundances statistically in our study. All SNRs were provided acceptable fits with the χ^2_ν of <1.38. The derived metal abundances for J0540.0-6944 (N159) were listed in table 4.9. The derived best-fit parameters for the thermal and non-thermal components were listed in table 4.4 and 4.7, respectively. In figure 4.6 we present the best-fit spectra.

The Comparison with the Previous Results

Of these SNRs, we performed the detailed spectroscopy for the first time in the following SNRs; J0453.9-7000 (B0454-7005) and J0543.1-6858 (DEM L299). We derived an absorbed flux which was converted to an estimated *ROSAT* PSPC count rate using the PIMMS tool from HEASARC. The *ROSAT* PSPC count rate for J0543.1-6858 (DEM L299) was estimated to be 2.44×10^{-1} counts $\mathrm{s^{-1}}$. We fitted these SNR with a single component APEC model again to calculate the absorbed flux from the *ROSAT* PSPC count rate with the PIMMS tool. These models provided acceptable fits with the χ^2_ν of ∼1. Then, we

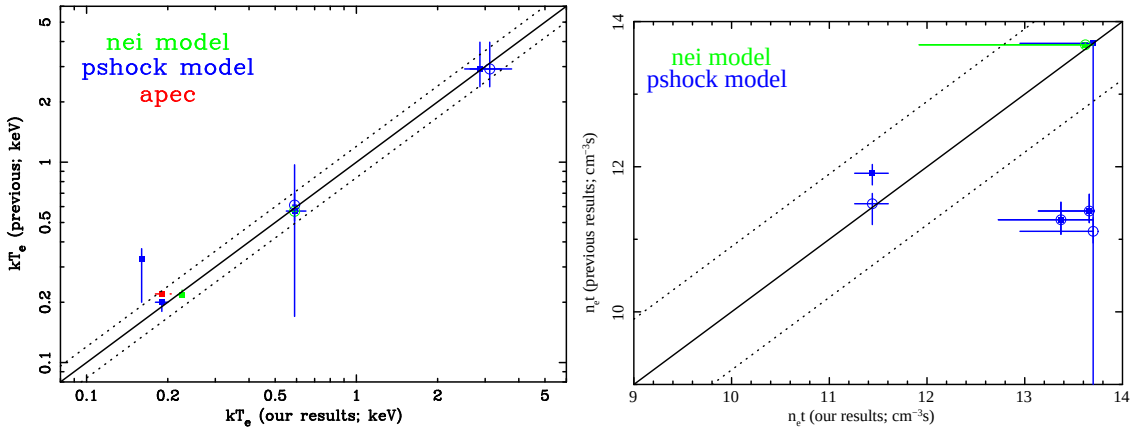

Figure 4.7: Comparison with the previous results of temperatures and ionization parameters. The horizontal and vertical axises are represented with the our and previous results, respectively. The green and blue data points are represented with NEI and PSHOCK models in the XSPEC library, respectively. The filled boxes and open circles are represented with the first and second VNEI components, respectively. Plasmas in collisional ionization equilibrium (~ 12 log(cm^{-3} s)) have relatively large uncertainties.

calculated the absorbed flux with the best-fit parameters. The absorbed flux in the 0.5–10.0 keV for J0543.1-6858 (DEM L299) was estimated to be 2.98×10^{-12} erg s^{-1}, which was larger than the absorbed flux observed by us. This may be due to a bright source close to this remnant. Unfortunately, J0453.9-7000 (B0454-7005) had no any references.

4.3.5 "$2kT1nt$–$2kT2nt$"

In this section, we present SNRs reproduced with "$2kT1nt$–$2kT2nt$". In our study, 6 SNRs were adopted with "$2kT1nt$–$2kT2nt$".

The Detailed Spectral Analysis with "$2kT1nt$–$2kT2nt$"

Here, we present SNRs reproduced with "$2kT1nt$–$2kT2nt$". Through the spectral analysis with "$1kT1nt$–$3kT3nt$" or "$1kT1nt$–$3kT3nt$ + Power law (1)(2)", we adopted "$2kT1nt$–$2kT2nt$" for the following 6 SNRs; J0505.9-6802 (N23), J0534.0-6955 (B0534-699), J0535.5-6916 (SN 1987A), J0547.0-6943 (DEM L316B), J0537.4-6628 (DEM L256), and J0547.8-7025 (B0548-704).

Of these SNRs, we contained the energy gain for J0505.9-6802 (N23) and J0534.0-6955 (B0534-699). In the early phase of the *Suzaku* mission, the energy gain has a large uncertainty (Koyama et al., 2007). The gain uncertainty is $\sim$ 10 eV, according to the previous studies on SNRs (Yamaguchi et al. 2008; Bamba et al. 2008; Someya et al. 2010). J0505.9-6802 (N23) is one of the early phase observations. If the energy offset is to be floated, that is converged to $-8.0^{+0.3}_{-1.0}$ eV and $-0.9^{+1.0}_{-0.9}$ eV, for the FI and BI spectra, respectively. Although these gain offset values are within the gain uncertainty, this study significant improvement the fit, while the difference in the temperature and the ionization parameter within $\sim$1 % at the 90 % confidence level. Moreover, we allowed the energy offset to be floated for J0534.0-6955 (B0534-699). As a result the energy offset

Table 4.8: The Best-Fit Parameters of the Thermal Component with " $2kT1nt$–$2kT2nt$ " and/or " $2kT1nt$–$2kT2nt$ + Power law (1) (2) " .*

	J0505.9-6802 (N23)	J0534.0-6955 (B0534-699)
$N_{\rm H}^{\rm G}$ ($\times 10^{20}$ cm^{-2})	5.80 (fixed)	6.49 (fixed)
$N_{\rm H}^{\rm L}$ ($\times 10^{21}$ cm^{-2})	$0.74^{+0.12}_{-0.13}$	4.22±0.01
$kT_{\rm e1}$ (keV)	$0.226^{+0.004}_{-0.008}$	$0.164^{+0.003}_{-0.002}$
$kT_{\rm e2}$ (keV)	0.59±0.01	0.58±0.01
$\log(n_{\rm e}t_1$ [cm^{-2} s])	$13.62^{+0.08}_{-1.39}$	$13.00^{+0.70}_{-0.78}$
$\log(n_{\rm e}t_2$ [cm^{-2} s])	-	-
$n_{\rm e}n_{\rm H}V_1$	$5.44^{+0.30}_{-0.27} \times 10^{59}$	$1.77^{+0.03}_{-0.01} \times 10^{60}$
$n_{\rm e}n_{\rm H}V_2$	$2.29^{+0.93}_{-0.11} \times 10^{59}$	$4.44^{+0.51}_{-0.26} \times 10^{58}$
Flux†	9.34×10^{-12}	2.45×10^{-12}
$\chi^2/d.o.f.$	109.7 (105)	280.8 (188)
	J0535.5-6916 (SN 1987A)	J0547.0-6943 (DEM L316B)
$N_{\rm H}^{\rm G}$ ($\times 10^{20}$ cm^{-2})	6.37 (fixed)	7.04 (fixed)
$N_{\rm H}^{\rm L}$ ($\times 10^{21}$ cm^{-2})	$1.47^{+2.77}_{-0.98}$	<1.41
$kT_{\rm e1}$ (keV)	$0.51^{+0.07}_{-0.04}$	0.62±0.05
$kT_{\rm e2}$ (keV)	$3.11^{+0.34}_{-0.41}$	$2.79^{+1.33}_{-0.66}$
$\log(n_{\rm e}t_1$ [cm^{-2} s])	$11.11^{+0.11}_{-0.30}$	$13.32^{+0.38}_{-1.32}$
$\log(n_{\rm e}t_2$ [cm^{-2} s])	-	-
$n_{\rm e}n_{\rm H}V_1$	$2.06^{+0.81}_{-0.61} \times 10^{59}$	$1.20^{+4.29}_{-0.55} \times 10^{58}$
$n_{\rm e}n_{\rm H}V_2$	$(3.85\pm0.51) \times 10^{58}$	$8.36^{+1.94}_{-1.87} \times 10^{57}$
Flux†	3.47×10^{-12}	8.16×10^{-13}
$\chi^2/d.o.f.$	218.9/223	60.4/60
	J0537.4-6628 (DEM L256)	J0547.8-7025 (B0548-704)
$N_{\rm H}^{\rm G}$ ($\times 10^{20}$ cm^{-2})	5.78 (fixed)	7.28 (fixed)
$N_{\rm H}^{\rm L}$ ($\times 10^{21}$ cm^{-2})	<0.99	$5.44^{+0.86}_{-0.99}$
$kT_{\rm e1}$ (keV)	$0.56^{+0.10}_{-0.07}$	0.19±0.01
$kT_{\rm e2}$ (keV)	-	$0.60^{+0.01}_{-0.02}$
$\log(n_{\rm e}t_1$ [cm^{-2} s])	$10.99^{+0.22}_{-0.29}$	$12.90^{+0.80}_{-1.02}$
$\log(n_{\rm e}t_2$ [cm^{-2} s])	$8.55^{+0.20}_{-0.55}$	-
$n_{\rm e}n_{\rm H}V_1$	$1.78^{+0.88}_{-0.45} \times 10^{57}$	$2.95^{+2.46}_{-1.45} \times 10^{59}$
$n_{\rm e}n_{\rm H}V_2$	$6.24^{+6.50}_{-3.33} \times 10^{57}$	$3.30^{+1.16}_{-1.00} \times 10^{58}$
Flux†	1.18×10^{-13}	1.28×10^{-12}
$\chi^2/d.o.f.$	69.8/47	267.3/200

* The errors in the parentheses represent the 90 % confidence intervals.
† Emission measure $EM = \int n_{\rm e}n_{\rm H}dV$, where $n_{\rm e}$ and V are the electron density and the plasma volume. The distance to SNRs in the LMC is assumed to be 50 kpc (Feast, 1999).

is converged to $-0.5^{+0.3}_{-0.1}$ eV and $-1.0^{+0.9}_{-0.5}$ eV, for the FI and BI spectra, respectively. The energy gain is within the calibration uncertainty (Koyama et al., 2007). The energy offset adjustment significantly improves the fit, while the difference in the temperature and ionization parameter were within ∼2 %. The derived metal abundances were listed

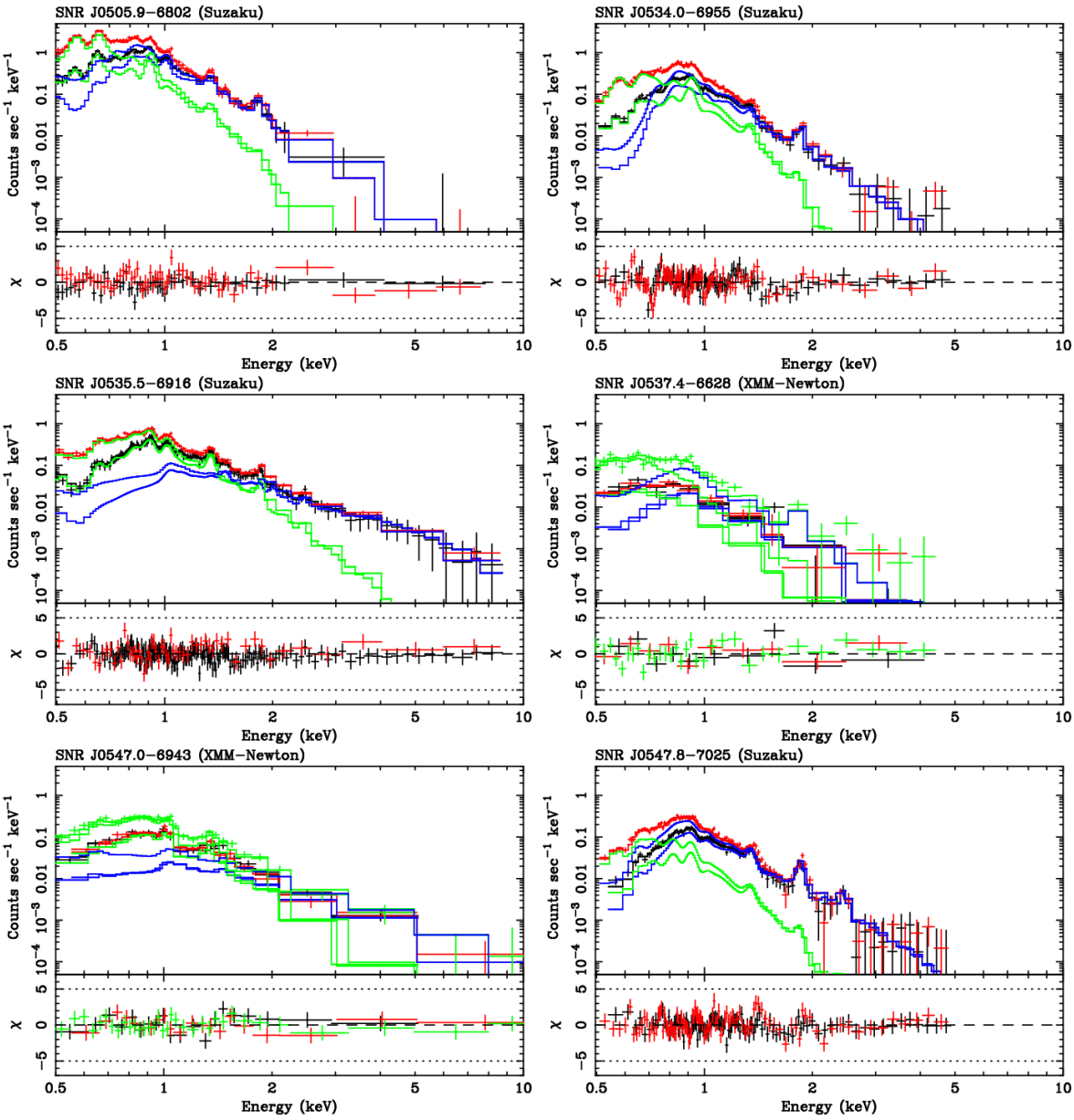

Figure 4.8: The data and the best-fit spectra. SNR names are on the top of each panel. The black and red crosses show the data points from the FI and BI CCDs in *Suzaku*, respectively. The black, red, and green crosses show the data points from the MOS1, MOS2 and pn in *XMM-Newton*, respectively. The black cross shows the data points from the ACIS in *Chandra*. In two components VNEI model, the green and blue solid histograms show the cool and hot component, respectively. The lower panel shows the residuals from the best-fit model.

in table 4.9.The best-fit parameters were listed in table 4.8. In figure 4.8 we present the best-fit spectra.

The Comparison with the Previous Results

In the previous observations, the several SNRs were reproduced with one or two component PSHOCK or APEC models attenuated by an interstellar absorption. If we adopted the same model for such SNRs, the derived results were compatible with the previous observations. Then, the same metal abundances were constrained with the our best-fit model. The comparison with the previous results are shown in figure 4.7. It is found that the temperature and ionization parameter for most SNRs are consistent with the previous results within ∼20 % and ∼10 % at the 90 % confidence level, respectively. The previous results are listed in appendix § F. In particular, of these SNRs, J0505.9-6802 (N23), J0535.5-6916 (SN 1987A), and J0547.0-6943 (DEM L316B) were compatible with the previous observations. The detailed analysis was summarized in appendix § E. However, several SNRs were significant difference from the previous results.

The low temperature components (0.15–0.37 keV; J0534.0-6955: B0534-699 and 0.25–1.75 keV; J0547.8-7025: B0548-704) were reported to have the ionization parameters of (0.74–4.25)$\times 10^{11}$ cm^{-3} s for J0547.8-7025 (B0548-704) and (1.54–5.26)$\times 10^{11}$ cm^{-3} s for J0534.0-6955 (B0534-699), respectively with *Chandra* (Hendrick et al., 2003). However, J0534.0-6955 (B0534-699) and J0547.8-7025 (B0548-704) were resolved clearly H- and He-like Oxygen Kα emission lines with *Suzaku*. As a result, this altered the estimation of the ionization parameter from $\sim 10^{11}$ cm^{-3} s to $\geq 10^{12}$ cm^{-3} s for each SNR, though the temperatures for each SNR were compatible with their results. For the similar discussions, see Someya et al. (2010) (or see appendix § E).

J0537.4-6628 (DEM L256) has the significant difference from the previous results (Klimek et al., 2010). They reproduced with a single component APEC model attenuated by an interstellar absorption. If we adopted the same model, the derived result was consistent with their result. Then, the temperature was estimated to be $0.19^{+0.02}_{-0.01}$ keV. However, since this model provided no longer an acceptable with with the χ^2 $(d.o.f.)$ of 112.6 (50), we adopted our best-fit model. This discrepancy may be due to our good photon statistics.

Although J0547.0-6943 (DEM L316B) was also compatible with the previous observations, this remnant was reproduced well with the high temperature plasma of $2.69^{+1.33}_{-0.66}$ keV, which was consistent with the previous result (5^{+5}_{-2} keV; Williams & Chu 2005). They also attempted to fit this high energy component with a single component POWER LAW model. The photon index and normalization were estimated to be $1.7^{+0.4}_{-0.2}$ and $5.3^{+0.6}_{-0.3} \times 10^{-5}$ photons keV^{-1} cm^{-2} s^{-1}. We therefore analyzed with their same model (i.e. "Model 1 + Power law (2)" in our analysis framework), and obtained the photonindex of $2.30^{+0.54}_{-0.46}$ and the normalization of $1.22^{+0.77}_{-0.27} \times 10^{-4}$ photons keV^{-1} cm^{-2} s^{-1}, which was roughly compatible with their result within a factor of two. After this study, the low temperature component was consisted between "$2kT1nt$" and "$2kT1nt$ + Power law (2)" within the statistical error at the 90 % confidence level. It was difficult to confirm this hard X-ray emission, though this emission had little important for discussion in the later sections.

Table 4.9: The derived metal abundance for SNRs in the LMC*.

		H	He	C	N	O	Ne	Mg	Si	S	Ar	Ca	Fe	Ni
J0449.3-6920	-	L	L	L	L	L	L	L	L	L	L	L	L	L
J0450.2-6922	B0450-6927	L	L	L	L	L	L	L	L	L	L	L	L	L
J0450.4-7050	B0450-709	L	L	L	L	L	L	L	L	L	L	L	L	L
J0453.2-6655	N4	L	L	L	L	0.11±0.03	$0.09^{+0.07}_{-0.04}$	$0.15^{+0.17}_{-0.14}$	<1.61	L	L	L	$0.18^{+0.07}_{-0.05}$	L
J0453.6-6829	B0453-685	L	L	L	L	$0.14^{+0.02}_{-0.05}$	$0.20^{+0.05}_{-0.04}$	$0.27^{+0.07}_{-0.06}$	$0.41^{+0.29}_{-0.13}$	L	L	L	0.17±0.03	L
J0453.9-7000	B0454-7005	L	L	L	L	L	L	L	L	L	L	L	L	L
J0454.8-6626	N11L	L	L	L	L	L	$0.47^{+0.11}_{-0.12}$	$0.28^{+0.27}_{-0.23}$	<0.81	L	L	L	0.35±0.07	L
J0455.6-6839	N86	L	L	L	L	L	L	L	L	L	L	L	L	L
J0459.9-7008	N186D	L	L	L	L	L	L	L	L	L	L	L	L	L
J0505.9-6802	N23	L	L	L	L	$0.35^{+0.02}_{-0.01}$	$0.51^{+0.04}_{-0.05}$	$0.42^{+0.05}_{-0.06}$	$0.42^{+0.12}_{-0.10}$	L	L	L	$0.24^{+0.01}_{-0.02}$	L
J0506.1-6541	-	L	L	L	L	L	L	L	L	L	L	L	L	L
J0518.7-6939	N120	L	L	L	L	$0.09^{+0.03}_{-0.02}$	$0.14^{+0.06}_{-0.05}$	$0.22^{+0.08}_{-0.14}$	<0.30	L	L	L	$0.22^{+0.06}_{-0.04}$	L
J0519.7-6926	B0520-694	L	L	L	L	$0.10^{+0.02}_{-0.01}$	$0.18^{+0.05}_{-0.03}$	$0.22^{+0.04}_{-0.07}$	$0.73^{+0.38}_{-0.33}$	L	L	L	$0.13^{+0.03}_{-0.02}$	L
J0523.1-6753	N44	L	L	L	L	L	$0.76^{+0.58}_{-0.33}$	$0.53^{+0.44}_{-0.28}$	L	L	L	L	$0.08^{+0.06}_{-0.04}$	L
J0525.4-6559	N49B	L	L	L	L	0.13±0.01	0.16±0.02	0.36±0.03	0.28±0.06	L	L	L	0.11±0.01	L
J0527.6-6912	B0528-692	L	L	L	L	L	L	L	L	L	L	L	L	L
J0531.9-7100	N206	L	L	L	L	L	$0.16^{+0.08}_{-0.07}$	$0.47^{+0.21}_{-0.16}$	<0.65	L	L	L	$0.12^{+0.02}_{-0.04}$	L
J0532.5-6732	B0532-675	L	L	L	L	$0.14^{+0.04}_{-0.03}$	$0.13^{+0.07}_{-0.03}$	<0.20	<0.70	L	L	L	$0.11^{+0.05}_{-0.03}$	L
J0534.0-6955	B0534-699	L	L	L	L	0.16±0.02	$0.28^{+0.03}_{-0.05}$	0.38±0.04	$0.46^{+0.08}_{-0.08}$	L	L	L	$0.82^{+0.04}_{-0.09}$	L
J0534.3-7033	DEM L238	L	L	L	L	L	L	L	L	L	L	L	L	L
J0535.5-6916	SNR 1987A	L	L	L	L	0.05±0.01	$0.17^{+0.05}_{-0.06}$	$0.24^{+0.06}_{-0.04}$	0.30±0.05	L	L	L	$0.08^{+0.02}_{-0.01}$	L
J0535.8-6918	Honeycomb	L	L	L	L	L	0.44±0.07	<0.55	<1.85	L	L	L	$0.16^{+0.05}_{-0.03}$	L
J0536.2-6912	30 DorC	L	L	L	L	L	L	L	L	L	L	L	L	L
J0537.4-6628	DEM L256	L	L	L	L	L	L	L	L	L	L	L	L	L
J0537.8-6910	N157B	L	L	L	L	L	$0.68^{+0.27}_{-0.16}$	$1.06^{+0.48}_{-0.29}$	$0.27^{+0.74}_{-0.27}$	L	L	L	0.11±0.04	L
J0540.0-6944	N159	L	L	L	L	L	$4.05^{+1.75}_{-1.86}$	$3.33^{+1.18}_{-1.86}$	$2.19^{+1.81}_{-1.72}$	L	L	L	$1.24^{+0.20}_{-0.17}$	L
J0540.2-6920	B0540-693	L	L	L	L	L	L	L	L	L	L	L	L	L
J0543.1-6858	DEM L299	L	L	L	L	L	L	L	L	L	L	L	L	L
J0547.0-6943	DEM L316B	L	L	L	L	$1.12^{+0.53}_{-0.71}$	$2.54^{+2.09}_{-1.67}$	$2.10^{+1.80}_{-1.41}$	$0.76^{+0.70}_{-0.56}$	L	L	L	$0.33^{+0.35}_{-0.22}$	L
J0547.4-6941	DEM L316A	L	L	L	L	L	$1.23^{+1.32}_{-0.70}$	$0.33^{+0.39}_{-0.16}$	<0.14	L	L	L	$0.34^{+0.11}_{-0.09}$	L
J0547.8-7025	B0548-704	L	L	L	L	$0.39^{+0.32}_{-0.17}$	$0.62^{+0.18}_{-0.22}$	$0.61^{+0.08}_{-0.10}$	$1.04^{+0.15}_{-0.20}$	$2.27^{+0.80}_{-0.74}$	L	L	$0.80^{+0.41}_{-0.22}$	L
J0550.5-6823	-	L	L	L	L	$0.19^{+0.15}_{-0.07}$	$0.26^{+0.82}_{-0.10}$	$0.82^{+0.60}_{-0.31}$	$2.28^{+1.65}_{-1.13}$	L	L	L	$0.14^{+0.10}_{-0.05}$	L

* The errors in the parentheses represent the 90 % confidence intervals. The ratios are all relative to solar (Anders & Grevesse, 1989). The abundances fixed at the LMC average (Russell & Dopita, 1992) are represented with "L".

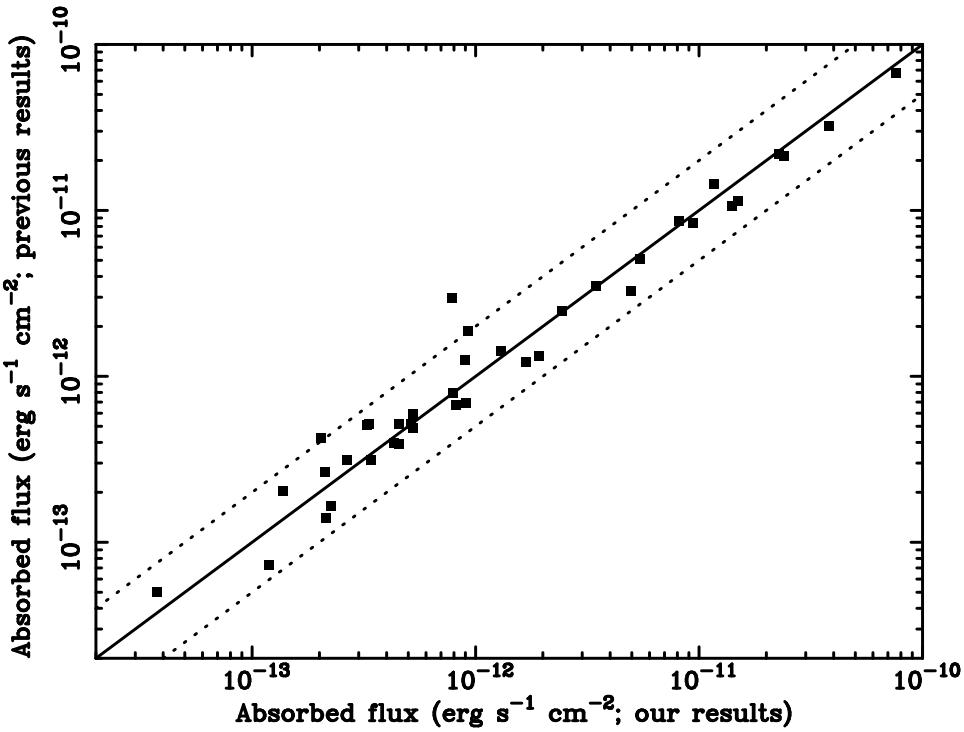

Figure 4.9: The observed flux (previous results; vertical axis)-flux (our results; horizontal axis) relation.

4.3.6 Systematic Error of Observed Fluxes

We confirm whether the derived absorbed fluxes are correct or not. In figure 4.9 we present the derived absorbed flux (previous results; vertical axis)-flux (our results; horizontal axis) relation.

We referred the absorbed fluxes in the following previous results. *ASCA* was observed the seven middle-aged SNRs (Hughes et al., 1998). They estimated the absorbed fluxes in the 0.5–5.0 keV band. Since the majority of the X-ray emission from many SNRs is concerned below 2keV, this energy band is little important compared with our estimation. Several SNRs were observed only *ROSAT* (Haberl & Pietsch, 1999). We can derive absorbed fluxes which can be converted to estimated *ROSAT* PSPC count rates using the PIMMS tool from HEASARC (e.g. Klimek et al. 2010). We therefore calculated the absorbed fluxes in the 0.5–10.0 keV from the *ROSAT* PSPC count rates with the best-fit parameters reproduced with a single component APEC model attenuated by a interstellar absorption (all best-fit spectra were reproduced well with the χ^2_ν of $\sim$1). On the other hand, we utilized *Chandra* online catalogue for several SNRs, and estimated the absorbed fluxes in the 0.5–10.0 keV with the best-fit model in this catalogue. Several SNRs have no any references above, we therefore utilized the absorbed fluxes in the 0.5–10.0 keV in the following references; J0449.3-6920 (Klimek et al., 2010), J0450.4-7050 (B0450-709; Williams et al. 2004), J0454.6-6713 (N9; Seward et al. 2006), J0506.1-6541 (Klimek et al., 2010), J0518.7-6939 (N120; Reyes-Iturbide et al. 2008), J0531.9-7100 (N206; Williams et al. 2005, J0535.5-6916 (SNR 1987A; Sturm et al. 2009), J0536.1-6735 (DEM L241; Bamba et al. 2006), J0536.2-6912 (30 Dor C; Bamba et al. 2004), J0537.4-6628 (DEM L256; Klimek et al. 2010), J0537.8-6910 (N157B; Chen et al. 2006), J0540.0-6944 (N159;

Seward et al. 2006), J0547.0-6943 (DEM L316B; Williams & Chu 2005), and J0547.4-6941 (DEM L316B; Williams & Chu 2005). Then, we also estimated the absorbed fluxes in the 0.5–10.0 keV for several SNRs with the best-fit model in their papers. Finally, unfortunately, since J0450.2-6922 (B0450-6927) and J0453.9-7000 (B0454-7005) had no any references, we could not plot on this figure. Our results have a good correlation with the previous results within ∼50 % (dotted lines in this figure). In this study, it was found that the source and background regions selected by us were correct.

Chapter 5

Discussion

5.1 Summary of the Observational Results

We analyzed 44 SNRs observed by *Suzaku*, *XMM-Newton* and *Chandra*, systemtically. In this section, we discuss comprehensively 31 SNRs which were analyzed in detail as follows; (1) their evolutionary phases, (2) empirical relations among the parameters, and (3) surrounding environments for each progenitor type.

5.2 Metal Abunadnce Ratios

The metal abundances are one of the important parameters to estimate an evolutionary phase of SNRs. SNRs in the free expansion phase may have enhanced metal abundances larger than 1 solar, while SNRs in the Sedov or radiative cooling phase may have abundance roughly close to the LMC average (Russell & Dopita 1992; Hughes et al. 1998). Since it was difficult to derive the absolute metal abundance for several SNRs, we decided to utilize the metal abundance ratio. In figure 5.1 we present the derived metal abundance ratios relative to the solar abundance (Anders & Grevesse, 1989) and normalized to oxygen. We did not present several SNRs which could not be derived the metal abundance ratio in our study.

In this figure, most SNRs have abundance roughly consistent to the LMC average (Russell & Dopita 1992; black dotted line and Hughes et al. 1998; red dotted line), which indicate that most SNRs are probably in the Sedov or later phases. In our study, the following SNRs show significant differences from the LMC average; J0540.0-6944 (N159; Seward et al. 2010), J0547.4-6941 (DEM L316A; Williams & Chu 2005), J0547.8-7025 (B0548-704; Hendrick et al. 2003), and J0550.5-6823. These SNRs (except J0550.5-6823) were reported to have enhanced metal abundances from the previous observations. Of these SNRs, several SNRs may have emissions from two different origins. For example, in the case of J0547.8-7025 (B0548-704), one is the ambient medium heated by the forward shock, the other is the ejecta heated by the reverse shock (Hendrick et al., 2003). This remnant was believed to be in the Sedov or later phase based on the relatively old age ($\sim 10,000$ yr; Hendrick et al. 2003), and so on. Therefore, it is difficult to exclude the possibility that these SNRs are not in the Sedov phase with only the metal abundance ratios. Unless otherwise stated, we include all the SNRs in latter discussions.

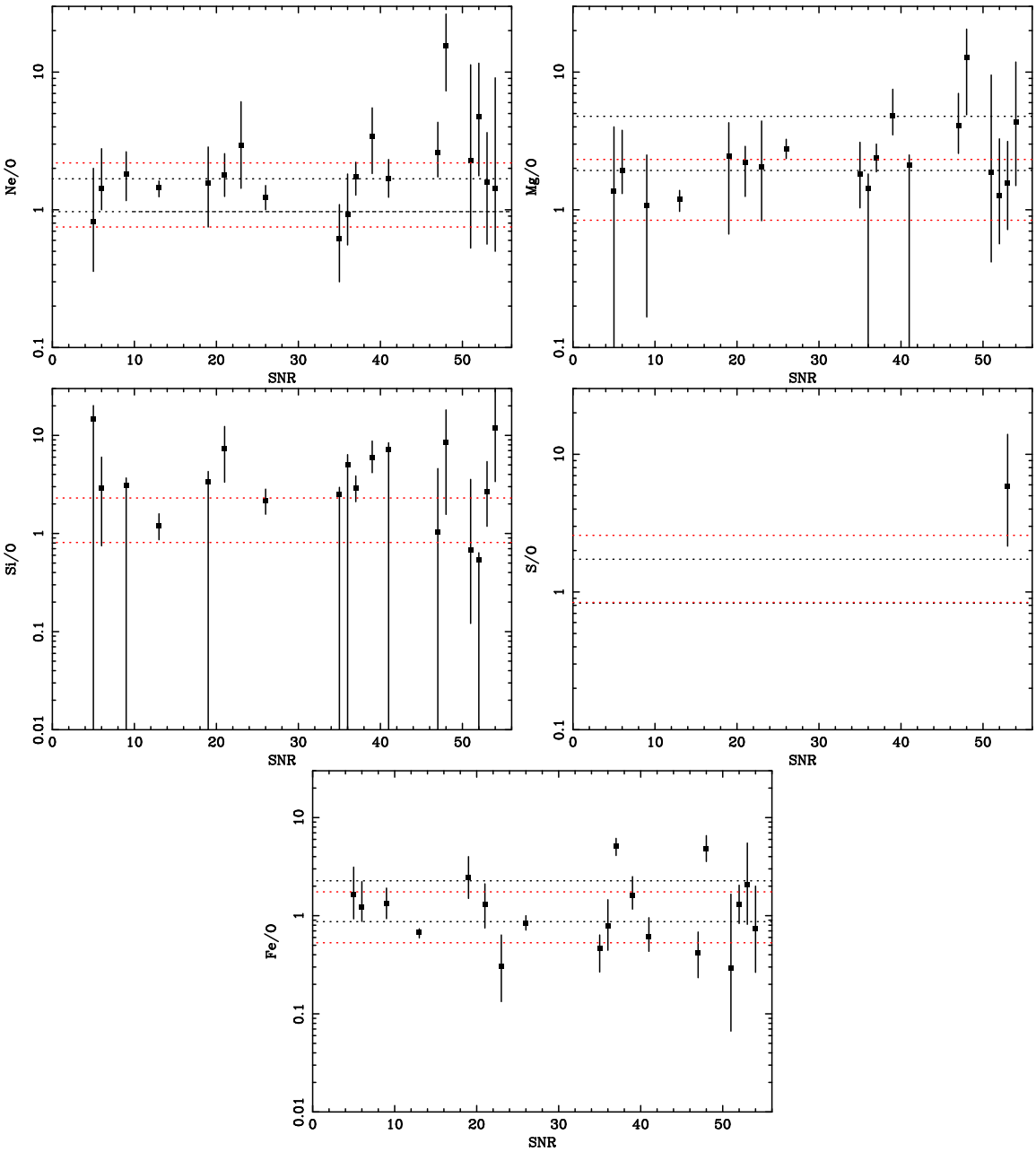

Figure 5.1: The derived metal abundance ratios (top left for Ne/O, top right for Mg/O, middle left for Si/O, middle right for S/O, and bottom Fe/O). The derived abundance ratios are compared to the LMC average (Russell & Dopita 1992; black dotted line and Hughes et al. 1998; red dotted line). The ratios are all relative to solar (Anders & Grevesse, 1989) and normalized to oxygen. Since the Si metal abundance has the large uncertainty (Russell & Dopita, 1992), we did not include the result in the figure. The numbers from left to right in the horizon axis indicate relative number of the SNRs from top to bottom in table 4.1.

5.3 Plasma Densities, Thermal energies and Masses

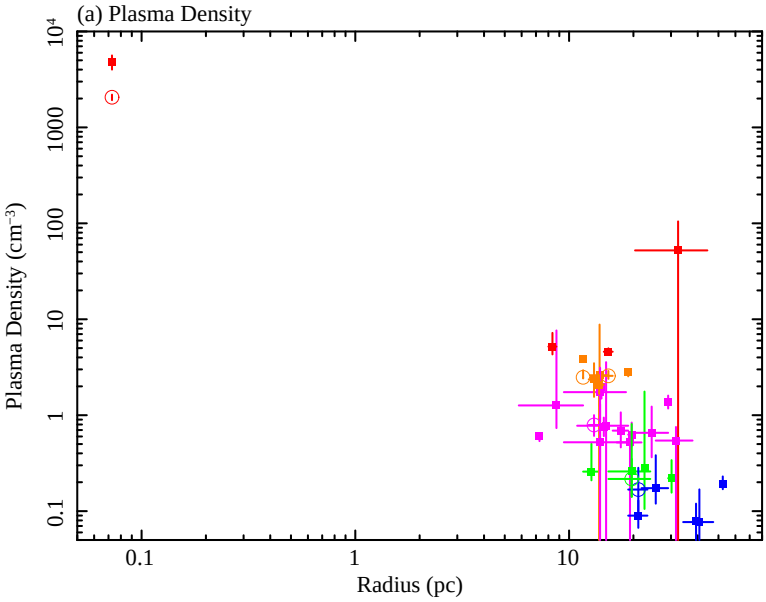

Figure 5.2: Evolutions of (a) a plasma density, (b) a thermal energy, and (c) a plasma mass as a function of SNR radius. The red, orange, magenta, green, and blue data points represent with the plasma densities of $n_{\rm e} \geq 4.0$, $4.0 > n_{\rm e} \geq 2.0$, $2.0 > n_{\rm e} \geq 0.4$, $0.4 > n_{\rm e} \geq 0.2$, and $0.2 > n_{\rm e}$ cm^{-3}, respectively. The filled boxes and open circles also represent the first and second VNEI components, respectively.

In this subsection, we derive plasma densities ($n_{\rm e}$), total thermal energies ($E_{\rm t}$), and plasma masses ($M_{\rm p}$). With the aid of the emission measure obtained from the spectral fitting, the volume of the plasma (V) and the volume filling factor (f), we calculated $n_{\rm e}$, taking into account $n_{\rm e} = 1.2 n_{\rm H}$ for fully ionized LMC abundance plasma ($n_{\rm H}$ is the hydrogen density in a post-shock plasma). The plasma mass is given by $M_{\rm p} = (n_{\rm H} + 4 n_{\rm He}) m_{\rm p} V f^{0.5}$, where $m_{\rm p}$ and $n_{\rm He}$ is the proton mass and the helium density. Assuming fully ionized plasma in the LMC abundance, the helium density is estimated to be $0.087 n_{\rm H}$. The total thermal energy is given by $E_{\rm t} = 3 n_{\rm e} k T_{\rm e} V f^{0.5}$, where k and $T_{\rm e}$ are the Boltzmann constant and the plasma temperature, respectively. Note that we assume that the electron and ion are in thermal equilibrium.

In the previous observation with *Einstein*, the plasma densities and the thermal energies of most SNRs were also estimated (e.g. Long 1983; Berkhuijsen 1986; Berkhuijsen 1987; Berkhuijsen 1988). In estimating the plasma density from the observed luminosity, they assumed the specific emissivity at 3×10^{-23} erg cm^{-3} s^{-1}. Since the specific emissivity depends on temperature, an ionization parameter, and a metal abundance, this assumption is not really correct. In other words, the derived emission measure included all these effects. Thus, the plasma density derived by us may be much reliable compared with the previous results. Moreover, we could actually determine the temperature through the spectral analysis. Thus, the thermal energy may be also estimated correctly compared with their estimation.

In order to estimate the plasma density, we need to know the volume of the plasma

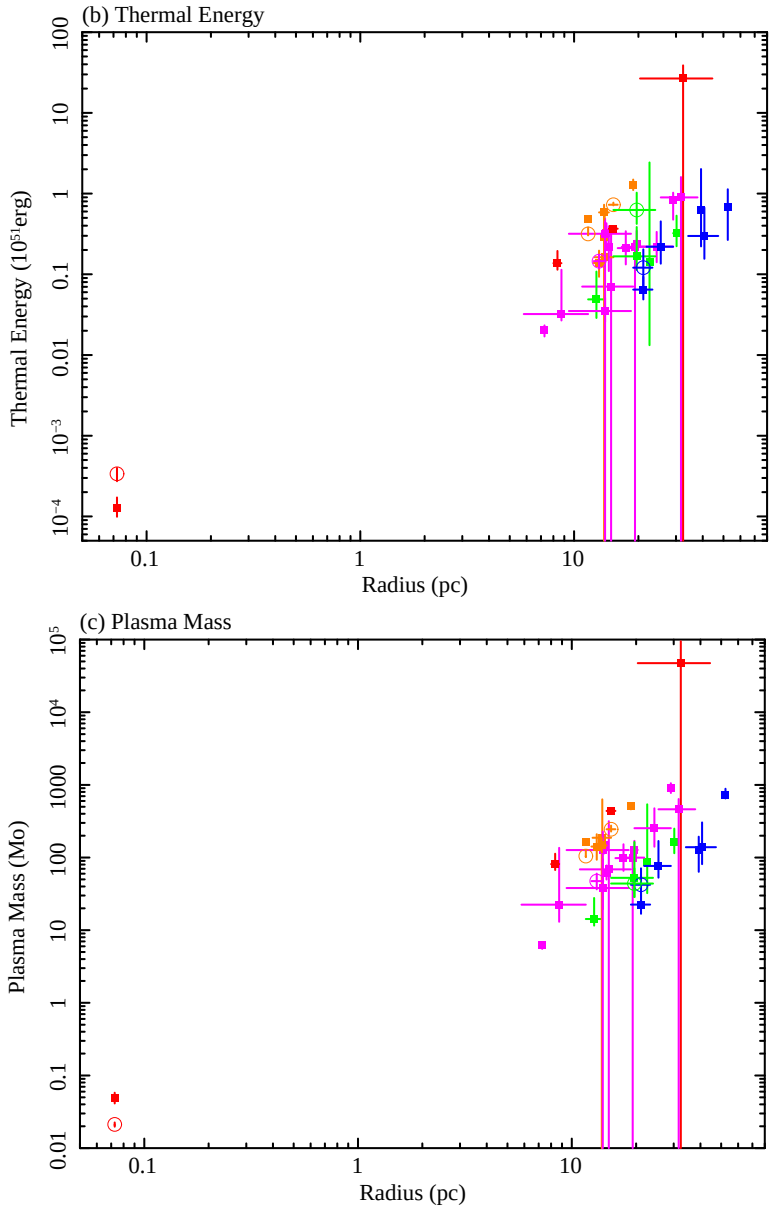

Figure 5.2: Continue.

from the X-ray image. The minimum ($D_{\rm min}$) and maximum ($D_{\rm max}$) diameters are listed in the fifth column of table 4.1. Assuming that the distance to the LMC is 50 kpc (Feast, 1999), we can calculate a real diameter with $D'_{\rm max,min} = 50$ kpc $\times$ tan(D$_{\rm max,min}$). Then, we defined the average radius as $< R >= (D'_{\rm min} + D'_{\rm max})/4$ in unit of pc. Under the assumption of the strong and adiabatic shock, the ambient medium is compressed in a shell with a width of 1/12 of the radius. Then, the plasma volume of the shell is given by

$$V_{\rm shell} = \frac{4}{3}\pi < R >^3 \left(1 - \left(\frac{11}{12}\right)^3\right) f \tag{5.1}$$

with the volume filling factor f. If the plasma is filled in a sphere, the estimation of the plasma density is doubled compared with the current estimation. In addition, the

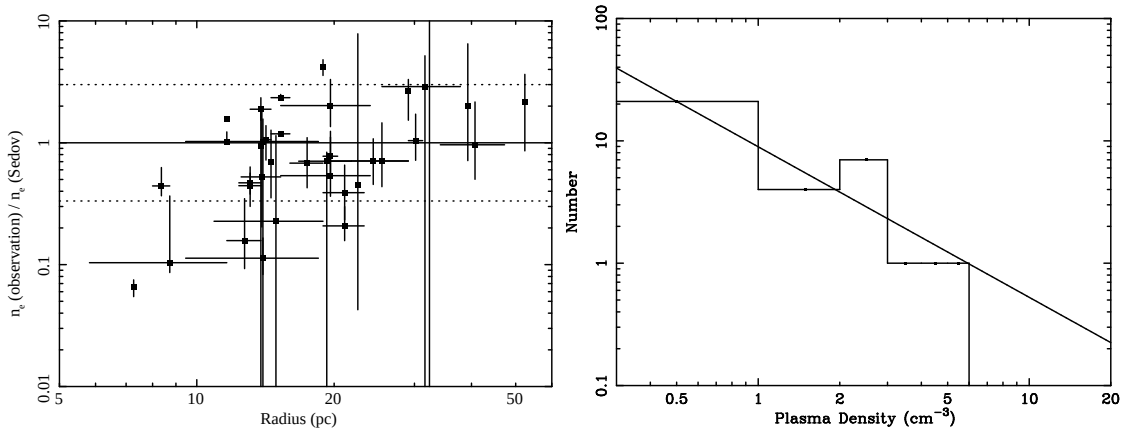

Figure 5.3: The ratio between the derived and simulated (based on the Sedov model) plasma density as a function of SNR radius (left), and the derived plasma density histogram (right).

maximum diameter may be twice as large as the average one for same sources, for example, for J0455.6-6839 (N86). In this case, the estimation of the plasma density is doubled at most and falls between those for the average and the maximum (or minimum) radii compared with the current estimation. In the later sections, we assume that the volume filling factor is 1.

To probe SNR evolution, we have to investigate the time dependence of the plasma parameters. However, it is generally difficult to estimate the age of the SNRs. We therefore used their radii to trace their evolutions. The radius would be good tracer of the age for the same plasma density. Figure 5.2 shows (a) the plasma density, (b) the thermal energy, and (c) the plasma mass as a function of SNR radius. This figure is compatible with the previous observations (e.g. Long 1983; Berkhuijsen 1986; Berkhuijsen 1987; Berkhuijsen 1988; Hughes et al. 1998). In this figure, the smallest SNR is J0535.5-6916 (SN 1987A), which we present as a typical SNR in the free expansion phase. Since we analyzed many SNRs, these relations could be presented as a function of plasma density for the first time.

Though we discuss the plasma density-radius relation in the later section, lager SNRs appear to have lower densities. The estimated thermal energies of most SNRs are below a typical explosion energy (10^{51} erg), and it appears to increase slightly with a radius for the same plasma density. The most naive interpretation is that the electron and proton temperatures are evolved into thermal equilibrium. In addition, thermal energies with larger plasma densities seem to reach thermal equilibrium faster because of the high collision rate. The estimated plasma masses of most SNRs exceed ~ 20 $M_\odot$, which support the interpretation that most SNRs are in the Sedov or later phase. It also appears to increase slightly with a radius for the same plasma density, and it can be interpreted that the blast wave sweep up an ambient medium, which also support that most SNRs are in the Sedov or later phase.

5.3.1 Comparison of the Plasma Densities with the Sedov Model and the Ambient Medium

In this subsection, we compare the plasma densities derived from the observations with those of the Sedov model. A ambient density (n_0) in the Sedov model is given by

$$n_0 = 570 \left(\frac{< R >}{1 \text{ pc}}\right)^{-3} \left(\frac{kT_\text{e}}{1 \text{ keV}}\right)^{-1} \left(\frac{E_0}{10^{51} \text{ erg}}\right) \text{ cm}^{-3}, \tag{5.2}$$

where $< R >$, kT_e, and E_0 are a mean blast wave shock radius defined in the previous section, a plasma temperature, and an initial explosion energy (Sedov, 1959). Assuming that electron and ion are in thermal equilibrium, we can calculate the ambient density (i.e. plasma density: $n_\text{e} = 4n_0$) for the initial explosion energy of 10^{51} erg. Figure 5.3 (left) shows the ratio between the derived and simulated plasma (ambient) density as a function of SNR radius. It is found that most SNRs are compatible with the Sedov model within a factor of three. Note that smaller SNRs trend to show the relatively larger difference from the Sedov model, probably because the electron and ion of these SNRs are in non-thermal equilibrium.

The plasma densities would be affected by the ambient mediums. Figure 5.3 (right) shows a histogram of the derived plasma density. The black solid line indicates the POWER LAW model with the index of 1.23. At the higher densities, it is expected many star are formed and many SNe explode. However, regions with high densities would be rather rare, while regions with low densities are seen much frequently in the LMC. Thus, the plasma (i.e. ambient) density would be proportion to $n_\text{e}^{-1.23}$. In the previous result, the density distribution in the LMC was given by n_0^{-1} (Badenes et al., 2010), which was roughly consistent with our estimation.

5.4 Dynamical Age vs. Cooling Timescale

In the previous discussions, we concluded that most SNRs are in the Sedov or later phase based on the metal abundance ratios and the plasma masses. However, of these SNRs, several SNRs may be possible in the radiative cooling phase. In this subsection, we examine the evolutionary phase of SNRs by comparing various timescales evaluated from observed parameters. We compared the dynamical age (t_sedov) and the cooling timescale (t_cool). Though we discuss in the later sections, the ionization age (t_ion) estimated from the ionization parameter ($n_\text{e}t_\text{ion}$) depends on their surrounding environment. We therefore do not use the ionization age in this subsection. A dynamical age is given by

$$t_\text{sedov} = 4.3 \times 10^2 \left(\frac{< R >}{1 \text{ pc}}\right) \left(\frac{kT_\text{e}}{1 \text{ keV}}\right)^{-0.5} \text{ yr}, \tag{5.3}$$

where $< R >$ and kT_e are a mean blast wave shock radius defined in the previous section and a plasma temperature (Sedov, 1959), respectively. Then, we assume that the electrons and ions are in thermal equilibrium to calculate the dynamical age. A cooling timescale at the beginning of the radiative cooling phase is also given by

$$t_\text{cool} = 2.7 \times 10^4 \left(\frac{E_0}{10^{51} \text{ erg}}\right)^{0.24} \left(\frac{n_0}{1 \text{ cm}^{-3}}\right)^{0.51} \text{ yr} \tag{5.4}$$

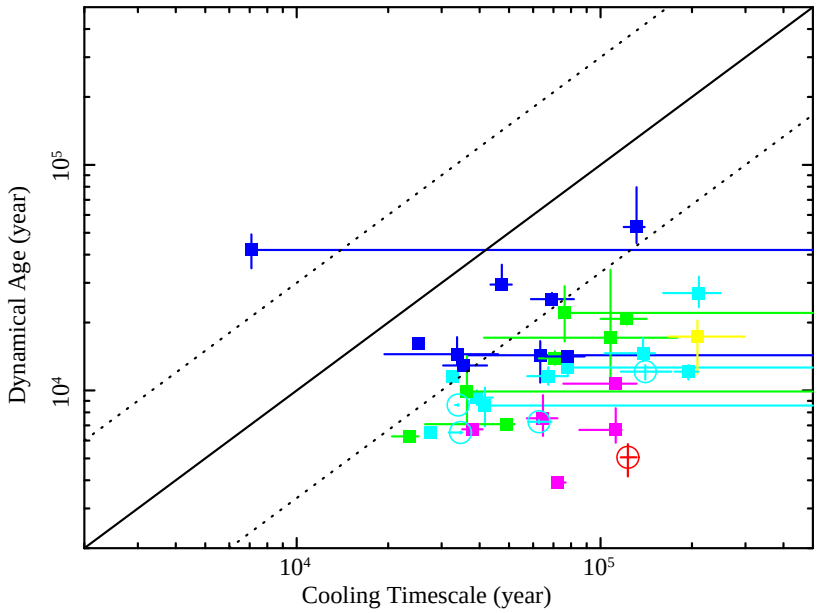

Figure 5.4: The dynamical age vs. cooling timescale between 2,000–500,000 yr. The blue, green, sky blue, magenta, yellow, orange, and red data points are represented with the temperature of 0.08< $kT_e \leq 0.2$, 0.2< $kT_e \leq 0.4$, 0.4< $kT_e \leq 0.6$, 0.6< $kT_e \leq 0.8$, 0.8< $kT_e \leq 1.0$, 1.0< $kT_e \leq 1.2$, 1.2≤ kT_e, respectively. The filled boxes and open circles are also represented with the first and second VNEI components, respectively. The dotted line indicates $\pm 3 \times t_{\rm sedov}$ ($t_{\rm cool}$).

(Falle, 1981), where E_0 and n_0 are an initial explosion energy and an ambient density. Under the assumption of the strong shock, the ambient density is given by $n_0 = n_e/4$. Then, we can calculate these timescales for the initial explosion energy of 10^{51} erg. If $t_{\rm cool} \simeq t_{\rm sedov}$ holds, SNR is considered to be at a late stage of the Sedov phase or at the initial radiative cooling phase. If, on the other hand, $t_{\rm seodv} < t_{\rm cool}$ holds, SNR would be still in the Sedov phase. Figure 5.4 shows the correlation between the derived dynamical age and cooling timescale. All SNRs have the younger dynamical ages compared with their cooling timescales, which suggest that these SNRs may have negligibly small radiative losses (i.e. Sedov phase).

Possibility of the Radiative Cooling Phase

Note that the plasma density depends on the volume filling factor (f). If the shock wave propagate in a high density region, the plasma volume should become smaller than the current estimation, resulting in a higher plasma density. We calculated the plasma volume assuming that the shell thickness became 1/12 of the radius, as expected for a spherical strong and adiabatic shock. This assumption holds only if SNRs are still in the Sedov phase. If SNRs enter the radiative cooling phase, the shell thickness should be smaller due to their radiative losses. The plasma density are probably larger than the current estimation. If, for instance, $f = 0.01$, the cooling timescale becomes three times larger than the current estimation. In particular, it is difficult to deny the possibility of the radiative cooling phase for the SNRs from the low temperature plasma (~ 0.2 keV).

Effect of Non-Thermal Equilibrium

Finally, we consider whether the plasma is still in non-thermal equilibrium. In this case, the electron temperature is lower than the ion temperature, which indicates older dynamical age compared with the "real" dynamical age estimated with the ion temperature. A plasma is considered to reach the thermal equilibrium at ∼10 pc ($n_0 = 1$ cm^{-3}) and ∼20 pc ($n_0 = 0.1$ cm^{-3}, e.g. figure 6 in Shimizu et al. 2011). Though we discuss in a later subsection, many SNRs seem to be close to thermal equilibrium. It is probably difficult to explain the relatively older dynamical ages with non-thermal equilibrium when the SNR contains the low temperature plasma (∼0.2 keV). Thus, then the low temperature plasma (∼0.2 keV) is present in the SNR, it is difficult to deny the possibility of the radiative cooling phase.

5.4.1 Comparison of the Dynamical Age with the Characteristic Age

When the SNR contains a pulsar, the characteristic age can be estimated from the spin-down rate of the pulsar. Among the SNRs, J0537.8-6910 (N157B) and J0540.2-6920 (B0540-693) have the characteristic ages of ∼5,000 yr (Marshall et al., 1998) and ∼1,660 yr (Seward et al., 1984), respectively. On the other hand, the dynamical age of J0537.8-6910 (N157B) was estimated to be 7500^{+2000}_{-1200} yr, which was consistent with the characteristic age. However, the dynamical age of J0540.2-6920 (B0540-693) was estimated to be 6300±500 yr, which was significantly different from the characteristic age. Hwang et al. (2001) reported the high temperature emission of $5.5^{+1.5}_{-1.1}$ keV from east side of the inner region with the spatially resolved analysis. If we adopt this high temperature, the dynamical age is estimated to be ∼1,500 yr, which is consistent with the characteristic age. Since we analyzed the X-ray emission from the whole remnant, this hard emission may be hidden by the strong non-thermal emission. Although we have only two examples, the characteristic ages may be compatible with the dynamical age.

5.5 Spectral Parameters in the Sedov Phase

In the previous discussions, we concluded the most SNRs are in the Sedov phase, though several SNRs are doubted to be in the radiative cooling phase. To understand with derived spectral parameters, we assumed the Sedov model (Sedov, 1959), in which a supernova with an explosion energy (E_0) expands into a homogeneous ISM. In this subsection, we summarize how to calculate for the spectral parameters in the Sedov phase. A radius and a plasma temperature at a shock front in the Sedov phase are given by

$$R_{\rm sedov} = 12.5 \left(\frac{t}{10^4\ {\rm yr}}\right)^{\frac{2}{5}} \left(\frac{E_0}{10^{51}\ {\rm erg}}\right)^{\frac{1}{5}} \left(\frac{n_0}{1\ {\rm cm}^{-3}}\right)^{-\frac{1}{5}}\ {\rm pc} \tag{5.5}$$

$$T_{\rm sedov} = kT_{\rm e} = 0.29 \left(\frac{t}{10^4\ {\rm yr}}\right)^{-\frac{6}{5}} \left(\frac{E_0}{10^{51}\ {\rm erg}}\right)^{\frac{2}{5}} \left(\frac{n_0}{1\ {\rm cm}^{-3}}\right)^{-\frac{2}{5}}\ {\rm keV}, \tag{5.6}$$

where t, E_0, and n_0 are an elapsed time after an explosion in yr, an initial explosion energy in erg, and a pre-shock density (an ambient density) in cm^{-3} (Sedov, 1959). Under the

assumption of the strong and adiabatic shock, the ambient medium is compressed into 1/12 of the radius. Then, the plasma volume is given by

$$V_{\rm shell} = \frac{4}{3}R^3\left(1-\left(\frac{11}{12}\right)^3\right)\ {\rm cm}^3. \tag{5.7}$$

With a plasma density ($n_{\rm e}$) and a hydrogen density ($n_{\rm H}$) in the post-shock plasma, an emission measure is also given by

$$EM = n_{\rm e}n_{\rm H}V_{\rm shell}\ {\rm cm}^{-3}. \tag{5.8}$$

With the equation 5.5 and 5.7, the emission measure ($EM_{\rm seodv}$) in the Seodv phase is given by

$$EM_{\rm sedov} = 8.84\times10^{59}\left(\frac{t}{10^4\ {\rm yr}}\right)^{\frac{6}{5}}\left(\frac{E_0}{10^{51}\ {\rm erg}}\right)^{\frac{3}{5}}\left(\frac{n_0}{1\ {\rm cm}^{-3}}\right)^{\frac{7}{5}}\ {\rm cm}^{-3}, \tag{5.9}$$

where we assumed simply $n_{\rm e} = n_{\rm H} = 4n_0$ under the jump condition.

In the plasma density-radius relation, the plasma densities have ∼4–0.04cm^{-3}, corresponds to the ambient densities of ∼1–0.01 cm^{-3} under the jump condition. In calculating the spectral parameters in the Sedov phase, we therefore assumed the ambient density of 1, 0.5, 0.1, 0.05, and 0.01 cm^{-3}. Then, we can calculate the spectral parameters in the Sedov phase with a variable parameter t at the initial explosion energy of 10^{51} erg. The initial explosion energy was estimated based on the Sedov model to be $E_0 = (1.1\pm0.5)\times10^{51}$ erg (Hughes et al., 1998).

5.6 Comparison of the Derived Spectral Parameters with the Sedov Model; Emission Measure & Temperature

The emission measure and the temperature in the thermal X-ray emission from SNRs are one of the basic spectral parameters. In this section, we discuss these parameters for each plasma density. In figure 5.5 (a), we present the correlation between the derived temperature and emission measure. A plasma temperature in the same density appears to decrease with an emission measure. Assuming the Sedov model, this relation has a good correlation between the derived and simulated spectral parameters for each plasma density, which is also supported that most SNRs are in the Sedov phase. In the following subsections, we discuss these relations in detail.

5.6.1 Emission Measure

In figure 5.5 (b), the emission measure in the same plasma density appears to increase with a radius, which are compatible with the Sedov model. We found that this relation has an excellent correlation between the derived and simulated parameters for each plasma density within a factor of five. This excellent correlation supports that the initial explosion energy of most SNRs is roughly to be 10^{51} erg.

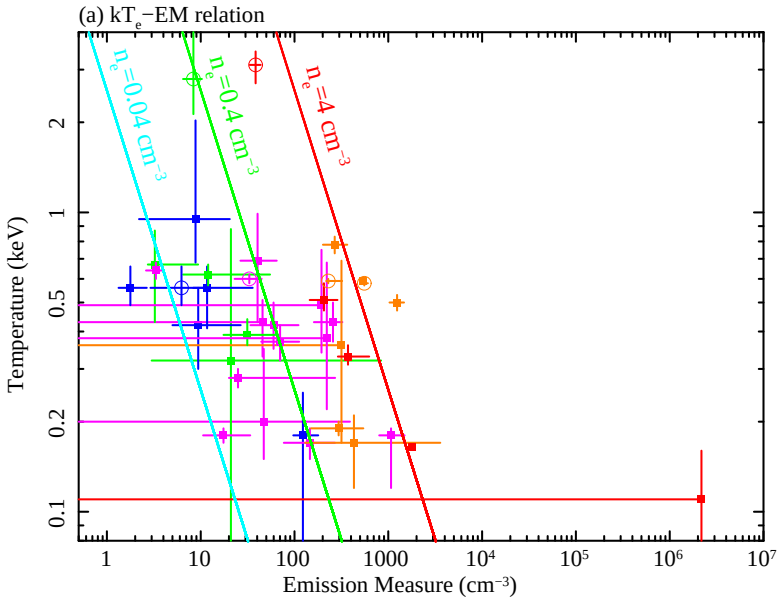

Figure 5.5: The relations between the observed parameters; (a) $kT_{\rm e}$-EM relation, (b) EM-R relation, and (c) $kT_{\rm e}$-R relation. The red, magenta, green, blue and sky blue solid lines are represented with the simulated spectral parameters in the Sedov phase with the ambient densities of 1 ($n_{\rm e}$ = 4), 0.5 ($n_{\rm e}$ = 2), 0.1 ($n_{\rm e}$ = 0.4), 0.05 ($n_{\rm e}$ = 0.2), and 0.01 ($n_{\rm e}$ = 0.04) cm^{-3}, respectively. The red, orange, magenta, green, and blue data points are represented with the plasma densities of $n_{\rm e} \geq 4$, $4 > n_{\rm e} \geq 2$, $2 > n_{\rm e} \geq 0.4$, $0.4 > n_{\rm e} \geq 0.2$, and $0.2 > n_{\rm e}$ cm^{-3}, respectively. The filled boxes and open circles are also represented with the first and second VNEI components, respectively.

In the previous section, we concluded that several SNRs with the low temperature plasma (∼0.2 keV) are possible in the radiative cooling phase. In this figure, all SNRs are compatible with the Sedov model, which seems to be in the Sedov phase. In the radiative cooling phase, the shell thickness should be smaller due to their radiative losses, resulting in a higher plasma density. Since the emission measure is proportion to $n_{\rm e}^2 V$, this may have not significant differences between the Sedov and radiative cooling phase because of the trade-off between the plasma density and volume.

5.6.2 Temperature

In figure 5.5 (c), the temperature in the same plasma density appears to decrease with a radius. However, the observed plasma temperatures seem to be the relatively lower than the Sedov model, though these trends are compatible with the Sedov model. Thus, most SNRs would be at least near thermal equilibrium. Shimizu et al. (2011) explained that the plasma reach in thermal equilibrium at ∼ 10 pc (n_0 = 1 cm^{-3}) and ∼ 20 pc (n_0 = 0.1 cm^{-3}) in their paper. Our results are compatible with their study.

To combine the equation 5.5 with 5.6, the plasma temperature in the Sedov phase is rewritten as

$$kT_{\rm e} = 5.6 \times 10^2 \left(\frac{E_0}{10^{51}\ {\rm erg}}\right) \left(\frac{n_0}{1\ {\rm cm}^{-3}}\right)^{-1} \left(\frac{R}{1\ {\rm pc}}\right)^{-3}\ {\rm keV}, \tag{5.10}$$

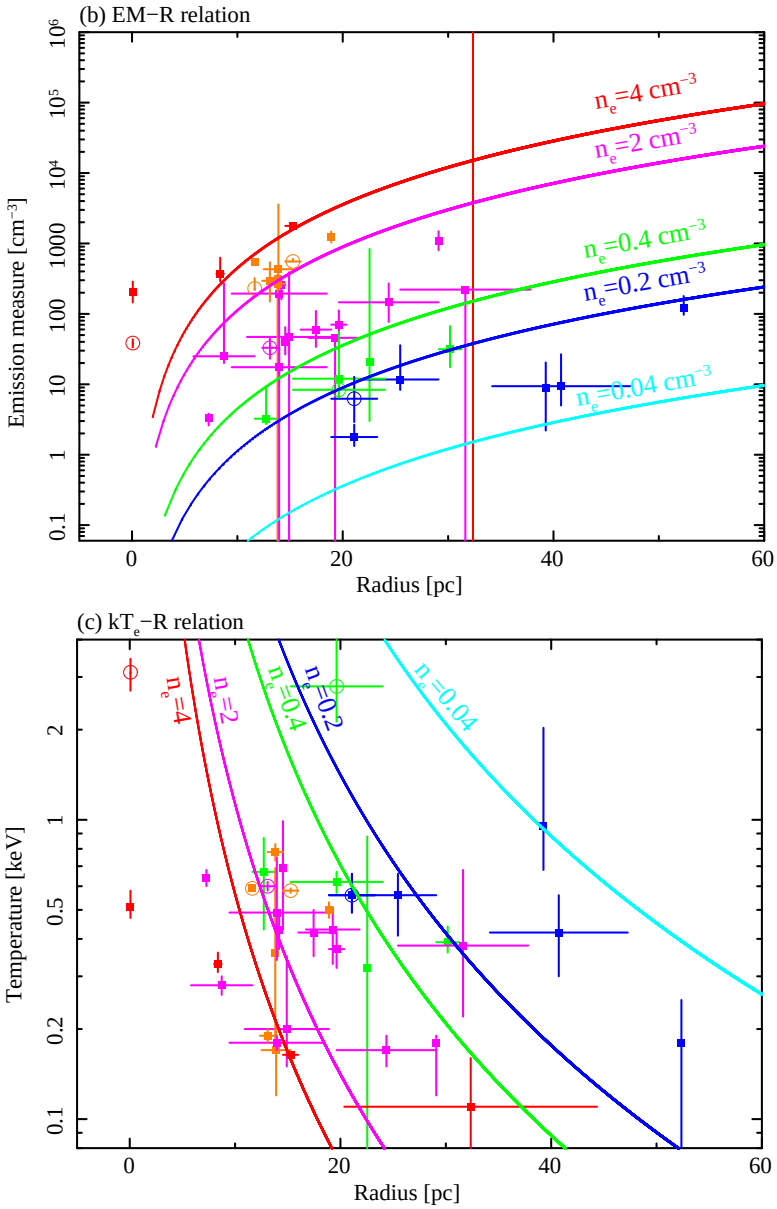

Figure 5.5: Continue.

where E_0, n_0, and R are an initial explosion energy, an ambient medium, and a blast wave radius. Then, under the assumption of the strong shock ($n_{\rm e} = 4n_0$), we can calculate the plasma temperature with the mean blast wave shock radius defined in the previous section at the initial explosion energy of 10^{51} erg. In figure 5.6 shows the ratio between the derived and simulated plasma temperatures. The plasma temperature calculated by the Sedov model corresponds to the ion (proton) temperature. Most SNRs were consistent with the Sedov model within a factor of three, which is supported that most SNRs were near thermal equilibrium. On the other hand, several SNRs with smaller radii were significant difference with the Sedov model, which was interpreted that these SNRs were in non-thermal equilibrium. This results are compatible with Shimizu et al. (2011). We compared the derived plasma parameter with the Sedov model for many SNRs for each plasma density for the first time. In addition, it appears to increase slightly with a radius

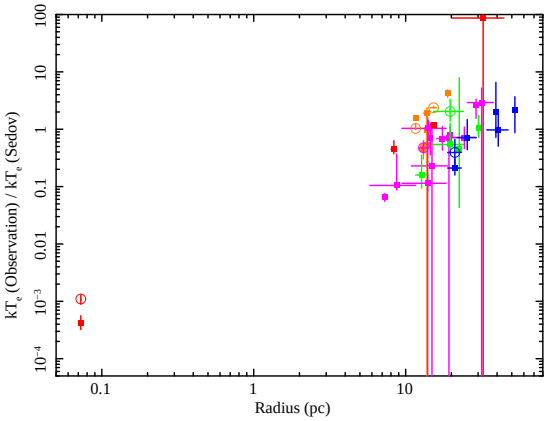

Figure 5.6: The ratio between the derived and simulated (based on the Sedov model) plasma temperature as a function of SNR radius. The red, orange, magenta, green, and blue data points are represented with the plasma densities of $n_e \geq 4$, $4 > n_e \geq 2$, $2 > n_e \geq 0.4$, $0.4 > n_e \geq 0.2$, and $0.2 > n_e$ cm^{-3}, respectively. The filled boxes and open circles are also represented with the first and second VNEI components, respectively.

in the same plasma density. The most simplest interpretation is that the electron and proton temperature are evolved into thermal equilibrium. Thermal energies with larger plasma densities would reach early in thermal equilibrium because of the high collision rate.

The derived plasma temperatures were to be below 1 keV for most SNRs. The typical velocity in the free expansion phase becomes ∼2,000–10,000 km s^{-1}, corresponds to the plasma temperature of ≫1 keV under the jump condition. In actually, several SNRs believed in the free expansion phase are observed to be the shock velocity of ∼3000–5000 km s^{-1} and the temperature of ∼0.4–7 keV (e.g. Kosenko et al. 2008; Kosenko et al. 2010; Vink 2008; Vink et al. 1998; Vink et al. 1996; Kinugasa & Tsunemi 1999; Hughes 2000; Hwang et al. 2002; Winkler et al. 2003; Yamaguchi et al. 2008). The observed low temperature plasmas (≪1 keV) are also suggested that most SNRs are at least in the Sedov phase.

5.7 Apparent Relations - Plasma Density-Radius Relation -

Figure 5.7 shows the plasma density-radius relation. A plasma density in the Sedov phase has a constant in a time (Sedov 1959). However, in this figure, larger SNRs appear to have lower densities. This effect discovered by McKee & Ostriker (1977) for the first time in our galaxy, which our result was compatible with their result. Moreover, many authors have already reported this effect (e.g. Long 1983; Berkhuijsen 1988; Hughes et al. 1998). In spite of many reports, this relation is the open question. We concluded that most SNRs were in the Sedov phase in the previous discussions, and several SNRs were also possible in the radiative cooling phase. In this section, we give a plausible explanation for this relation.

First, we consider the timescales of each phase. At the end of the free expansion phase,

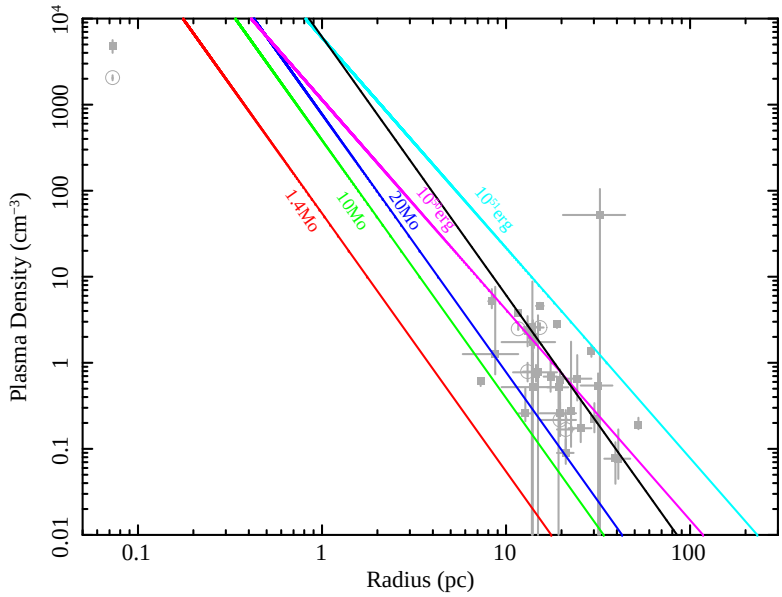

Figure 5.7: The plasma density-radius relation. The red (1.4 $M_\odot$), green (10 $M_\odot$) and blue (20 $M_\odot$) solid lines are represented with at the end of the free expansion phase. The purple (10^{51} erg) and sky blue (10^{51} erg) are also represented with at the beginning of the radiative cooling phase. The filled boxes and open circles are represented with the first and second VNEI components, respectively. The solid black line is represented with the best-fit model.

a swept-up mass becomes comparable to that of an ejecta mass. Then, the age at this stage is given by

$$t_{\rm free} \simeq 2.0 \times 10^3 \left(\frac{E_0}{10^{51}\ {\rm erg}}\right)^{-\frac{1}{2}} \left(\frac{M_0}{10\ {\rm M}_\odot}\right)^{\frac{5}{6}} \left(\frac{n_0}{1\ {\rm cm}^{-3}}\right)^{\frac{1}{3}}\ {\rm yr}, \tag{5.11}$$

where E_0, M_0, and n_0 are an initial explosion energy in erg, an ejecta mass in $M_\odot$, and an ambient density in cm^{-3}, respectively. On the other hand, at the beginning of the radiative cooling phase, the age at this stage is also given by

$$t_{\rm cool} \simeq 2.7 \times 10^4 \left(\frac{E_0}{10^{51}\ {\rm erg}}\right)^{0.34} \left(\frac{n_0}{1\ {\rm cm}^{-3}}\right)^{-0.52}\ {\rm yr} \tag{5.12}$$

(Falle, 1981). As a result, the timescale in the Sedov phase is estimated to be $t_{\rm sedov} = t_{\rm cool} - t_{\rm free}$ yr. Assuming the initial explosion energy of 10^{51} erg and the ejecta mass of 10 $M_\odot$, the ratio between the timescales in the free expansion and Sedov phase is given by $t_{\rm sedov}/t_{\rm free} = 13.5(n_0/1\ {\rm cm}^{-3})^{-0.89} - 1 \simeq 13.5({\rm n}_0/1\ {\rm cm}^{-3})^{-0.89}$. It is found that the Sedov phase are roughly ten times longer than the free expansion phase. Many SNRs therefore would appear to concentrate in the Sedov phase, which is compatible with the previous discussions. Next, we estimate the plasma density-radius relation for each phase. Under the assumption of the strong shock, the plasma density-radius relation in the free expansion phase is given by

$$R_{\rm free} = 4.6 \left(\frac{M_0}{10\ {\rm M}_\odot}\right)^{\frac{1}{3}} \left(\frac{n_{\rm e}}{4\ {\rm cm}^{-3}}\right)^{-\frac{1}{3}}\ {\rm pc}, \tag{5.13}$$

while that in the radiative cooling phase is given by

$$R_{\rm cool} = 20 \left(\frac{E_0}{10^{51}\ {\rm erg}}\right)^{0.295} \left(\frac{n_{\rm e}}{4\ {\rm cm}^{-3}}\right)^{-0.409}\ {\rm pc} \tag{5.14}$$

(Falle, 1981). Then, we calculated the plasma density-radius relation for each phase. In figure 5.7 we present the simulated plasma density-radius relations for each phase, ejecta mass, and initial explosion energy. Assuming the initial explosion energy of 10^{51} erg, it is also found that most SNRs are in the Sedov phase, which is also compatible with the previous discussions. Since smaller SNRs have higher plasma densities, such SNRs would disappear early on the sky due to their radiative losses. On the other hand, SNRs with smaller plasma densities would survive until larger radii. Thus the plasma density-radius relation can be understood to result from the deceleration in the Sedov phase, and a transition to the radiative cooling phase at a radius that depends on a local gas density. In actually, several SNRs observed by us have possible in the radiative cooling phase. This result supports our interpretation. The similar discussion are also performed by Badenes et al. (2010) and Fusco-Femiano & Preite-Martinez (1984). However, we concluded that most SNRs were in the Sedov phase from our observational study for the first time. Finally, SNRs with a small radius in a low ambient medium may not be visible in the X-ray band due to the low X-ray luminosity (selection effect).

The physical interesting case is the power law index of -3. Then, the plasma temperature have a constant in a time (see § 5.8). Assuming the power law index of -3, the best-fit model was estimated to be $n_{\rm e} = 6100^{+2900}_{-1900}(R/1\ {\rm pc})^{-3}$ at the 90 % confidence level as shown in figure 5.7.

5.8 Apparent Relations - Temperature Distribution -

From the plasma density-radius relation, larger SNRs appear to have lower plasma densities, while smaller SNRs have higher plasma densities. Because of the trade-off between the radius and the plasma density, it can be expected that the plasma temperature in the Sedov phase probably appears to concentrate around one. Figure 5.8 shows the temperature histogram. We found that the plasma temperature concentrated around ∼0.4 keV. Another peak around ∼ 0.2 keV may be in the radiative cooling phase. Thus, we fitted this histogram with a single component GAUSSIAN model, and obtained the central temperature of 0.42±0.23 keV at the 68 % confidence level.

To combine the equation 5.5 with 5.6, the plasma temperature in the Sedov phase is rewritten as

$$kT_{\rm e} = 5.6 \times 10^2 \left(\frac{E_0}{10^{51}\ {\rm erg}}\right) \left(\frac{n_0}{1\ {\rm cm}^{-3}}\right)^{-1} \left(\frac{R}{1\ {\rm pc}}\right)^{-3}\ {\rm keV}, \tag{5.15}$$

where E_0, n_0, and R are an initial explosion energy, an ambient medium, and a radius, respectively. If the ambient medium is proportion to R^{-3}, the shock temperature has a constant in a time. In the previous section, we obtained that the plasma density-radius relation was estimated to be $n_{\rm e} = 4n_0 = 6100^{+2900}_{-1900}(R/1\ {\rm pc})^{-3}\ {\rm cm}^{-3}$ at the 90 % confidence level. With this equation, we can calculate the ambient density for each radius,

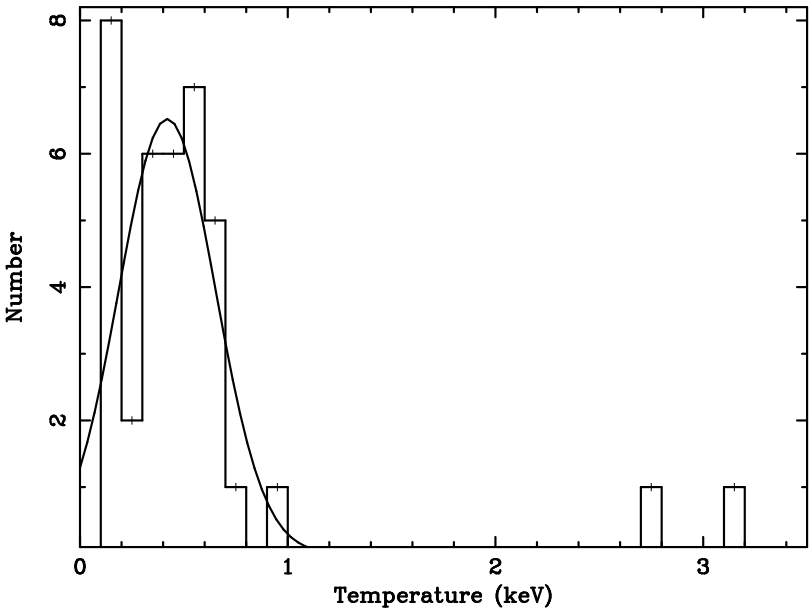

Figure 5.8: The temperature histogram. The bin size is 0.1 keV. The black solid line is represented with the GAUSSIAN model with the central temperature of 0.42 ± 0.23 keV at the 68 % confidence level.

and estimate the plasma temperature with equation 5.15 for each radius. As a result, to combine this equation with equation 5.15, the plasma temperature is estimated to be $kT_{\rm e} = 0.37^{+0.16}_{-0.12}(E_0/10^{51}$ erg) keV, which is roughly compatible with the previous estimation (0.42 ± 0.23 keV). Then, we assumed the initial explosion energy of 10^{51} erg.

We therefore concluded that the temperature distribution in the Sedov phase appears to concentrate around 0.42 ± 0.23 keV because of the trade-off between the radius and the plasma density.

5.9 Ionization Age vs. Dynamical Age

In this section, we discuss the correlation between the ionization and dynamical ages for each progenitor type. The ionization age ($t_{\rm ion}$) is estimated from the ionization parameter ($n_{\rm e}t_{\rm ion}$), taking into account the derived plasma density ($n_{\rm e}$). In figure 5.9 we present a part of the correlation between derived ionization and dynamical ages. Several SNRs with the ionization age of $> 10^5$ yr have large uncertainties because of collisional ionization equilibrium ($n_{\rm e}t_{\rm ion} > 10^{12}$ cm^{-3} s) in detail. In this figure, between these ages in Type Ia SNRs have a relatively good agreement, while the ionization ages in CC SNRs continue to remain low. This discrepancy of these SNRs cannot be resolved by considering the volume filling factor, since that would increase our estimation for the plasma density, and consequently lower the inferred ionization ages even further. In the later subsection, we discuss a plausible explanation.

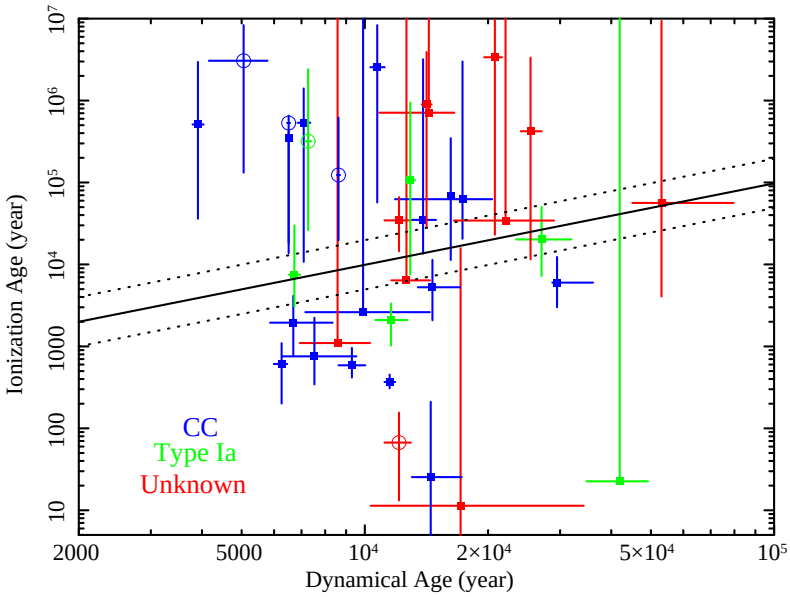

Figure 5.9: SNR age determined from the derived ionization parameter vs. the dynamical age derived from the Sedov model. The blue, green, and red data points are represented with CC, Type Ia, and unknown SNe, respectively. The filled boxes and open circles are represented with the first and second VNEI components, respectively.

5.9.1 Cavity Explosion

Hughes et al. (1998) analyzed the seven middle-aged SNRs (6 SNRs; CC and 1 SNR; Type Ia). In their paper, it was not coincident that several CC SNRs were significant deference between the derived ionization and dynamical ages, which were compatible with the our results. They interpreted that these SNRs exploded within a preexisting low-density cavity in an ambient medium. The low interior density would allow the blast wave to propagate rapidly without deceleration for a long time. On the other hand, a dynamical age based on the Sedov model is considered that the blast wave propagates with deceleration from the beginning. Thus, an ionization age would be younger than a dynamical age.

CC SNRs were identified mainly based on their surrounding environment (Chu & Kennicutt, 1988), such as its proximately to the HII region, the OB association, the high density of OB stars, and so on. Such surrounding environments may make a large cavity in the ambient medium through SNe which exploded in the past. On the other hand, Type Ia SNR elapse a few Gyr until its explosion. As a result, the blast wave would propagate in the relatively dense uniform medium. Thus, these SNRs would have the relatively good correlation between the ionization and dynamical ages. We support the previous interpretation (Hughes et al., 1998).

Chapter 6

Summary & Conclusion

We performed the systematic X-ray study of the supernova remnants in the Large Magellanic Cloud for the first time. The important results are summarized as follows:

- We analyzed 44 SNRs observed by *Suzaku*, *XMM-Newton*, and *Chandra*: 23 SNRs with *Suzaku*, 28 SNRs with *XMM-Newton*, and 4 SNRs with *Chandra*. We analyzed the all the data systematically and estimated the plasma parameters in uniform way for the first time. From the plasma parameters such as plasma mass, abundance pattern, dynamical age, and so on, we concluded that most of our samples are in the Sedov phase. In addition, we found that the emission measure coincide excellently with the prediction of the Sedov model as a function of plasma density for the first time. Futhermore, the plasma temperature also showed relatively good coincidence with the Sedov model.

- The plasma density-radius relation was found to be explained by the deceleration in the Sedov phase, and a transition to the radiative cooling phase at a radius which depends on a local gas density. Though the similar interpretation was discussed by Badenes et al. (2010) and Fusco-Femiano & Preite-Martinez (1984), our explanation is based on the observational results that most SNRs were in the Sedov phase, and several SNRs had possible in the radiative cooling phase. We also concluded the temperature in the Sedov phase is apparently concentrated around $\sim$0.4 keV due to the cancelation of the radius dependence and the plasma density dependence for the first time.

- We found that the ionization ages for Type Ia SNRs were roughly compatible with the dynamical age within a factor of three, while those for several CC SNRs showed large discrepancy. We concluded that several CC SNRs exploded in a preexisting very low-density cavity, while Type Ia SNe exploded in the relatively dense surrounding medium. This have already been reported in the previous results (Hughes et al., 1998). Our results also support their interpretation.

Appendix A

Instruments

A.1 The *Suzaku* Stellite

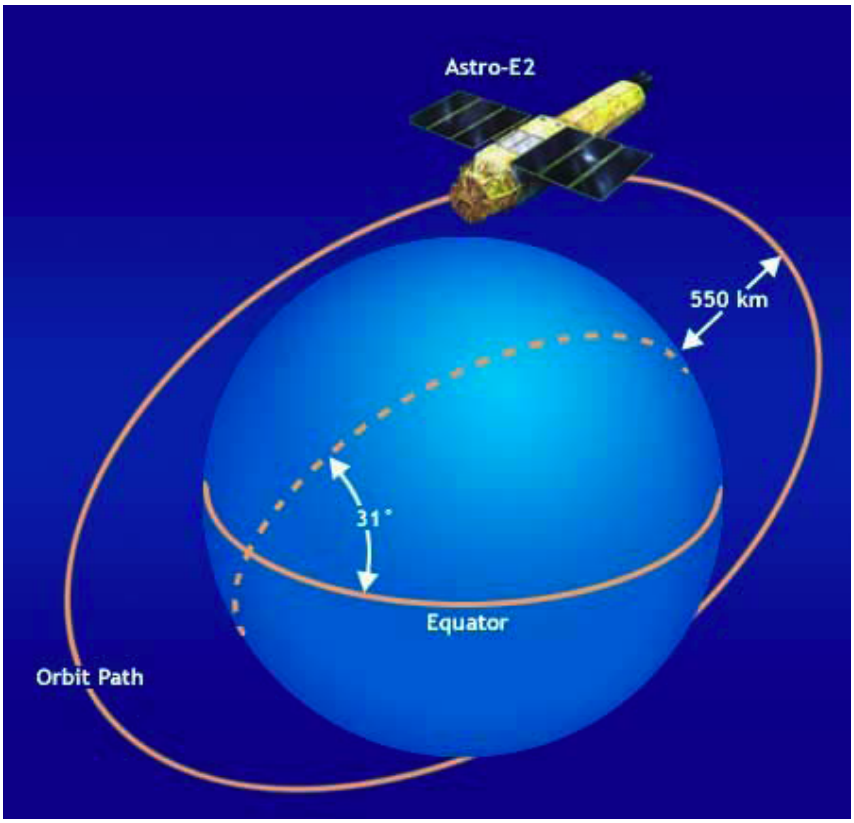

Figure A.1: The *Suzaku* orbit. This figure was taken by the *Suzaku* technical description.

Suzaku, the Japanese 5th X-ray astronomical satellite, was launched on July, 2005 (Mitsuda et al., 2007). *Suzaku* places in a near-circular orbit with the apogee of 568 km, the inclination of 31.9 deg degrees, and the orbital period of about 96 minutes (figure A.1). The maximum slew rate of the spacecraft is 6 degrees/min, and setting to the final attitude takes ∼10 minutes, using the star trackers.

The scientific payload of *Suzaku* (figure A.2) initially consisted of three distinct co-

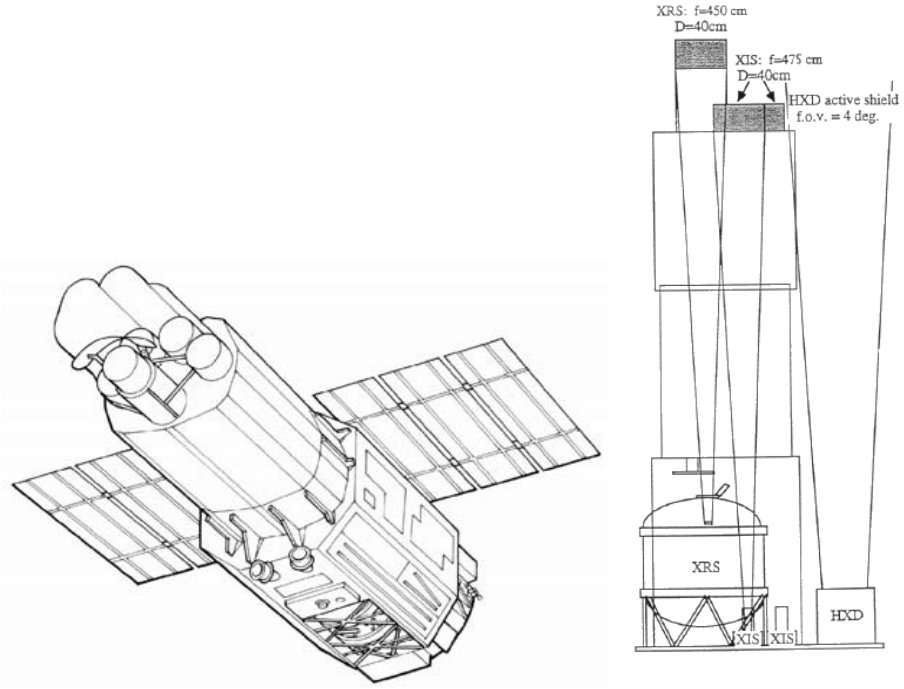

Figure A.2: Left: Schematic picture of the *Suzaku* satellite. Right: A side view of the instruments and telescopes on *Suzaku* (Mitsuda et al., 2007).

aligned scientific instruments. There are four X-ray sensitive imaging CCD cameras (X-ray Imaging Spectrometer, or XISs; Koyama et al. 2007), which have capable of moderate energy resolution, three front-side illuminated (FI; energy range 0.4–12 keV corresponding to XIS0, XIS2, XIS3) and one back-side illuminated (BI; energy range 0.2–12 keV for XIS1). Each CCD camera has a single CCD chip with an array of 1024×1024 picture elements ("pixel"), and covers an 17'.8×17'.8 region on the sky. Each pixel is 24 μm square, and the size of the CCD is 25×25 mm. Each XIS is located on the focal plane of a dedicated X-ray telescope. The second instrument is the non-imaging, collimated Hard X-ray Detector (HXD), which extends the bandpass of the observatory to much higher energies with its 10–600 keV. The X-ray Spectrometer (XRS) is no longer operational. All of the instruments on *Suzaku* operate simultaneously. Each of the co-alligned XRTs features an X-ray mirror with an angular resolution (expressed as Half-Power Diameter, or HPD) of ∼2' (figure A.3). Figure A.3 shows the total effective area of the XIS + XRT. K-shell absorption edges from oxygen (0.54 keV) and aluminum (1.56 keV) in the blocking filter are present, as well as a number of weak M-shell features between 2–3 keV arising from the gold coated on the front surface of the XRT reflector. In this paper, we only used XISs. In the following section, we explain these instruments in detail.

A.1.1 X-ray Telescopes (XRTs)

Suzaku has five light-weight thin-foil X-ray Telescopes (XRTs). The XRTs have been developed jointly by NASA/GSFC, Nagoya University, Tokyo Metropolitan University, and ISAS/JAXA. These are grazing-incidence reflective optics consisting of compactly

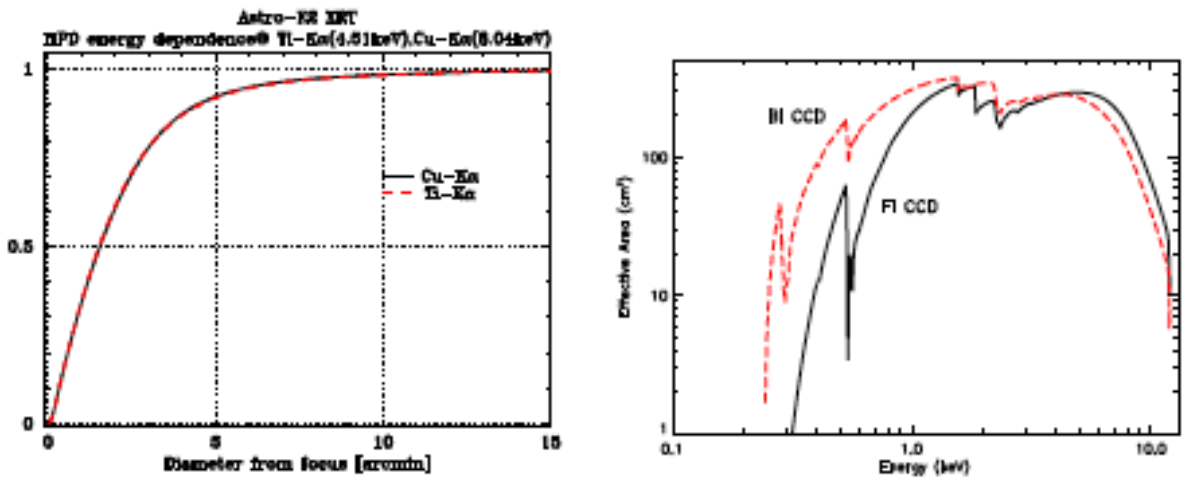

Figure A.3: Left: The Encircled Energy Function (EEF) showing the fractional energy within a given radius for one quadrant of the XRT-I telescopes on *Suzaku* at 4.5 and 8.0 keV (Serlemitsos et al., 2007). Right: XIS effective area of one XRT + XIS system, for the FI and BI CCDs. no contamination.

nested, thin conical elements. Because of the reflectors' small thickness they permit high density nesting and thus provide large collecting efficiency with a moderate imaging capability in the energy range of 0.2–12 keV, all accomplished in telescope units under 20 kg each.

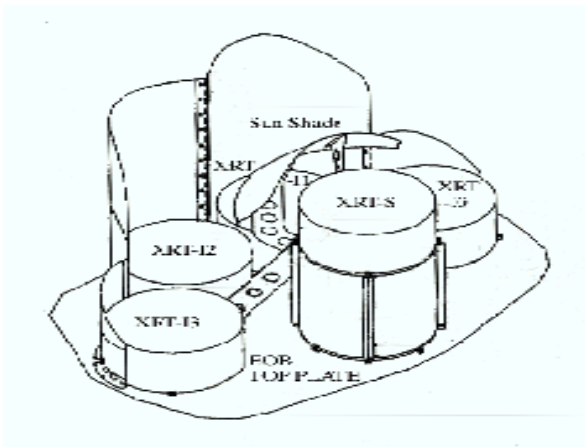

Figure A.4: Layout of the XRTs on the *Suzaku* spacecraft (Serlemitsos et al., 2007).

Four XRTs onboard *Suzaku* (XRT-I) are used for the XIS, and the other XRT (XRT-S) is for the XRS. The XRTs are arranged on the top plate of the Extensible Optical Bench (EOB) in the manner shown in figure A.4 The external dimensions of the 4 XRT-Is are the same (see table A.1, which also includes a comparison with the *ASCA* telescopes). The HPD of the XRTs range from 1'.8 to 2'.3, which is the diameter within half of the focused X-ray is enclosed. The angular resolution dose not significantly depend on the

Table A.1: Telescope dimensions and design parameters of XRT-I, compared with *ASCA* XRT.

	Suzaku	*ASCA*
Number of telescopes	4	4
Focal length	4.75 m	3.5 m
Inner diameter	118 mm	120 mm
Outer diameter	399 mm	345 mm
Height	279 mm	220 mm
Mass/Telescope	19.6 kg	9.8 kg
Number of nested shells	175	120
Reflectors/Telescope	1400	960
Geometric area/Telescope	873 cm^2	558 cm^2
Reflecting surface	Gold	Gold
Substrate material	Aluminum	Aluminum
Substrate thickness	155 μm	127 μm
Reflector slant height	101.6 mm	101.6 mm

energy of the incident X-ray in the energy range of *Suzaku* , 0.2–12 keV. The effective areas are typically 440 cm^2 at 1.5 keV and 250 cm^2 at 8 keV. The focal lengths are 4.75 m for the XRT-I. Individual XRT quadrants have their component focal lengths deviated from the design values by a few cm. The optical axis of the quadrants of each XRT are aligned within 2' from the mechanical axis. The field of view (the diameter for a half of the effective area) for XRT-Is is about 17' at 1.5 keV and 13' at 8 keV.

Basic Component of XRT

The *Suzaku* XRTs consist of closely nested thin-foil reflectors, reflecting X-ray at small grazing angles. An XRT is a cylindrical structure, having the following layered components: 1. a thermal shield at the entrance aperture to help maintain a uniform temperature; 2. a pre-collimator mounted on metal rings for stray light elimination; 3. a primary stage for the first X-ray reflection; 4. a secondary stage for the second X-ray reflection; 5. a base ring for structural integrity and interface with the EOB. All these components, expect the base rings, are constructed in 90° segments. Four of these quadrants are coupled together by interconnect-couples and also by the top and base rings (see figure A.5). The telescope housings are made of aluminum for an optimal strength to mass ratio. Including the alignment bars, collimating pieces, screws and washers, couplers, retaining plates, housing panels, and rings, each XRT-I consists of over 4112 mechanically separated parts. In total, nearly 7000 qualified reflectors were used and over 1 million cm^2 of gold surface was coated.

Reflectors

Each reflector consists of a substrate also made of aluminum and an epoxy layer that couples the reflecting gold surface to the substrate. The reflectors are nominally 178 μm in thickness. In shape, each reflector is a 90° segment of a section of a cone. The cone angle is designed to be the angle of on-axis incidence for the primary stage. They are

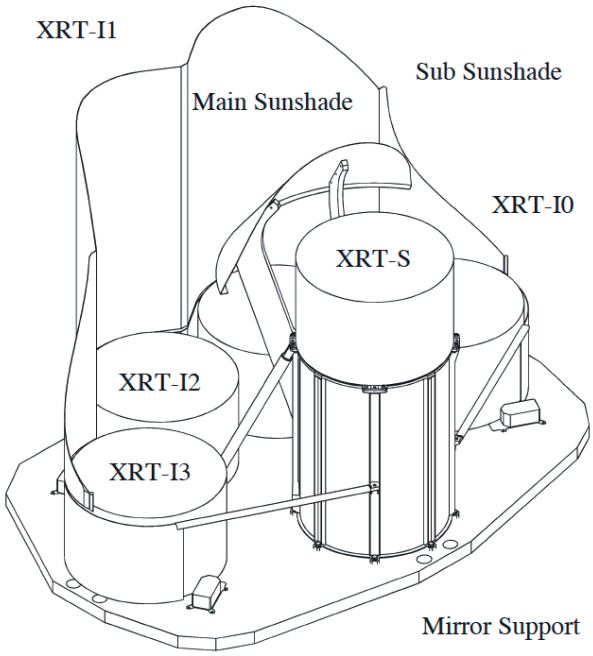

Figure A.5: A *Suzaku* X-ray Telescope Serlemitsos et al. (2007).

Table A.2: Design parameters for pre-colimator.

	XRT-I
Number of collimators	4
Height	32 mm
Blade substrate	aluminum
Blade thickness	120 μm
Blade height	22 mm
Height from blade top to reflector top	30 mm
Number of nested shells	175
Blade/Telescope	700
Mass/Collimator	2.7 kg

101.6 mm in slant length and with radii extending approximately from 60 mm at the inner part to 200 mm at the outer part. All reflectors are positioned with grooved alignment bars, which hold the foils at their circular edges. There are 13 alignment bars at each face of quadrant, separated at approximately 6.4° apart. In the *Suzaku* XRTs, the conical approximation of the Wolter-I type geometry is used. This approximation fundamentally limits the angle resolution achievable. More significantly, the combination of the figure error in the replication mandrels and the imperfection in the thermo-forming process (to about 4 micrometers in the low frequency components of the figure error in the axial direction) limits the angular resolution to about 1 arcmin (Misaki et al., 2004).

Pre-collimator

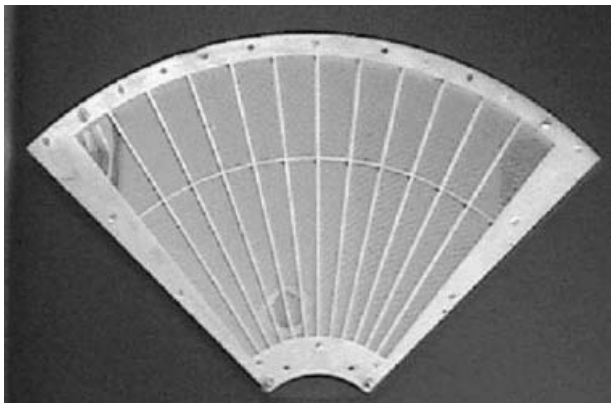

Figure A.6: A thermal shield. This picture was adapted from Serlemitsos et al. (2007).

The pre-collimator, which blocks off stray light that otherwise would enter the detector at a larger angle than intended, consists of concentrically nested aluminum foils similar to that of the reflector substrates (Mori et al., 2005). They are shorter, 22 mm in length, and thinner, 120 μm in thickness. They are positioned in a fashion similar to that of the reflectors, by 13 grooved aluminum plates at each circular edge of the pieces. They are installed on top of their respective primary reflectors along the axial direction. Due to their smaller thickness, they do not significantly reduce the entrance aperture in that direction more than the reflectors already do. Pre-collimator foils do not have reflective surfaces (neither front nor back). The relevant dimensions are listed in table A.2.

Thermal Shields

The *Suzaku* XRTs are designed to function in a thermal environment of 20±7.5 °C. The thermal shield (figure A.6) is mechanically sustained by a frame made of aluminum, with a thickness of 4 mm. The frame is 4 mm thick, has thirteen spokes which are along the alignment bars of the XRT. A stainless steel mesh with a wire pitch, width and thickness of 3 mm, 0.1 mm and 0.15 mm, respectively. Finally, polyethylene teleftalate (PET) film as thin as 0.24 μm, coated with aluminum layer with thickness of 30 nm on the surface oriented to the space, is adhered to the mesh with epoxy. The reflectors, due to its composite nature and thus its mismatch in coefficients of thermal expansion, suffer from thermal distortion that degrades the angular resolution of the telescopes in temperature outside this range. Thermal gradient also distorts the telescope in a larger scale. Even though sun shields and other heating elements on the spacecraft help in maintaining a reasonable thermal environment, thermal shields are integrated on top of the pre-collimator stage to provide the needed thermal control. **Focal Positions and Angular Resolutions**

Verification of the imaging capability of the XRTs has been made with the data of SS Cyg in quiescence taken during 2005 November 2 01:02UT-23:39UT. Total exposure time was 41.3 ks. CC Cyg is selected for this purpose because it is a point source and moderately bright (3.5, 5.9, 3.7 and 3.5 $\mathrm{c\,s^{-1}}$ for XIS0 through XIS3), and hence, it is needless to care about pile-up even at the image core. Figure A.7 shows the images and the point-spread functions (PSFs) of the all the XRT-I+XIS modules. The HPD is obtained to be 1'.8, 2'.3, 2'.0 and 2'.0 for XRT-I0, 1, 2 and 3, respectively. These values are in

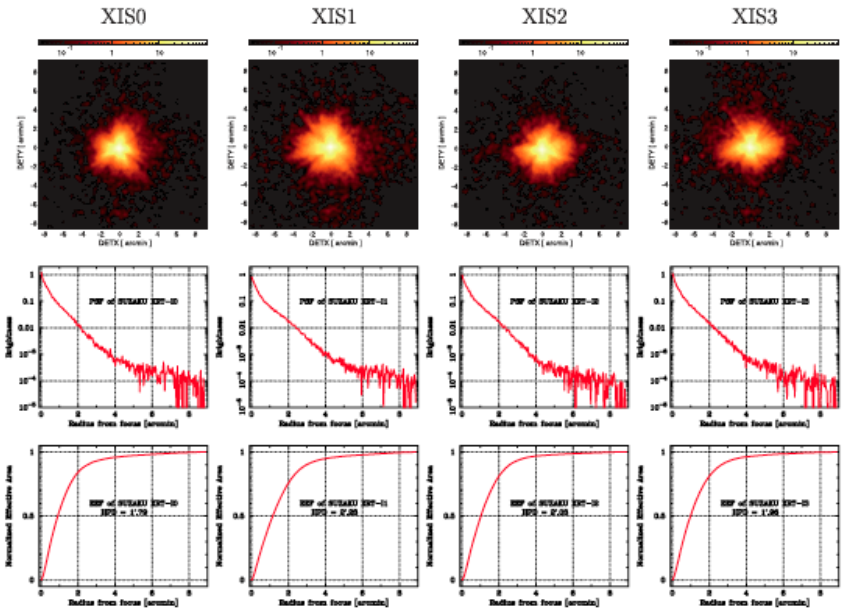

Figure A.7: Top to bottom; Image, Point-Spread Function (PSF), and EEF of the four XRT-I modules in the focal plane Serlemitsos et al. (2007). All the images are binned with 2×2 pixels followed by being smoothed with a Gaussian with a sigma of 3 pixels, where the pixel size is 24 μm. The EEF is normalized to unity at the edge of the CCD chips (a square of 17'.8 on a side). With this normalization, the HPD of the XRT-I0 thorough I3 is 1'.8, 2'.3, 2'.0 and 2'.0, respectively.

general consistent with those expected from ground-based calibration measurements.

Optical Axes, Effective Area and Vignetting Functions

A series of offset observations of the Crab observations were carried out in August and September 2005 at carious off-axis angles of 0', 3'.5 and 7'. The intensity of the Crab nebula is evaluated for each pointing and for each XIS module separately. By finding the maximum throughput angle, we also have obtained a direction of the optical axis of each telescope. The result is shown in figure A.8. The optical axes locate roughly within 1' from the XIS aim point. This implies that the efficiency of all the XRT-Is is more than 97 % even at 10 keV when we observe a point source on the XIS aim point. The vignetting curves calculated by the ray-tracing simulator are compared with the observed intensities of the Crab Nebula at carious off-axis angles in figure A.9. These figures roughly show that effective area is calibrated to within ∼10% over the XIS field of view. We expect most of these deviations can be attributed to scattering of the optical axis orientations of the four quadrants within a telescope.

Stray Light

In-flight stray-light observations were carried out with the Crab Nebula at off-axis angles of 20' (4 pointings), 50' (4 pointings) and 120' (4 pointings) in August and September. Figure A.10 shows an example of 20'-off image of XRT-I3 together with simulation results of the same off-axis angle for the cases with and without pre-collimator. It is seen that the pre-collimator works for reducing the stray light in orbit.

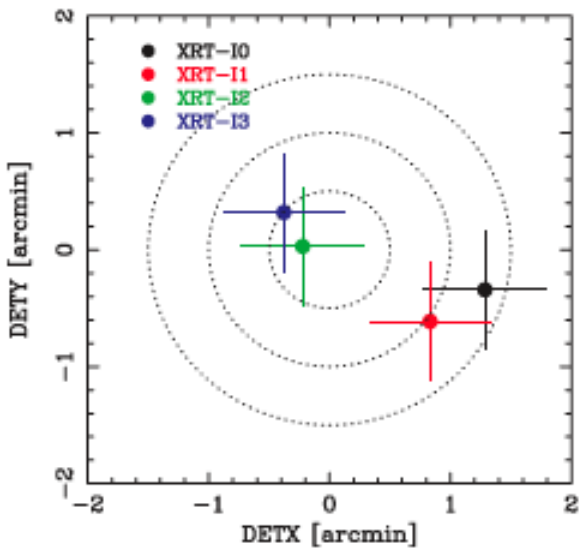

Figure A.8: Locations of the optical axis of each XRT-I module in the focal plane determined from the observations of the Crab Nebula in 2005 August-Septermber. This figure implies that the image on each XIS detector becomes brightest when a target star is placed at the position of the corresponding cross. The dotted circles are drawn every 30" in radius from the XIS-default position. This figure was adapted from Serlemitsos et al. (2007).

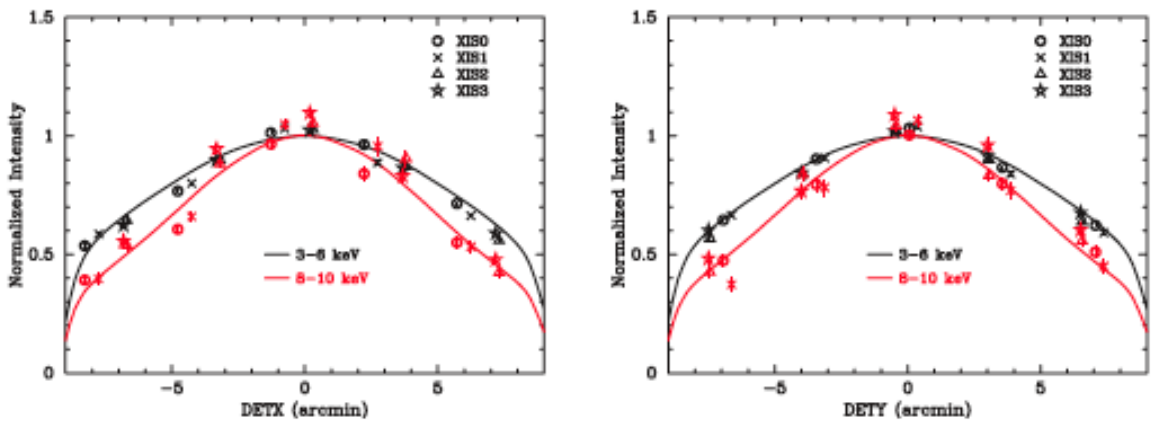

Figure A.9: Vignetting of the four XRT-I modules using the data of the Crab Nebula taken during 2005 August 22–27 in the two energy bands 3–6 keV and 8–10 keV. The model curves are calculated with the ray-tracing simulator with the spectral parameters of $N_{\rm H} = 0.33 \times 10^{22}$ cm^{-2}, photon index = 2.09, and the normalization = 9.845 photons cm^{-2} s^{-1} keV^{-1} at 1 keV. Note that the abrupt drop of the model curves at ∼8' is due to the source approaching the detector edge. The excess of the data points of XIS1 is probably due to insufficient calibration of the BI CCD. This figure was adapted from Serlemitsos et al. (2007).

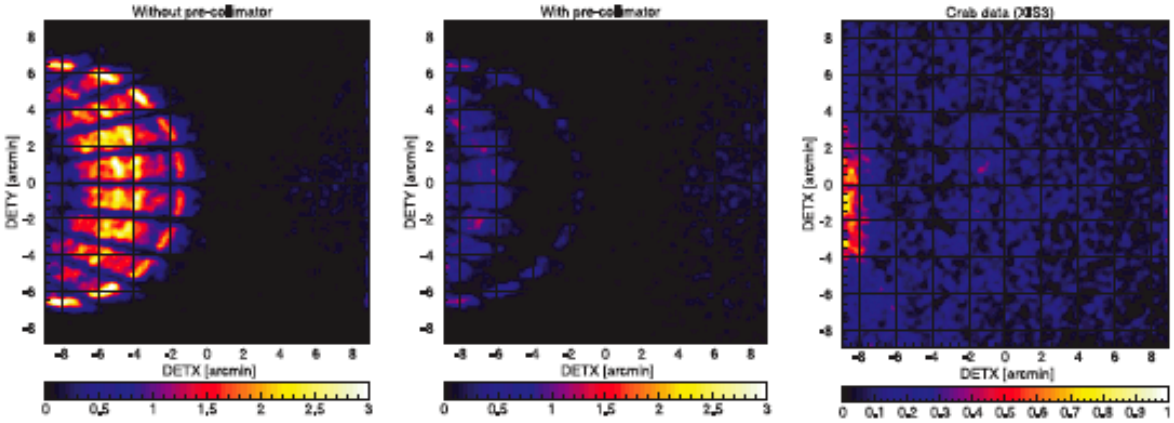

Figure A.10: Focal plane images formed by stray light (Serlemitsos et al., 2007). The left and middle panels show simulated images of a monochromatic point-like source of 4.51 keV locating at (DETX, DETY) = (-20', 0') in the cases of without and with the pre-collimator, respectively. The radial dark lanes are the shades of the alignment bars. The right panels is the in-flight stray image of the Crab Nebula in the 2.5–5.5 keV band located at the same off-axis angle. The unit of the color scale of this panel is counts per 16 pixels over the entire exposure time of ∼8.4 ks. the counting rate from the whole image is 0.78±0.01 $\mathrm{c\,s^{-1}}$ including background. Note that the intensity of the Crab Nebula measured with XIS3 at the XIS-default position is 458±3 $\mathrm{c\,s^{-1}}$ in the same 2.5–5.5 keV band. All the images are binned with 4×4 pixels followed by being smoothed with a Gaussian with a sigma of 2 pixels, where the pixel size is 24 μm.

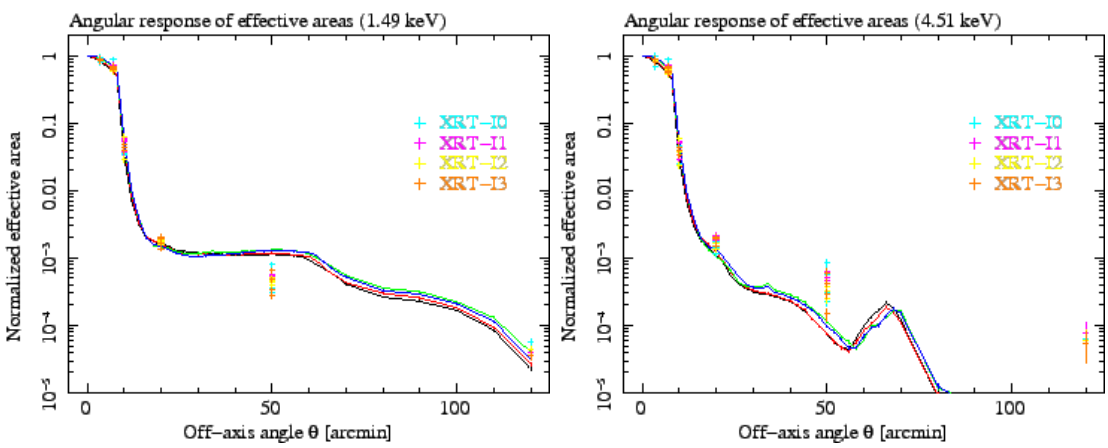

Figure A.11: Angular responses of the XRT-I at 1.5 (left) and 4.5 keV (right) up to 2 degrees (see *Suzaku* technical description). The effective area is normalized at on-axis. The integration ares is corresponding to the detector size of XIS (17'.8×17'.8). The three solid lines in the plots correspond to different parameters of ray-tracing program while the crosses are the normalized effective area using the Crab pointings.

Figure A.11 shows angular responses of the XRT-I at 1.5 and 4.5 keV up to 2 degrees. The effective area is normalized at on-axis. The integration area is corresponding to the detector size of XIS (17'.8×17'.8). The plots are necessary to plan observations of diffuse sources or faint emissions near bright sources, such as outskirts of cluster of galaxies.

The three solid lines in the plot correspond to different parameters of ray-tracing program while the crosses are the normalized effective area using the Crab pointings. For example, the effective area of the stray light at 1.5 keV is $\sim 10^{-3}$ at angles smaller than 70 arcmin off axis and $< 10^{-3}$ at angles larger than 70 arcmin off. The measured flux of stray lights are in good agreement with that of raytracing within an order.

A.1.2 X-ray Imaging Spectrometer (XIS)

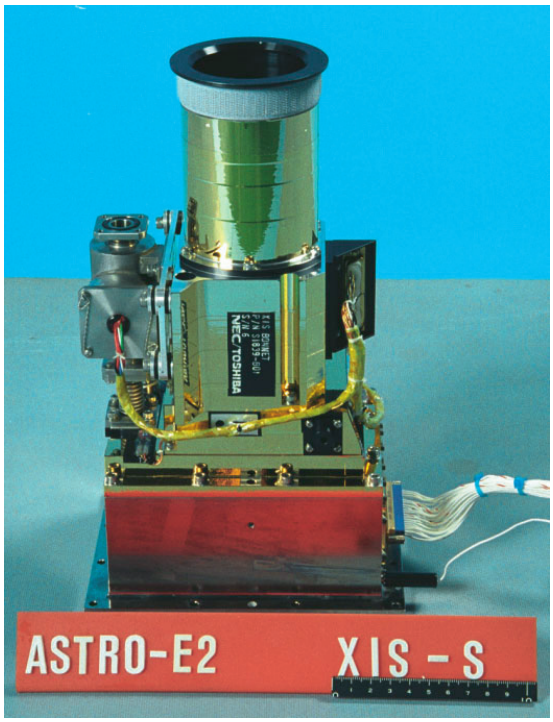

Figure A.12: The XIS detector before installation onto *Suzaku*. This picture was adapted from Koyama et al. (2007).

Suzaku has four X-ray Imaging Spectrometers (XIS), which are shown in figure A.12. These employ X-ray sensitive silicon charge-coupled devises (CCDs), which are operated in a photon-counting mode, similar to that used in the *ASCA* SIS, *Chandra*/ACIS, and *XMM-Newton* EPIC. In general, X-ray CCDs operate by converting an incident X-ray photon into a charge cloud, with the magnitude of charge proportional to the energy of the absorbed X-ray. This charge is then shifted out onto the gate of an output transistor via an application of time-varying electrical potential. This results in a voltage level (often referred to as "pulse hight") proportional to the energy of the X-ray photon.

The XIS has been partially developed at MIT (CCD sensors, analog electronics, thermo-electric coolers, and temperature control electronics), while the digital electronics

and a part of the sensor housing were developed in Japan, jointly by Kyoto University, Osaka University, Rikkyo University, Ehime University and ISAS/JAXA.

A CCD has a gate structure on one surface to transfer the charge packets to the readout gate. The surface of the chip with the gate structure is called the "front side". A front-side illuminated CCD (FI CCD) detects X-ray photons that pass through its gate structures, i.e. from the front side. Because of the additional photo-electric absorption at the gate structure, the low-energy quantum detection efficiency (QDE) of the FI CCD is rather limited. Conversely, a back-side illuminated CCD (BI CCD) receives photons from "back", or the side without the gate structure. For this purpose, the undepleted layer of the CCD is completely removed in the BI CCD, and a thin layer to enhance the electron collection efficiency is added in the back surface. A BI CCD retains a high QDE even in sub-keV energy band because of the absence of gate structure on the photon-detection side. However, a BI CCD tends to have a slightly thinner depletion layer, and the QDE is therefore slightly lower in the high energy band. The decision to use only one BI CCD and three FI CCDs was made because of both the slight additional risk involved in the new technology BI CCDs and the need to balance the overall efficiency for both low and high energy photons.

To minimize the thermal noise, the sensors need to be kept at ~ -90 °C during observations. This is accomplished by thermo-electric coolers (TECs), controlled by TEC Control Electronics, or TCE. The Analog Electronics (AE) drives the CCD clocks, reads and amplifies the data from the CCDs, performs the analog-to-digital conversion, and toutes the signals to the Digital Electronics (DE). The AE and TCE are located in the same housing, and together, they are called the AE/TCE23 for XIS2 and 3. The digital electronics system for the XISs consists of two Pixel Processing Units (PPU) and one Main Processing Unit (MPU); PPU01 is associated with AE/TCE01, and PPU23 is associated with AE/TCE23. The PPUs receive the raw data from AE, carry out event detection, and send event data to the MPU. The MPU edits and packets the event data, and sends them to the satellite main digital processor.

To reduce contamination of the X-ray signal by optical and UV light, each XIS has as Optical Blocking Filter (OBF) located in front of it. The OBF is made of polyimide with a thickness of 1200 Å of aluminum (400 Å on one side and 800 Å on the other side). To facilitate the in-flight calibration of the XISs, each CCD sensor has two ^{55}Fe calibration sources. One is installed on the door on illuminate the whole chip, while the other is located on the side wall of the housing and is collimated in order to illuminate two corners of the CCD. The door-mounted source was used for initial calibration only; once the door is opened, it dosel not illuminate the CCD. The collimated source can easily be seen in two corners of each CCD. A small number of these X-rays scatter onto the entire CCD. In addition to the emission lines created by these sources, we can utilize a new feature of the XIS CCDs, "charge injection capability", to assist with calibration. This allows an arbitrary amount of charge to be input to the pixels at the top row of the imaging region (exposure area), i.e. the far side from the frame-store region. The charge injection capability may be used to measure the CTI (charge transfer inefficiency) of each column, or even to reduce the CTI. How the charge injection capability will be used is still in progress as of this writing.

Pulse Height Determination, Residual Dark-current Distribution, and Hot Pixels

When a CCD pixel absorbs an X-ray photon, the X-ray is converted to an electric charge, which in turn produces a voltage at the analog output of the CCD. This voltage ("pulse-height") is proportional to the energy of the incident X-ray. In order to determine the true pulse-height corresponding to the input X-ray energy, it is necessary to subtracted the *Dark Levels* and correct possible *optical Light Leaks*.

Dark Levels are non-zero pixel pulse-heights caused by leakage currents in the CCD. In addition, optical and UV light may enter the sensor due to imperfect shielding ("light leak"), producing pulse heights that are not related to X-rays. In the case of the *ASCA* SIS, these were handled via a signal mechanism: Dark Levels of 16×16 pixels were sampled and their (truncated) average was calculated for every exposure. Then the same average Dark Level was used to determine the pulse-height of each pixel in the sample. After the launch of *ASCA*, it was found that the Dark Levels of different pixels were actually different, and their distribution around the average did not necessarily follow a Gaussian. The non-Gaussian distribution evolved with time (referred to as Residual Dark-current Distribution or RDD), and resulted in a degradation of the energy resolution due to incorrect Dark Levels.

For the *Suzaku* XIS, Dark Levels and Light Leaks are calculated separately in normal mode. Dark Levels are defined for each pixel; those are expected to be constant for a given observation. The PPU calculates the Dark Levels in the Dark Initial mode (one of the special diagnostic modes of the XIS); those are stored in the Dark Level RAM. The average Dark Level is determined for each pixel, and if the dark level is higher than the hot-pixel threshold, this pixel is labeled as a *hot pixel*. Dark Levels can be update by the Dark Update mode, and sent to the telemetry by the Dark Frame mode. Unlink the case of *ASCA*, Dark Levels are not determined for every exposure, but the same Dark Levels are used for many exposures unless they are initialized or updated. Analysis of the *ASCA* data showed that Dark Levels tend to change mostly during the SAA passage of the satellite. Dark Update mode may be employed several times a day after the SAA passage.

Hot pixels are pixels which always output over threshold pulse-heights even without input signals. Hot pixels are not usable for observation, and their output has to be disregarded during scientific analysis. The *ASCA* SIS did not identify hot pixels on-board, and all the hot pixel data were telemetered and removed during the data analysis procedure. The number of hot pixels increased with time, and eventually occupied significant parts of the telemetry. In the case of XIS, hot pixels are detected on-board by the Dark Initial/Update mode, and their positions and pulse-heights are stored in the Hot-pixel RAM and sent to the telemetry. Thus, hot pixels can be recognized on-board, and they are excluded from the event detection processes. It is also possible to specify the hot pixels manually. There are, however, some pixels which output over threshold pulse-heights intermittently. Such pixels are called flickering pixels. It is difficult to identify and remove the flickering pixels on board; they are inevitably output to the telemetry and need to be removed during the ground processing. Flickering pixels sometimes cluster around specific columns, which makes it relatively easy to identify.

The Light Leaks are calculated on board with the pulse height data after the subtraction of the Dark Levels. A truncated average is calculated for 64×64 pixels (this size may be changed in the future) in every exposure and its running average produces the Light Leak. Thus, the Light Leak is basically the same as the Dark Level in *ASCA* XIS. The Dark Levels and the Light Leaks are merged in the parallel-sum (P-sum) mode, so

Dark Update mode is not available in P-Sum mode. The Dark Levels, which are defined for each pixel as the case of the normal mode, are update every exposure. It may be considered that the Light Leak is defined for each pixel in P-Sum mode.

On-board Event Analysis

The main purpose of the on-board processing of the CCD data is to reduce the total amount transmitted to ground. For this purpose, the PPU searches for a characteristic pattern of charge distribution (called an event) in the pre-processed (post-Dark Levels and Light Leaks subtraction) frame data. When an X-ray photon is absorbed in a pixel the photoionized electrons can spread into at most four adjacent pixels. An event is recognized when a valid pulse-heights in the eight adjacent pixels (e.g. it is the peak value in the 3×3 pixel grid). The coordinated of the central pixel are considered the location of the event. Pulse-height data for the adjacent 5×5 square pixels are sent to the Event RAM as well as the pixel location.

The MPU reads the Event RAM and edits the data to the telemetry format. The amount of information sent to telemetry depends on the editing mode of the XIS. All the editing modes (in normal mode) are designed to send the pulse heights of at least 4 central pixels of an event to the telemetry, because the charge cloud produced by an X-ray photon can spread at most 4 pixels. Information of the surrounding pixels may or may not output to the telemetry depending on the editing mode. The 5×5 mode outputs the most detailed information to the telemetry, i.e. all 25 pulse-heights from the 5×5 pixels containing the event. The size of the telemetry data per event is reduced by a factor of 2 in 3×3 mode.

Photon pile-up

The XIS is essentially a position-sensitive integrating instrument, with the nominal interval between readouts of 8 s. If more then one photon strike the same CCD pixel, or one of its immediate neighbors during the integration time, these cannot be correctly detected as independent photons: this is the phenomenon of photon pile-up. Here, the modest angular resolution of the *Suzaku* XRT is an advantage: the central 3×3 pixel area receives 2% of the total counts of a point source, and ∼10% of the counts fall within ∼0.15 arcmin of the image center. We calculated the count rate at which 50% of the events within the central 3×3 pixels are piled-up (the pile-up fraction goes down as we move out of the image center; this fraction is $< 5\%$ for the 0.15 arcmin radius)–although we offer no formal justification for this particular limit, this is compatible with our *ASCA* SIS experience (i.e., at this level, the pile-up effects do not dominate the systematic uncertainties).

XIS background rate

All four XISs have low background level, due to a combination of the low *Suzaku* orbit and the instrument design. Below 1 keV, the high sensitivity and energy resolution of the XIS1 combined with this low background means that *Suzaku* is the superior instrument for observing soft sources with low surface brightness. At the same time, the large effective area at Fe K (comparable to the XMM pn) combined with this low background make *Suzaku* a powerful tool for investigation hot and/or high energy sources as well.

In the XIS, the background originates from the cosmic X-ray background (CXB) combined with charged particles (the non-X-ray background, or NXB). Currently, flickering

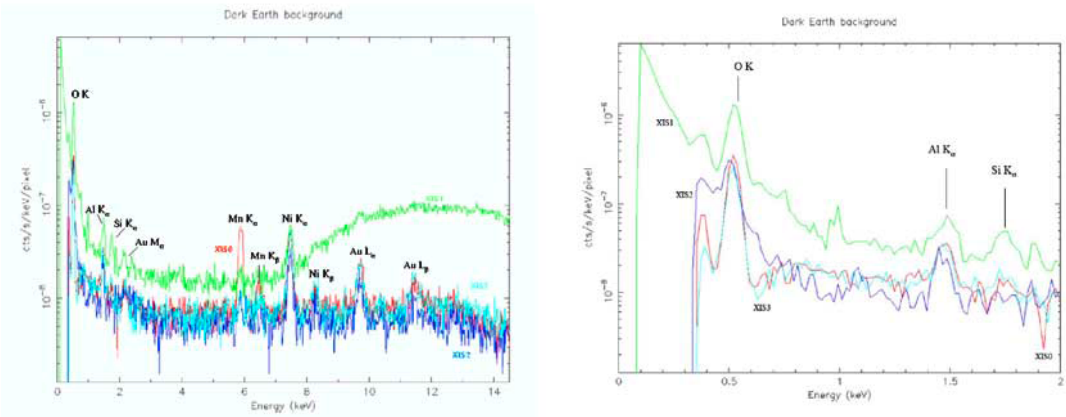

Figure A.13: Left: The XIS background rate for each of the four XIS detectors, with prominent fluorescent lines marked. These spectra are based on ∼110–160 ksec of observations towards the dark Earth. These spectra dose not included Cosmic X-ray background (CXB). Right: The XIS background rate for each of the four XIS detectors, showing only energies between 0.1–2.0 keV. Below 0.3 keV the background rate for the FI chips cannot be determined due to their low effective area.

Table A.3: Major XIS Background Emission Lines.

Line	Energy	XIS-S0	XIS-S1	XIS-S2	XIS-S3
	keV		10^{-9}c/s/pixel		
O-K	0.5249	18.5±0.5	$69.3^{+2.7}_{-2.6}$	$14.3^{+1.5}_{-1.3}$	$14.1^{+1.1}_{-1.2}$
Al-K	1.846	1.98±0.23	3.01±0.51	$1.50^{+0.31}_{-0.28}$	$1.57^{+0.25}_{-0.23}$
Si-K	2.307	$0.299^{+0.2080}_{-0.2074}$	2.21±0.45	0.0644(< 0.282)	$0.543^{+0.212}_{-0.213}$
Au-M	2.1229	0.581±0.234	$1.13^{+0.280}_{-0.291}$	$0.359^{+0.211}_{-0.212}$	$6.69^{+2.91}_{-2.90}$
Mn-Kα	5.898	$8.35^{+0.36}_{-0.34}$	0.648±0.289	$0.299^{+0.209}_{-0.2086}$	$0.394^{+0.181}_{-0.18}$
Mn-Kβ	6.490	$1.03^{+0.22}_{-0.216}$	0.294(<0.649)	0.00(<0.111)	$0.428^{+0.225}_{-0.226}$
Ni-Kα	7.470	7.20±0.31	6.24±0.53	$3.78^{+0.26}_{-0.25}$	$7.13^{+0.36}_{-0.37}$
Ni-Kβ	8.265	0.583±0.183	$1.15^{+0.5}_{-0.489}$	0.622±0.206	$0.983^{+0.247}_{-0.249}$
Au-Lα	9.671	$3.53^{+0.27}_{-0.28}$	$3.28^{+1.16}_{-0.99}$	$1.88^{+0.31}_{-0.28}$	$3.54^{+0.36}_{-0.35}$
Au-Lβ	11.514	$2.25^{+0.78}_{-0.59}$	2.91±1.29	$0.752^{+0.428}_{-0.340}$	$2.67^{+0.61}_{-0.53}$

pixels are a negligible component of the background. In the dark data (i.e., the NXB), the background rate between 1–12 keV in is 0.11 $\mathrm{c\,s^{-1}}$ in the FI CCDs and 0.40 $\mathrm{c\,s^{-1}}$ in the BI CCD (see figure A.13: left). Note that these are the fluxes after the grade selection is applied with only grade 0, 2, 3, 4 and 6 selected (see below). There are also fluorescence features arising from the calibration source as well as material in the XIS and XRTs. The Mn lines are due to the scattered X-ray from the calibration sources. As shown in table A.3 the Mn lines are almost negligible expect for XIS0. The O lines are mostly contamination from the day earth (see below). The other lines are fluorescent lines from the material used for the sensor. Table A.3 shows the current best estimated for the strength of these emission features, along with their 90% upper and lower limits.

The background rate on the FI chips (including all the grades) is normally less than

400 counts/frame (50 $c\dot{s}^{-1}$) when no class discriminator is applied. On the BI chip, the rate is normally less than 150 counts/frame (18.75 $c\,s^{-1}$). The background rate on the FI chips is expected reduce significantly when the class discriminator is applied. But little change is anticipated for the BI chip. Since 5×5, 3×3, and 2×2 modes require on average 40, 20, and 10 bytes per event, the minimum telemetry required for any source is ∼58 kbits/s for 5×5 mode, ∼31 kbits/s for 3×3, and ∼17 kbit/s for 2×2 mode, if no class discriminator is used.

Out-of-time events

X-ray photons detected during the frame-store transfer do not correspond to the true image, but instead appear as a streak or blur in the readout direction. These events are called out-of-time events, and they are an intrinsic feature of CCD detectors. Similar streaks are seen from bright sources observed with *Chandra* and *XMM-Newton*. Out-of-time events produce a tail in the image, which can be an obstacle to detecting a low surface brightness feature in an image around a bright source. Thus the out-of-time events reduce the dynamic range of the detector. Since XIS spends 25 ms n the frame-store transfer, about 0.3% (= 0.025/8×100) of all events will be out-of-time events. However, because the orientation of the CCD chip is different among the sensors, one can in principle distinguish a true feature of low surface brightness and the artifact due to the out-of-time events by comparing the images from two or more XISs.

Day Earth Contamination

When the XIS filed of view is close to the day earth (i.e., Sun lit Earth), fluorescent lines from the atmosphere contamination low-energy part of the XIS data, especially in the BI chip. Most prominent is the oxygen line, but the nitrogen line may be also noticed (figure A.13). These lines are mostly removed when we apply the standard data screening criteria (cutting data during that XIS FOV is at least 20 degree away from the day earth) in the ground processing. However, small amount of contamination can remain. This contamination may be further reduced if we subtract appropriate background. This subtraction, however, may be imperfect. Thus, when neutral oxygen or nitrogen lines are detected in the XIS data, contamination from the day earth should be suspected.

Radiation Damage and On-board Calibration of the XIS

The performance of X-ray CCDs gradually degrades in the space environment due to the radiation damage. This generally causes an increase in the dark current and a decrease of the charge transfer efficiency (CTE). In the case of XIS, the increase of the dark current is expected to be small due to the low (−90°C) operating temperature of the CCD. However, a decrease in CTE is unavoidable. Thus, continuous calibration of CCD an orbit is essential to the good performance of the XIS. For this purpose, we use a radio isotope source and charge injection as explained below:
(i) Each XIS carries ^{55}Fe calibration sources near the two corners of the chip, which is used to monitor the instrument gain.
(ii) Each XIS CCD is equipped with charge injection capability, which is useful to measure and even suppress CTI (charge transfer inefficiency, which leads to a degradation of the energy resolution)

Nonetheless, it is difficult to predict based on existing data how well we can calibrate the long-term performance change of XIS on orbit.

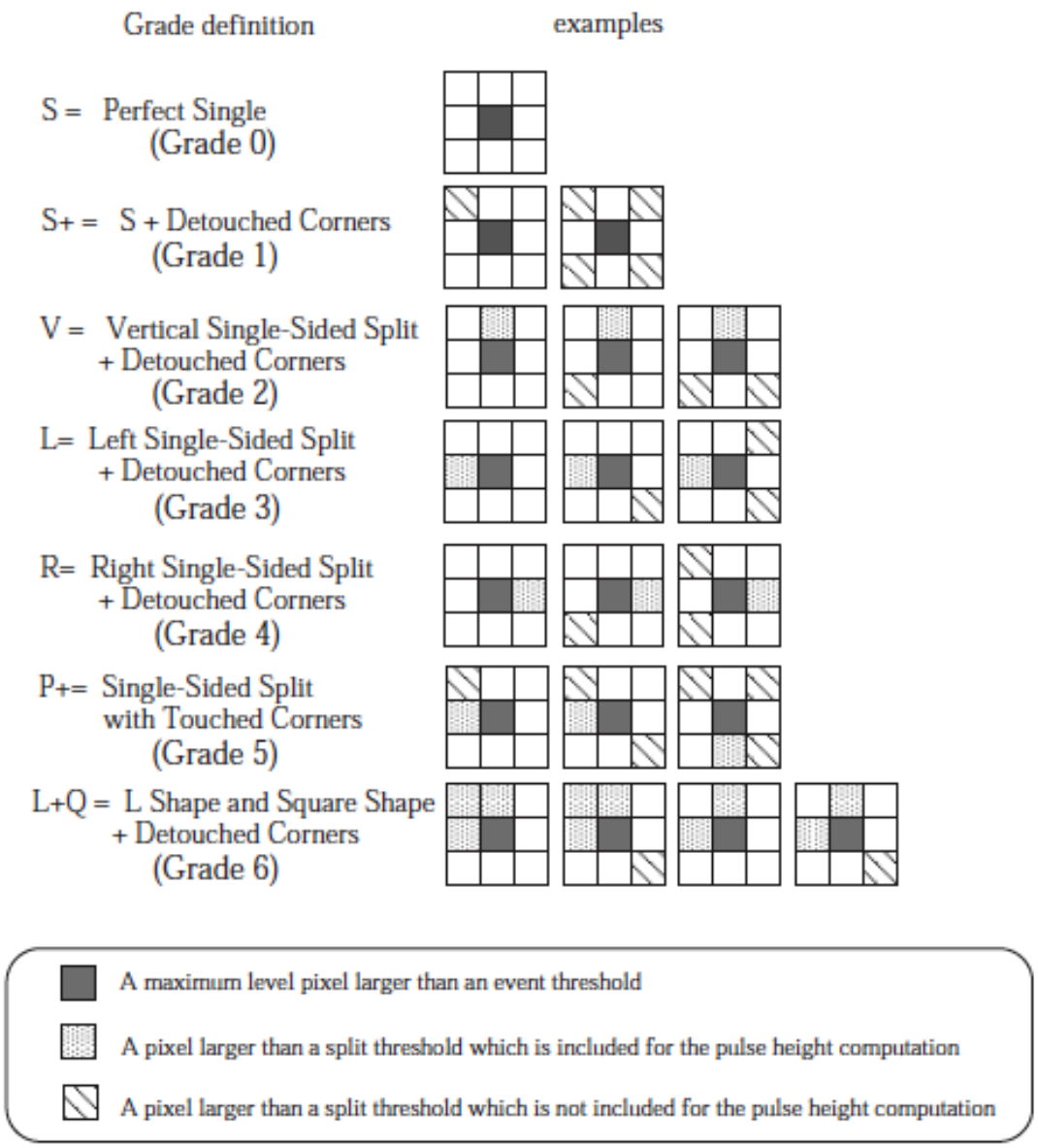

Figure A.14: Definition of GRADE of CCD events.

On-ground event selection

Internal (non X-ray) background events can be efficiency removed using the pattern on CCD pixels (GRADE), the position (STATUS) and time of an event. The definition of FRADE is shown in figure A.14. Most of X-ray events take GRADE = 0, 2, 3, 4, or 6. On the other hand, most of the events of other GRADEs are dominated by non X-ray events, and should be excluded. STUTAS parameter stores the pixels on the segment boundaries can be removed by selecting the events with STATUS<121072. The parameters used in good time interval (GTI) selection are shown in table A.4. The signal to noise ratio can be improved with an appropriate GTI criteria, indicated in table A.4.

Table A.4: Parameters used in GTI selection of *Suzaku*

Parameter	Definition	Recommended value to use
SAA	Whether the satellite was in the SAA or not	eq.0
T_SAA	Time after the last SAA duration (s)	>255
ELV	Elevation angle from the Earth limb (degree)	>5
DYE_ELV	Elevation angle from the day Earth limb (degree)	>20
COR	Cut off rigidity of the cosmic ray (GeV/c/particle)	>8

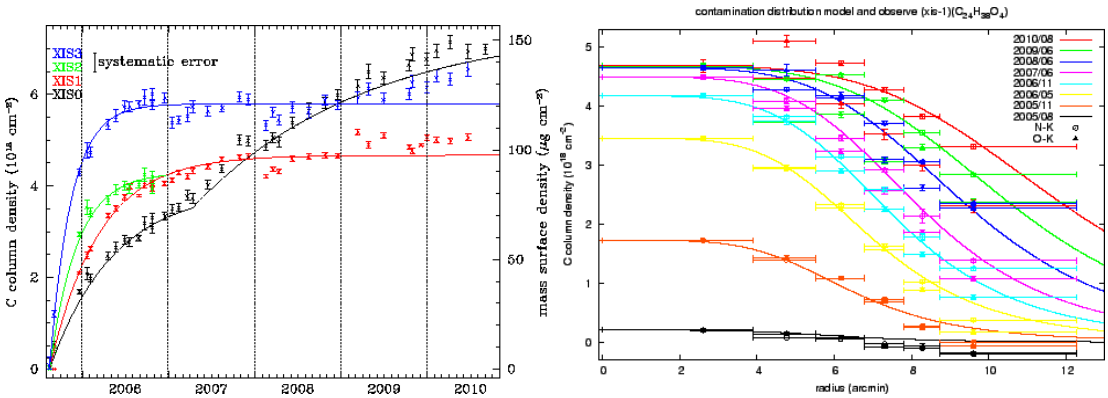

Figure A.15: Left: The time history of the contamination of all four XIS detectors, measured at the center of the OBF. Right: The radial profile of the contamination of the BI chip.

Contamination correction

The OBF has been gradually contaminated in time by out-gassing from the satellite. The contamination rate after the XIS door-open is unexpectedly high, and the rate is different from sensor to sensor. Moreover, the thickness of the contamination varies with position on the OBF.

The contamination has caused a significant reduction in low-energy response since launch. We therefore need to include additional, time-varing low energy absorption in the response function. This is given as a function of both the observation data after the XIS door-open, and of detector coordinates (specifying the position on the OBF). For this purpose, we measured the on-axis extra absorption by observing a SNR 1E0102-72 and an isolated neutron star RX J1856.5-3754. At the time of writing, we have not conclusively determined the chemical composition for the contamination material(s). From the overall spectral shape in the low energy absorption for all the available X-ray sources and the best guess for the out-gassing source in *Suzaku*, we assume that the contamination contains predominantly C and O with the number ratio C/O = 6. Figure A.15 shows the time histories of the contamination accumulated on the OBF. Empirically, the time dependence of the contamination thickness is assumed to follow the exponential form as; $N_{\rm c} = a - b \times \exp -day/c$, where $N_{\rm c}$ is the carbon column density in units of 10^{18} cm^{-6} (C/O = 6). To measure the off-axis absorption, we used diffuse X-ray from the bright Earth rim and the Cygnus Loop. The former emits characteristic K lines of $N_{\rm I}$ and $O_{\rm I}$ (neutral atoms) and

the latter provides K lines from C_{VI}, N_{VII}, O_{VII} and C_{VIII} (He-like or H-like atoms). Since the former can be observed frequently, we trace the time history of on-axis absorption over successive one month periods after the XIS door-open (13 August, 2005). With the two reasonable assumptions that (1) the N:O line ratio is uniform over the filed of view and (2) the contamination is azimuthal constant, we can derive the radial profiles of the column density. This radial profile is approximated by a function of $\frac{1}{[1+\{\frac{r}{a(t)}\}^{b(t)}]}$. The time dependent parameters, $a(t)$ and $b(t)$ are determined and update regularly.

A.2 *XMM-Newton* Satellite

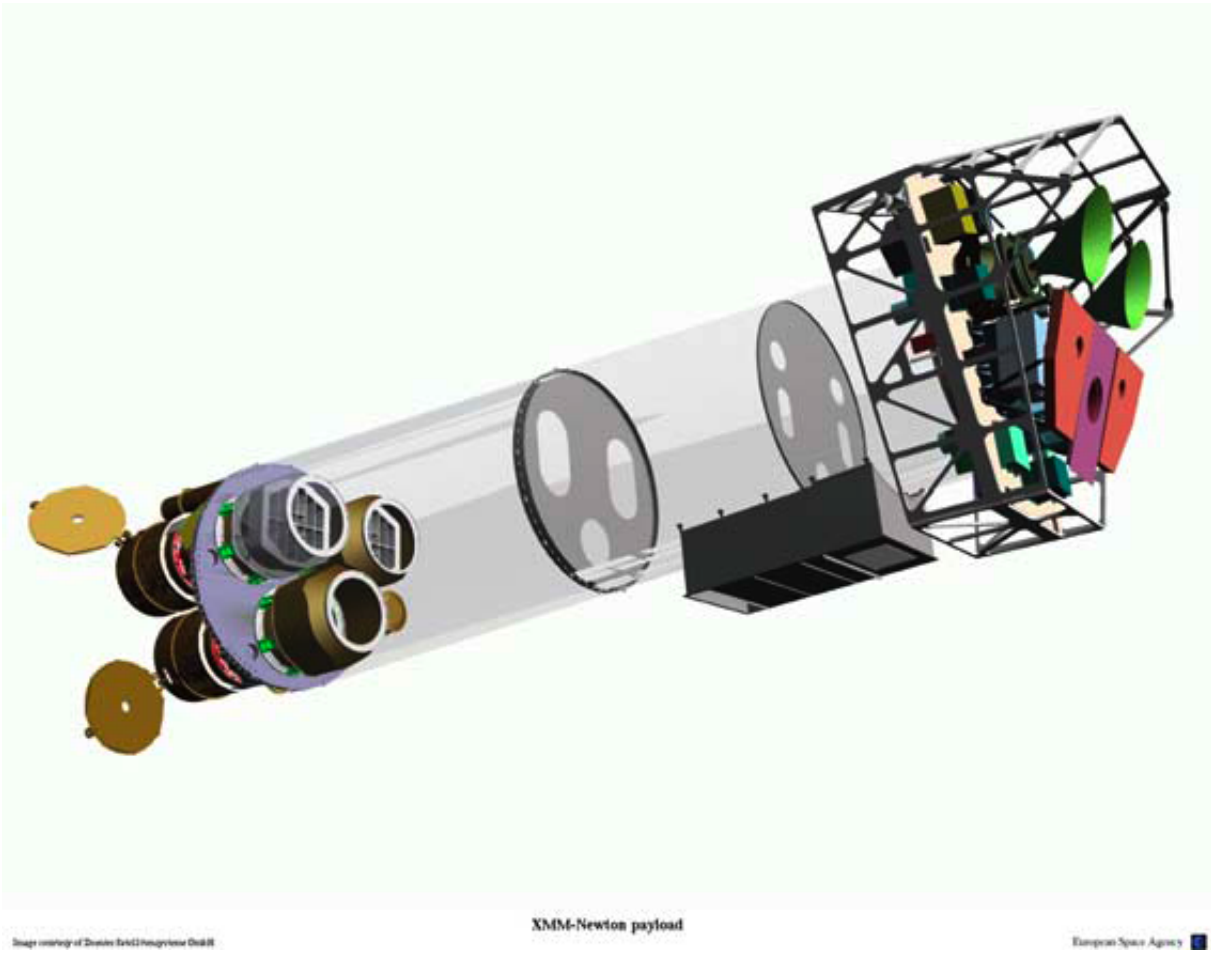

Figure A.16: Sketch of the *XMM-Newton* payload. The mirror modules, two of which are equipped with Reflecting Grazing Arrays, are visible at the lower left. At the right end of the assembly, the focal X-ray instruments are shown: The EPIC MOS cameras with their radiators (black:green horns), the radiator of the EPIC pn camera (violet) and those of the (light blue) RGS detectors (in pink). The OM telescope is obscured by lower mirror module.

The ESA (European Space Agency) X-ray satellite *XMM-Newton* was launched on 10 December 1999 from Kourou (French Guiana), by the Ariane-V rocket (Jansen et al.,

2001). It was placed into a highly eccentric orbit, with an apogee of about 115,000 km, a perigee of about 6,000 km, and an orbital inclination of 33°, which provides the best visibility in the southern celestial sky. Although the orbital period 48 hours, the exposure available for scientific data analysis is limited to 39 hours (140 ksec) per orbit. This is because observations are not carried out when the satellite altitude is less than 46,000 km, where the radiation background related to the Earth's magnetosphere is severe. *XMM-Newton* provides the following three type of science instrument; European Photon Imaging Camera (EPIC), Reflection Grating Spectrometer (RGS) and Optical Monitor (OM). The three EPIC cameras; the two different types of CCD camera, MOS and pn, and the two detectors of the RGS spectrometers reside in the focal planes of the X-ray telescopes, while the OM has its own telescope. A sketch of *XMM-Newton* payload is displayed in figure A.16.

There are in total six science instruments on board *XMM-Newton*, which are operated simultaneously. The instruments can be operated independently and each in different modes of data acquisition.

In the following sections, we described the X-ray telescopes and EIPC cameras, because we mainly use these instruments in our study. We summarize the basic performance of the EPIC cameras in table A.5.

Table A.5: Basic performance of the EPIC detectors

	EPIC-MOS	EPIC-pn
Illumination method	Front illuminated	Back illuminated
Pixel size	40 μm	150 μm
	1."1	4."1
Field of View (FOV)	30'	30'
PSF (FWHM/HEM)	5"/14"	6"/15"
Spectral resolution	∼70 eV	∼80 eV
Timing resolution	1.5 ms	0.03 ms
Bandpass	0.15–12 keV	0.15–15 eV

A.2.1 X-ray Telescopes

Contamination correction

XMM-Newton's three XRTs are co-aligned with an accuracy of better than about 1 arcmin. Each of the three telescopes consists of 58 Wolter type-I mirrors, and the mirror grazing incidence angles range between 17 and 42 arcmin. The focal length is 7.5 m and the diameter of the largest mirrors is 70 cm. One telescope with the pn camera at the focal point has a light path as shown figure A.17. The two others have grating assemblies in their light paths, diffracting part of the incoming radiation onto their secondary focus (see figure A.18). About 44 % of the incoming light focused by the XRT is directed onto the MOS camera at the prime focus, while 40 % of the radiation is dispersed by a grating array onto a linear strip of CCDs. The remaining light is absorbed by the support structures of the RGAs.

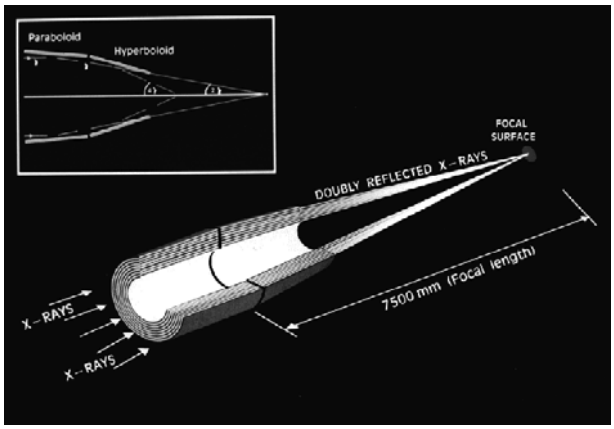

Figure A.17: The light path in *XMM-Newton*'s XRT with the pn camera in focus.

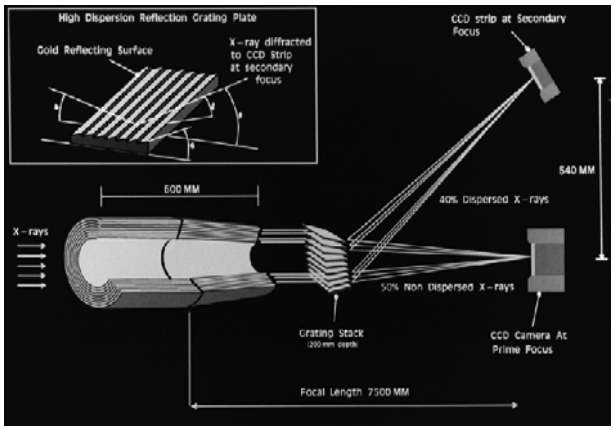

Figure A.18: The light path in *XMM-Newton*'s XRT with the MOS camera and RGA.

Point-spread function (PSF) of XRTs

A point-spread function (PSF) determines the imaging quality of an XRT. Figure A.19 shows the in orbit on-axis images obtained by each detector. The radial substructures are caused by the spiders holding the mirror shells. Figure A.20 displays the azimuthally averaged profile of the PSF of one XRT together with the best-fit King profile, which has the form $A\left(\frac{1}{\left[\left\{1+\left(\frac{r}{r_c}\right)^2\right\}^{\alpha}\right]}\right)$, where r is the radial distance from the center of the PSF, r_c is the core radius and α is the slope of the King model. Figure A.20 shows the encircled energy function (EEF) as a function of radius from the center of the PSF for several different energies. For on-axis source, high energy photons are reflected and focused predominantly by the inner shells of the XRTs. The inner shells apparently give better focus than the average of all shells, hence the EEF increase with increasing photon energy. A half energy width (HEW), which means the width including half of all the reflected photons, of the PSF can be derived from EEF. Table A.6 lists the on-axis HEW of the different XRTs measured in orbit and on ground.

The PSFs of the XRTs depend on the source off-axis angle. As the off-axis angle

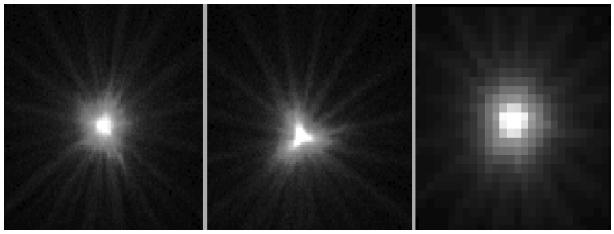

Figure A.19: On-axis images of the MOS1, MOS2 and on XRTs (left to right). The images are 110 arcsec wide and a logarithmic scale has been used to visualize the wings of the point spread function.

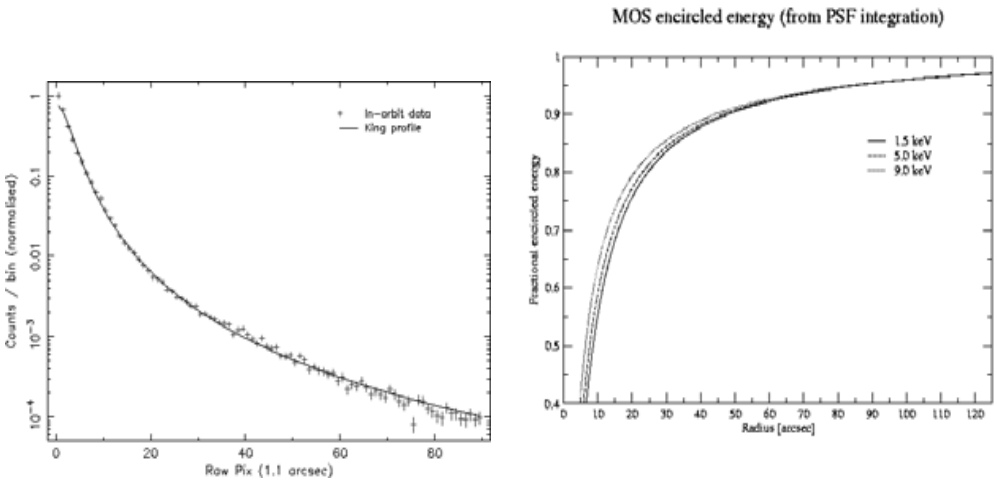

Figure A.20: Left: Radial counts distribution for the on-axis PSF of the MOS1 XRT in the 0.75–2.25 keV energy range. The solid line indicates the best-fit King profile. Right: The encircled energy function as a function of angular radius (an-axis) at different energies. The curve are calculated assuming a fraction encircled energy of 100 % at a radial distance of 5 arcmin.

increases, the HEW of PSF becomes larger.

Effective Area (EA) of XRTs

An effective area is an indicator of ability of collecting photons. *XMM-Newton* carries the XRT with the largest effective area of focusing telescope ever. The total mirror geometric effective area (EA) is about 1,550 cm^2 at 1.5 keV energy for each telescope, i.e., 4,650 cm^2 in total. Figure A.21 shows the on-axis effective area of all *XMM-Newton* XRTs. The EAs of the two MOS cameras are lower than that of the pn, because only part of the incoming radiation falls onto these detectors, which are partially obscured by the RGAs (see figure A.18). Not only the shape of the X-ray PSF, but also the effective area of the XRT is a function of off-axis angle within the field of view. Decreasing of photons reflected effectively in the XRT arises from an increasing off-axis angle. This effect is called vignetting. Figure A.21 displays the vignetting function as a function of off-axis angle for several different energies. The vertical axis is normalized by the on-axis effective area.

Table A.6: The on-axis in orbit and on ground 1.5 keV HEW of the different XRT.

Instr.	pn	MOS1	MOS2
	orbit/ground	orbit/ground	orbit/ground
HEW [arcsec]	15.2/15.2	13.8/13.6	13.0/12.8

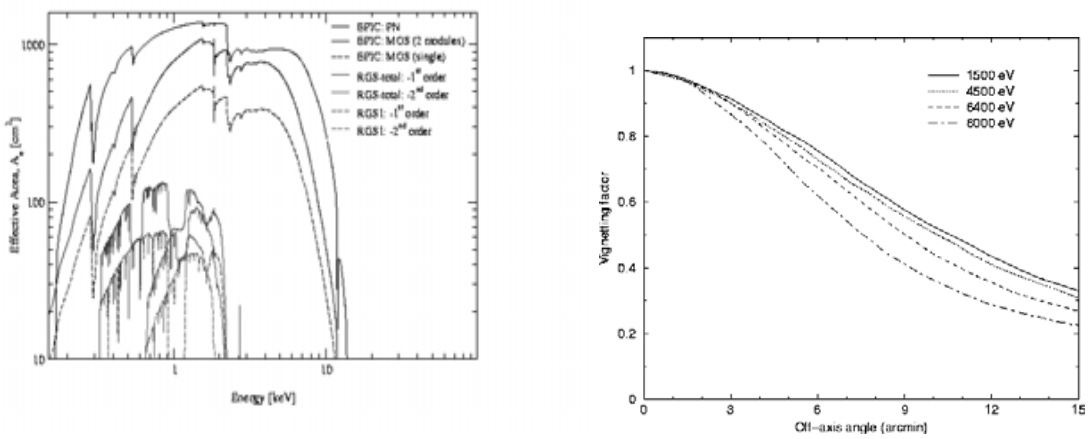

Figure A.21: Left: The net effective area of all *XMM-Newton* XRT, combined with the response characteristics of the focal detectors. Right: Vignetting function as a function of off-axis angle at several different energies (based on simulations).

Straylight Rejection

X-ray straylight is produced by rays which are singly reflected by the mirror hyperbolas and which reach the sensitive area of the focal plain detectors. Thus, an X-ray baffle was implemented to shadow those singly reflected rays. It consists of two sieve plates made of concentric annulus aperture stops located in front of the mirrors at 85 mm and 145 mm, respectively. The design is such that the entrance annular aperture of each mirror remains unobstructed for on-axis rays. The collecting area of straylight in the EPIC detector as a function of off-axis angle for a pint source is about 3 cm^2 for stray sources located between 20 arcmin and 1.4° from the optical axis. The ratio of the X-ray straylight collecting area to the on-axis effective area is smaller than 0.2 % at 1.5 keV for a point source located at off-axis angles of 0.4–1.4° and negligible at higher off-axis angles. Figure A.22 displays the effect of straylight, which is obtained from the observation of GRS 1758-258 (a black hole candidate near the Galactic center). Some sharp arcs are caused by single mirror reflections of photons possibly from GX 5-1 which is located at off-axis angle of 40 arcmin to the north and outside the field of view.

A.2.2 European Photon Imaging Camera (EPIC)

Two of *XMM-Newton* X-ray telescopes are equipped with EPIC MOS (Metal Oxide Semidonductor, Turner et al. 2001) CCD arrays, the third carries a different CCD camera

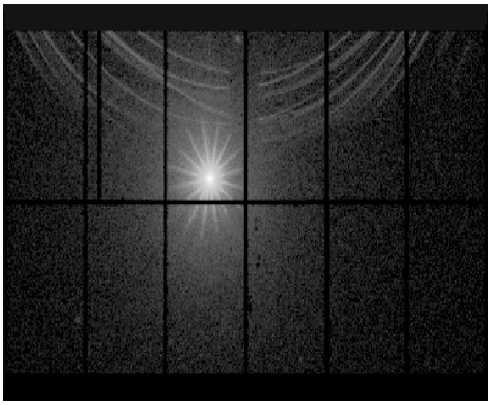

Figure A.22: The effect of straylight in pn image of GRS 1758-258.

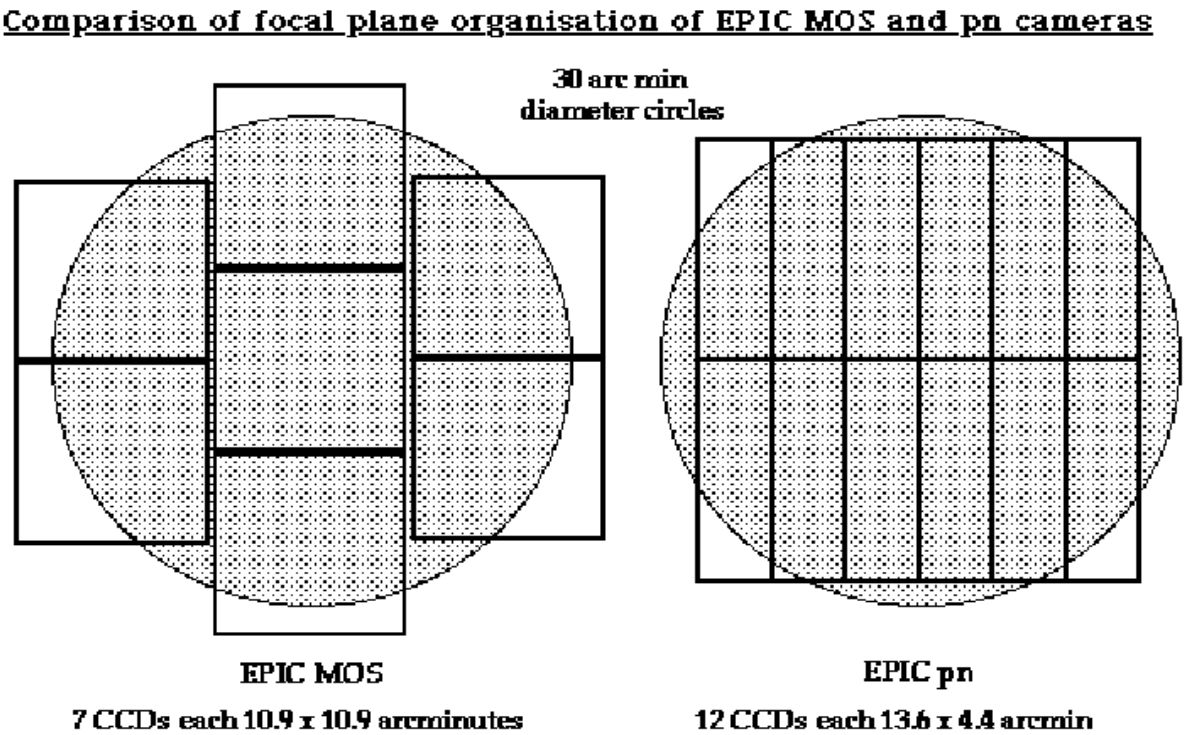

Figure A.23: A rough sketch of the field of view of the two types of EPIC cameras (MOS, left; pn, right). The shaded circle depicts a 30 arcmin diameter area which is equivalent with the XRT field of view.

called EPIC pn (Strüder et al., 2001). The EPIC cameras offer the possibility to perform extremely sensitive imaging observations over a filed of view of 30 arcmin and the energy range from 0.15 to 15 keV, with moderate spectral ($\frac{E}{\Delta E}$ ~20–50) and angular resolution (15 arcsec HEW). The detector layout and the baffled X-ray telescope FOV of both types of EPIC cameras are shown in figure A.23. The pn chip array is slightly offset with respect to the optical axis of its X-ray telescope so that the nominal, on-axis observing position does not fall on the central chip boundary. This ensures that more than 90 % of the energy of an on-axis point source are collected on one pn CCD chip. Two EPIC

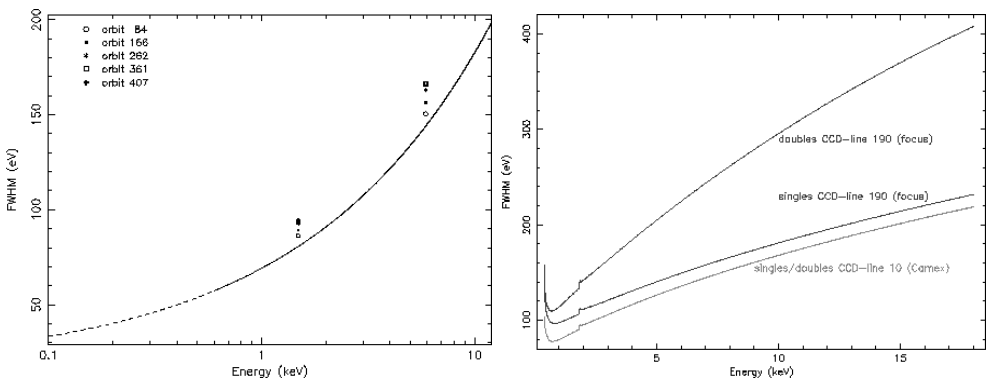

Figure A.24: Left: The EPIC MOS energy resolution (FWHM) as a function of energy. The solid curve is a best-fit $E^{0.5}$ function to ground calibration data between 0.1–12.0 keV. Below around 0.6 keV (shown by the dotted region), surface charge loss effects distort the main photopeak significantly from a Gaussian from and, hence the effective energy resolution The measured in-flight FWHM of the Al Kα (1.487 keV) and Mn Kα (5.893 keV) lines are also plotted. Right: The EPIC pn energy resolution (FWHM) as a function of energy. Curve are given for single and double events (fill frame mode) at the focus position node.

MOS cameras are rotated by 90° with respect to each other. The dead spaces between the MOS chips are not gaps, but unusable areas due to detector edges (the MOS chip physically overlap each other, the center one being located slightly behind the ones in the outer ring). All EPIC cameras are operated in photon counting mode with a fixed, mode dependent frame read-out frequency.

Angular Resolution

The EPIC MOS and pn cameras have pixels with sizes of 40 and 150 μm, respectively. For the focal length of the X-ray telescopes (7.5 m), these pixel size corresponds to 1.1 arcsec and 4.1 arcsec on the sky. Since they are smaller than the HEW of XRT (15 arcsec), EPIC's angular resolution is basically determined by the PSF of the mirror modules.

Energy Resolution

The resolving power of EPIC cameras is determined by the intrinsic energy resolution of the individual pixels. Figure A.24 shows the energy resolution (FWHM) of MOS and pn, respectively. The measured in-flight FWHM of the Al Kα (1.5 keV) and Mn Kα (5.9 keV), which are the on-board calibration lines, are also plotted in figure A.24. It is well known that the energy resolution of MOS cameras has been gradually decrease due to the CTI (charge transfer inefficiency) effect, which means the imperfect transfer of charge as it is transported through the CCD to the output amplifiers. The lated calibration status is found at *XMM-Newton* Science Operation Center [1]. The accuracy of the energy determination is above 10 eV over the full energy range and for all modes expect for MOS timing mode.

[1] http://xmm.vilspa.esa.es/external/xmm_sw_cal/calib/documentation.shtml#EPIC

Quantum Efficiencies

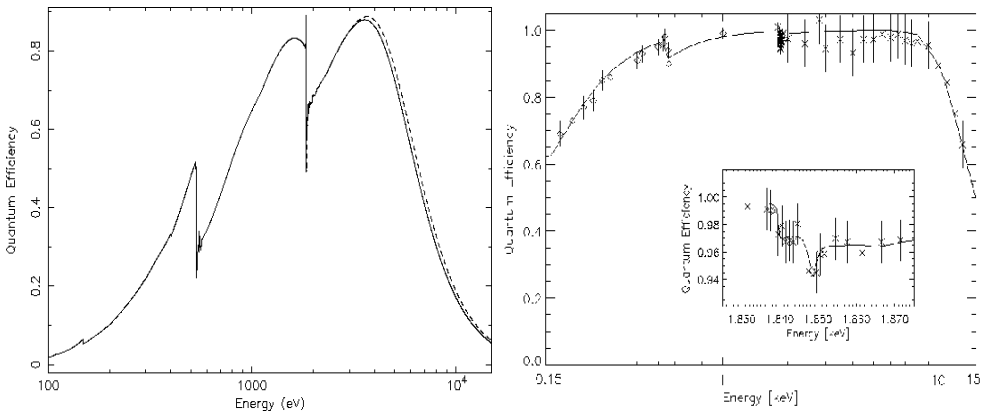

Figure A.25: Left: Quantum efficiency of the EPIC MOS camera as a function of photon energy, Right: Quantum efficiency of the EPIC pn camera as a function of photon energy.

The quantum efficiency of both types of EPIC CCD chips as a function of photon energy is displayed in figure A.25. These chips were calibrated using laboratory X-ray beams, synchrotron generated monochromatic X-ray beams, before launch, and celestial X-ray source measurements We can see the typical X-ray absorption fine structure (XAFS) behavior around the silicon K edge at 1.838 keV. Ground calibration measurements have shown that the quantum efficiency of MOS CCDs is uniform above 400 eV. Below this energy, spatial variations are seen as patches in the outer parts of the CCDs where the response is degraded. This inhomogeneity is currently not taken into account by the *XMM-Newton* science analysis system (SAS).

EPIC Filters

The EPIC CCDs are not only sensitive to X-ray photons, but also to IR, visible and UV light. Therefore, if an astronomical target has a high optical to X-ray flux ratio, there is a possibility that the X-ray signal becomes contaminated by those photons. To prevent such a contribution, each EPIC camera is equipped with a set of 3 separate aluminised optical blocking filters, named thick, medium and thin. The thick filter should be used for all point source targets up to m_{V} of 1–4 (MOS) or 0–3 (pn). The medium filter is about 10^3 less efficient than the thick filter, therefore, it is useful for preventing optical contamination from point sources as bright as m_{V} =8–10. The thin filter is about 10^5 less efficient than the thick filter, so the use of this filter will be limited to point sources with the optical magnitudes about 14 magnitudes fainter than the corresponding thick filter limitations.

Event Pattern

An absorbed sometimes deposits its energy over more than one pixels. This is called split event, and in this case the charges must be summed up over the relevent pixels. This process is automatically done by analysis software. The split pattern is classified in figure A.26. The patterns 0–12 for MOS and 0–4 for pn are considered to be X-ray events, while the others are false events induced by charged particles. Because of its much larger pixel size than MOS, the charge split occurs less frequently in pn (Turner et al., 2001).

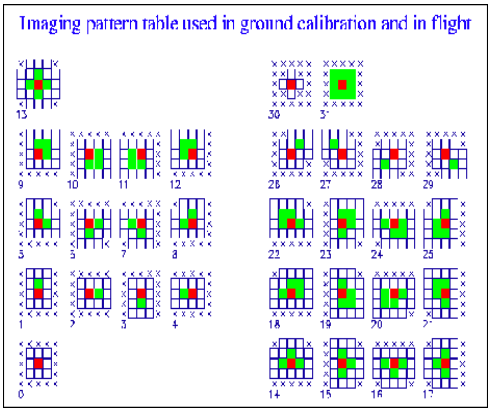

Figure A.26: Event patterns recognized by the MOS (pn) detector. The red pixel is the centre pixel, its signal is above threshold and is the largest signal in the 3×3 inner matrix. The green pixels have signals above threshold. The white pixels have signal below threshold. The crosses indicates pixels no considered.

Any events which located at around an edge or bad pixel are flagged by negative value. These events have possibility that the energy of these events are not correct. If we make a condition that the events flag = 0, we remove the events which are located around the edge or bad pixel.

A.2.3 EPIC Background

The EPIC background can be divided into two parts: a cosmic X-ray background (CXB), and an instrumental background. The latter component may be further divided into a detector noise component, which becomes important at low energy (i.e. below 200 eV), and a second component which is due to the particle interaction. This last component is characterized by a flat spectrum and is particularly important at high energies (i.e. above a few keV).

The particle induced background can be divided into two components: an external 'flaring' component, characterized by strong and rapid variability, which is often totally absent and a second more stable internal component. The flaring component is currently attributed to soft protons, which are presumably funneled towards the detectors by the X-ray mirrors. The stable component is due to the interaction of high-energy particles with the structure surrounding the detectors and possibly the detector themselves. We summarize the all background component below.

- Cosmic X-ray Background
- Instrumental Background
  - Detector component (below 200 eV)
  - Particle component (above a few keV)
    - flaring component (attributed soft photons)
    - stable component (attributed high-energy particles)

In the following we describe some of the main properties of both components.

Temporal Properties

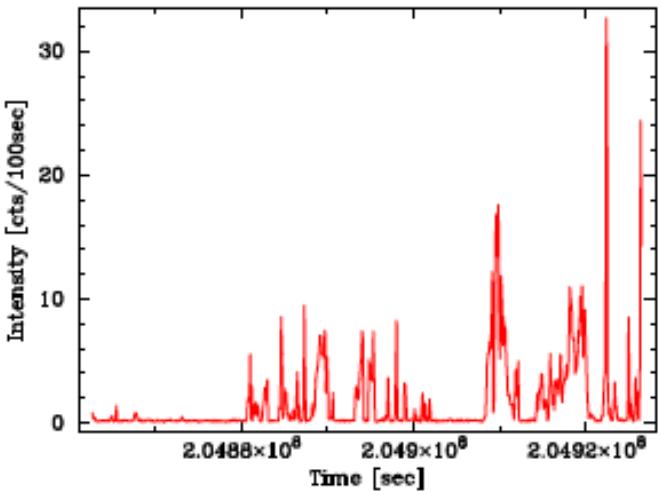

Figure A.27: An example of light curve from a MOS1 observation badly affected by proton flares.

As shown in figure A.27, the EPIC background count rate often exhibits sudden increases by as large as two orders of magnitudes, called 'flares'. Such phenomena are not observed in the *ASCA* SIS and *Suzaku* XIS. This is mainly due to the difference in their orbits. *ASCA* had an almost circular orbit with an altitude of 520–620 km, while *XMM-Newton* take highly eccentric orbit, with apogees of ∼115,000 km and perigees of ∼6,000 km. Therefore, *XMM-Newton* fly mostly outside the Earth's magneto-sphere. Now it is known that the background flares are caused by soft protons with energies below 1 MeV, reflected and focused by the X-ray mirrors. The spectra of soft proton flares are variable and no clear correlation is found between intensity and spectral shape. The current understanding is that soft protons are most likely organized in clouds populating the Earth's magnetosphere. The number of such clouds encountered by *XMM-Newton* in its orbit depends upon many factors, such as the altitude of the satellite, its position with respect to the magneto-sphere, and the amount of solar activity.

The EPIC background events in quiescent (non-flaring) periods are produced mainly by the interaction of high energy particles with the structure surrounding the detectors, and the detectors themselves. This component varies only by a small fraction, and on relatively longer timescale. On a representative time scale of several tens ksec, the standard deviation of both pn and MOS count rate is about 8 % (Katayama et al. 2004; Pizzolato et al. 2001; Read & Ponman 2003).

Spectral Properties

In figure A.28, we show the MOS1 and pn spectra extracted from a blank sky region. These background spectra consists of non X-ray background (NXB) and CXB. The NXB is induced mainly by charged particles. The CXB is mainly dominates at lower energies by soft thermal emission around the solar system. The entire background spectra are

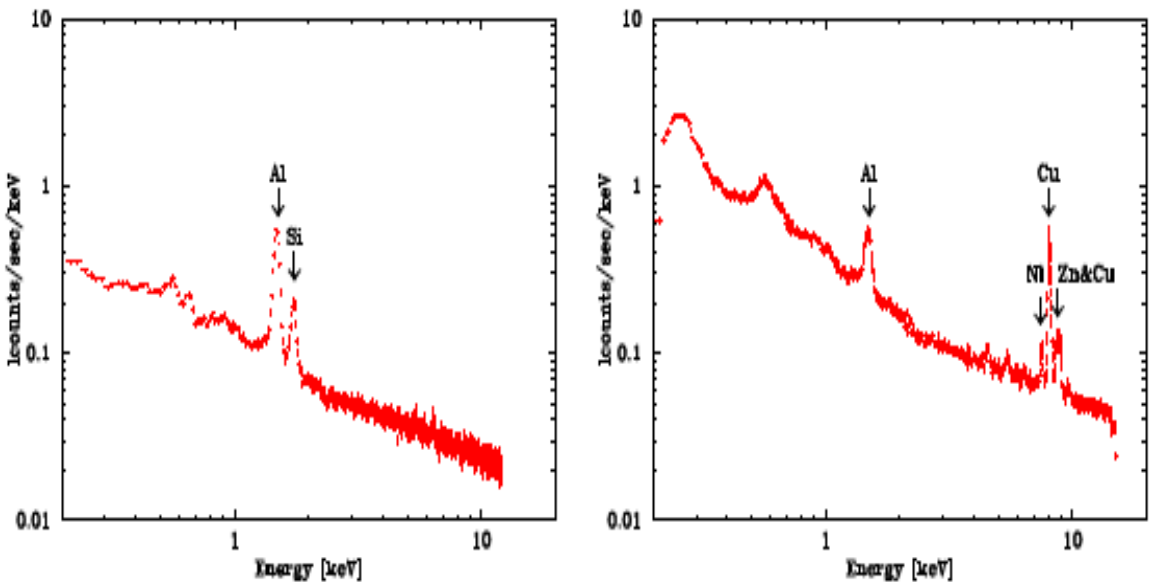

Figure A.28: MOS1 (left) and pn (right) background spectrum from a blank sky region. In the left figure, the prominent features around 1.5 and 1.7 keV are Al K and Si K fluorescence lines, respectively. On the other hands, the prominent features, in right figure, are identified as Al-K (1.5 keV), Cr-K (5.5 keV), Ni-K, Cu-K, Zn-K (8.0 keV) and Mo-K (17.5 keV), respectively.

dominated by the NXB at high energy regions, and the CXB becomes more important as the energy decreases. Their contributions are comparable at the energy of $\sim$ 1 keV.

Figure A.28 shows several distinct fluorescence lines. In pn spectra, Al-K, Ni, Cu, and Zn-K complex lines are prominent, while Al and Si-K lines are outstanding in the MOS spectra. These lines are emitted from surrounding materials such as electronic circuit boards for the signal readout, excited by high energy charges particles. Both the pn and MOS spectra rise below $\sim$0.5 keV, due to the detector noise which is more time variable than the continuum above 0.5 keV.

Spatial Properties

Because the CXB surface brightness is highly uniform, its brightness distribution on the focal plane obeys the effective area. Due to the vignetting effect, the CXB brightness is highest at the detector center, and gradually decreases toward the periphery. However, NXB brightness distribution on the focal plane depends on the position in the same detector. The distribution to Si-K line in the MOS is concentrated along the edges of some CCDs. This is attributed to Si-K X-rays escaping from the back side of a neighboring CCD. The asymmetric distribution arises because the 7 CCD chips slightly overlap with one another when viewed from the telescope, although their 3-dimensinal positions are offset along the optical axis. This layout is intended to reduce the gaps between CCD chips.

Spatial distributions of emission lines are rather complicated. Figure A.29 show some background images in limited energy bands. The emission in the Cu-K band is very weak

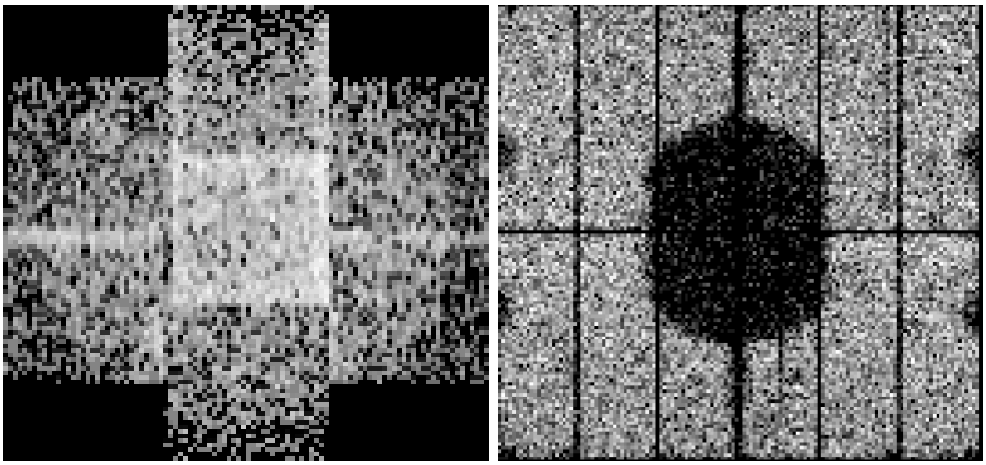

Figure A.29: The MOS (left) and pn (right) background image. The MOS image in the energy band centered on Si-K fluorescent line region. As the same, the pn image in the Cu-K fluorescent line energy region.

at the center of pn (figure A.29 right). Actually, the Cu-K line is insignificant in the spectrum extracted there. The Cu-K line image with the central hole agrees with the layout of electronics boards beneath the pn CCDs, indicating that the Cu-K photons come from them. The same mechanism produces semicircular dark regions at the right and reft side.

The continuum components of the NXB also have inhomogeneous distribution on the focal plane. The NXB image shows central excess brightness, by about 25 %. The shape is similar to the central hole seen in the Cu-K band image (figure A.29), although in this case the brightness shows excess, not a deficit.

As is implied by these non-uniform distributions of carious components, the background spectrum strongly depends on the detector position. Therefore, when we use other observations as the background fields, we must extract the background spectrum from the same detector region as the analyzing target.

A.3 The *Chandra* Satellite

Chandra is placed highly elliptical orbit with an apogee of 132,200 km and a perigee of 16,700 km in December 2008. This elliptical orbit allows for high observing efficiency of ∼160 ksec long continuous observation.

High Resolution Mirror Assembly (HRMA) consists of nested set of four paraboloid hyperboloid (Wolter-I) grazing-incidence X-ray mirror pairs, with the largest having a diameter of 1.2 m. The focal length is 10 m. In the optical path just behind the HRMA, two gratings spectrometers can be placed. High-Energy Transmission Grazing (HETG) achieves resolving power ($\frac{E}{\Delta E}$) up to 1000 in the band between 0.4 keV and 10.0 keV when operated with ACIS-S. Low Energy Transmission Grating (LETG) provides the highest spectral resolution on *Chandra* at low (0.08–0.2 keV) energies when operated with HRC-S. The scientific payload on the focal plane consists of four distinct co-aligned instruments (figure A.31). These are two CCD arrays (Advanced CCD Imaging Spectrometer, or

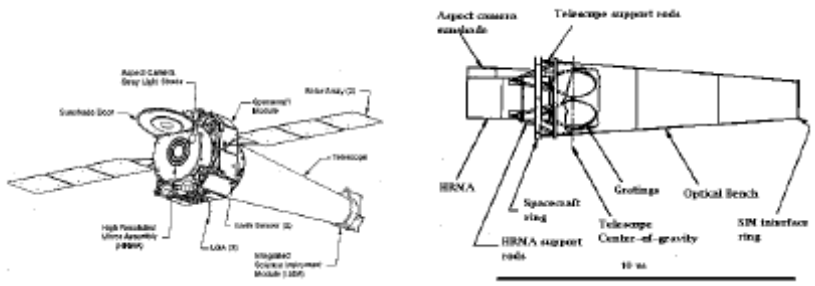

Figure A.30: Left: The *Chandra* Observatory with certain subsystems labeled. LGA is an acronym for the Low Gain Antenna. Right: Major components of the telescope system. The grating assemblies are also shown.

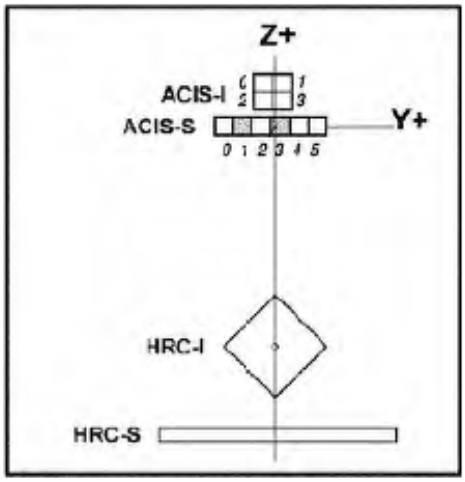

Figure A.31: Arrangement of the ACIS and the HRC in the focal plane. The view is along the axis of the telescope from the direction of the mirrors. For reference, the two back-illuminated ACIS-S chips are shaded. Numbers indicate positions of chips I0–I3 and S0–S5. SIM motion can be used to place the aimpoint at any point on the vertical solid line.

ACIS), ACIS-I and ACIS-S. ACIS-I is comprised of 4 chips of CCDs and was designed for CCD imaging and spectrometry. ACIS-S is comprised of 6 CCDs and can be sued both for CCD imaging spectrometry and also for high-resolition spectroscopy in conjunction with the HETG grating. The second instruments are two microchannel plate (MCP) imaging detector (High Resolution Camera, or HRC), HRC-I and HRC-S. The HRC-I designed for wide-field imaging; and, HRC-S designed to serve as a readout for the LETG. We only use ACIS in the following analysis.

A.3.1 High Resolution Mirror Assembly (HRMA)

The *Chandra* X-ray telescope consists of 4 pairs of concentric thin-walled, grazing-incidence Wolter Type-I mirrors called the High Resolution Mirror Assembly (HRMA). The front

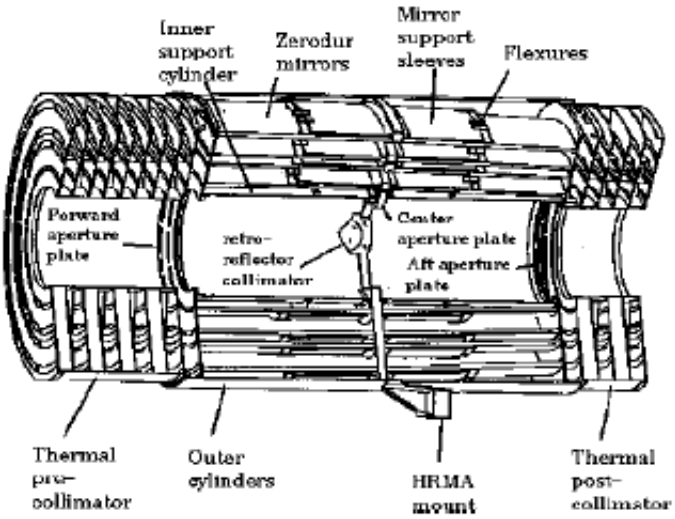

Figure A.32: The four nested HRMA mirror pairs and associated structures.

Table A.7: *Chandra* HRMA characteristics

Optics	Wolter Type-I
Mirror coating	Iridium (330 Å, nominal)
Focal length	10.070±0.003 m
PSF FWHM (with detector)	<0."5
Effective area:	800 cm^2 at 0.25 keV
	400 cm^2 at 5.0 keV
	100 cm^2 at 8.0 keV

mirror of each pair is a paraboloid ($P_{\rm n}$) and the back a hyperboloid ($H_{\rm n}$). The eight mirrors were fabricated from Zerodur glass, polished, and coated with iridium on a binding layer of chromium.

Physical Configuration

The HRMA, as shown in figure E.3, contains the nested mirrors, center, forward and after aperture plates, baffles, inner and outer cylinders, mounts, pre- and post-coliimators, fiducial light transfer components, mirror support sleeves, forward and after contamination covers, flux contamination monitors, and thermal control hardware. The pair diameters range from about 0.65 to 1.23 m. The distance from the center of the Central Aperture Plate (CAP) separating the paraboloid and hyperboloid mirrors to the HRMA focus is 10.0548 m, with each mirror pair varying slightly about this value. An annular on-axis beam enters each mirror pair, is reflected from paraboloids and hyperboloids and exits to converge to a focus. The HRMA characteristics are listed in table A.7.

Effective Area

The unobstructed geometric aperture of the HRMA is 1145 cm^2. The obstruction of

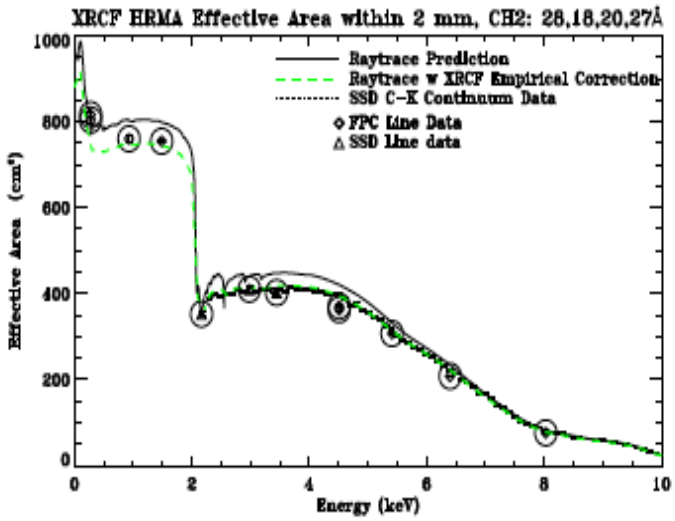

Figure A.33: The HRMA effective area from the raytrace prediction as a function of energy. The raytrace includes the effects of molecular contamination of variable thickness on the mirrors. The dotted line (tp emphasize that these measurements were taken simultaneously) with error bars shows the data taken with a solid state detector (SSD) with a C-K continuum source. Data obtained from spectral line sources with a flow proportional counter (FPC) are shown as diamonds; obtained with a solid state detector (SSD) are shown as triangles. All the line measurements are circled for clarity. The dashed (green) line shows the absolute HRMA effective area with the X-Ray Calibration Facility (XRCF) empirical correction.

the HRMA aperture by supporting struts is less than 10 %. Since the reflectivity of the mirror optics depends on photon energy as well as grazing angle, the HRMA throughput varies with X-ray energy (figure A.33).

Contamination Problem

There was an insignificant layer of molecular contamination on the mirrors. Subsequent in-flight gratings observations of blazers showed evidence for systematic effects near the Ir-M edges of the coating on the mirror and using these data and raytrace simulations, it was estimated that a 22 $\AA$ layer of hydrocarbon was present on the mirror optics.

Since the initial, ad-hoc, empirical correction of the HRMA model had already corrected for most of the effects of the molecular contamination, the addition of another 22 $\AA$ of contamination in the raytrace model post-launch was an over-correction.

A.3.2 Advanced CCD Imaging Spectrometer (ACIS)

The advanced CCD Imaging Spectrometer (ACIS) offers the capability to simultaneously acquire high-resolution images and moderate resolution spectra. The instrument can also be used in conjunction with the High Energy Transmission Grating (HETG) or Low Energy Transmission Grating (LETG) to obtain higher resolution spectra. ACIS contains 10 planar, 1024×1024 pixel CCDs (figure A.34); four arranged in a 2×2 array (ACIS-I)

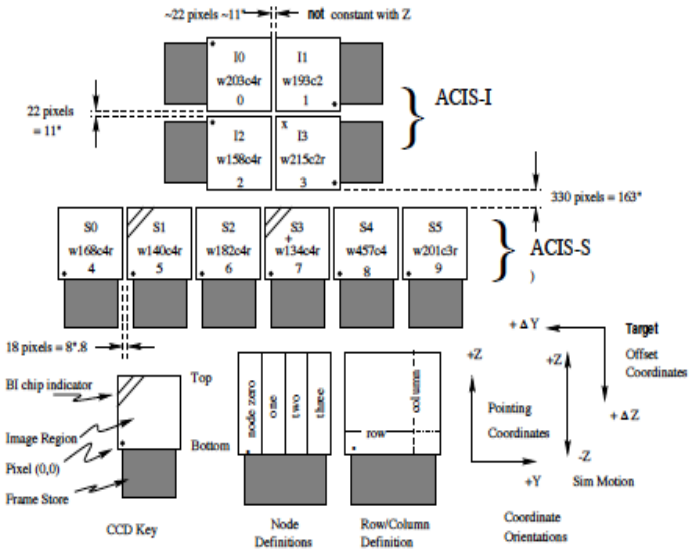

Figure A.34: A schematic drawing of the ACIS focal plane; insight to the terminology is given in the lower left. Note the nominal aimpoints: on S3 (the '+') and on I3 (the 'x'). It is standard practice to add an offset to all observations on S3 to move the source away from the node 0–1 boundary. Note the differences in the orientation of the I and S chips, important when using Sub array. Note also the (Y, Z) coordinate system and the target offset convention as well as the SIM motion (+/- Z). The view is along the optical axis, from the source toward the detectors, (-X). The numerous ways to refer to a particular CCD are indicated: chip letter+number, chip serial number, and ACIS chip number. The node numbering scheme is illustrated lower center.

used for imaging, and six arranged in a 1×6 array (ACIS-S) used either for imaging or as a grating readout. One chip (ACIS-S3) covers an 8'×8' region on the sky.

Energy Resolution

The ACIS FI CCDs originally approached the theoretical limit for the energy resolution at almost all energies, while the BI CCDs exhibited poorer resolution. The pre-launce energy resolution as a function of energy is shown in figure A.35. The loss of energy resolution is due to increased charge transfer inefficiency (CTI) caused by low energy protons encountered during radiation belt passages and Rutherford scattering through the X-ray telescope into the focal plane. Subsequent to the discovery of the degradation, operational procedures were changed, ACIS is not left at the focal position during radiation belt passages. Since this procedure was initiated, no further degradation in performance has been encountered beyond with the proton-damage scenario - it is far more difficult for low-energy protons from the direction of the HRMA to deposit their energy in the buried channels of the BI devices, since the channels are near the gates and the fates face in the direction opposite to the HRMA. Thus the energy resolution for the two BI devices remains nearly at pre-launch values. The position-dependent energy resolution of the FI chips depends significantly on the ACIS operating temperature.

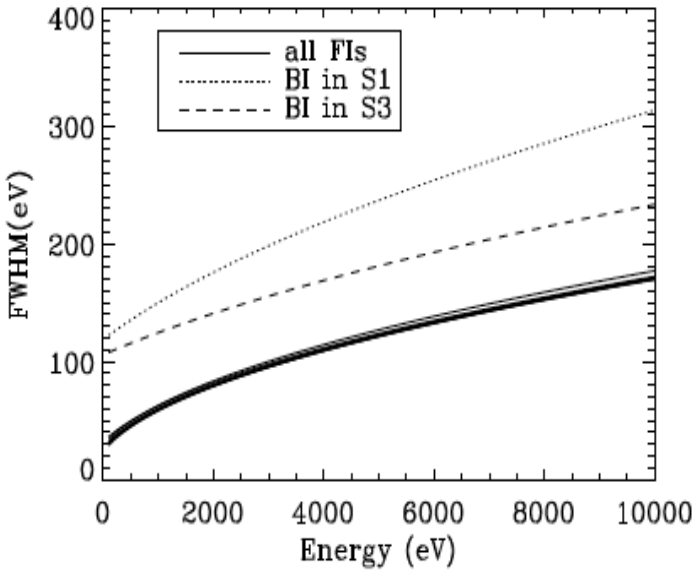

Figure A.35: The ACIS pre-launch energy resolution as a function of energy.

Appendix B

Selected Regions

In figure B.1 we present the *Suzaku*, *XMM-Newton*, and *Chandra* images in the 0.5–2.0 keV (left) and 2.0-10.0 keV (right) of individual remnants. The images are smoothed by a GAUSSIAN function with σ =3–20 pixels. The background are not subtracted. In these figures, the solid and dotted circles are represented with the selected source and background regions, respectively. The solid line is also represented with 1 arcmin. The images from all two MOS and four (or three) XIS modules were combined. The coordinate is represented with the equatorial coordinate system for the epoch 2000. The calibration sources at the corners were masked for *Suzaku*/XIS modules.

B.1 Notes on Individual Objects

As for J0453.6-6829 (B0453-685), since the brightnesses between the low and high energy bands had strongly different contrast, we modified the color scale in each energy band. On the other hand, J0455.6-6839 (N86) and J0527.6-6912 (B0528-692) were out of the FOV of the MOS detectors, we presented only the pn images. J0529.9-6701 (DEM L241) and J0537.6-6920 (B0538-6922) could not be detected the X-ray photons clearly. In these figures, the circles were presented with the remnant radii estimated by the previous observations with the different wavelength (Badenes et al., 2010), respectively. Finally, though J0532.5-6732 (B0532-675) was in the lack of the MOS 1 detector, we combined all two MOS modules.

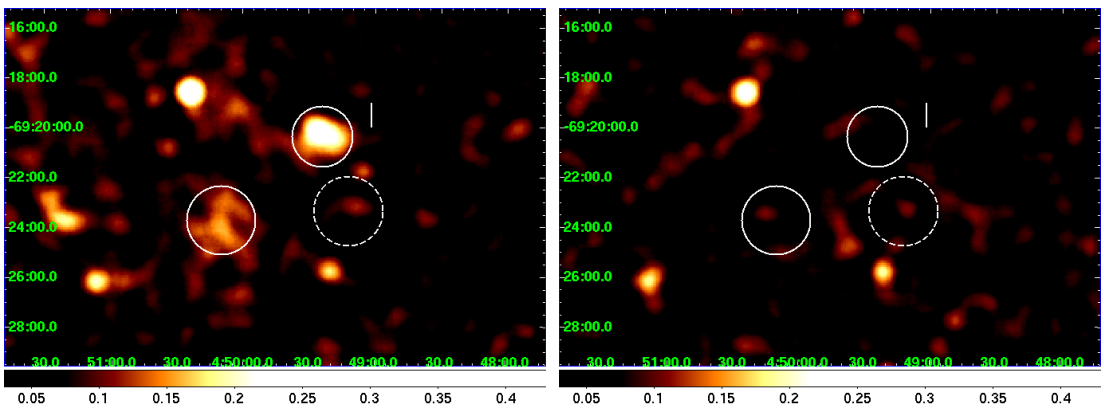

Figure B.1: The *XMM-Newton* X-ray SNR image; J0449.3-6920 (right) and J0450.2-6922 (left; B0450-69270).

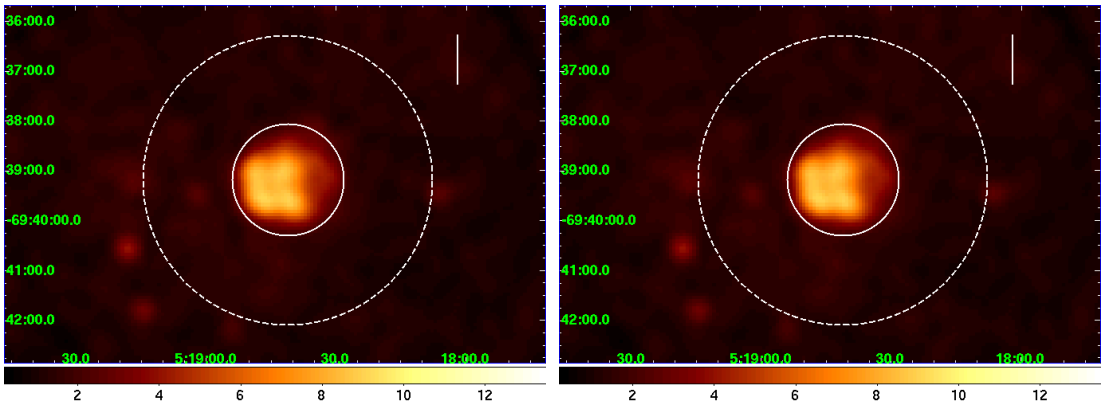

Figure B.1: The *XMM-Newton* X-ray SNR image; J0518.7-6939 (N120).

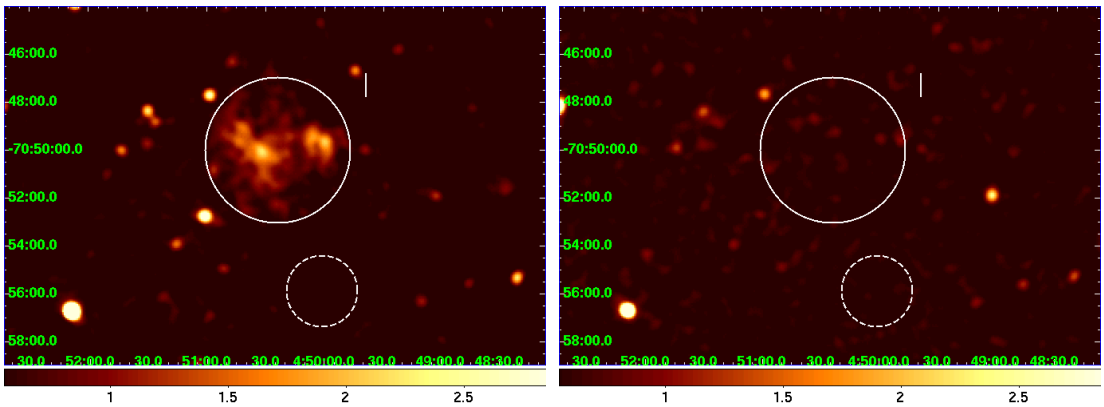

Figure B.1: The *XMM-Newton* X-ray SNR image; J0450.4-7050 (B0450-709).

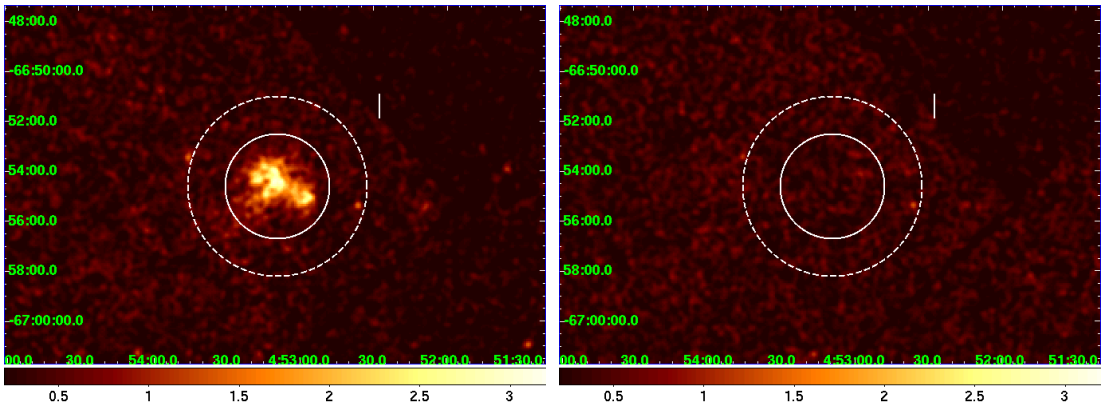

Figure B.1: The *XMM-Newton* X-ray SNR image; J0453.2-6655 (N4).

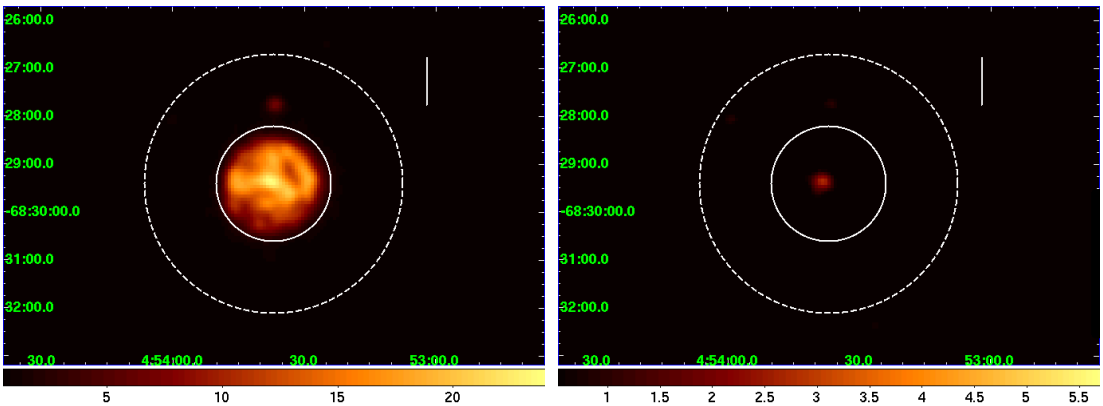

Figure B.1: The *XMM-Newton* X-ray SNR image; J0453.6-6829 (B0453-685).

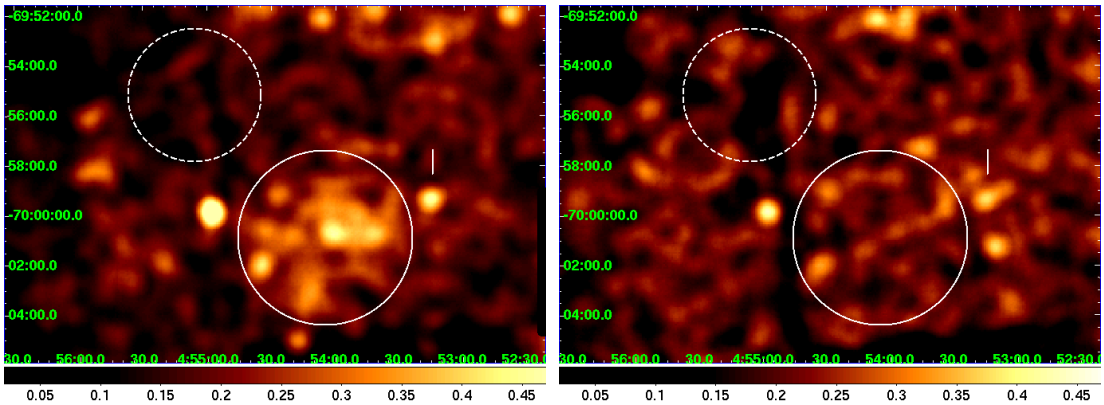

Figure B.1: The *Chandra* X-ray SNR image; J0453.9-7000 (B0454-7005).

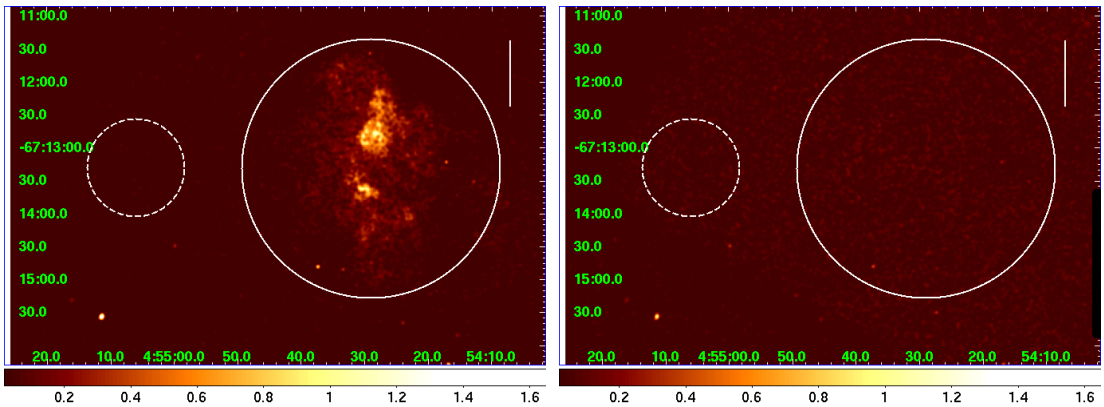

Figure B.1: The *Chandra* X-ray SNR image; J0454.6-6713 (N9).

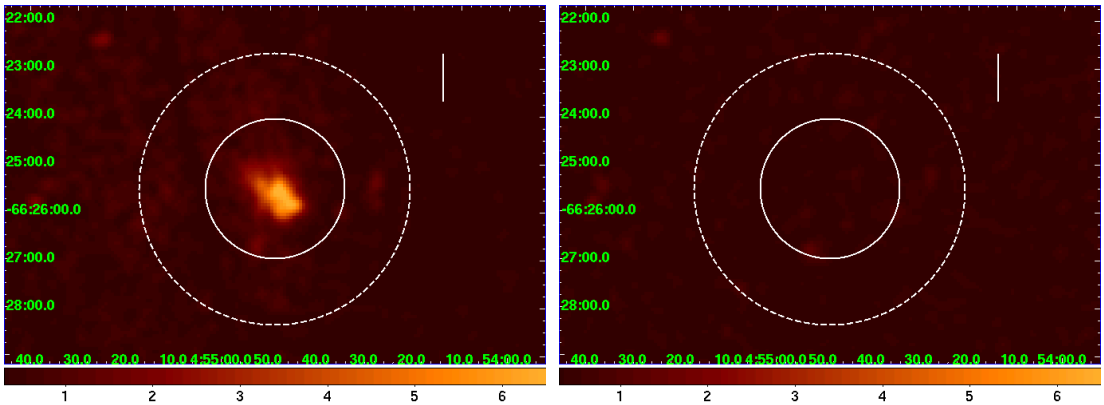

Figure B.1: The *XMM-Newton* X-ray SNR image; J0454.8-6626 (N11L).

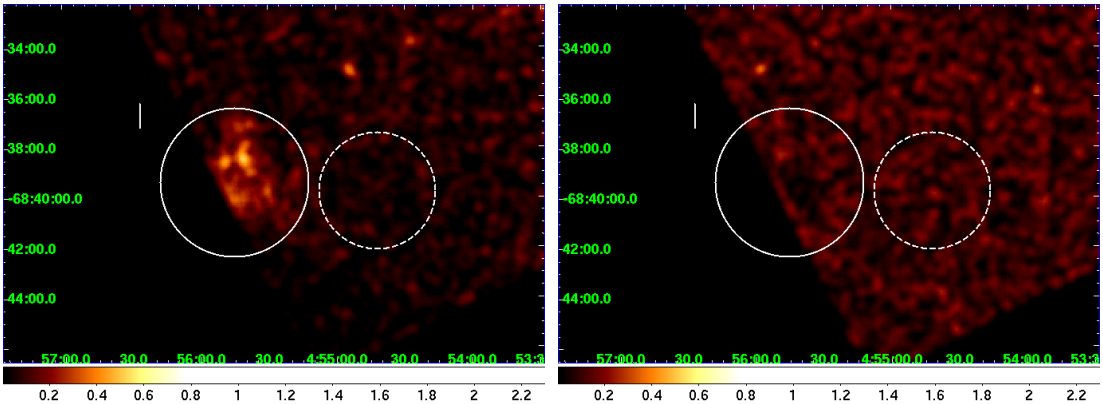

Figure B.1: The *XMM-Newton* X-ray SNR image; J0455.6-6839 (N86).

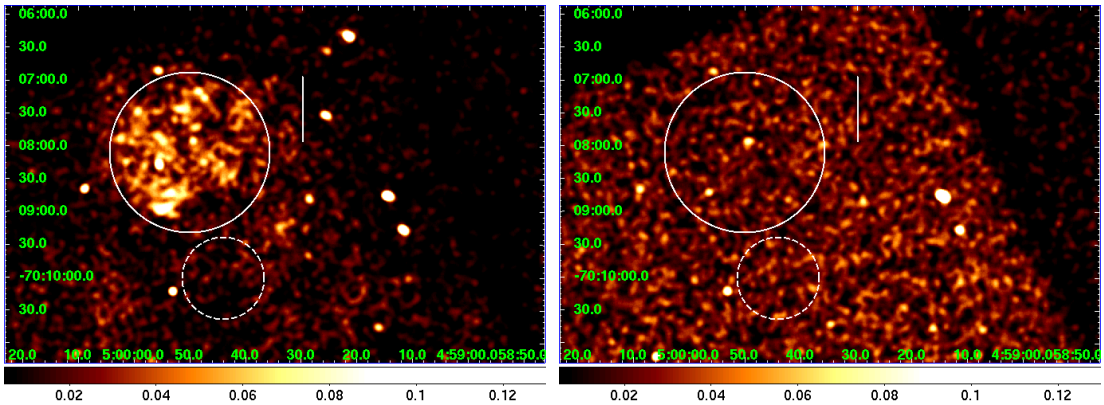

Figure B.1: The *Chandra* X-ray SNR image; J0459.9-7008 (N186D).

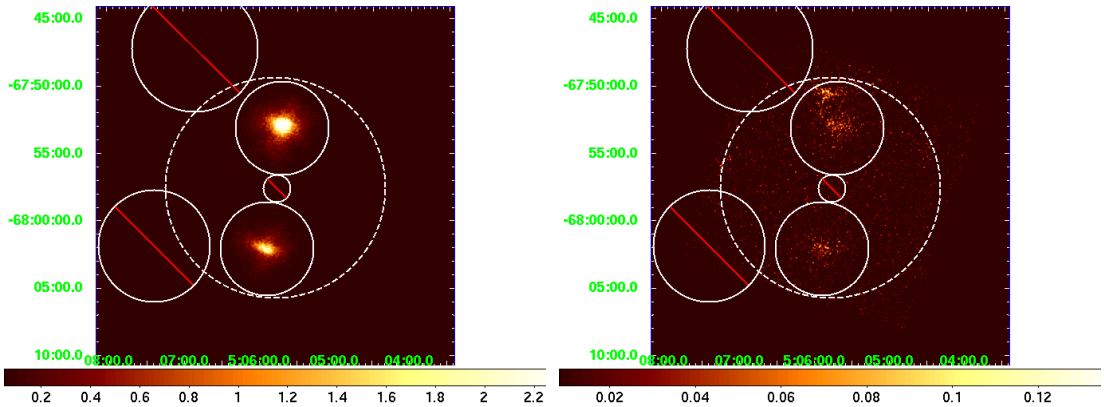

Figure B.1: The *Suzaku* X-ray SNR image; J0505.7-6753 (DEM L71; top) and J0505.9-6802 (N23; bottom).

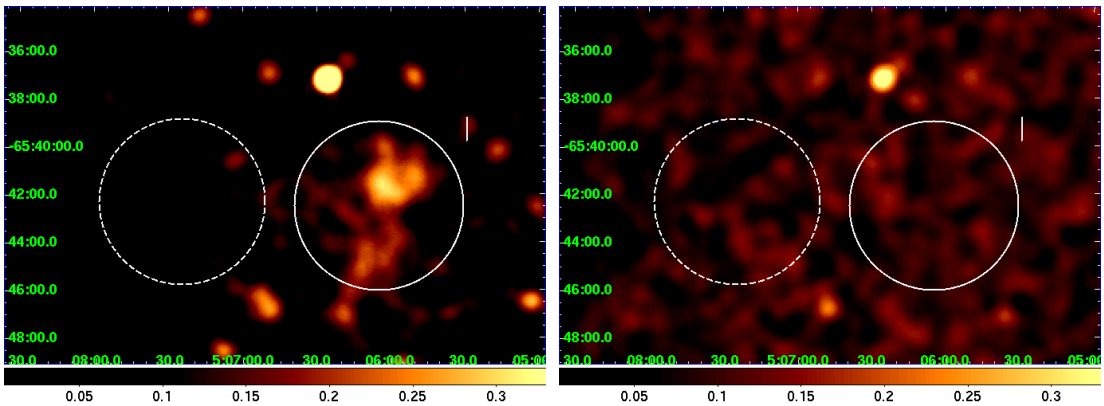

Figure B.1: The *XMM-Newton* X-ray SNR image; J0506.1-6541.

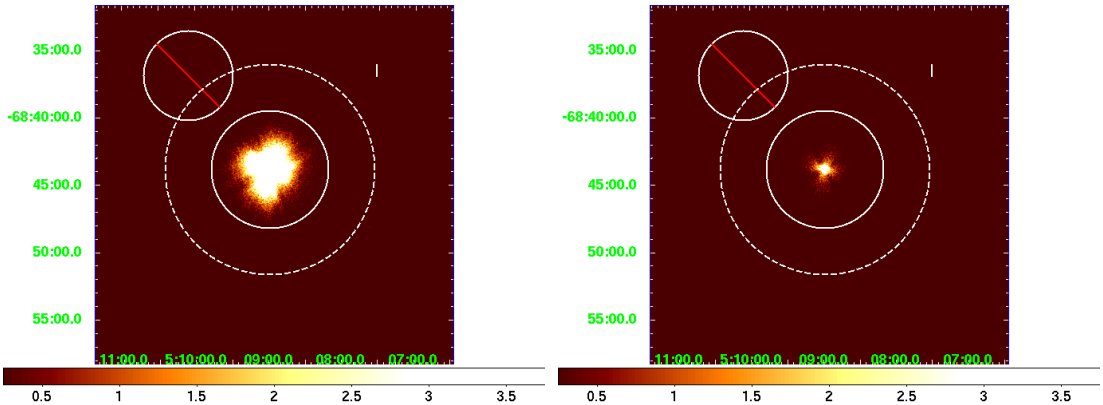

Figure B.1: The *Suzaku* X-ray SNR image; J0509.0-6844 (N103B).

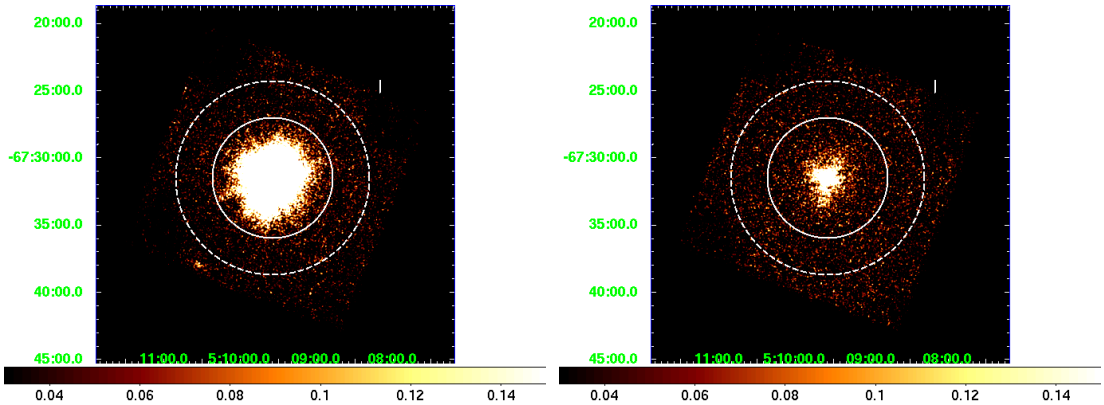

Figure B.1: The *Suzaku* X-ray SNR image; J0509.5-6731 (B0509-67.5).

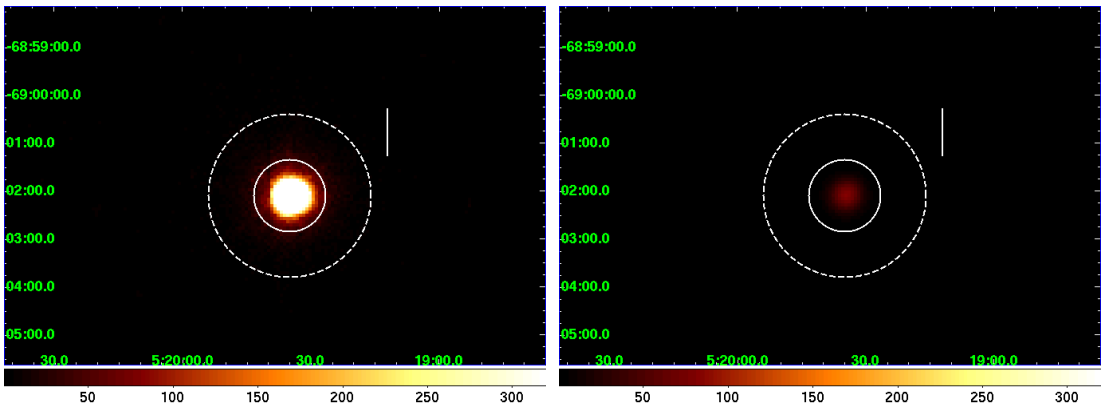

Figure B.1: The *XMM-Newton* X-ray SNR image; J0519.6-6902 (B0519-690).

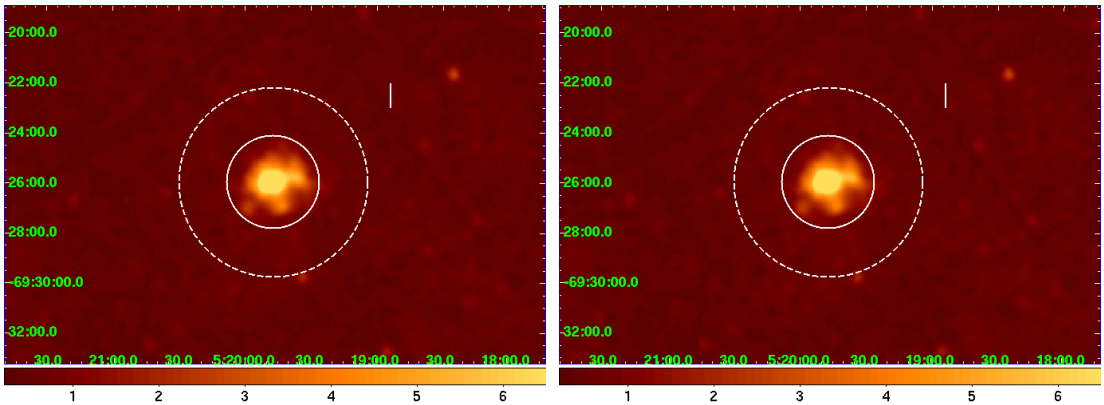

Figure B.1: The *XMM-Newton* X-ray SNR image; J0519.7-6926 (B0520-694).

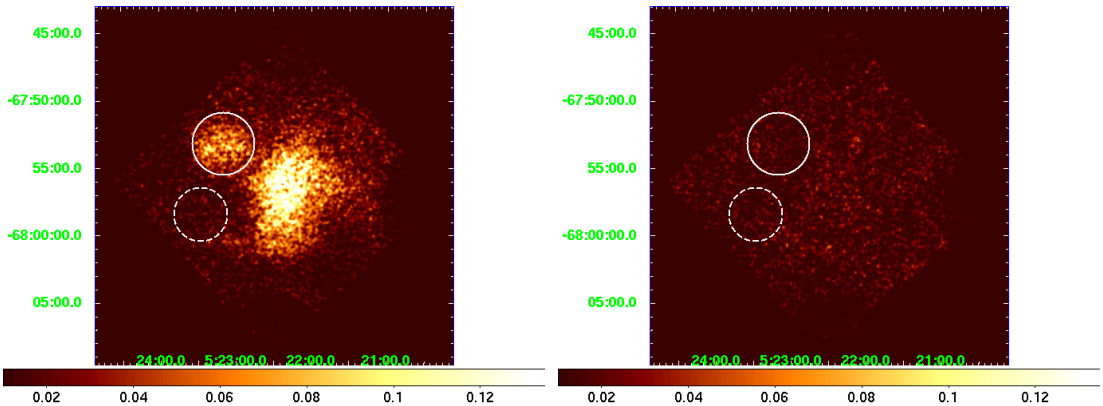

Figure B.1: The *Suzaku* X-ray SNR image; J0523.1-6753 (N44).

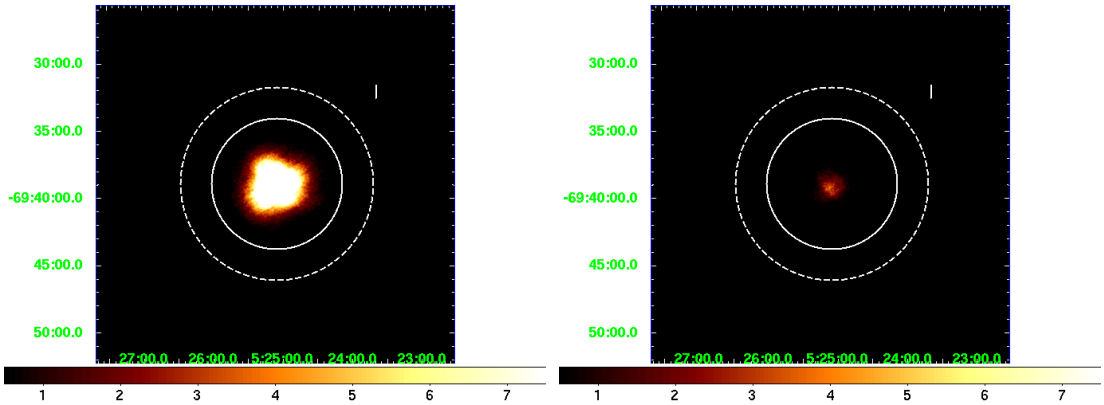

Figure B.1: The *Suzaku* X-ray SNR image; J0525.1-6938 (N132D).

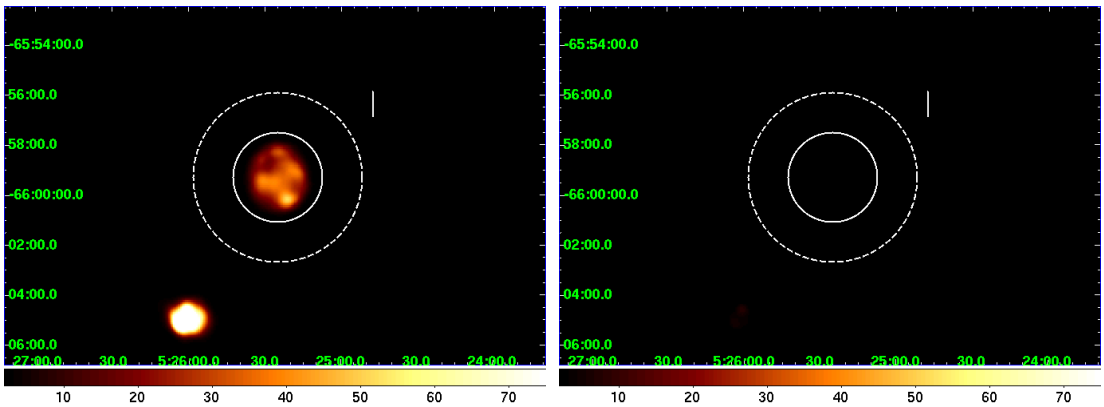

Figure B.1: The *XMM-Newton* X-ray SNR image; J0525.4-6559 (N49B).

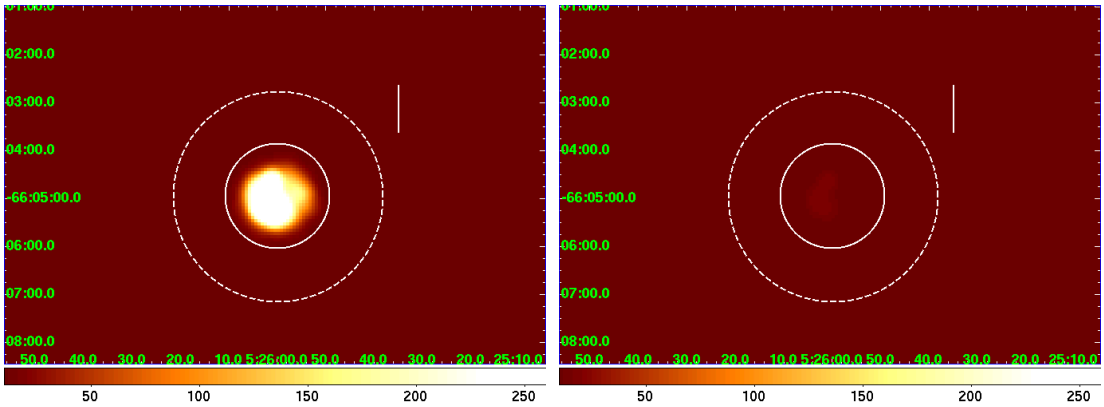

Figure B.1: The *XMM-Newton* X-ray SNR image; J0526.0-6605 (N49).

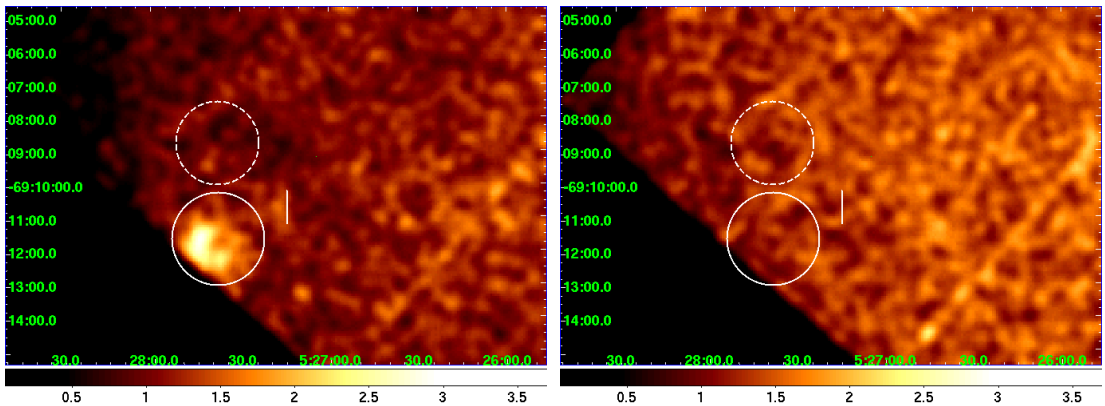

Figure B.1: The *XMM-Newton* X-ray SNR image; J0527.6-6912 (B0528-692) .

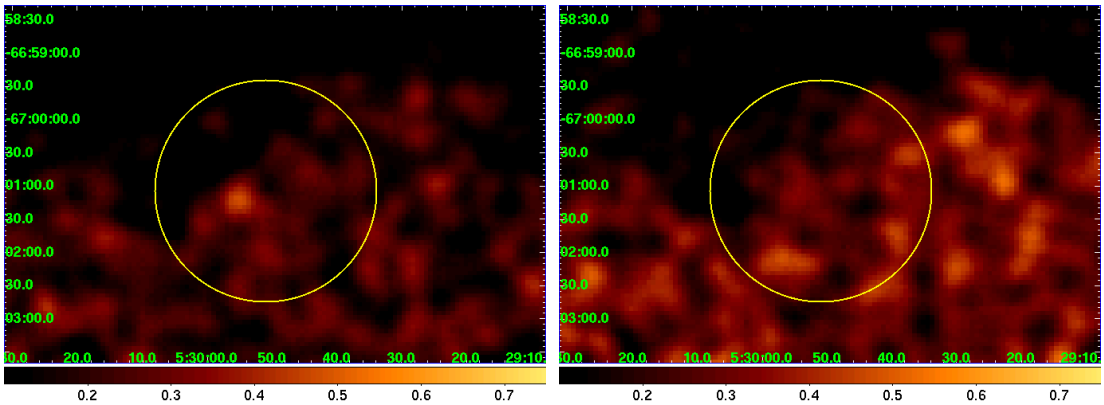

Figure B.1: The *XMM-Newton* X-ray SNR image; J0529.9-6701 (DEM L214).

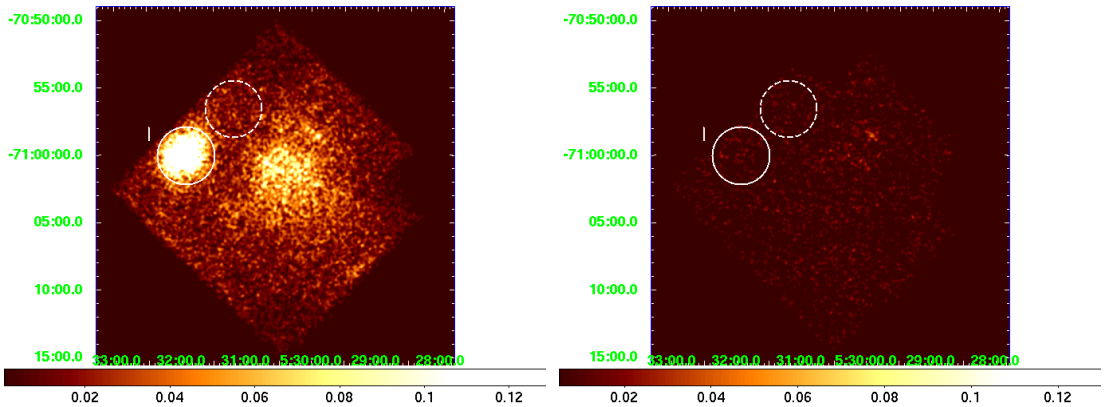

Figure B.1: The *Suzaku* X-ray SNR image; J0531.9-7100 (N206).

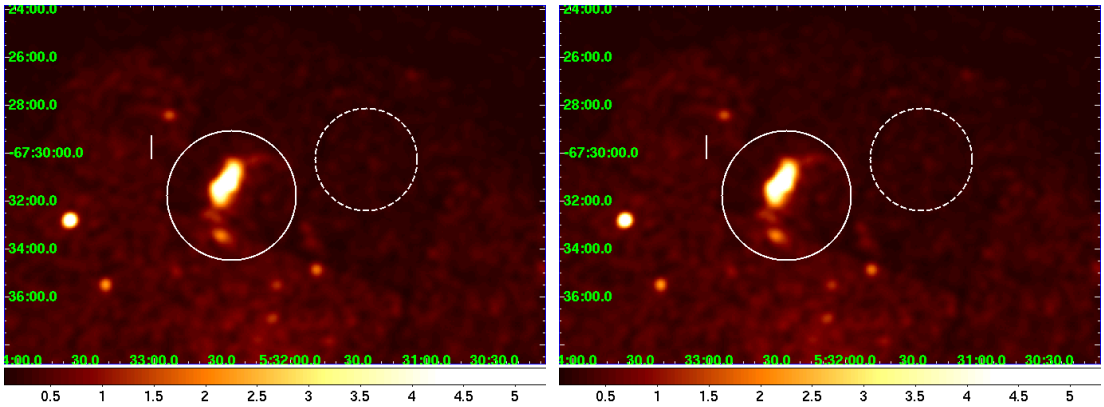

Figure B.1: The *XMM-Newton* X-ray SNR image; J0532.5-6732 (B0532-675).

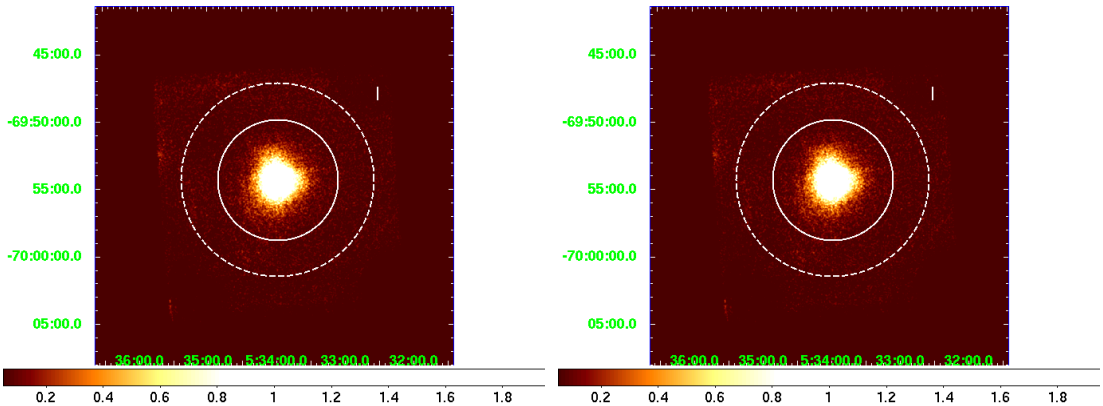

Figure B.1: The *Suzaku* X-ray SNR image; J0534.0-6955 (B0534-699).

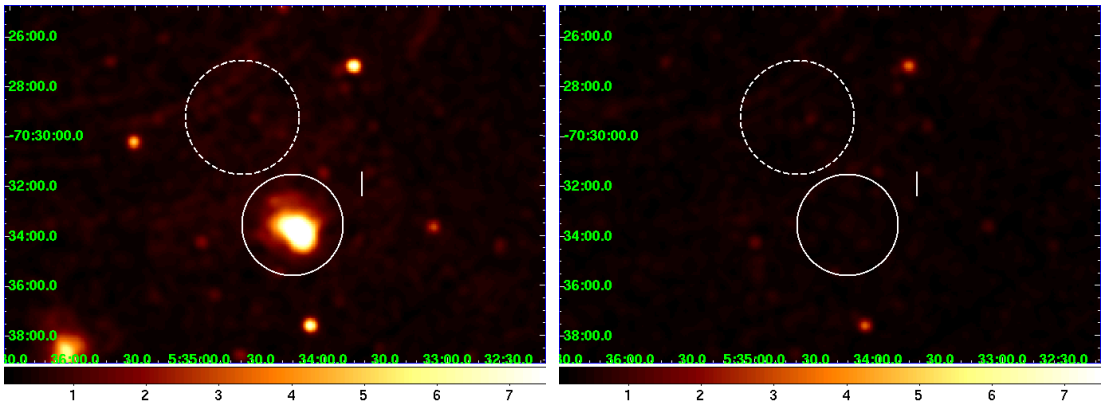

Figure B.1: The *XMM-Newton* X-ray SNR image; J0534.3-7033 (DEM L238).

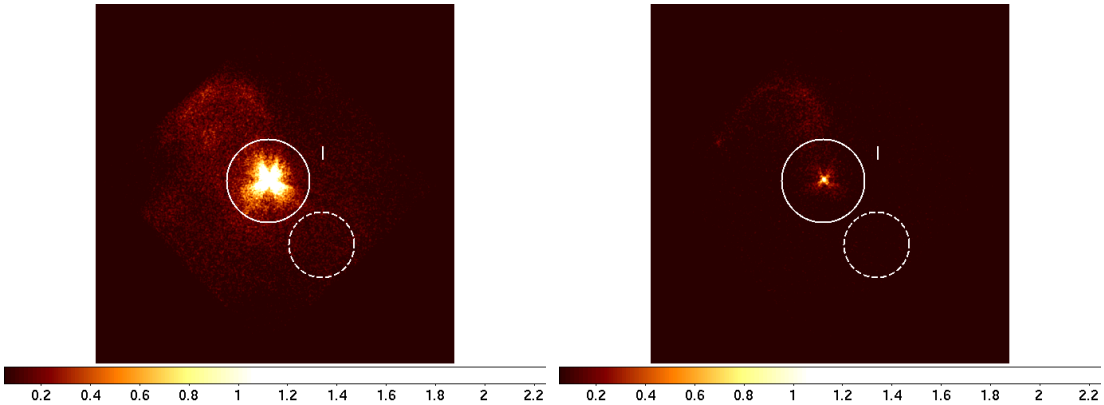

Figure B.1: The *Suzaku* X-ray SNR image; J0535.5-6916 (SNR 1987A).

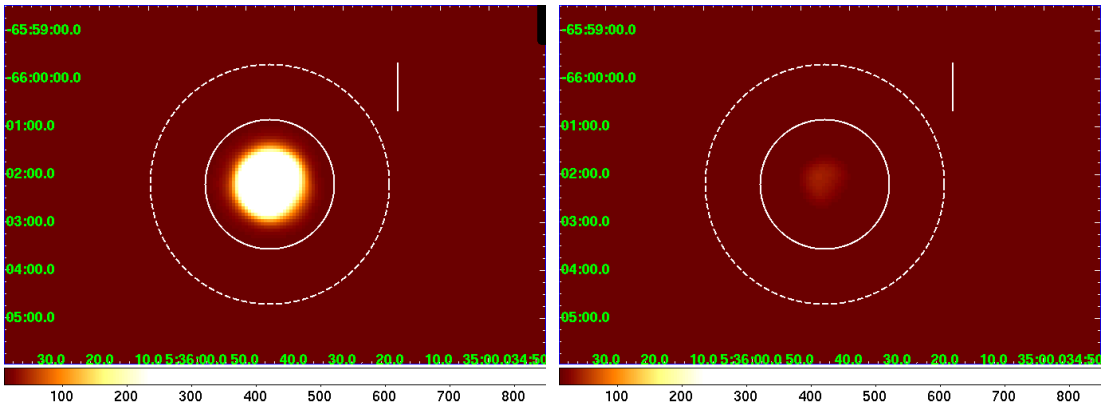

Figure B.1: The *XMM-Newton* X-ray SNR image; J0535.7-6602 (N63A).

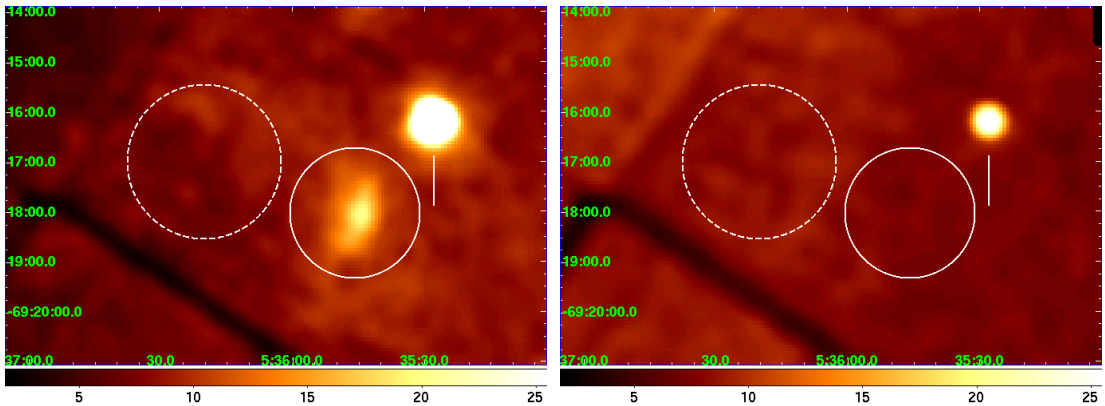

Figure B.1: The *XMM-Newton* X-ray SNR image; J0535.8-6918 (Honeycomb).

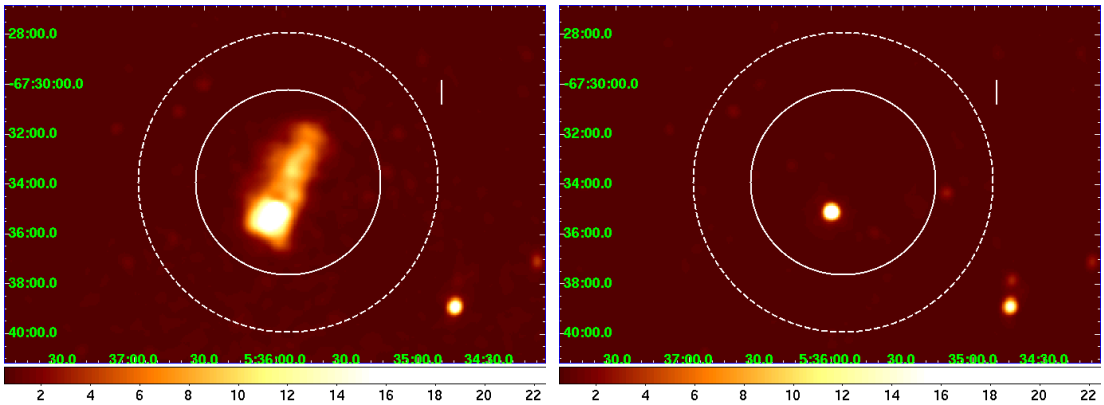

Figure B.1: The *XMM-Newton* X-ray SNR image; J0536.1-6735 (DEM L241).

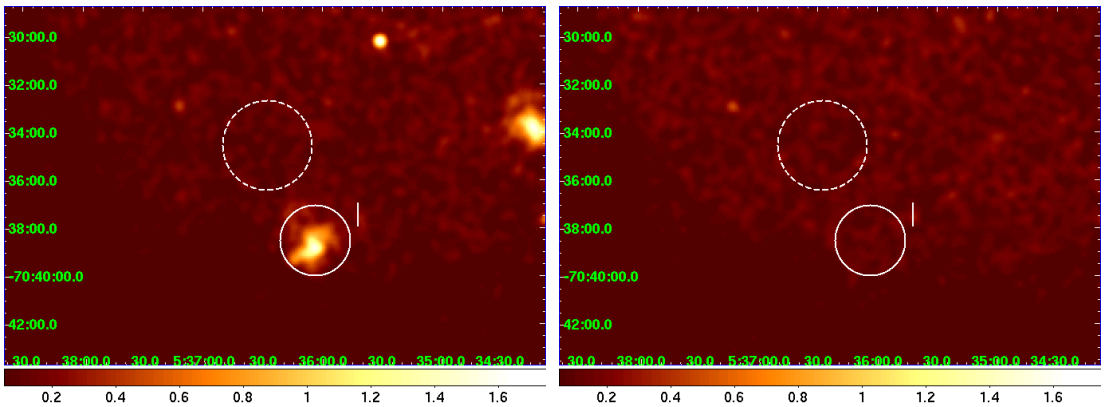

Figure B.1: The *XMM-Newton* X-ray SNR image; J0536.1-7039 (DEM L249).

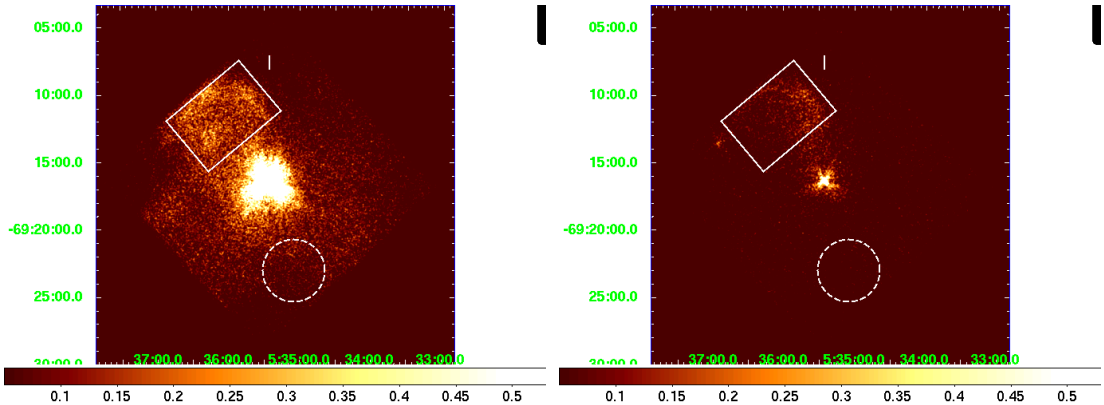

Figure B.1: The *Suzaku* X-ray SNR image; J0536.2-6912 (30 Dor C).

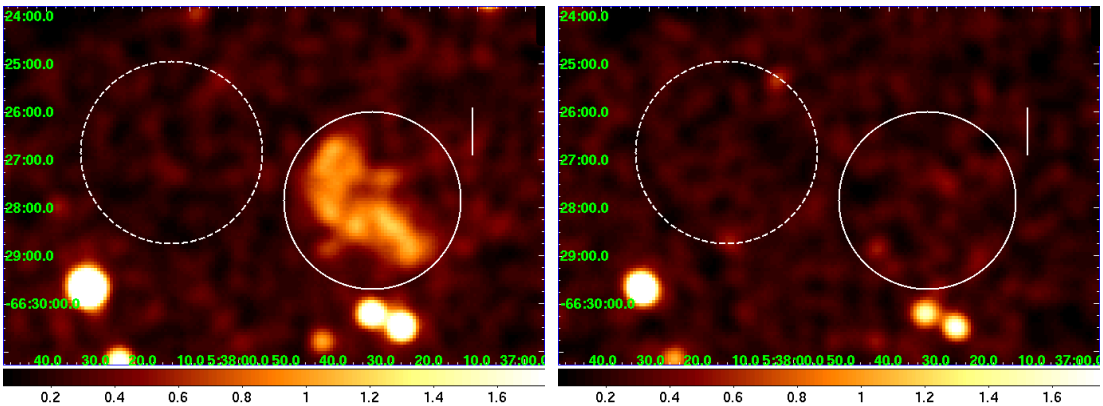

Figure B.1: The *XMM-Newton* X-ray SNR image; J0537.4-6628 (DEM L256).

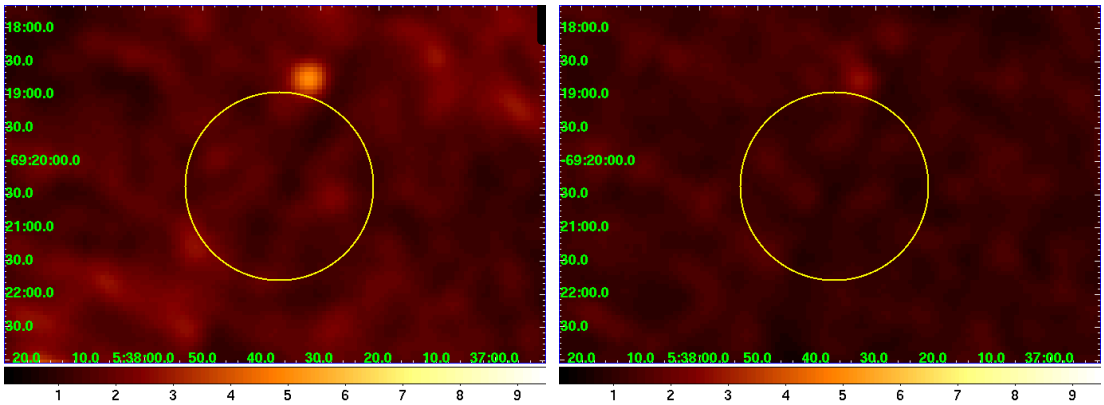

Figure B.1: The *XMM-Newton* X-ray SNR image; J0537.6-6920 (B0538-6922).

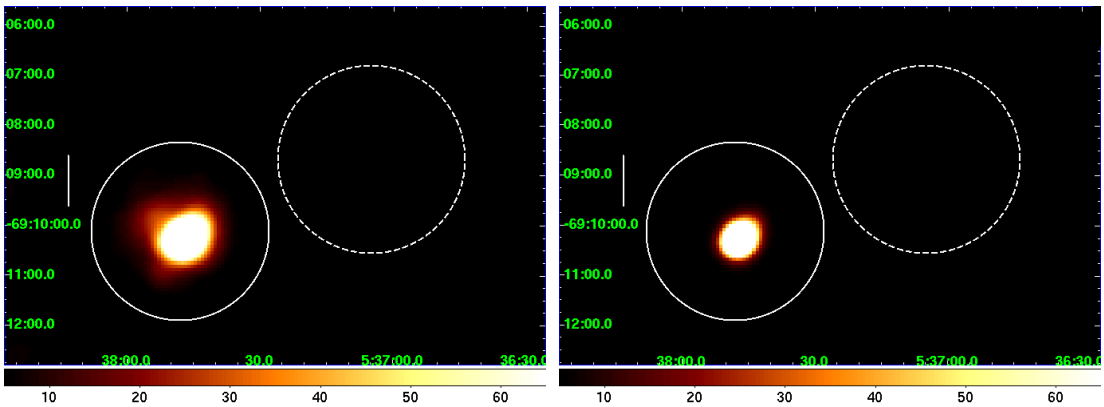

Figure B.1: The *XMM-Newton* X-ray SNR image; J0537.8-6910 (N157B).

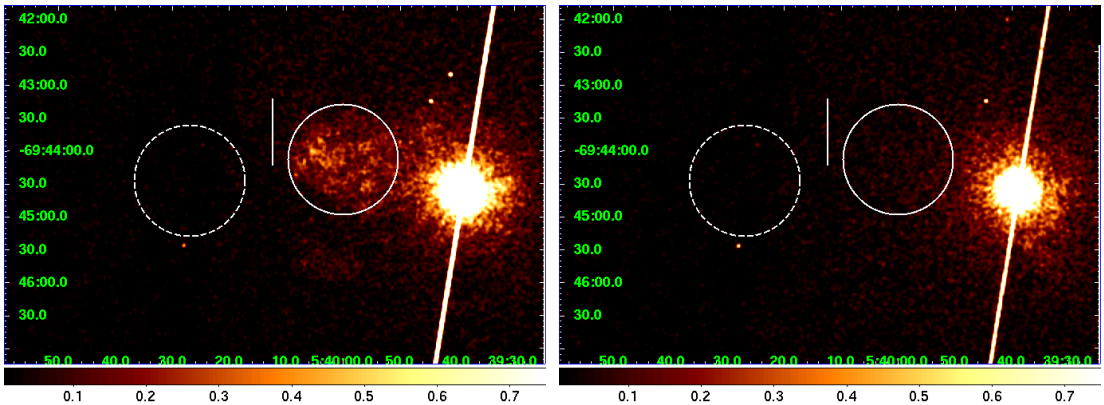

Figure B.1: The *Chandra* X-ray SNR image; J0540.0-6944 (N159).

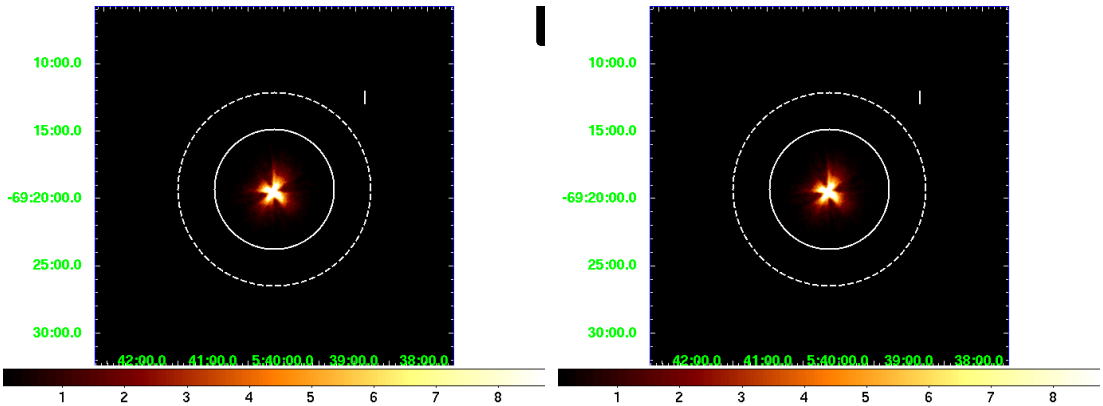

Figure B.1: The *Suzaku* X-ray SNR image; J0540.2-6920 (B0540-693).

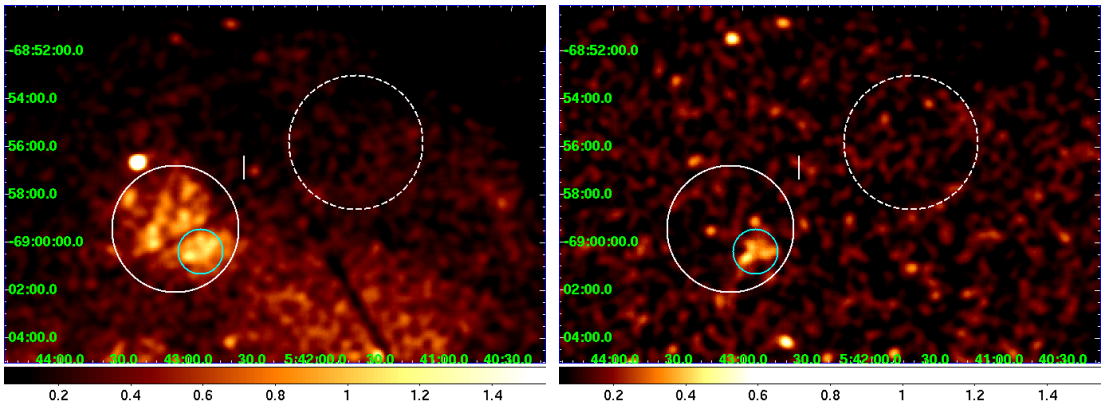

Figure B.1: The *XMM-Newton* X-ray SNR image; J0543.1-6858 (DEM L299).

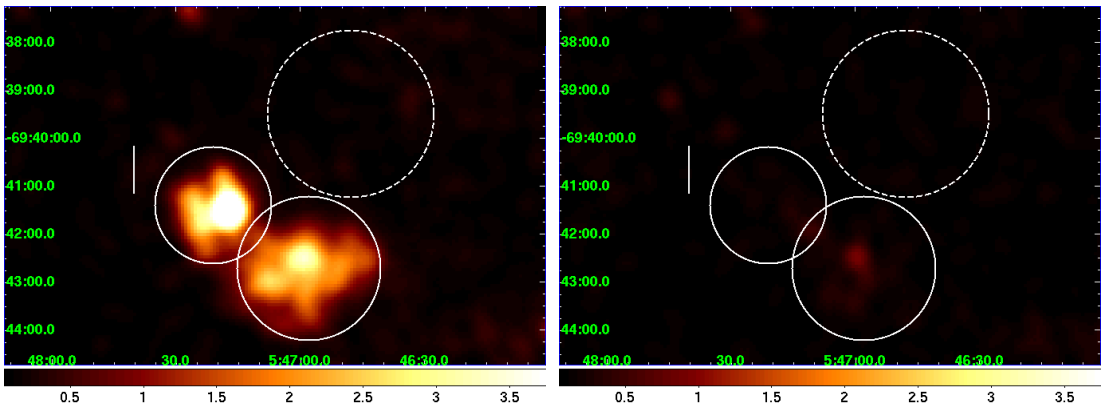

Figure B.1: The *XMM-Newton* X-ray SNR image; J0547.0-6943 (DEM L316B; right and DEM L316A; left).

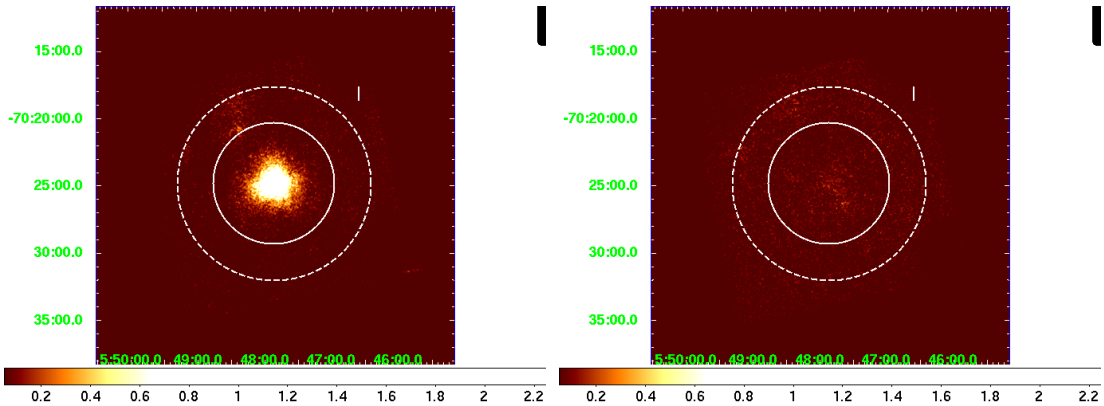

Figure B.1: The *Suzaku* X-ray SNR image; J0547.8-7025 (B0548-704).

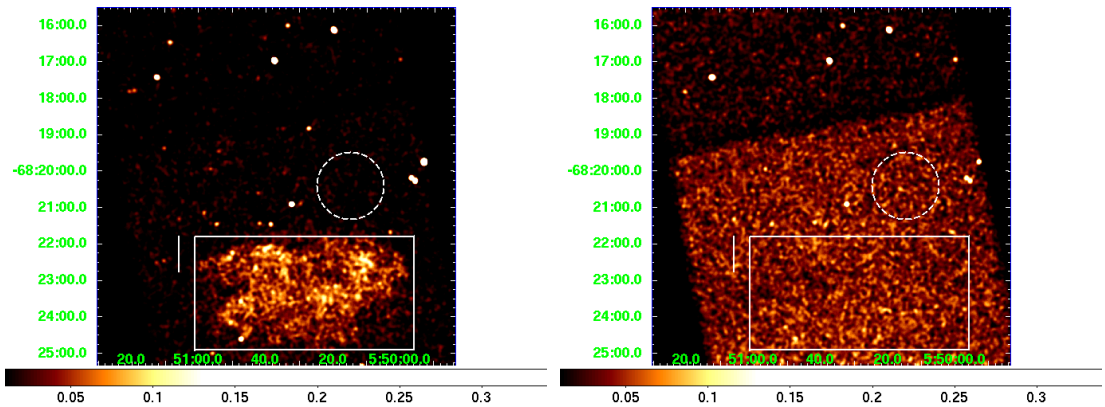

Figure B.1: The *Chandra* X-ray SNR image; J0550.5-6823.

Appendix C

Individual Analysis

C.1 The Hard Diffuse Emission from J0543.1-6858 (DEM L299)

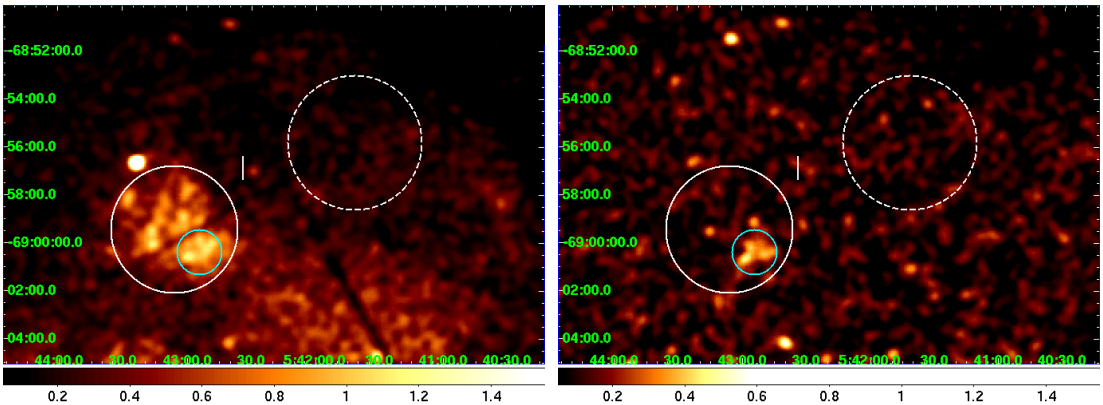

Figure C.1: The J0543.1-6858 (DEM L299) images in the 0.5–2.0 (left) and 2.0–10.0 keV (right). The white solid and dotted circles are represented with the source and background regions. The sky blue solid circle is also represented with the source region of the hard diffuse emission (source A).

We found the diffuse emission (source A) in the hard X-ray image (see figure C.1; right), and analyzed the source A with "$1kT1nt$ + power law (2)". In order to exclude the source photons, we selected the sky blue region in figure C.1 to cover the source A. The background region was also utilized the same one with J0543.1-6858 (DEM L299). Through the spectral analysis, the normalization of the thermal and non-thermal components were set to vary, and the other parameters were fixed at the best-fit parameters of J0543.1-6858 (DEM L299). In figure C.2 we present the best-fit spectrum of the source A. The best-fit parameters of this entire remnant and the source A are summarized in table C.1.

The flux of the source A was estimated to be 0.19×10^{-12} erg s cm^{-2}, corresponded to ∼40 % of the hard X-ray emission from the entire remnant. The hard X-ray emission from the entire remnant did not be explained only with the source A. The remaining

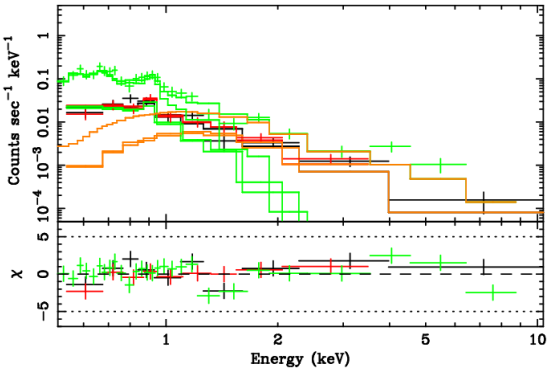

Figure C.2: The black, red and green crosses show the data points from the MOS1, MOS2 and pn, respectively. The green and orange solid histograms show the thermal and non-thermal components, respectively. The lower panel shows the residuals from the best-fit model.

Table C.1: The best-fit parameters of the entire remnant and the source A.*

Parameters	Entire SNR	Source A
$N_{\rm H}^{G}$ ($\times 10^{20}$ cm^{-2})	6.54 (fixed)	6.54 (fixed)
$N_{\rm H}^{L}$ ($\times 10^{21}$ cm^{-2})	$8.35^{+0.58}_{-0.62}$	8.35 (fixed)
Γ	$2.56^{+0.50}_{-0.42}$	2.56 (fixed)
Flux ($\times 10^{-12}$ erg s^{-1} cm^{-2}‡)	$0.48^{+0.11}_{-0.08}$	0.19±0.03
$kT_{\rm e}$ (keV)	0.18±0.01	0.18 (fixed)
$\log(n_{\rm e}t)$ (cm^{-3} s^{-1})	$11.4^{+0.3}_{-0.2}$	11.4 (fixed)
EM ($\times 10^{60}$ cm^{-2}†)	$1.08^{+0.21}_{-0.31}$	0.19±0.02
χ^2 ($d.o.f.$)	184.3 (134)	69.8 (45)

* The errors in the parentheses represent the 90 % confidence intervals.
† Emission measure $EM = \int n_{\rm e} n_{\rm H} dV$, where $n_{\rm e}$ and V are the electron density and the plasma volume. The distance to SNRs in the LMC is assumed to be 50 kpc (Feast, 1999)
‡ Intrinsic flux in the 0.5–10.0 keV band.

hard X-ray emission may be accumulated point-like sources. In actually, there are several point-like sources in figure C.1 (right).

C.2 J0505.7-6753 (DEM L71)

We identified the point-like source J050550.3-675017 close to J0505.7-6753 (DEM L71) in the hard X-ray band image. This source have been identified as the quasar located at $z = 0.07$ from the SIMBAD database. Since this source cannot be separates well by *Suzaku* spatially, we have attempted to analyze *Chandra* data in order to characterize its X-ray emission. In doing this, we utilize the *Chandra* data for this SNR observed on 2004 July 6–7 using the ACIS detector in full-frame time exposure mode. Standard cleaning procedure were applied to the data, and the resultant dead-time corrected useful exposure time was

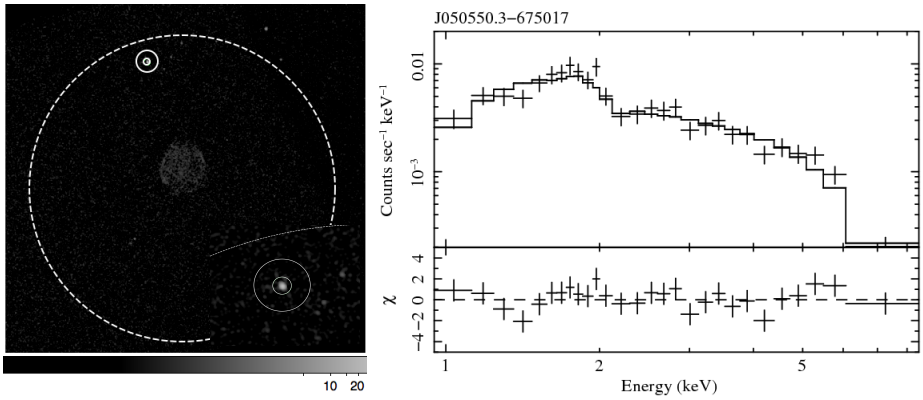

Figure C.3: Left: J050550.3-675017 image in the 2.0-10.0 keV. The source and background regions of this point source are represented with the solid circle and annulus, respectively. The dotted circle is also represented with the source region observed by *Suzaku*. The lower right in this figure is the expanded figure around this point source. Right: The upper panel shows the background-subtracted ACIS spectrum of J050550.3-675017. The lower panel shows the residuals to the fit.

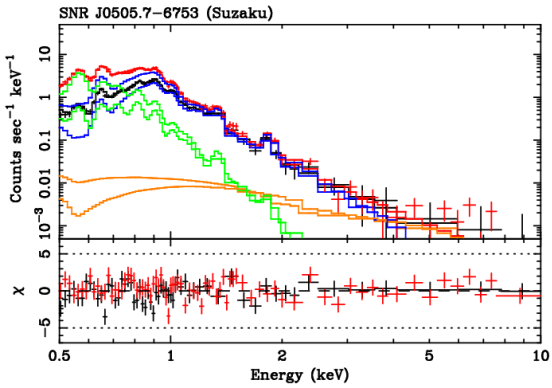

Figure C.4: The data and the best-fit spectra. SNR names are on the top of each panel. The black and red crosses show the data points from the FI and BI CCDs in *Suzaku*, respectively. In two components VNEI model, the green and blue solid histograms show the cool and hot component, respectively. The lower panel shows the residuals from the best-fit model. The black solid histogram shows the non-thermal component.

54 ksec. In figure C.3, we present the image taken by *Chandra* in the 2.0–10.0 keV band. J0505.7-6753 (DEM L71) and J050550.3-675017 are clearly separated. We fitted this point source with a single POWER LAW model attenuated by an photoelectric absorption. The best-fit parameters were the hydrogen column density of $1.04^{+0.27}_{-0.23} \times 10^{22}$ cm^{-3}, the photon index of $1.59^{+0.25}_{-0.21}$, and the intrinsic flux of $(0.25\pm0.03) \times 10^{-12}$ erg s^{-1} cm^{-2} in the 2.0–10.0 keV. This model provided an acceptable fit with the χ^2 $(d.o.f)$ of 26.5 (25).

By freezing all parameters of this source, we carried out the spectral analysis with "$1kT1nt$–$2kT1nt$ + Power law (2)". In the early phase of the *Suzaku* mission, the energy gain has a large uncertainty (Koyama et al., 2007). The gain uncertainty is $\sim$ 10 eV, according to the previous studies on SNRs (Yamaguchi et al. 2008; Bamba et al. 2008;

Someya et al. 2010). J0505.7-6753 (DEM L71) is one of the early phase observations. If the energy offset is to be floated, that is converged to $\sim -8 \pm 1$ eV and $\sim 5 \pm 1$ eV, for the FI and BI spectra, respectively. Although these gain offset values are within the gain uncertainty, this study significantly improved the fit, while the difference in the temperature and the ionization parameter are within ~ 4 % at the 90 % confidence level. In figure C.4 we present the best-fit spectrum with "$2kT1nt$". This model is utilized for discussions.

Appendix D

Systematic Errors of Spectral Modeling

In this chapter, we check the systematic errors of the spectral modelings.

D.1 Spectral Modeling

In this section, we increased model parameters until χ^2_ν of $\leq$1.25, 1.75 and 2.00 to check the systematic errors of the spectral modelings. In this section, we did not utilize "$3kT3nt$" model, since the X-ray emission from such SNRs was complex.

D.1.1 χ^2_ν of $\leq$2.00

In this subsection, we increased model parameters until χ^2_ν of $\leq$2.00. The adopted models are summarized in table D.1. In this threshold, we altered best-fit models for the following 7 SNRs; J0505.7-6753 (DEM L71), J0505.9-6802 (N23), J0534.3-7033 (DEM L238), J0536.1-7039 (DEM L249), J0537.4-6628 (DEM L256), J0547.0-6943 (DEM L316B), and J0547.8-7025 (B0548-704). The others are adopted the same parameters in chapter § 4. The detailed spectral analysis of J0505.7-6753 (DEM L71) is summarized in appendix § C.2. In figure D.1 we present the altered best-fit spectra. The best-fit parameters of these SNRs are summarized in table D.2.

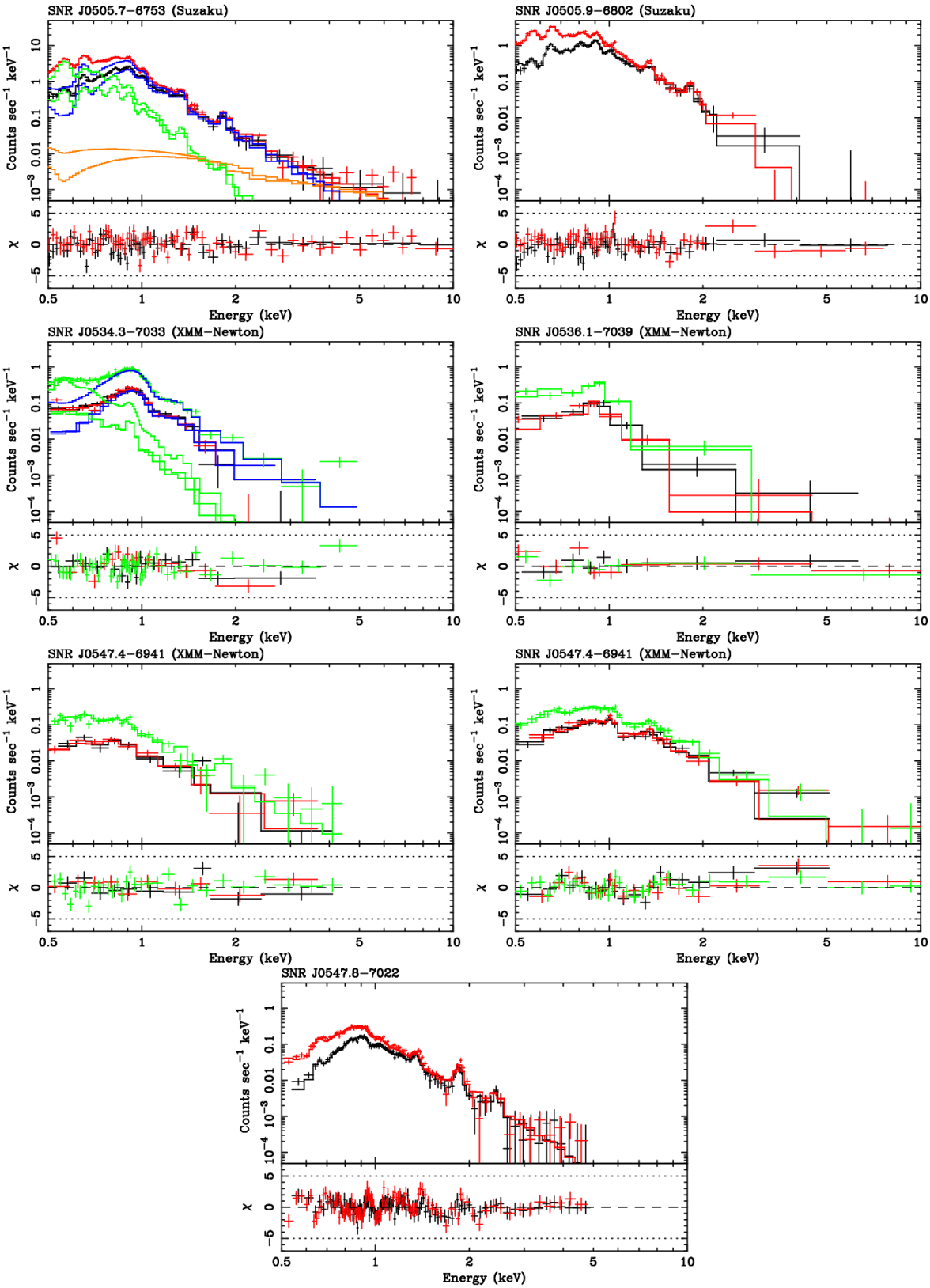

Figure D.1: The data and the best-fit spectra. SNR names are on the top of each panel. The black and red crosses show the data points from the FI and BI CCDs in *Suzaku*, respectively. The black, red and green crosses show the data points from the MOS1, MOS2 and pn in *XMM-Newton*. The orange solid histogram is represented with the non-thermal component. The green and blue solid histograms are represented with the thermal components. The lower panel shows the residuals from the best-fit model. The adopted threshold is the χ^2_ν of ≤ 2.00.

Table D.1: The χ^2 ($d.o.f./\chi^2_\nu$) for all models*.

Name	Other name	$1kT1nt$	$2kT1nt$	$1kT2nt$	$2kT2nt$	$3kT3nt$
			χ^2 ($d.o.f/\chi^2_\nu$)			
J0449.3-6920	-	**5.7 (20/0.29)**	-	-	-	-
J0450.2-6922	B0450-6927	**17.8 (24/0.74)**	-	-	-	-
J0450.4-7050	B0450-709	**43.7 (53/0.82)**	-	-	-	-
J0453.2-6655	N4	**93.6 (95/0.99)**	-	-	-	-
J0453.6-6829	B0453-685	**224.0 (167/1.34)**	-	-	-	-
J0453.9-7000	B0454-7005	**67.9 (50/1.36)**	-	-	-	-
J0454.6-6713	N9	100.3 (30/3.34)	68.7 (28/2.45)	73.4 (28/2.62)	68.6 (27/2.54)	54.3 (24/2.26)
J0454.8-6626	N11L	**114.1 (108/1.06)**	-	-	-	-
J0455.6-6839	N86	**18.7 (17/1.10)**	-	-	-	-
J0459.9-7008	N186D	**12.5 (10/1.25)**	-	-	-	-
J0505.7-6753	DEM L71	554.3 (125/4.43)	**191.2 (123/1.55)**	-	-	-
J0505.9-6802	N23	**163.1 (107/1.52)**	-	-	-	-
J0506.1-6541	-	**47.5 (48/0.99)**	-	-	-	-
J0509.0-6844	N103B	-	-	-	-	-
J0509.5-6731	B0509-67.5	-	-	-	-	-
J0518.7-6939	N120	**100.7 (77/1.31)**	-	-	-	-
J0519.6-6902	B0519-690	-	-	-	-	-
J0519.7-6926	B0520-694	**133.0 (122/1.09)**	-	-	-	-
J0523.1-6753	N44	**36.2 (44/0.82)**	-	-	-	-
J0525.1-6938	N132D	12425.7 (1066/11.7)	7204.2 (1064/6.8)	5569.7 (1064/5.2)	5010.4 (1063/4.7)	4185.5 (1060/4.0)
J0525.4-6559	N49B	**213.7 (156/1.37)**	-	-	-	-
J0526.0-6605	N49	1669.3 (260/6.42)	674.7 (258/2.62)	813.6 (258/3.15)	535.1 (257/2.08)	394.1 (254/1.55)
J0527.6-6912	B0528-692	**36.3 (38/0.96)**	-	-	-	-
J0531.9-7100	N206	**69.2 (83/0.83)**	-	-	-	-
J0532.5-6732	B0532-675	**81.9 (76/1.08)**	-	-	-	-
J0534.0-6955	B0534-699	429.2 (190/2.26)	**280.8 (188/1.49)**	-	-	
J0534.3-7033	DEM L238	284.1 (82/3.47)	**160.3 (80/2.00)**	-	-	-
J0535.5-6916	SNR 1987A	455.3 (225/2.03)	**218.9 (223/0.98)**	-		-
J0535.7-6602	N63A	9088.3 (712/12.8)	3176.0 (710/4.5)	2417.1 (710/3.4)	3305.5 (709/4.6)	2297.692 (706/3.3)
J0535.8-6918	Honeycomb	**126.5 (95/1.33)**	-	-	-	-
J0536.1-6735	DEM L241	450.4 (181/2.49)	443.3 (179/2.48)	412.6 (179/2.31)	418.6 (178/2.35)	457.6 (175/2.62)
J0536.1-7039	DEM L249	**31.6 (19/1.66)**	-	-	-	-
J0536.2-6912	30 DorC	**100.8 (69/1.46)**	-	-	-	-
J0537.4-6628	DEM L256	**83.0 (49/1.69)**	-	-	-	-
J0537.8-6910	N157B	**469.2 (486/0.97)**	-	-	-	-
J0540.0-6944	N159	**91.6 (77/1.19)**	-	-	-	-
J0540.2-6920	B0540-693	**526.6 (512/1.03)**	-	-	-	-
J0543.1-6858	DEM L299	**184.3 (134/1.38)**	-	-	-	-
J0547.0-6943	DEM L316B	**107.8 (66/1.63)**	-	-	-	-
J0547.4-6941	DEM L316A	**89.1 (72/1.24)**	-	-	-	-
J0547.8-7025	B0548-704	**304.4 (202/1.51)**	-	-	-	-
J0550.5-6823	-	**29.3 (25/1.17)**	-	-	-	-

* The adopted models were represented with in bold type. The adopted threshold is the χ^2_ν of ≤ 2.00.

Table D.2: The Best-Fit Parameters of the Thermal Component.*

	J0505.7-6753 (DEM L71)	J0505.9-6802 (N23)
$N_{\rm H}^{\rm G}$ ($\times 10^{20}$ cm^{-2})	5.75 (fixed)	5.80 (fixed)
$N_{\rm H}^{\rm L}$ ($\times 10^{21}$ cm^{-2})	<0.12	$3.68^{+0.14}_{-0.10}$
$kT_{\rm e1}$ (keV)	0.29±0.01	0.41±0.01
$kT_{\rm e2}$ (keV)	0.79±0.01	-
$\log(n_{\rm e}t_1$ [cm^{-2} s])	$10.92^{+0.03}_{-0.02}$	10.63±0.03
$\log(n_{\rm e}t_2$ [cm^{-2} s])	-	-
$n_{\rm e}n_{\rm H}V_1$	$2.65^{+0.21}_{-0.30} \times 10^{59}$	$1.29^{+0.07}_{-0.03} \times 10^{60}$
$n_{\rm e}n_{\rm H}V_2$	$2.28^{+0.22}_{-0.41} \times 10^{59}$	-
Flux†	1.52×10^{-11}	9.22×10^{-13}
$\chi^2/d.o.f.$	191.2 (123)	163.1 (107)
	J0534.3-7033 (DEM L238)	J0536.1-7039 (DEM L249)
$N_{\rm H}^{\rm G}$ ($\times 10^{20}$ cm^{-2})	6.90 (fixed)	7.06 (fixed)
$N_{\rm H}^{\rm L}$ ($\times 10^{21}$ cm^{-2})	<0.88	$16.3^{+9.8}_{-9.3}$
$kT_{\rm e1}$ (keV)	0.18±0.01	0.10±0.02
$kT_{\rm e2}$ (keV)	$0.77^{+0.01}_{-0.03}$	-
$\log(n_{\rm e}t_1$ [cm^{-2} s])	$13.17^{+0.53}_{-1.35}$	$13.47^{+0.22}_{-1.60}$
$\log(n_{\rm e}t_2$ [cm^{-2} s])	-	-
$n_{\rm e}n_{\rm H}V_1$	$1.75^{+1.62}_{-0.69} \times 10^{58}$	$1.26^{+9.76}_{-1.00} \times 10^{62}$
$n_{\rm e}n_{\rm H}V_2$	$8.39^{+1.98}_{-2.49} \times 10^{57}$	-
Flux†	5.26×10^{-13}	4.56×10^{-13}
$\chi^2/d.o.f.$	160.0/80	31.6/19
	J0537.4-6628 (DEM L256)	J0547.8-7025 (DEM L316B)
$N_{\rm H}^{\rm G}$ ($\times 10^{20}$ cm^{-2})	5.78 (fixed)	7.04 (fixed)
$N_{\rm H}^{\rm L}$ ($\times 10^{21}$ cm^{-2})	$1.34^{+1.77}_{-1.17}$	$1.68^{+0.83}_{-0.62}$
$kT_{\rm e1}$ (keV)	$1.17^{+0.77}_{-0.40}$	$0.66^{+0.04}_{-0.06}$
$kT_{\rm e2}$ (keV)	-	-
$\log(n_{\rm e}t_1$ [cm^{-2} s])	$10.10^{+0.29}_{-0.18}$	$13.32^{+0.38}_{-1.24}$
$\log(n_{\rm e}t_2$ [cm^{-2} s])	-	-
$n_{\rm e}n_{\rm H}V_1$	$0.15^{+5.35}_{-0.04} \times 10^{58}$	$5.39^{+1.70}_{-1.42} \times 10^{59}$
$n_{\rm e}n_{\rm H}V_2$	-	-
Flux†	1.19×10^{-13}	6.93×10^{-13}
$\chi^2/d.o.f.$	83.0/49	107.8/66
	J0547.8-7025 (B0548-704)	
$N_{\rm H}^{\rm G}$ ($\times 10^{20}$ cm^{-2})	7.28 (fixed)	
$N_{\rm H}^{\rm L}$ ($\times 10^{21}$ cm^{-2})	<0.70	
$kT_{\rm e1}$ (keV)	0.69±0.03	
$kT_{\rm e2}$ (keV)	-	
$\log(n_{\rm e}t_1$ [cm^{-2} s])	$10.82^{+0.04}_{-0.08}$	
$\log(n_{\rm e}t_2$ [cm^{-2} s])	-	
$n_{\rm e}n_{\rm H}V_1$	$4.29^{+0.60}_{-0.52} \times 10^{58}$	
$n_{\rm e}n_{\rm H}V_2$	-	
Flux†	1.29×10^{-12}	
$\chi^2/d.o.f.$	304.4/202	

* The errors in the parentheses represent the 90 % confidence intervals. The adopted threshold is the χ^2_ν of ≤ 2.00.

† Emission measure $EM = \int n_{\rm e}n_{\rm H}dV$, where $n_{\rm e}$ and V are the electron density and the plasma volume. The distance to SNRs in the LMC is assumed to be 50 kpc (Feast, 1999).

D.1.2 χ^2_ν of $\leq$1.75

In this subsection, we increased model parameters until χ^2_ν of $\leq$1.75. The adopted models are summarized in table D.3. In this threshold, we altered best-fit models for the following 6 SNRs; J0505.7-6753 (DEM L71), J0505.9-6802 (N23), J0536.1-7039 (DEM L249), J0537.4-6628 (DEM L256), J0547.0-6943 (DEM L316B), J0547.8-7025 (B0548-704). The others are adopted the same parameters in chapter § 4.The detailed spectral analysis of J0505.7-6753 (DEM L71) is summarized in appendix § C.2. In figure D.2 we present the altered best-fit spectra. The best-fit parameters of these SNRs are summarized in table D.4.

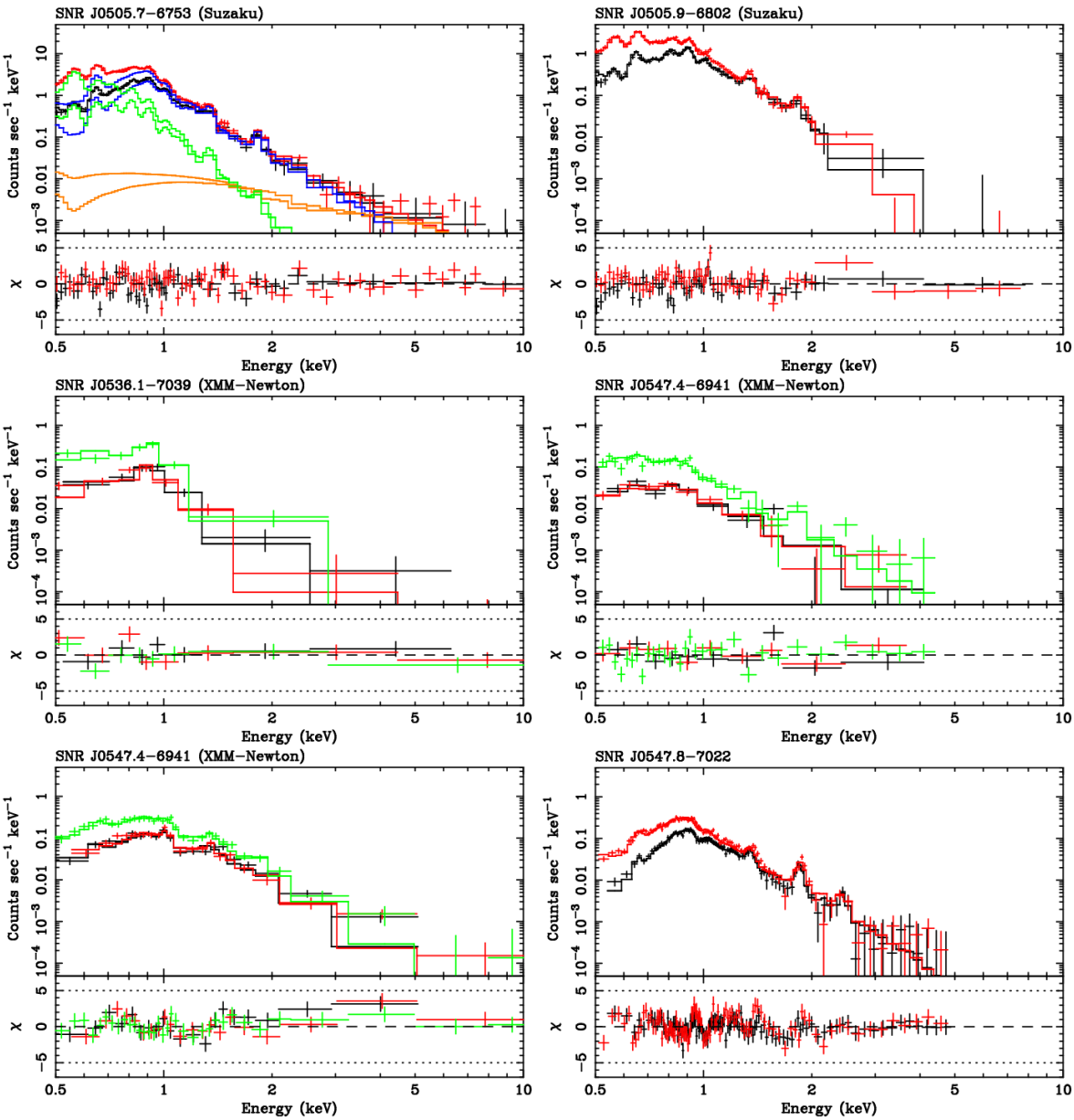

Figure D.2: The data and the best-fit spectra. SNR names are on the top of each panel. The black and red crosses show the data points from the FI and BI CCDs in *Suzaku*, respectively. The black, red and green crosses show the data points from the MOS1, MOS2 and pn in *XMM-Newton*. The orange solid histogram is represented with the non-thermal component. The green and blue solid histograms are represented with the thermal components. The lower panel shows the residuals from the best-fit model. The adopted threshold is the χ^2_ν of ≤ 1.75.

Table D.3: The χ^2 ($d.o.f./\chi^2_\nu$) for all models*.

Name	Other name	$1kT1nt$	$2kT1nt$	$1kT2nt$	$2kT2nt$	$3kT3nt$
			χ^2 ($d.o.f/\chi^2_\nu$)			
J0449.3-6920	-	**5.7 (20/0.29)**	-	-	-	-
J0450.2-6922	B0450-6927	**17.8 (24/0.74)**	-	-	-	-
J0450.4-7050	B0450-709	**43.7 (53/0.82)**	-	-	-	-
J0453.2-6655	N4	**93.6 (95/0.99)**	-	-	-	-
J0453.6-6829	B0453-685	**224.0 (167/1.34)**	-	-	-	-
J0453.9-7000	B0454-7005	**67.9 (50/1.36)**	-	-	-	-
J0454.6-6713	N9	100.3 (30/3.34)	68.7 (28/2.45)	73.4 (28/2.62)	68.6 (27/2.54)	54.3 (24/2.26)
J0454.8-6626	N11L	**114.1 (108/1.06)**	-	-	-	-
J0455.6-6839	N86	**18.7 (17/1.10)**	-	-	-	-
J0459.9-7008	N186D	**12.5 (10/1.25)**	-	-	-	-
J0505.7-6753	DEM L71	554.3 (125/4.43)	**191.2 (123/1.55)**	276.4 (123/2.25)	189.4 (122/1.55)	187.7 (119/1.58)
J0505.9-6802	N23	**163.1 (107/1.52)**	109.7 (105/1.05)	120.5 (105/1.15)	-	-
J0506.1-6541	-	**47.5 (48/0.99)**	-	-	-	-
J0509.0-6844	N103B	-	-	-	-	-
J0509.5-6731	B0509-67.5	-	-	-	-	-
J0518.7-6939	N120	**100.7 (77/1.31)**	-	-	-	-
J0519.6-6902	B0519-690	-	-	-	-	-
J0519.7-6926	B0520-694	**133.0 (122/1.09)**	-	-	-	-
J0523.1-6753	N44	**36.2 (44/0.82)**	-	-	-	-
J0525.1-6938	N132D	12425.7 (1066/11.7)	7204.2 (1064/6.8)	5569.7 (1064/5.2)	5010.4 (1063/4.7)	4185.5 (1060/4.0)
J0525.4-6559	N49B	**213.7 (156/1.37)**	-	-	-	-
J0526.0-6605	N49	1669.3 (260/6.42)	674.7 (258/2.62)	813.6 (258/3.15)	535.1 (257/2.08)	**394.1 (254/1.55)**
J0527.6-6912	B0528-692	**36.3 (38/0.96)**	-	-	-	-
J0531.9-7100	N206	**69.2 (83/0.83)**	-	-	-	-
J0532.5-6732	B0532-675	**81.9 (76/1.08)**	-	-	-	-
J0534.0-6955	B0534-699	429.2 (190/2.26)	**280.8 (188/1.49)**	304.0 (188/1.62)	218.2 (1.17)	
J0534.3-7033	DEM L238	284.1 (82/3.47)	160.0 (80/2.00)	172.5 (80/2.16)	160.0 (79/2.03)	153.0 (76/2.01)
J0535.5-6916	SNR 1987A	449.3 (225/2.00)	**218.9 (223/0.98)**	304.0 (188/1.62)		-
J0535.7-6602	N63A	9088.3 (712/12.8)	3176.0 (710/4.5)	2417.1 (710/3.4)	3305.5 (709/4.6)	2297.692 (706/3.3)
J0535.8-6918	Honeycomb	**126.5 (95/1.33)**	-	-	-	-
J0536.1-6735	DEM L241	450.4 (181/2.49)	443.3 (179/2.48)	412.6 (179/2.31)	418.6 (178/2.35)	457.6 (175/2.62)
J0536.1-7039	DEM L249	**31.6 (19/1.66)**	-	-	-	-
J0536.2-6912	30 DorC	**100.8 (69/1.46)**	-	-	-	-
J0537.4-6628	DEM L256	**83.0 (49/1.69)**	-	-	-	-
J0537.8-6910	N157B	**469.2 (486/0.97)**	-	-	-	-
J0540.0-6944	N159	**91.6 (77/1.19)**	-	-	-	-
J0540.2-6920	B0540-693	**526.6 (512/1.03)**	-	-	-	-
J0543.1-6858	DEM L299	**184.3 (134/1.38)**	-	-	-	-
J0547.0-6943	DEM L316B	**107.8 (66/1.63)**	-	-	-	-
J0547.4-6941	DEM L316A	**89.1 (72/1.24)**	-	-	-	-
J0547.8-7025	B0548-704	**304.4 (202/1.51)**	-	-	-	-
J0550.5-6823	-	**29.3 (25/1.17)**	-	-	-	-

* The adopted models were represented with in bold type. The adopted threshold is the χ^2_ν of ≤ 1.75.

Table D.4: The Best-Fit Parameters of the Thermal Component.*

	J0505.7-6753 (DEM L71)	J0505.9-6802 (N23)
$N_{\rm H}^{\rm G}$ ($\times 10^{20}$ cm^{-2})	5.75 (fixed)	5.80 (fixed)
$N_{\rm H}^{\rm L}$ ($\times 10^{21}$ cm^{-2})	<0.12	$3.68^{+0.14}_{-0.10}$
$kT_{\rm e1}$ (keV)	0.29±0.01	0.41±0.01
$kT_{\rm e2}$ (keV)	0.79±0.01	-
$\log(n_{\rm e}t_1$ [cm^{-2} s])	$10.92^{+0.03}_{-0.02}$	10.63±0.03
$\log(n_{\rm e}t_2$ [cm^{-2} s])	-	-
$n_{\rm e}n_{\rm H}V_1$	$2.65^{+0.21}_{-0.30} \times 10^{59}$	$1.29^{+0.07}_{-0.03} \times 10^{60}$
$n_{\rm e}n_{\rm H}V_2$	$2.28^{+0.22}_{-0.41} \times 10^{59}$	-
Flux†	1.52×10^{-11}	9.22×10^{-13}
$\chi^2/d.o.f.$	191.2 (123)	163.1 (107)
	J0536.1-7039 (DEM L249)	J0537.4-6628 (DEM L256)
$N_{\rm H}^{\rm G}$ ($\times 10^{20}$ cm^{-2})	7.06 (fixed)	5.78 (fixed)
$N_{\rm H}^{\rm L}$ ($\times 10^{21}$ cm^{-2})	$16.3^{+9.8}_{-9.3}$	$1.34^{+1.77}_{-1.17}$
$kT_{\rm e1}$ (keV)	0.10±0.02	$1.17^{+0.77}_{-0.40}$
$kT_{\rm e2}$ (keV)	-	-
$\log(n_{\rm e}t_1$ [cm^{-2} s])	$13.47^{+0.22}_{-1.60}$	$10.10^{+0.29}_{-0.18}$
$\log(n_{\rm e}t_2$ [cm^{-2} s])	-	-
$n_{\rm e}n_{\rm H}V_1$	$1.26^{+9.76}_{-1.00} \times 10^{62}$	$0.15^{+5.35}_{-0.04} \times 10^{58}$
$n_{\rm e}n_{\rm H}V_2$	-	-
Flux†	4.56×10^{-13}	1.19×10^{-13}
$\chi^2/d.o.f.$	31.6/19	83.0/49
	J0547.8-7025 (DEM L316B)	J0547.8-7025 (B0548-704)
$N_{\rm H}^{\rm G}$ ($\times 10^{20}$ cm^{-2})	7.04 (fixed)	7.28 (fixed)
$N_{\rm H}^{\rm L}$ ($\times 10^{21}$ cm^{-2})	$1.68^{+0.83}_{-0.62}$	<0.70
$kT_{\rm e1}$ (keV)	$0.66^{+0.04}_{-0.06}$	0.69±0.03
$kT_{\rm e2}$ (keV)	-	-
$\log(n_{\rm e}t_1$ [cm^{-2} s])	$13.32^{+0.38}_{-1.24}$	$10.82^{+0.04}_{-0.08}$
$\log(n_{\rm e}t_2$ [cm^{-2} s])	-	-
$n_{\rm e}n_{\rm H}V_1$	$5.39^{+1.70}_{-1.42} \times 10^{59}$	$4.29^{+0.60}_{-0.52} \times 10^{58}$
$n_{\rm e}n_{\rm H}V_2$	-	-
Flux†	6.93×10^{-13}	1.29×10^{-12}
$\chi^2/d.o.f.$	107.8/66	304.4/202

* The errors in the parentheses represent the 90 % confidence intervals. The adopted threshold is the χ^2_ν of ≤ 1.75.

† Emission measure $EM = \int n_{\rm e}n_{\rm H}dV$, where $n_{\rm e}$ and V are the electron density and the plasma volume. The distance to SNRs in the LMC is assumed to be 50 kpc (Feast, 1999).

D.1.3 χ^2_ν of $\leq$1.25

In this subsection, we increased model parameters until χ^2_ν of $\leq$1.25. The adopted models are summarized in table D.5. In this threshold, we altered best-fit models for the following 5 SNRs; J0453-6829 (B0453-685), J0525.3-6559 (N49B), J0534.0-6955 (B0534-699), J0536.2-6912 (30 Dor C), J 0547.8-7025 (B0548-704). The others are adopted the same parameters in chapter § 4.In figure D.3 we present the altered best-fit spectra. The best-fit parameters of these SNRs are summarized in table D.6.

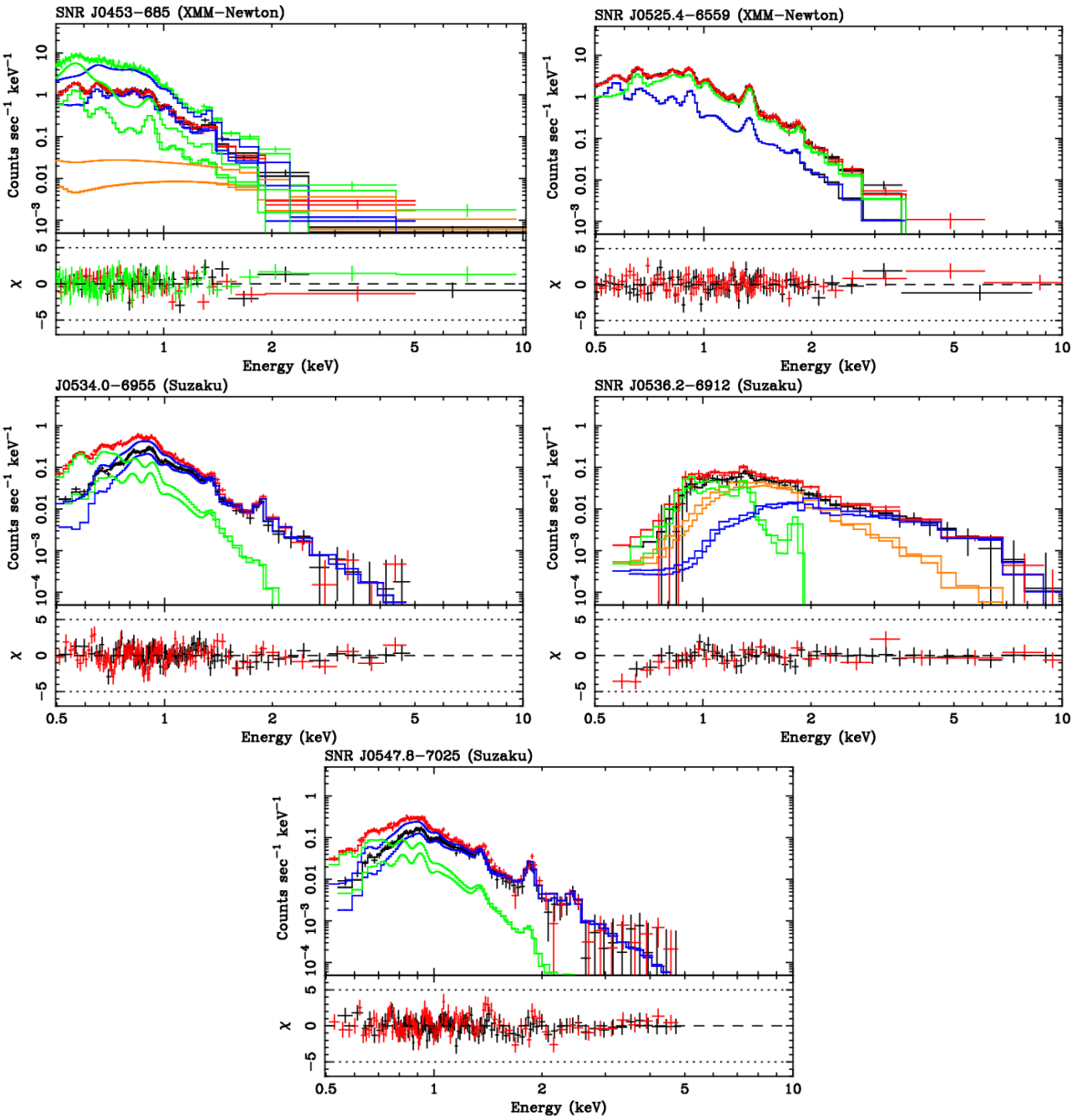

Figure D.3: The data and the best-fit spectra. SNR names are on the top of each panel. The black and red crosses show the data points from the FI and BI CCDs in *Suzaku*, respectively. The black, red and green crosses show the data points from the MOS1, MOS2 and pn in *XMM-Newton*. The orange solid histogram is represented with the non-thermal component. The green and blue solid histograms are represented with the thermal components. The lower panel shows the residuals from the best-fit model. The adopted threshold is the χ^2_ν of ≤ 1.25.

Table D.5: The χ^2 ($d.o.f./\chi^2_\nu$) for all models*.

Name	Other name	$1kT1nt$	$2kT1nt$	$1kT2nt$	$2kT2nt$	$3kT3nt$
		χ^2 ($d.o.f/\chi^2_\nu$)				
J0449.3-6920	-	**5.7 (20/0.29)**	-	-	-	-
J0450.2-6922	B0450-6927	**17.8 (24/0.74)**	-	-	-	-
J0450.4-7050	B0450-709	**43.7 (53/0.82)**	-	-	-	-
J0453.2-6655	N4	**93.6 (95/0.99)**	-	-	-	-
J0453.6-6829	B0453-685	224.0 (167/1.34)	222.3 (165/1.35)	**196.4 (165/1.19)**	-	-
J0453.9-7000	B0454-7005	67.9 (50/1.36)	64.9 (48/1.35)	64.6 (48/1.35)	64.6 (47/1.37)	63.4 (44/1.44)
J0454.6-6713	N9	100.3 (30/3.34)	68.7 (28/2.45)	73.4 (28/2.62)	68.6 (27/2.54)	54.3 (24/2.26)
J0454.8-6626	N11L	**114.1 (108/1.06)**	-	-	-	-
J0455.6-6839	N86	**18.7 (17/1.10)**	-	-	-	-
J0459.9-7008	N186D	**12.5 (10/1.25)**	-	-	-	-
J0505.7-6753	DEM L71	554.3 (125/4.43)	191.2 (123/1.55)	276.4 (123/2.25)	189.4 (122/1.55)	187.7 (119/1.58)
J0505.9-6802	N23	163.1 (107/1.52)	**109.7 (105/1.05)**	120.5 (105/1.15)	-	-
J0506.1-6541	-	**47.5 (48/0.99)**	-	-	-	-
J0509.0-6844	N103B	-	-	-	-	-
J0509.5-6731	B0509-67.5	-	-	-	-	-
J0518.7-6939	N120	100.7 (77/1.31)	96.1 (75/1.28)	100.1 (75/1.33)	95.1 (74/1.29)	95.2 (71/1.34)
J0519.6-6902	B0519-690	-	-	-	-	-
J0519.7-6926	B0520-694	**133.0 (122/1.09)**	-	-	-	-
J0523.1-6753	N44	**36.2 (44/0.82)**	-	-	-	-
J0525.1-6938	N132D	12425.7 (1066/11.7)	7204.2 (1064/6.8)	5569.7 (1064/5.2)	5010.4 (1063/4.7)	4185.5 (1060/4.0)
J0525.4-6559	N49B	213.7 (156/1.37)	158.0 (154/1.03)	**151.3 (154/0.98)**	-	-
J0526.0-6605	N49	1669.3 (260/6.42)	674.7 (258/2.62)	813.6 (258/3.15)	535.1 (257/2.08)	394.1 (254/1.55)
J0527.6-6912	B0528-692	**36.3 (38/0.96)**	-	-	-	-
J0531.9-7100	N206	**69.2 (83/0.83)**	-	-	-	-
J0532.5-6732	B0532-675	**81.9 (76/1.08)**	-	-	-	-
J0534.0-6955	B0534-699	429.2 (190/2.26)	280.8 (188/1.49)	304.0 (188/1.62)	**218.2 (187/1.17)**	-
J0534.3-7033	DEM L238	284.1 (82/3.47)	160.0 (80/2.00)	172.5 (80/2.16)	160.0 (79/2.03)	153.0 (76/2.01)
J0535.5-6916	SNR 1987A	455.3 (225/2.03)	**218.9 (223/0.98)**	304.0 (188/1.62)		-
J0535.7-6602	N63A	9088.3 (712/12.8)	3176.0 (710/4.5)	2417.1 (710/3.4)	3305.5 (709/4.6)	2297.692 (706/3.3)
J0535.8-6918	Honeycomb	126.5 (95/1.33)	119.5 (93/1.29)	118.2 (93/1.27)	116.8 (92/1.27)	118.5 (89/1.33)
J0536.1-6735	DEM L241	450.4 (181/2.49)	443.3 (179/2.48)	412.6 (179/2.31)	418.6 (178/2.35)	457.6 (175/2.62)
J0536.1-7039	DEM L249	31.6 (19/1.66)	28.8 (17/1.69)	28.8 (17/1.69)	28.3 (16/1.77)	27.7 (13/2.13)
J0536.2-6912	30 DorC	100.8 (69/1.46)	92.3 (67/1.38)	100.7 (67/1.50)	**76.9 (66/1.17)**	-
J0537.4-6628	DEM L256	83.0 (49/1.69)	74.3 (47/1.58)	69.8 (47/1.49)	68.14 (46/1.48)	67.08 (43/1.56)
J0537.8-6910	N157B	**469.2 (486/0.97)**	-	-	-	-
J0540.0-6944	N159	**91.6 (77/1.19)**	-	-	-	-
J0540.2-6920	B0540-693	**526.6 (512/1.03)**	-	-	-	-
J0543.1-6858	DEM L299	184.3 (134/1.38)	175.1 (132/1.33)	174.4 (132/1.32)	165.1 (131/1.26)	162.9 (128/1.27)
J0547.0-6943	DEM L316B	107.8 (66/1.63)	**60.4 (64/0.94)**	100.1 (64/1.56)	-	-
J0547.4-6941	DEM L316A	**89.1 (72/1.24)**	-	-	-	-
J0547.8-7025	B0548-704	304.4 (202/1.51)	267.3 (200/1.34)	273.1 (200/1.37)	**240.3 (199/1.21)**	-
J0550.5-6823	-	**29.3 (25/1.17)**	-	-	-	-

* The adopted models were represented with in bold type. The adopted threshold is the χ^2_ν of ≤ 1.25.

Table D.6: The Best-Fit Parameters of the Thermal Component.*

	J0453.6-6829 (B0453-685)	J0525.4-6559 (N49B)
$N_{\rm H}^{\rm G}$ ($\times 10^{20}$ cm^{-2})	6.40 (fixed)	5.53 (fixed)
$N_{\rm H}^{\rm L}$ ($\times 10^{21}$ cm^{-2})	<0.33	$2.11^{+0.43}_{-0.28}$
$kT_{\rm e1}$ (keV)	$0.44^{+0.05}_{-0.03}$	$0.54^{+0.04}_{-0.03}$
$kT_{\rm e2}$ (keV)	-	-
$\log(n_{\rm e}t_1$ [cm^{-2} s])	$11.18^{+0.13}_{-0.14}$	$11.05^{+0.07}_{-0.08}$
$\log(n_{\rm e}t_2$ [cm^{-2} s])	$9.87^{+0.32}_{-0.73}$	$10.03^{+0.16}_{-0.15}$
$n_{\rm e}n_{\rm H}V_1$	$1.37^{+0.19}_{-0.31} \times 10^{59}$	$6.42^{+1.38}_{-1.23} \times 10^{59}$
$n_{\rm e}n_{\rm H}V_2$	$5.29^{+1.08}_{-0.98} \times 10^{58}$	$2.33^{+0.76}_{-0.45} \times 10^{59}$
Flux†	4.98×10^{-12}	1.40×10^{-11}
$\chi^2/d.o.f.$	196.4 (165)	151.3/154
	J0534.0-6955 (B0534-699)	J0536.2-6912 (30 Dor C)
$N_{\rm H}^{\rm G}$ ($\times 10^{20}$ cm^{-2})	6.49 (fixed)	6.36 (fixed)
$N_{\rm H}^{\rm L}$ ($\times 10^{21}$ cm^{-2})	$1.84^{+00.52}_{-0.12}$	$42.8^{+3.16}_{-3.84}$
$kT_{\rm e1}$ (keV)	$0.179^{+0.001}_{-0.002}$	0.09 ± 0.01
$kT_{\rm e2}$ (keV)	$0.73^{+0.03}_{-0.01}$	$2.74^{+1.20}_{-0.48}$
$\log(n_{\rm e}t_1$ [cm^{-2} s])	$13.00^{+0.70}_{-0.36}$	$13.57^{+0.13}_{-1.70}$
$\log(n_{\rm e}t_2$ [cm^{-2} s])	$10.85^{+0.00}_{-0.00}$	$13.38^{+0.32}_{-1.81}$
$n_{\rm e}n_{\rm H}V_1$	$4.79^{+1.19}_{-2.83} \times 10^{59}$	$4.14^{+9.23}_{-1.40} \times 10^{63}$
$n_{\rm e}n_{\rm H}V_2$	$3.28^{+2.48}_{-0.14} \times 10^{58}$	$6.07^{+2.44}_{-2.64} \times 10^{58}$
Flux†	2.45×10^{-12}	1.63×10^{-12}
$\chi^2/d.o.f.$	218.2 (187)	76.9/66
	J0547.8-7025 (B0548-704)	
$N_{\rm H}^{\rm G}$ ($\times 10^{20}$ cm^{-2})	7.28 (fixed)	
$N_{\rm H}^{\rm L}$ ($\times 10^{21}$ cm^{-2})	$3.42^{+1.13}_{-0.10}$	
$kT_{\rm e1}$ (keV)	0.20 ± 0.01	
$kT_{\rm e2}$ (keV)	$0.73^{+0.07}_{-0.05}$	
$\log(n_{\rm e}t_1$ [cm^{-2} s])	$12.94^{+0.76}_{-1.35}$	
$\log(n_{\rm e}t_2$ [cm^{-2} s])	$10.85^{+0.06}_{-0.13}$	
$n_{\rm e}n_{\rm H}V_1$	$2.57^{+2.07}_{-1.63} \times 10^{59}$	
$n_{\rm e}n_{\rm H}V_2$	$3.49^{+0.62}_{-0.58} \times 10^{58}$	
Flux†	1.29×10^{-12}	
$\chi^2/d.o.f.$	304.4/202	

* The errors in the parentheses represent the 90 % confidence intervals. The adopted threshold is the χ^2_ν of ≤ 1.25.

† Emission measure $EM = \int n_{\rm e}n_{\rm H}dV$, where $n_{\rm e}$ and V are the electron density and the plasma volume. The distance to SNRs in the LMC is assumed to be 50 kpc (Feast, 1999).

D.2 Comparison

In this section, we check the systematic errors of the spectral modeling for main discussions in the following subsections.

D.2.1 Ne/O

Figure D.4 (Ne/O) shows the derived metal abundance ratios. The adopted thresholds are the χ^2_ν of < 1.50 (top), 2.00 (middle left), 1.75 (middle right), and 1.25 (bottom).

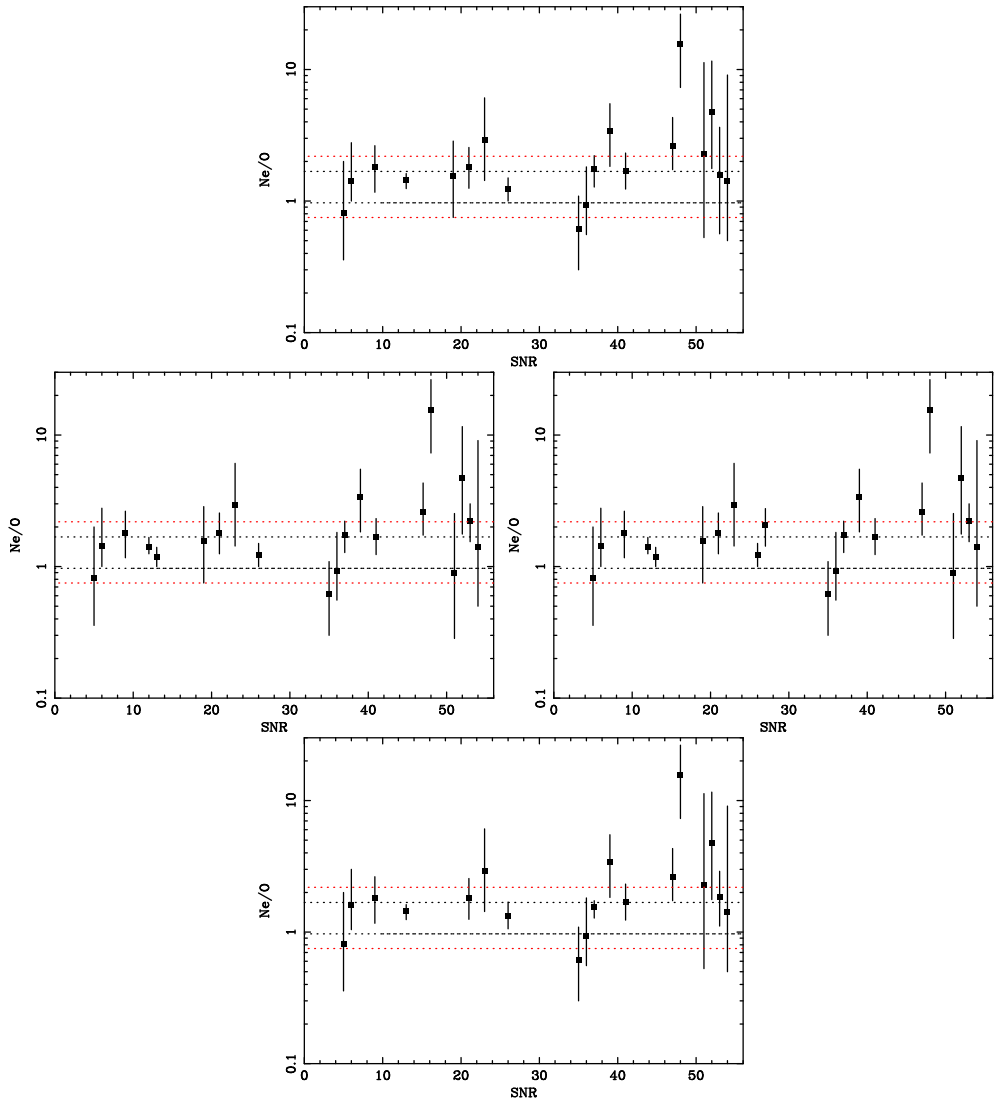

Figure D.4: The derived metal abundance ratios (Ne/O). The derived abundance ratios are compared to the LMC average (Russell & Dopita 1992; black dotted line and Hughes et al. 1998; red dotted line). The ratios are all relative to solar (Anders & Grevesse, 1989) and normalized to oxygen. The numbers from left to right in the horizon axis are represented with SNRs from top to bottom in table 4.1. The adopted thresholds are the χ^2_ν of < 1.50 (top), 2.00 (middle left), 1.75 (middle right), and 1.25 (bottom).

D.2.2 Mg/O

Figure D.5 (Mg/O) shows the derived metal abundance ratios. The adopted thresholds are the χ^2_ν of < 1.50 (top), 2.00 (middle left), 1.75 (middle right), and 1.25 (bottom).

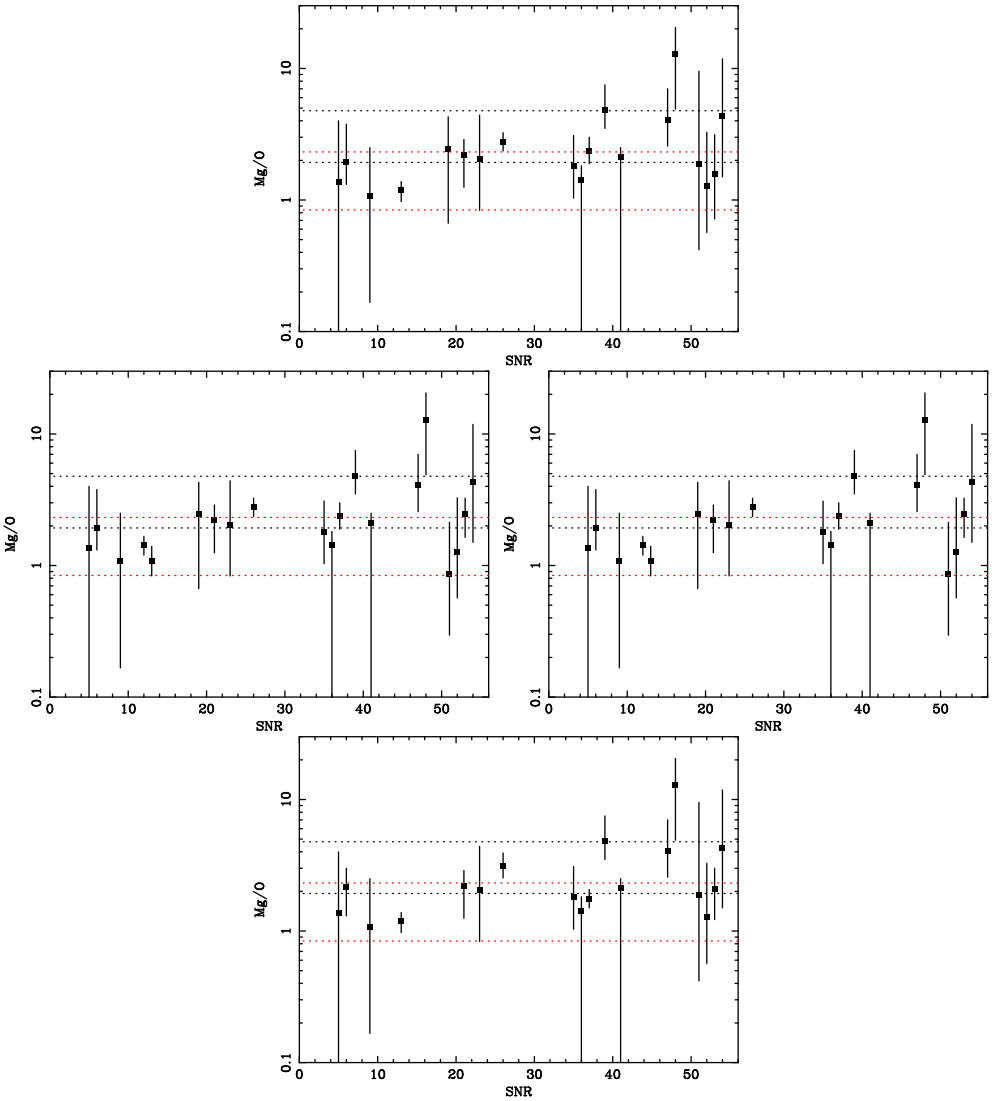

Figure D.5: The derived metal abundance ratios (Mg/O). The derived abundance ratios are compared to the LMC average (Russell & Dopita 1992; black dotted line and Hughes et al. 1998; red dotted line). The ratios are all relative to solar (Anders & Grevesse, 1989) and normalized to oxygen. The numbers from left to right in the horizon axis are represented with SNRs from top to bottom in table 4.1. The adopted thresholds are the χ^2_ν of < 1.50 (top), 2.00 (middle left), 1.75 (middle right), and 1.25 (bottom).

D.2.3 Si/O

Figure D.6 (Si/O) shows the derived metal abundance ratios. The adopted thresholds are the χ^2_ν of < 1.50 (top), 2.00 (middle left), 1.75 (middle right), and 1.25 (bottom).

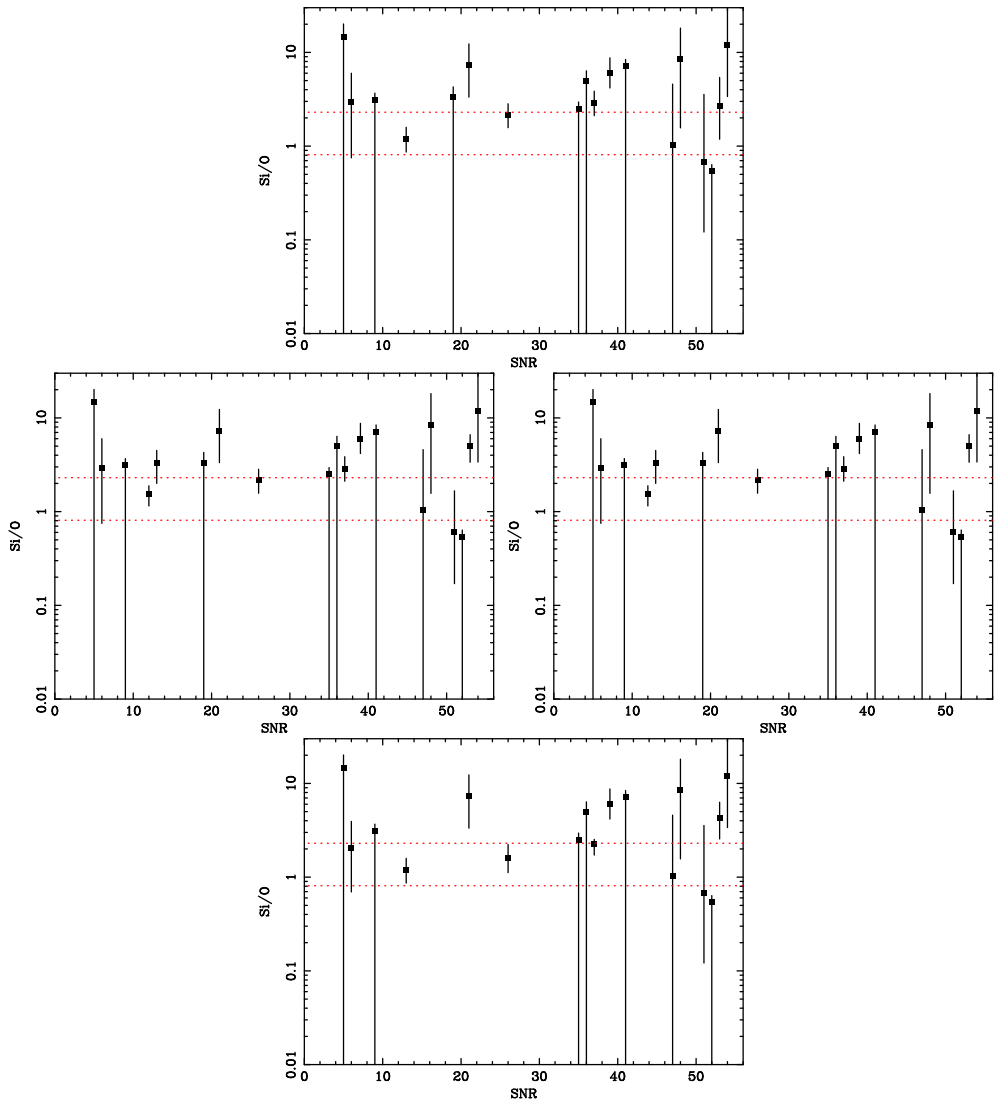

Figure D.6: The derived metal abundance ratios (Si/O). The derived abundance ratios are compared to the LMC average (Russell & Dopita 1992; black dotted line and Hughes et al. 1998; red dotted line). The ratios are all relative to solar (Anders & Grevesse, 1989) and normalized to oxygen. Since the Si metal abundance has the large uncertainty (Russell & Dopita, 1992), we dose not represent that. The numbers from left to right in the horizon axis are represented with SNRs from top to bottom in table 4.1. The adopted thresholds are the χ^2_ν of < 1.50 (top), 2.00 (middle left), 1.75 (middle right), and 1.25 (bottom).

D.2.4 S/O

Figure D.7 (S/O) shows the derived metal abundance ratios. The adopted thresholds are the χ^2_ν of < 1.50 (top), 2.00 (middle left), 1.75 (middle right), and 1.25 (bottom).

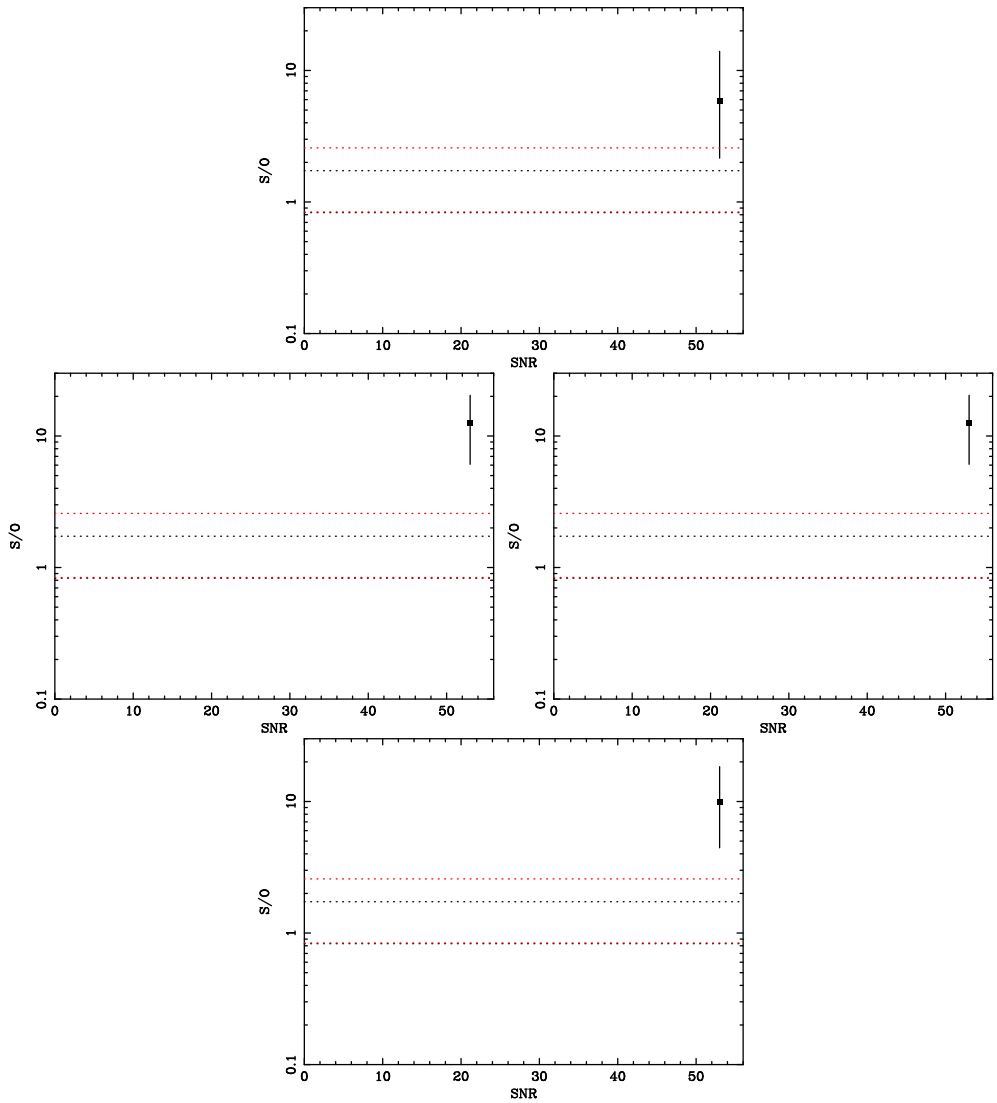

Figure D.7: The derived metal abundance ratios (S/O). The derived abundance ratios are compared to the LMC average (Russell & Dopita 1992; black dotted line and Hughes et al. 1998; red dotted line). The ratios are all relative to solar (Anders & Grevesse, 1989) and normalized to oxygen. The numbers from left to right in the horizon axis are represented with SNRs from top to bottom in table 4.1. The adopted thresholds are the χ^2_ν of < 1.50 (top), 2.00 (middle left), 1.75 (middle right), and 1.25 (bottom).

D.2.5 Fe/O

Figure D.8 (S/O) shows the derived metal abundance ratios. The adopted thresholds are the χ^2_ν of < 1.50 (top), 2.00 (middle left), 1.75 (middle right), and 1.25 (bottom).

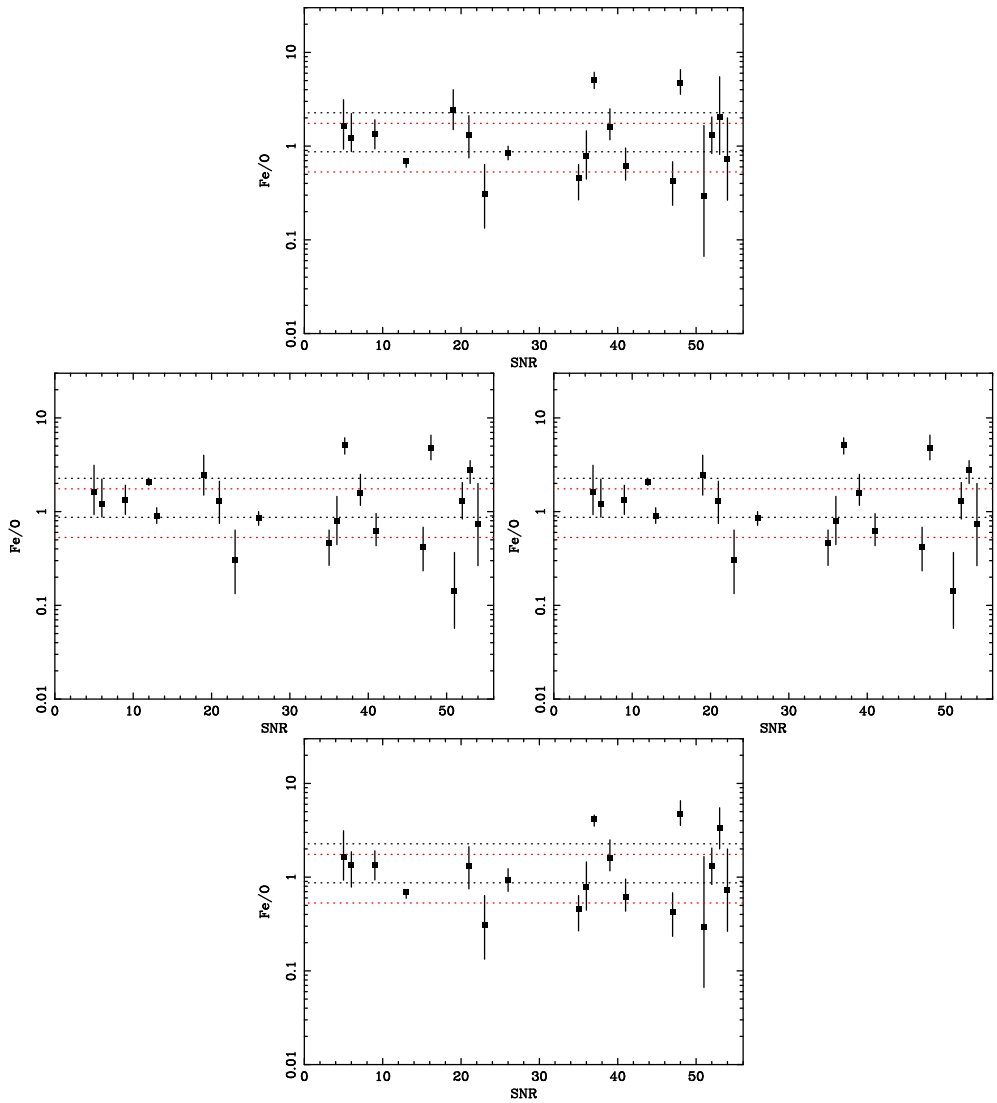

Figure D.8: The derived metal abundance ratios (Fe/O). The derived abundance ratios are compared to the LMC average (Russell & Dopita 1992; black dotted line and Hughes et al. 1998; red dotted line). The ratios are all relative to solar (Anders & Grevesse, 1989) and normalized to oxygen. The numbers from left to right in the horizon axis are represented with SNRs from top to bottom in table 4.1. The adopted thresholds are the χ^2_ν of < 1.50 (top), 2.00 (middle left), 1.75 (middle right), and 1.25 (bottom).

D.2.6 Plasma Densities

Figure D.9 shows the derived plasma densities as a function of SNR radius. The adopted thresholds are the χ^2_ν of < 1.50 (top), 2.00 (middle left), 1.75 (middle right), and 1.25 (bottom).

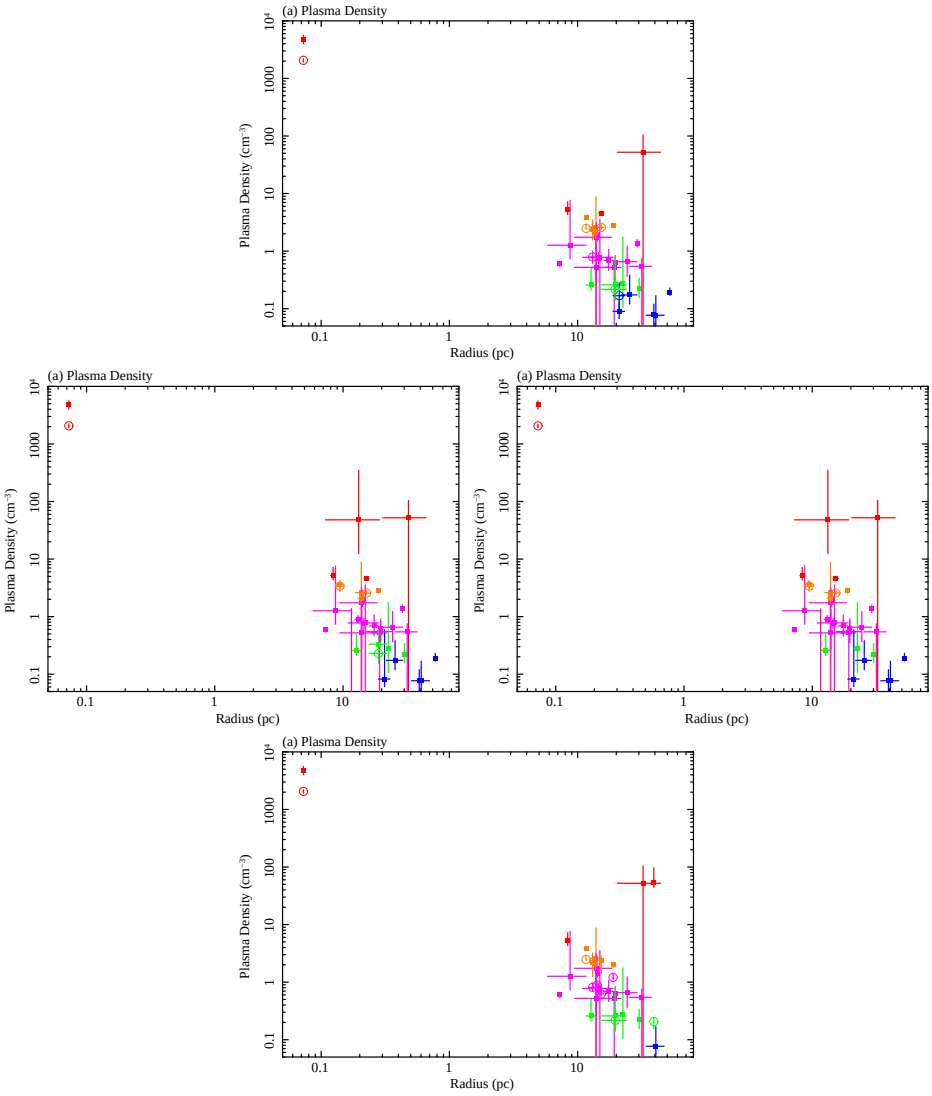

Figure D.9: Evolutions of the plasma density as a function of SNR radius. The red, orange, magenta, green, and blue data points are represented with the plasma densities of $n_{\rm e} \geq 4.0$, $4.0 > n_{\rm e} \geq 2.0$, $2.0 > n_{\rm e} \geq 0.4$, $0.4 > n_{\rm e} \geq 0.2$, and $0.2 > n_{\rm e}$ cm^{-3}, respectively. The filled boxes and open circles are also represented with the first and second vnei components, respectively. The adopted thresholds are the χ^2_ν of < 1.50 (top), 2.00 (middle left), 1.75 (middle right), and 1.25 (bottom).

D.2.7 Thermal Energies

Figure D.10 shows the derived thermal energies as a function of SNR radius. The adopted thresholds are the χ^2_ν of < 1.50 (top), 2.00 (middle left), 1.75 (middle right), and 1.25 (bottom).

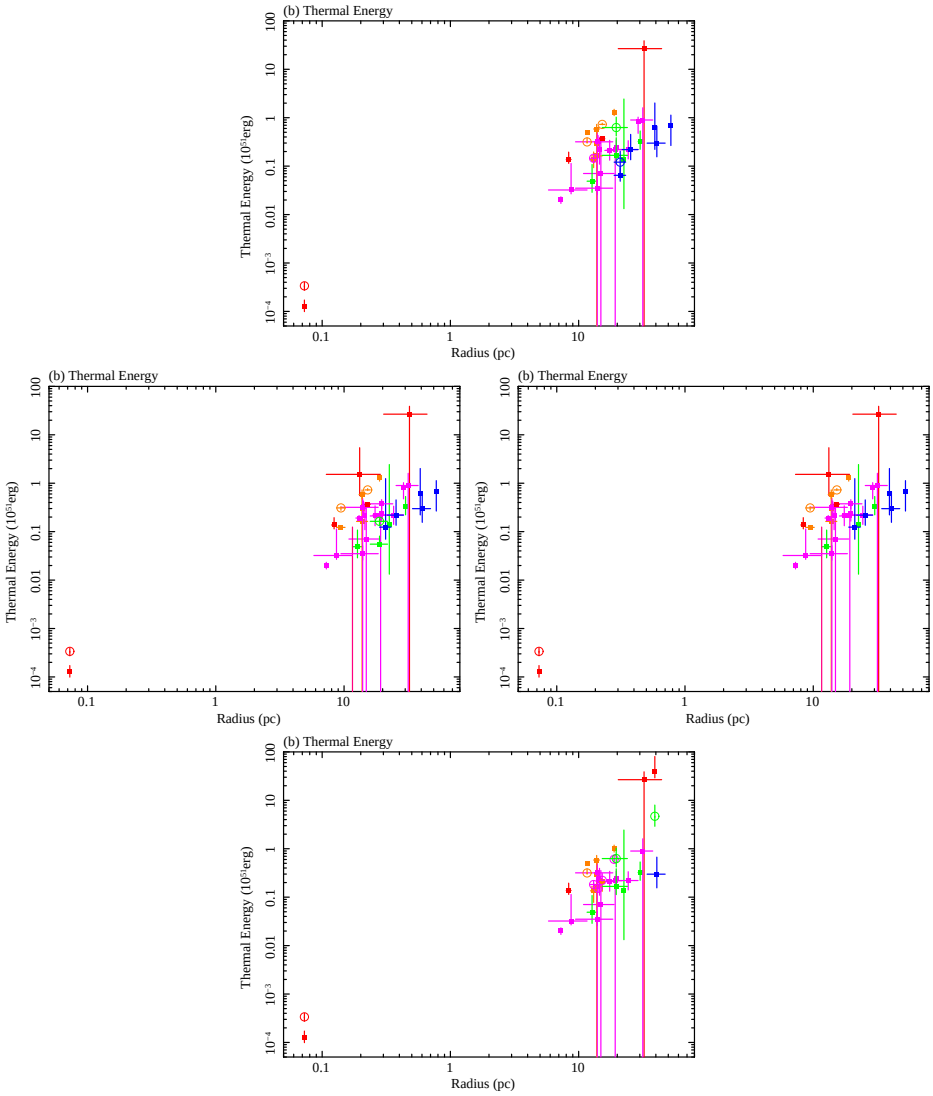

Figure D.10: Evolutions of the thermal energy as a function of SNR radius. The red, orange, magenta, green, and blue data points are represented with the plasma densities of $n_{\rm e} \geq 4.0$, $4.0 > n_{\rm e} \geq 2.0$, $2.0 > n_{\rm e} \geq 0.4$, $0.4 > n_{\rm e} \geq 0.2$, and $0.2 > n_{\rm e}$ cm^{-3}, respectively. The filled boxes and open circles are also represented with the first and second vnei components, respectively. The adopted thresholds are the χ^2_ν of < 1.50 (top), 2.00 (middle left), 1.75 (middle right), and 1.25 (bottom).

D.2.8 Plasma Masses

Figure D.11 shows the derived plasma masses as a function of SNR radius. The adopted thresholds are the χ^2_ν of < 1.50 (top), 2.00 (middle left), 1.75 (middle right), and 1.25 (bottom).

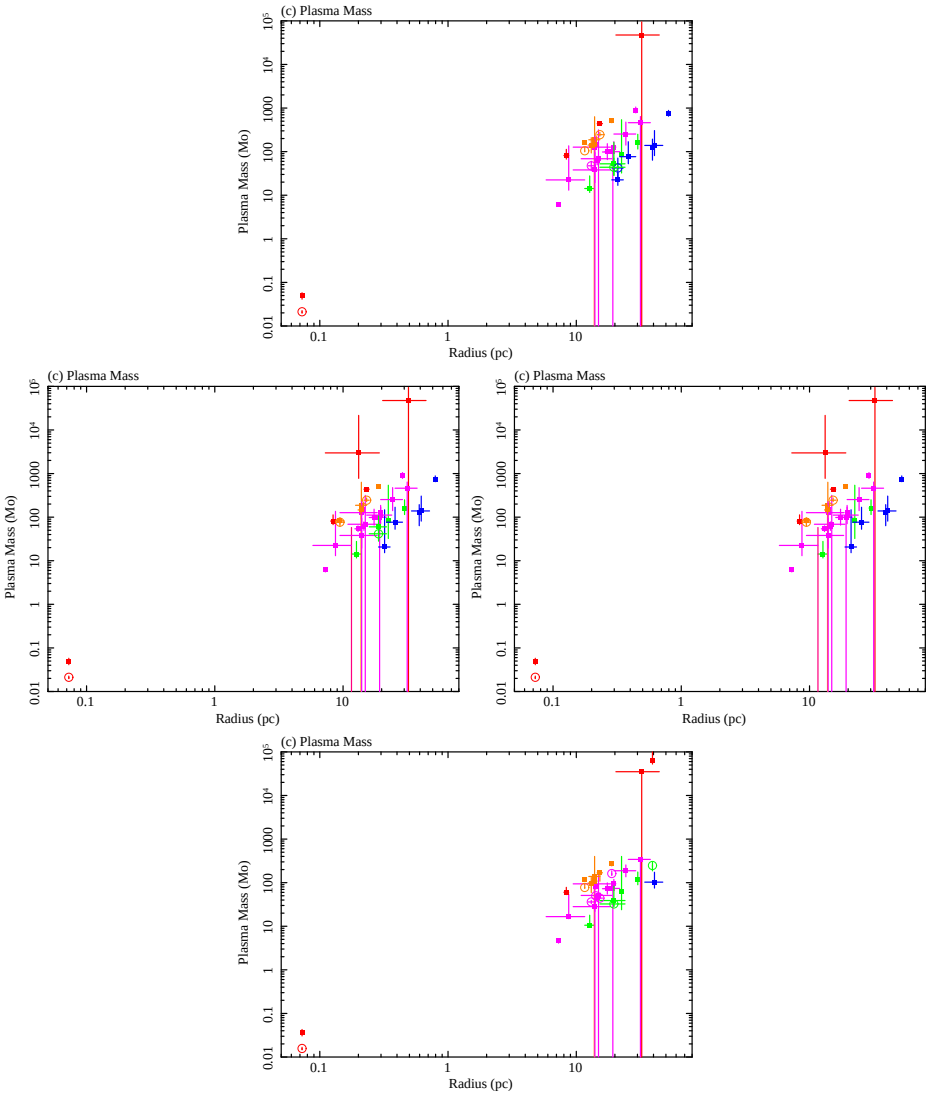

Figure D.11: Evolutions of the plasma mass as a function of SNR radius. The red, orange, magenta, green, and blue data points are represented with the plasma densities of $n_e \geq 4.0$, $4.0 > n_e \geq 2.0$, $2.0 > n_e \geq 0.4$, $0.4 > n_e \geq 0.2$, and $0.2 > n_e$ cm^{-3}, respectively. The filled boxes and open circles are also represented with the first and second vnei components, respectively. The adopted thresholds are the χ^2_ν of < 1.50 (top), 2.00 (middle left), 1.75 (middle right), and 1.25 (bottom).

D.2.9 Dynamical Age vs. Cooling Timescale

Figure D.12 shows the correlation between the dynamical age and the cooling timescale. The adopted thresholds are the χ^2_ν of < 1.50 (top), 2.00 (middle left), 1.75 (middle right), and 1.25 (bottom).

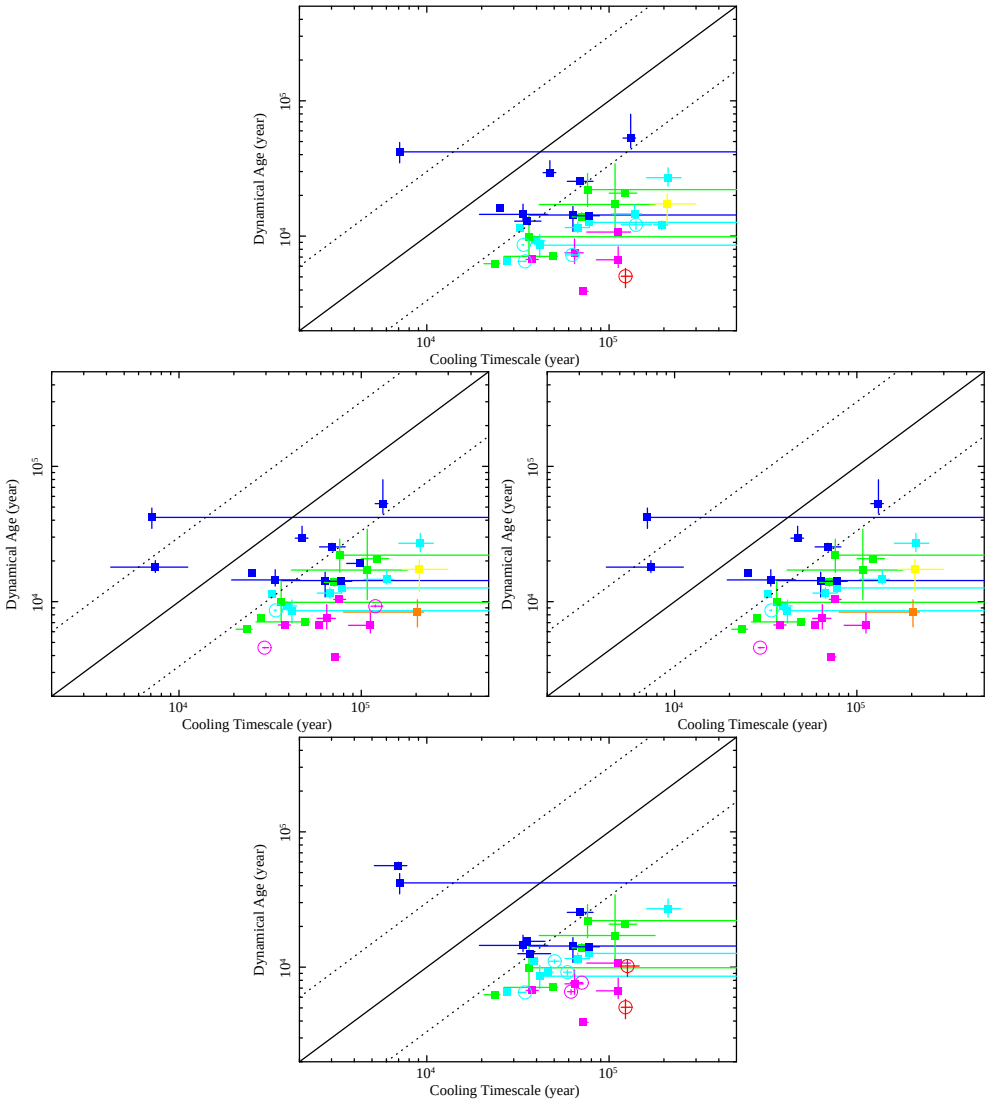

Figure D.12: The dynamical age vs. cooling timescale between 2,000–500,000 yr. The blue, green, sky blue, magenta, yellow, orange, and red data points are represented with the temperature of $0.2 \geq kT_{\rm e} > 0.08$, $0.4 \geq kT_{\rm e} > 0.2$, $0.6 \geq kT_{\rm e} > 0.4$, $0.8 \geq kT_{\rm e} > 0.6$, $1.0 \geq kT_{\rm e} > 0.8$, $1.2 \geq kT_{\rm e} > 1.0$, and $kT_{\rm e} > 1.2$ keV respectively. The filled boxes and open circles are also represented with the first and second VNEI components, respectively. The dotted line indicates $\pm 3 \times t_{\rm sedov}$ ($t_{\rm cool}$).The adopted thresholds are the χ^2_ν of < 1.50 (top), 2.00 (middle left), 1.75 (middle right), and 1.25 (bottom).

D.2.10 Temperature vs. Emission Measure

Figure D.13 shows the correlation between the plasma temperature and the emission measure. The adopted thresholds are the χ^2_ν of < 1.50 (top), 2.00 (middle left), 1.75 (middle right), and 1.25 (bottom).

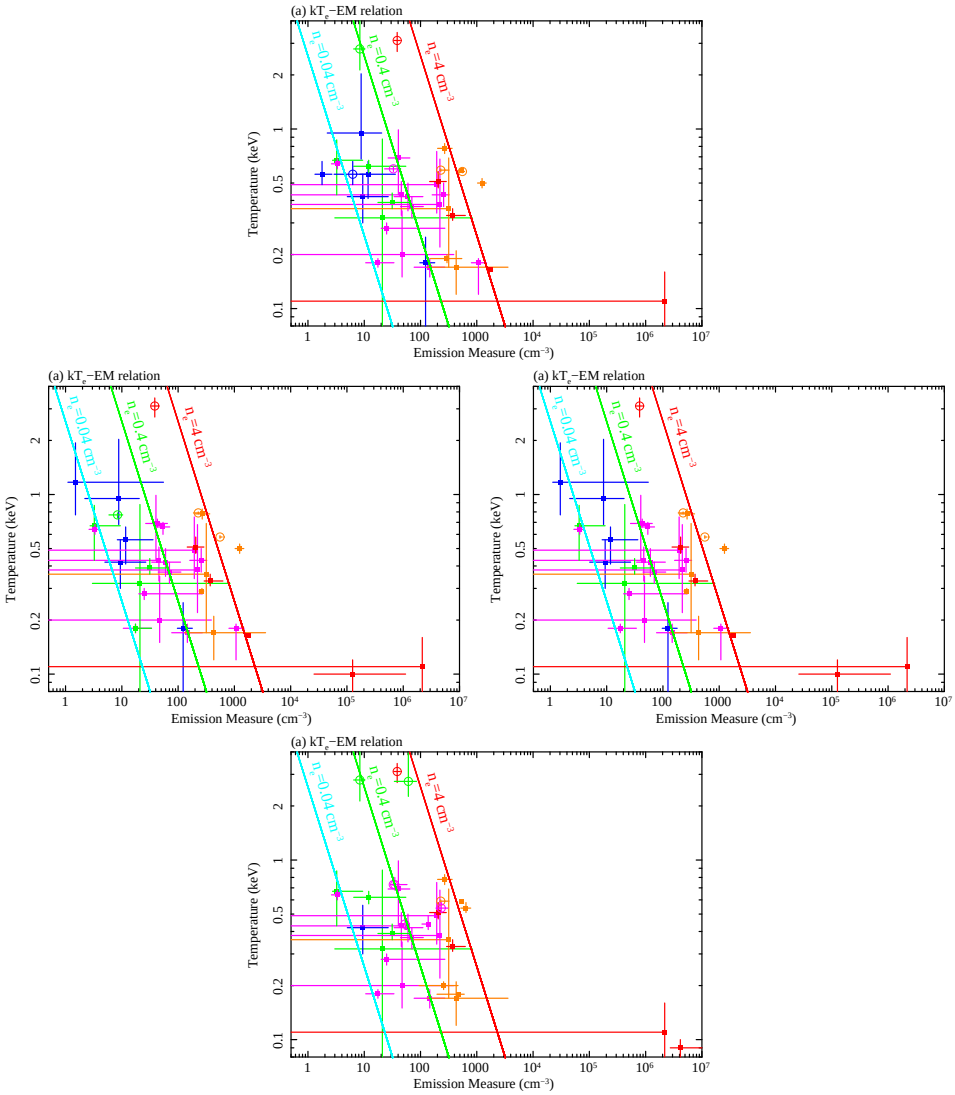

Figure D.13: The relations between the observed parameters; $kT_{\rm e}$-EM relation.The red, green, and sky blue solid lines are represented with the simulated spectral parameters in the Sedov phase with the ambient densities of 1 ($n_{\rm e} = 4$), 0.1 ($n_{\rm e} = 0.4$), and 0.01 ($n_{\rm e} = 0.04$) cm^{-3}, respectively. The red, orange, magenta, green, and blue data points are represented with the plasma densities of $n_{\rm e} \geq 4$, $4 > n_{\rm e} \geq 2$, $2 > n_{\rm e} \geq 0.4$, $0.4 > n_{\rm e} \geq 0.2$, and $0.2 > n_{\rm e}$ cm^{-3}, respectively. The filled boxes and open circles are also represented with the first and second VNEI components, respectively. The adopted thresholds are the χ^2_ν of < 1.50 (top), 2.00 (middle left), 1.75 (middle right), and 1.25 (bottom).

D.2.11 Emission Measure

Figure D.14 shows the derived emission measure as a function of SNR radius. The adopted thresholds are the χ^2_ν of < 1.50 (top), 2.00 (middle left), 1.75 (middle right), and 1.25 (bottom).

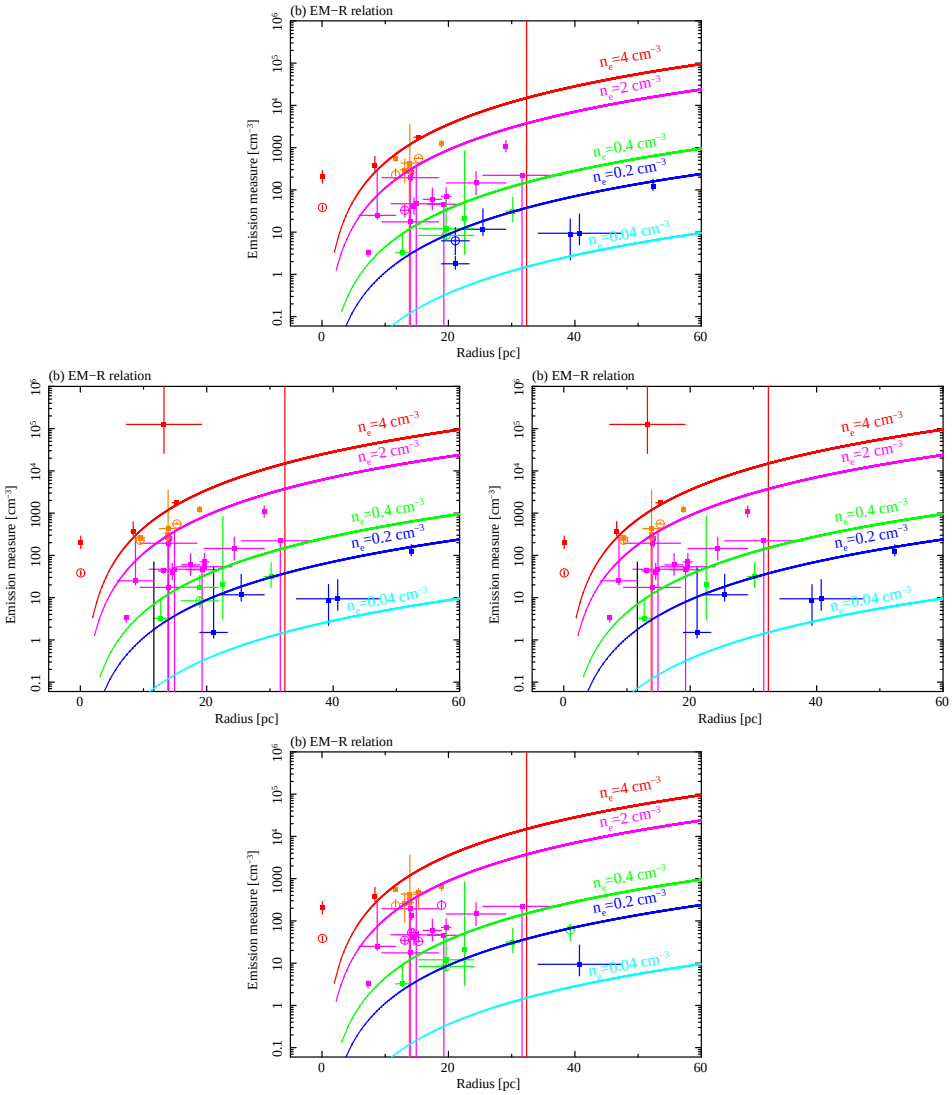

Figure D.14: The relations between the observed parameters; *EM-R* relation. The red, magenta, green, blue and sky blue solid lines are represented with the simulated spectral parameters in the Sedov phase with the ambient densities of 1 ($n_\mathrm{e} = 4$), 0.5 ($n_\mathrm{e} = 2$), 0.1 ($n_\mathrm{e} = 0.4$), 0.05 ($n_\mathrm{e} = 0.2$), and 0.01 ($n_\mathrm{e} = 0.04$) cm^{-3}, respectively. The red, orange, magenta, green, and blue data points are represented with the plasma densities of $n_\mathrm{e} \geq 4$, $4 > n_\mathrm{e} \geq 2$, $2 > n_\mathrm{e} \geq 0.4$, $0.4 > n_\mathrm{e} \geq 0.2$, and $0.2 > n_\mathrm{e}$ cm^{-3}, respectively. The filled boxes and open circles are also represented with the first and second VNEI components, respectively. The adopted thresholds are the χ^2_ν of < 1.50 (top), 2.00 (middle left), 1.75 (middle right), and 1.25 (bottom).

D.2.12 Temperature

Figure D.15 shows the correlation between the plasma temperature as a function of SNR radius. The adopted thresholds are the χ^2_ν of < 1.50 (top), 2.00 (middle left), 1.75 (middle right), and 1.25 (bottom).

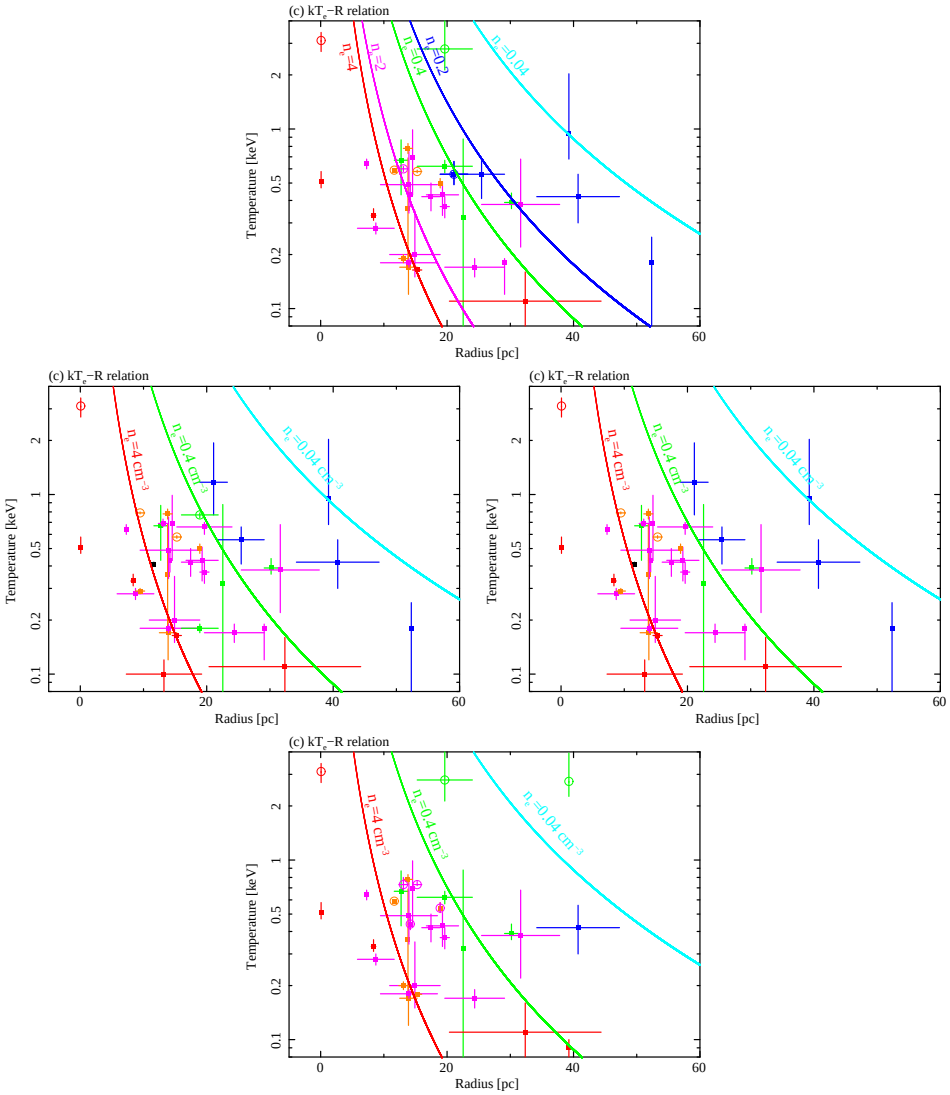

Figure D.15: The relations between the observed parameters; $kT_{\rm e}$-R relation.The red, green, and sky blue solid lines are represented with the simulated spectral parameters in the Sedov phase with the ambient densities of 1 ($n_{\rm e} = 4$), 0.1 ($n_{\rm e} = 0.4$), and 0.01 ($n_{\rm e} = 0.04$) cm^{-3}, respectively. The red, orange, magenta, green, and blue data points are represented with the plasma densities of $n_{\rm e} \geq 4$, $4 > n_{\rm e} \geq 2$, $2 > n_{\rm e} \geq 0.4$, $0.4 > n_{\rm e} \geq 0.2$, and $0.2 > n_{\rm e}$ cm^{-3}, respectively. The filled boxes and open circles are also represented with the first and second VNEI components, respectively. The adopted thresholds are the χ^2_ν of < 1.50 (top), 2.00 (middle left), 1.75 (middle right), and 1.25 (bottom).

D.2.13 Plasma Density-Radius Relation & Temperature Distribution

In table D.7 we present the best-fit model of the plasma density-radius relations and temperature distributions. We gave the plasma density-radius relation by $n_{\rm e}$ $(4n_0) = a(R/1\ {\rm pc})^{-3}$. $kT_{\rm e}^{sedov}$ and $kT_{\rm e}^{obs}$ are the simulated (based on the Sedov model) and observed plasma temperatures, respectively.

Table D.7: Plasma density-radius relations and temperature distributions.

	Threshold			
	<1.5	<2.00	<1.75	<1.25
a	6100^{+2900}_{-1900}	4700^{+3000}_{-1800}	4600^{+3000}_{-1800}	4600^{+2200}_{-1500}
$kT_{\rm e}^{sedov}$ (keV)	$0.37^{+0.16}_{-0.12}$	$0.48^{+0.29}_{-0.19}$	$0.49^{+0.31}_{-0.19}$	$0.49^{+0.23}_{-0.16}$
$kT_{\rm e}^{obs}$ (keV)	0.42±0.23	0.38±0.27	0.37±0.29	0.42±0.25

D.2.14 Cavity Explosion

Figure D.16 shows the correlation between the dynamical and ionization ages. The adopted thresholds are the χ^2_ν of < 1.50 (top), 2.00 (middle left), 1.75 (middle right), and 1.25 (bottom).

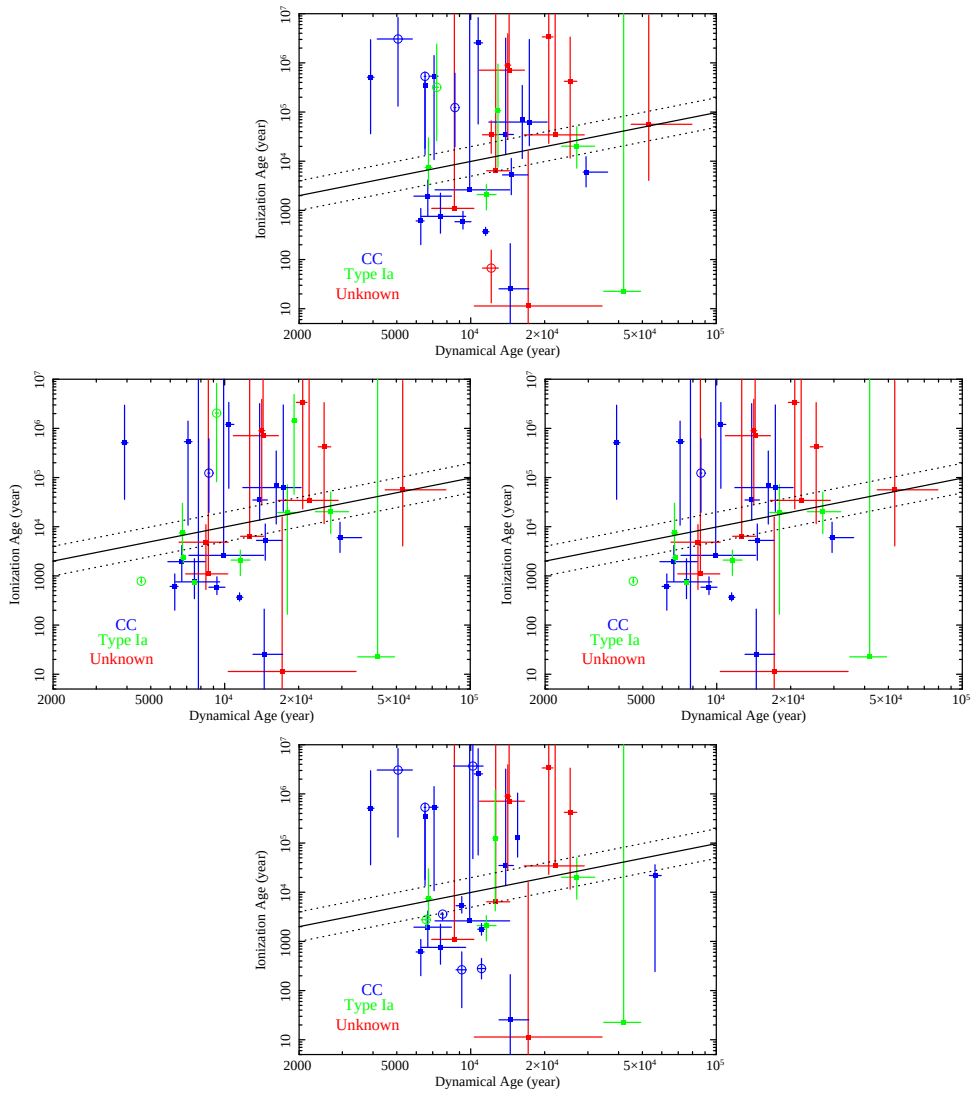

Figure D.16: SNR age determined from the derived ionization parameter vs. the dynamical age derived from the Sedov model. The blue, green, and red data points are represented with CC, Type Ia, and unknown SNe, respectively. The filled boxes and open circles are represented with the first and second VNEI components, respectively. The adopted thresholds are the χ^2_ν of < 1.50 (top), 2.00 (middle left), 1.75 (middle right), and 1.25 (bottom).

Appendix E

Analysis of N23

We also derived new results from the individual analysis of our samples, we analyzed the supernova remnant N23 using the X-ray Imaging Spectrometer (XIS) onboard Suzaku in detail.

E.1 Overview of N23

SNR N23 is identified as a SNR with radio observations at 5 and 14.7 GHz for the first time (Milne et al., 1980). Its X-ray emission extends $100'' \times 120''$ in the sky (24×29 pc at a distance of 50 kpc), showing a semi-circular morphology with only the south-eastern hemisphere being bright (Hughes et al., 2006). The X-ray images by *Chandra* is shown in figure E.3 in the later section. Based on the *ASCA* observation, Hughes et al. (1998) classified N23 as a young SNR with an age of $\sim$ 3800 yr from the spectrum of the entire remnant. Hughes et al. (2006) carried out spatially resolved spectroscopy of N23 with *Chandra*, and estimated the age of north-western rim to be $\sim$4600 yr. These observations result in consistent estimation of the temperature and the ionization parameter ($n_{\rm e}t$) in the bright south-eastern shell, which is $\sim$0.5–0.7 keV and $\sim 10^{10}$–10^{11} cm^{-3} s, respectively. They are, however, not be able to resolve hydrogenic and He-like Kα lines from Oxygen clearly because of limited energy resolution below $\sim$1 keV. In addition, Hughes et al. (2006) have revealed that there is a point source around the center of N23. From its 0.5–10 keV flux ($\sim 10^{-14}$ erg cm^{-2} s^{-1}) and power-law spectrum with a photon index of 2.2, the source is probably a rotation-powered pulsar and/or a pulsar wind nebula. If so, the progenitor of N23 is a core-collapsed massive star (Hayato et al., 2006). We summarize, in this chapter, the results of *Suzaku* observation and analysis on N23. Unless otherwise stated, figure in this chapter are taken from Someya et al. (2010). In this chapter, we will show that we have clearly resolved H- and He-like Kα emission lines from oxygen for the first time, which leads to identification of a new low temperature plasma in collisional ionization equilibrium. Based on these results, we discuss evolutionary phase for this remnant.

E.2 Observation & Data Reduction

N23 was observed with *Suzaku* (Mitsuda et al., 2007) on 2005 August 16–17. The observation log is summarized in table E.1. *Suzaku* is equipped with four modules of the

Table E.1: observation log.

Observation ID	100003010
Observation mode	Full window, no burst, no SCI
Start Date (UT)	2005/08/16–17
Exposure (ksec)	7.1
Count rate* (cts s^{-1})	FI: 0.6 BI: 1.2

* Count rate of FI and BI-CCD. Count rate of N23 in the 0.5–2.0 band within a 3′.3 radius circle after the background subtraction.

XIS (Koyama et al., 2007). They are adapted at the focal plane of the X-Ray Telescopes (XRT; Serlemitsos et al. 2007). The *Suzaku* XIS image of N23 below 2 keV is shown in Fig. E.1.

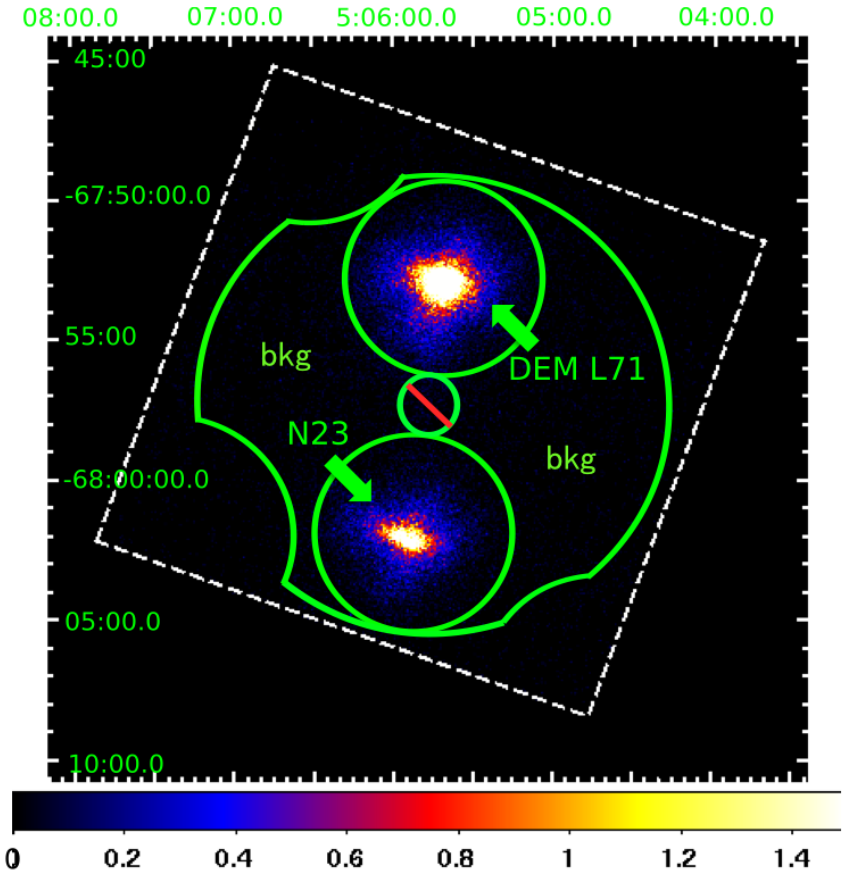

Figure E.1: Suzaku XIS X-ray image of the N23 in the bands 0.2–2 keV. Another nearby SNR, DEM L71, is also shown. The images from all the four XIS modules are combined. The green circles with a radius of 3.'3 are integration regions of the source photons from N23. The background photons were extracted from annular region which was removed the source and a center regions. The calibration sources at the corners are masked.

Data reduction and analysis of the present data were carried out using the HEADAS software package version 6.5.1. The data processed by *Suzaku* pipeline processing software

(ver 2.0) were analyzed. We only used the data taken with the 5×5 editing mode in the high and super-high data rates because of the editing mode of 2×2 has uncertainty in the response matrices of the XIS. In screening the data, we removed time intervals while the elevation angle from the night earth is less than 5°. In the standard data screening procedure, the time interval during which the elevation angle from the day earth is less than 20°. This results in, however, only 5.6 ksec data available. We thus reduce the day-earth elevation angle by degrees by closely comparing resulting spectra and have finally found that the solar X-ray contamination does not raise any spectral modification even if we reduce the day earth elevation down to 5° (DYE_ELV > 5°) for the XIS data. Owing to this study, the total exposure time has increased to 7.1 ksec.

E.3 Spectral Analysis

E.3.1 Extraction of Source and Background Photons

In extracting source photons, we adopt a circular aperture with a radius of 3.'3 centered on N23 (the green circle centered on N23 in Fig. E.1). For the background, we have collected photons from the entire CCD area out of the source extraction region, except for outer edge regions illuminated by ^{55}Mn isotopes adapted in the camera bodies of all the XIS modules, the central circular region with a radius of ∼1.'5, and the 3.'3 circular region centered on the other SNR DEM L71. We combined the spectra from the XIS adopting the FI-CCDs (XIS0, XIS2, and XIS3) into a single spectrum, and refer to it as the FI spectrum hereafter. The BI spectrum is the same as that solely from the XIS1 data. In the spectral analysis, we use XSPEC version 11.3.2aj. The XIS response matrix (RMF) and auxiliary response file (ARF) are calculated using XISRMFGEN (version 2007-05-14) and XISARFGEN (version 2008-04-05), respectively (Ishisaki et al., 2007). The RMFs and ARFs from the FI-CCDs are combined with the ftools ADDRMF and MARFRMF.

E.3.2 Spectral Models

From the *ASCA* observations of LMC SNRs, it is found that the spectra of N23 is well represented by an optically thin thermal emission model in ionization non-equilibrium (Hughes et al., 1998). In characterizing the spectra of the SNR, we thus adopt the non-equilibrium ionization model, or VNEI model in the XSPEC model library (Hamilton et al. 1983, Borkowski et al. 1994, Liedahl et al. 1995, Borkowski et al. 2001). The VNEI model provides the plasma temperature $kT_{\rm e}$, the ionization timescale $n_{\rm e}t$ where t is the elapsed time since the shock occurs, the metal abundances, and the normalization parameter $\frac{10^{-14}}{4\pi D^2}\int n_{\rm e} n_{\rm H} dV$ where D is the distance to the source, $n_{\rm e}$ and $n_{\rm H}$ are the electron and hydrogen density respectively, and dV is the volume element of the SNR.

The emission spectra are attenuated by photoelectric absorption due to metals contained in the interstellar matter within our galaxy and LMC. Since the metal abundances of these two absorption components are significantly different, we consider them separately in the spectral evaluation as follows. We assume solar composition (Anders & Grevesse, 1989) for the absorbing matter in the Galaxy, and denote its hydrogen column density as $N_{\rm H}^{\rm G}$. The value of $N_{\rm H}^{\rm L}$ toward N23 is obtained by the Galactic HI survey, which is $5.8\times10^{20}{\rm cm}^{-2}$ (Dickey & Lockman, 1990). We utilize the PHABS model in XSPEC to represent the galactic absorption, and freeze $N_{\rm H}^{\rm G}$ at these values in the spectral fitting

described below. The average metal abundances of LMC, on the other hand, are measured by Russell & Dopita (1992), which is ∼0.3 solar on average over major metals. We reflect these abundances on the VPHABS model, and set the column density associated with LMC $N_{\rm H}^{\rm L}$ free to vary in the following spectral fit process.

Table E.2: Best-fit parameters for N23.

	$1kt1nt$	$1kT2nt$	$2kT1nt$	$2kT2nt$
$N_{\rm H}^{G}$ ($\times 10^{20}$ cm^{-2})	5.8(fix)	5.8 (fix)	5.8(fix)	5.8(fix)
$N_{\rm H}^{L}$ ($\times 10^{21}$ cm^{-2})	1.6(1.3–1.9)	< 0.16	1.5(0.6–1.9)	0.9(0.6–1.9)
$kT_{\rm e1}$ (keV)	0.548(0.544–0.567)	0.572(0.557–0.580)	0.569(0.556–0.593)	0.581(0.551–0.597)
$kT_{\rm e2}$ (keV)	–	–	0.218(0.214–0.230)	0.225(0.214–0.230)
$\log(n_e t)_1$ (cm^{-3} s)	10.51(10.48–10.55)	10.50(10.45–10.52)	13.68(11.92–13.70)	12.04(11.87–13.70)
$\log(n_e t)_2$ (cm^{-3} s)	–	13.18(12.77–13.70)	–	13.63(13.27–13.70)
$Norm_1$ ($\times 10^{-2}$)	1.87(1.74–1.90)	0.34(0.31–0.68)	0.83(0.64–1.00)	0.78(0.66–0.98)
$Norm_2$ ($\times 10^{-2}$)	–	0.73(0.67–0.81)	2.54(1.93–2.96)	1.93(1.47–3.51)
C	0.30(fix)	0.30(fix)	0.30(fix)	0.30(fix)
N	< 0.02	0.09(0.04–0.25)	0.54(0.12–1.05)	0.37(0.23–0.94)
O	0.093(0.089–0.098)	0.27(0.26–0.28)	0.33(0.25–0.50)	0.34(0.28–0.49)
Ne	0.15(0.14–0.16)	0.43(0.39–0.46)	0.49(0.35–0.70)	0.49(0.40–0.66)
Mg	0.14(0.12–0.17)	0.31(0.27–0.35)	0.39(0.33–0.60)	0.39(0.32–0.47)
Si	0.28(0.19–0.36)	0.34(0.24–0.43)	0.41(0.30–0.52)	0.42(0.32–0.55)
Fe	0.111(0.105–0.117)	0.18(0.17–0.22)	0.24(0.19–0.33)	0.24(0.19–0.33)
χ^2_ν(d.o.f.)	1.45(99)	1.11(97)	1.00(97)	1.00(96)
offset FI (eV)	$-8.7(-11.0$–$-7.8)$	$-8.1(-9.1$–$-5.9)$	$-8.1(-9.0$–$-7.1)$	$-8.0(-9.0$–$-7.1)$
offset BI (eV)	$-1.0(-1.6$– $0.0)$	$-1.0(-2.1$– $0.0)$	-1.0(-2.8– 0.0)	$-0.3(-1.3$– $0.0)$

In evaluating the spectrum of N23 through spectral fitting, we begin with a single component VNEI model attenuated by photoelectric absorption. Since the carbon abundance cannot be constrained because of the large interstellar absorption at carbon Kα line energies, we fixed it to the LMC value (Russell & Dopita, 1992). In the early phase of the *Suzaku* mission, the energy gain has a large uncertainty (Koyama et al., 2007). The gain uncertainty is $\sim \pm 10$ eV, according to the previous studies on SNRs (Bamba et al., 2008; Yamaguchi et al., 2008). We therefore have allowed the energy offset to be floated. As a result, the energy offset is converged to ~ -8 eV and ~ -1 eV, for the FI and BI spectra, respectively. These gain offset values are within the gain uncertainty. The result is summarized in the second column of table E.2 labelled '$1kT1nt$'. The best fit results in $kT_{\rm e} \simeq 0.548$ keV and $\log(n_{\rm e}t$ [cm^{-3} s]$) \simeq 10.51$ with a χ^2 (d.o.f.) of 144 (99). These parameters are roughly consistent with those from the *Chandra* observation (Hughes et al., 2006). Note that, if we do not float the energy gain, the best-fit parameters are $kT_{\rm e} \simeq 0.552$ keV and $\log(n_{\rm e}t$ [cm^{-3} s]$) \simeq 10.54$ with a χ^2 (d.o.f.) of 219 (101). Hence, the energy offset adjustment significantly improves the fit, while the differences in the temperature and the ionization timescale (in logarithm) are within ~ 1 %.

As noticed from this table, however, the single component VNEI model no longer provides an acceptable fit ($\chi^2_\nu \simeq 1.5$). We thus have appended another VNEI model. To reduce the number of model parameters as much as possible, we constrained either $kT_{\rm e}$ or $n_{\rm e}t$ common between the two VNEI components, and fit them to the data separately. The resultant best-fit parameters are also listed in table E.2, labelled '$1kT2nt$' and '$2kT1nt$', respectively. Although the $1kT2nt$ model improves the fit significantly, the reduced χ^2

value indicates that it is still not acceptable. The improvement of the $2kT1nt$ model, on the other hand, is more remarkable, and it provides an acceptable fit at the 90% confidence level. The best-fit model is shown in Fig. E.2. This result indicates that there

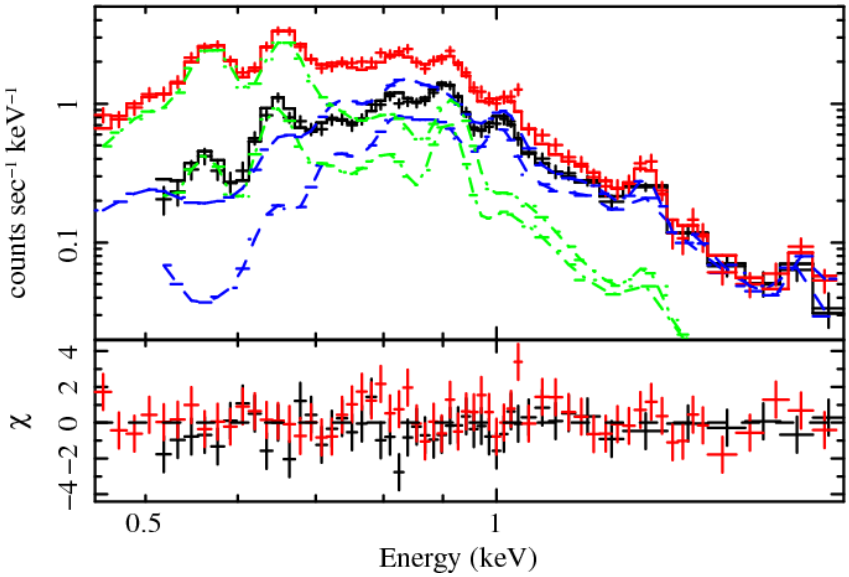

Figure E.2: The data and the best-fit '$2kT1nt$' model of N23. in the 0.45–2.0 keV band. The black and red crosses show the data point from the FI and BI CCDs, respectively. The solid histograms with the same color are the best-fit model. The blue and green broken histograms show the components with $kT_{\rm e}$=0.57 and 0.22 keV, respectively. The lower panel shows the residuals from the best-fit model.

exists another optically thin thermal plasma component with a temperature of ∼0.2 keV, in addition to the 0.5–0.6 keV component so far known. The discovery of the new low temperature component is brought about by the clear resolution of the Oxygen Kα lines by the *Suzaku* XIS. Consequently, the best-fit value of the ionization timescale now becomes $\log(n_{\rm e}t\ [{\rm cm}^{-3}\,{\rm s}]) \sim 12$. This is significantly larger than that from the *ASCA* and *Chandra* observations ($10^{10} - 10^{11}$ cm^{-3} s).

In the *Chandra* observation, more than $\sim$ 30 % of the total emission comes from the eastern rim (Hughes et al., 2006). Since our *Suzaku* observation covers the remnant entirely, the best-fit parameters we have obtained are a kind of mean weighted mainly on this extended bright rim region (see Fig. E.3).

We finally remove the constraint of the ionization timescale between the two VNEI components and set them free to vary independently. The results are summarized in the '$2kT2nt$' column of table E.2. This change, however, is not effective in improving the fit. We therefore adopt the $2kT1nt$ model for N23 for discussion in later sections.

E.4 Discussion

E.4.1 Densities, total energy, and swept up mass

In this section, we aim to derive electron number densities of the SNR plasma ($n_{\rm e}$) and ambient ISM (n_0), total thermal energy of the plasma ($E_{\rm t}$), swept up mass ($M_{\rm swept}$). With

the aid of the normalization obtained from the spectral fitting, the volume of the plasma (V) and the volume filling factor (f), we calculated $n_{\rm e}$, taking into account $n_{\rm e}$=1.2$n_{\rm H}$ for fully ionized solar abundance plasma. Assuming the strong shock, pre-shock density (e.g. ISM density; n_0) is obtained to be $n_0 = (n_{\rm H}/4)$. The swept-up mass is given by $M_{\rm swept} = n_{\rm H} m_{\rm p} f V$, where $m_{\rm p}$ is the proton mass. The total energy is given by $E_{\rm t} = 3 n_{\rm e} k T f V$, where k and T is the Boltzmann constant and the temperature of the plasma, respectively. Note that we assume that electrons and ions temperature are in thermal equilibrium. The age of the plasma $t_{\rm ion}$ is obtained from the ionization parameter ($n_{\rm e}t$) which is evaluated from the spectral fitting.

In order to estimate the densities, we need to know the volume of the plasma from an X-ray image. Since the *Suzaku* XIS has only moderate imaging capability, we carried out *Chandra* imaging analysis first. We analyzed the *Chandra* ACIS data of N23 (seq# 500212) observed on 2002 December 29–30. Images are extracted from a standard cleaned event file using the DMCOPY command. Fig. E.3 shows the X-ray images in the (a) 0.2–0.8 keV and (b) 1.5–2.0 keV energy bands. The low and high energy bands were chosen to

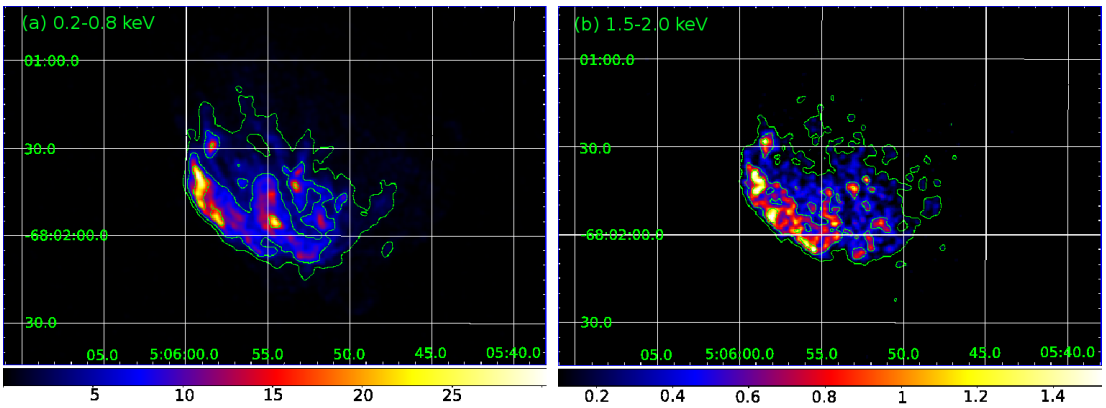

Figure E.3: Smoothed *Chandra* image of N23 (a) in the 0.2–0.8 keV and (b) in the 1.5–2.0 keV band. The contours overlaid with labels of 1.0, 5.0, 15.0 (left) and 0.1, 0.5, 1.0 counts pixel^{-1}

show the contribution from the ∼0.2 keV and the ∼0.6 keV components, respectively. In both images, the structure of N23 shows a bright hemisphere with ∼35″ (8.5 pc) radius. We therefore assumed that the N23 plasma distributes in the shell of the hemisphere with a radius and a thickness of 35″ and 2.7″ (0.7 pc), the latter of which is 1/12 of the shell radius expected for the ISM compressed in the case of the strong and adiabatic shock, which assumption is to be considered later in § 4.2. As a result, the volume of the plasma becomes $V = 9.3 \times 10^{57}$ cm^3.

The other parameters are summarized in table E.3. As shown in Fig. E.3, the emission from N23 is highly anisotropic. We therefore normalized the volume filling factor f by 0.1 ($\equiv f_{0.1}$). The plasma density estimated from the low and high temperature components are $\sim$ 31 cm^{-3} and $\sim$ 18 cm^{-3}, respectively, as shown in table E.3. This density estimation is roughly consistent with that of the southeastern rim region with the *Chandra* observation ($\sim$ 10–23 cm^{-3}; Hughes et al. 2006). With this normalization, the ISM density estimated from the low and high temperature components are $\sim$ 8 cm^{-3} and $\sim$ 4 cm^{-3}, respectively. One may imagine that this high density is realized through

Table E.3: Input and derived properties for N23.

Property	Value	
	low-T component	high-T component
$kT_{\rm e}$ (keV)	0.22	0.57
R (pc)	8.5	8.5
V (10^{57} cm^3)	9.3	9.3
$n_{\rm e}$ (cm^{-3})	$31.3^{+2.5}_{-4.1} f_{0.1}^{-1/2}$	$18.0^{+1.6}_{-2.2} f_{0.1}^{-1/2}$
n_0 (cm^{-3})	$7.9^{+0.6}_{-1.0} f_{0.1}^{-1/2}$	$4.4^{+0.3}_{-0.6} f_{0.1}^{-1/2}$
$E_{\rm t}$ (10^{50} erg)	$0.3\pm0.1 f_{0.1}^{1/2}$	$0.4\pm0.1 f_{0.1}^{1/2}$
$M_{\rm swept}$ (M$_\odot$)	$21^{+2}_{-3} f_{0.1}^{1/2}$	$12^{+1}_{-2} f_{0.1}^{1/2}$
$t_{\rm ion}$ (yr)	$> 1000 f_{0.1}^{1/2}$	$> 1500 f_{0.1}^{1/2}$

collision of the ejecta with molecular clouds. According to a radio observation (Banas et al., 1997), however, no CO emission was discovered from a region including N23. We thus consider that N23 explodes into a relatively dense part of the ISM ($\sim$ 10 cm^{-3}). It is suggested this high density is related geometrically with the open cluster HS 114 (Hodge & Sexton, 1966) near the remnant (Hughes et al., 2006). Finally, total ejecta mass is given by $M_{\rm low} + M_{\rm high}$, where $M_{\rm low}$ and $M_{\rm high}$ are the mass of low and high temperature components, respectively. Total ejecta mass therefore is calculated to be $\sim$30 $M_\odot$. Hence the plasma chiefly comprises of the swept-up ISM.

E.4.2 SNR phase

In this section, we consider evolutionary phase of N23 by comparing various timescales evaluated from observed parameters. We compare the Sedov time scale ($t_{\rm Sedov}$), the plasma age ($t_{\rm ion}$) estimated from the ionization parameter, and the cooling time scale ($t_{\rm cool}$) of N23. $t_{\rm Sedov}$ is based on the concept of Sedov simple blast wave model (Sedov 1959), in which a supernova with explosion energy (E_0) expands into homogeneous ISM, which is given by

$$t_{\rm Sedov} = 4.3 \times 10^2 \left(\frac{R}{1\ {\rm pc}}\right) \left(\frac{kT_e}{1\ {\rm keV}}\right)^{-0.5}\ {\rm yr}, \tag{E.1}$$

where R is the blast wave shock radius and $T_{\rm e}$ is the shock temperature. $t_{\rm cool}$ is defined as the time scale of the temperature distribution having started to deviate from that of the Sedov model, which is written as

$$t_{\rm cool} = 2.7 \times 10^4 \left(\frac{E_0}{10^{51}\ {\rm erg}}\right)^{0.24} \left(\frac{n_0}{1\ {\rm cm}^{-3}}\right)^{-0.52}\ {\rm yr} \tag{E.2}$$

(Falle, 1981). If $t_{\rm cool} \simeq t_{\rm Sedov}$ holds, the SNR is considered to locate at a late stage of the Sedov phase or at an initial radiative phase. If, on the other hand, $t_{\rm Sedov} < t_{\rm cool}$ holds, the SNR is regarded as being still in the Sedov phase. We assume that the explosion energy is 10^{51} erg in eq. (E.2).

We discovered the new soft emission component with a temperature of $\sim$0.22 keV, in addition to the 0.5–0.7 keV component so far known. This SNR therefore is doubted

Table E.4: The characteristic ages for N23.

	low-T component	high-T component
$t_{\rm Sedov}$ (10^4 yr)	0.8	0.5
$t_{\rm cool}$ (10^4 yr)	$0.9 f_{0.1}^{0.26}$	$1.2 f_{0.1}^{0.26}$
$t_{\rm ion}$ (10^4 yr)	$> 0.1 f_{0.1}^{1/2}$	$> 0.2 f_{0.1}^{1/2}$

in the late stage of the Sedov phase or the initial radiative cooling phase. Accordingly, we need to update the remnant age estimation. The Sedov time scale and the cooling time scale calculated with eq. (E.1) and (E.2) are summarized in table E.4, together with the ionization age $t_{\rm ion}$ obtained based on the spectral fit. Since the spectral fit with the '$2kT1nt$' model provides only the lower limit for the ionization timescale $n_{\rm e}t$, we only have a lower limit for $t_{\rm ion}$. We thus have decided to estimate the remnant age with eq. (1) and (2). Using eq. (E.1) with $R = 8.5$ pc, $t_{\rm Sedov}$ estimated from the low and high temperature components becomes ∼8000 and ∼5000 yr, respectively, which are consistent with the lower limit of $t_{\rm ion}$. This is a direct consequence of eq. (E.1), implying $t_{\rm Sedov}$ being proportional to $T_{\rm e}^{-1/2}$. The high temperature component is younger than the low temperature component. In the Sedov scheme, this can be interpreted as the high temperature component being heated recently. On the other hands, $t_{\rm cool}$ of the low and high temperature components are $9300 f_{0.1}^{0.26}$ and $12000 f_{0.1}^{0.26}$, respectively, using eq. (E.2) with n_0 given in table E.3 (§E.4.1). Since $t_{\rm Sedov} \simeq t_{\rm cool}$ for both components, N23 is likely to be at a late stage of the Sedov phase, and if so, its age is ∼8000 yr old from the newly discovered low temperature component.

Note, however, that this discussion depends on the estimation of the volume filling factor f. Accounting for the highly anisotropic image (Fig. E.3), we have normalized f by 0.1. However, if the shock wave of N23 propagates in a higher density ISM, like the edge of the open cluster HS 114 (Hodge & Sexton, 1966), the total volume should be smaller for the given emission measure, resulting in a smaller f. If, for instance, $f = 0.01$, $t_{\rm cool}$ of the low and high temperature components are ∼5000 and ∼7000 yr, respectively. Since $t_{\rm cool} \simeq t_{\rm Sedov}$, the low temperature component should be regarded as in the radiative phase. In addition, we would also like to remark that, in § E.4.1, we have calculated the plasma volume, assuming that the shell thickness is 1/12 of the shell radius, which is expected for a spherical strong shock. This holds only if N23 is still in the Sedov (adiabatic) phase. If N23 has been in the radiative phase, then the shell thickness should be smaller due to radiative cooling, and hence, the plasma density would be larger than the current estimation. As a result, the cooling time scale estimated from eq. (E.2) should be smaller, and $t_{\rm cool} \simeq t_{\rm Sedov}$. Consequently, we cannot deny possibility that N23 has been in the radiative phase.

In summary, the age of N23 is estimated to be ∼8000 yr from the newly discovered low temperature component as long as it still stays in Sedov phase. This condition is, however, uncertain, because the discussion depends on the volume filling factor of the plasma. If, for instance, the shock propagate in the higher density ISM, N23 may have already entered into the radiative cooling phase. In this case, the remnant age estimated from the cooling timescale is smaller.

Finally, we can make an independent age estimation from the central source detected

by *Chandra* (Hayato et al., 2006). Its luminosity is 1×10^{34} erg in the 0.5–10.0 keV (Hayato et al., 2006). If the central source is a pulsar (although the pulsation has not been detected), the characteristic age is $\sim 10^3$–$10^{4.5}$ years (Possenti et al., 2002), which is consistent with our age estimation update.

E.4.3 Abundance

The main component of X-ray emission originates from the swept-up ISM in N23. Hence the elemental abundances of N23 reflect those of its environment. Figure E.4 shows the abundances obtained from the spectral analysis (table E.2). The abundances of N, O,

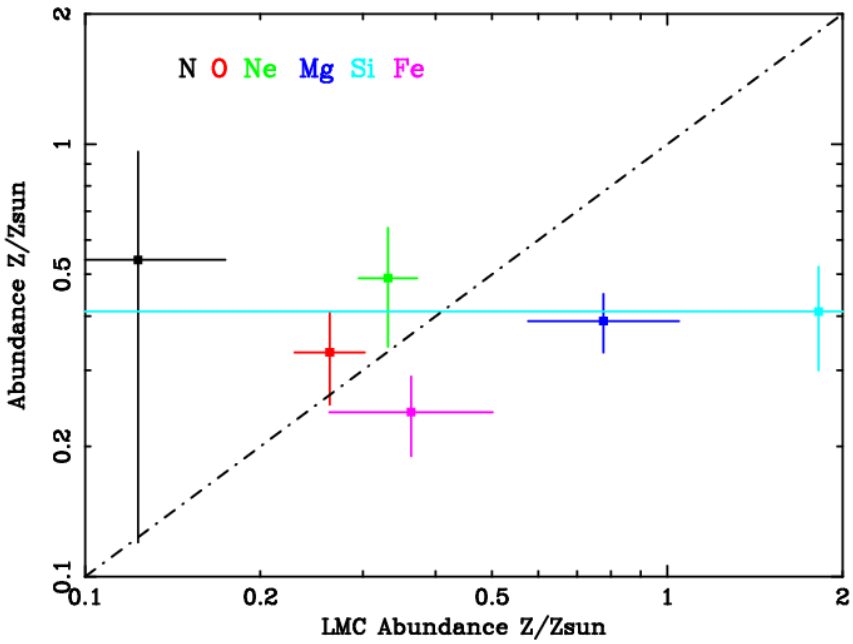

Figure E.4: Elemental abundance as derived from fits to the XIS data. The derived N23 abundance value is the square. The ratios are all relative to solar (Andres & Grevesse 1989). The silicon abundance in Russell & Dopita's work is highly uncertain as indicated by our use of a large error bar for this species. Dashed line represents the abundance in these SNRs are same to the LMC average.

Ne and Fe agree roughly with the LMC average (Russell & Dopita, 1992). The Si and Mg abundances are smaller than those obtained (Russell & Dopita 1992), although their errors are relatively large. The Mg and Si abundances obtained by Suzaku are consistent with those from *ASCA* (Hughes et al. 1998), respectively, which seem slightly less than the LMC average.

E.5 Summary

We observed N23 in the Large Magellanic Cloud with *Suzaku*, and discovered the new soft emission component with a temperature of ~ 0.22 keV, in addition to the ~ 0.5–0.7 keV component so far known. This alters the estimate of the ionization parameter

($n_e t$) significantly from $\sim 10^{10} - 10^{11}$ cm^{-3} s to $\sim 10^{12}$ cm^{-3} s. With the aid of *Chandra* imaging capability, we are able to calculate the density of the plasma, and have confirmed that the supernova explosion of N23 occurred in a high density region with an ISM density of ∼4–8 cm^{-3}. The relatively high ambient density may be related to the open cluster HS 114 (Hodge & Sexton, 1966) near the remnant (Hughes et al., 2006). This remnant had the low temperature plasma (∼0.2 keV) in collisional ionization equilibrium, which was doubted in the late stage of the Sedov phase or the initial radiative cooling phase. We therefore investigated these phases for this remnant. The parameters of the plasma from our analysis indicate that N23 is either at a late stage of the Sedov phase or in the radiative cooling phase. In the detailed study, we found that such SNRs with the low temperature plasma in collisional ionization equilibrium would be at least in the late stage of the Sedov phase. Assuming it is still in the Sedov phase, we have estimated the age of the remnant to be ∼8000 yr from the newly discovered soft component, which is twice as old as the estimation by Hughes et al. (1998). Given the uncertainty ofthe volume filling factor, however, we cannot deny the possibility that N23 has already entered into the radiative phase.

The abundances of N23 is roughly consistent with the LMC average (Russell & Dopita 1992). The Si and Mg abundances obtained by spectral fitting are smaller than those obtained by Russell & Dopita (1992), although their errors on Si and Mg abundances are relatively large. The Mg and Si abundances obtained by *Suzaku* are consistent with those from *ASCA* (Hughes et al. 1998).

Appendix F

Notes on Individual Objects

In this section, we summarize manly the typical X-ray observation for each SNR.

J0449.3-6920

This remnant was discovered in MCELS using reliable [SII]/Hα ratio, with SNRs typically having this ratio >0.4 (Fesen et al., 1985). In the recent *XMM-Newton* observation, the extended X-ray emission was reproduced well with a single component APEC model attenuated by the interstellar absorption with the temperature of 0.19 keV and the hydrogen column density of 3.7×10^{21} cm^{-2} (Klimek et al., 2010). Although the emission measure was presented in their paper, the absorbed flux was estimated to be 5.0×10^{-14} erg s^{-1} cm^{-3}. This morphology seems to interact between the hot interior (X-ray) and the cool shel (optical).

J0450.2-6922 (B0450-6927)

This remnant seems to have the patchy morphology in the radio band with 5 and 6 mJy beam^{-1} (Payne et al., 2008). The radio diameter was estimated by them to be $\sim 3'.5$, corresponded to the X-ray diameter. The detailed spectroscopies in the X-ray band have not been performed from past to present.

J0450.4-7050 (B0450-709)

J0450.4-7050 (B0450-709) is the large known remant in the LMC (Mathewson et al., 1985). The optical size is $\sim 6'.5 \times 4'.7$, corresponds to 98×70 pc at the LMC distance of 50 kpc (Feast, 1999). This SNR is not near any known OB association of bright HII region, and the surface density of OB star is low in its vicinity (Chu & Kennicutt, 1988). This remnant has an [SII]/Hα ratio of 0.7 and a radio spectral index estimated at -0.2, which clearly confirm its identity as SNR (e.g. Mathewson et al. 1985). The X-ray emission region is smaller than the optical shell, with the brightest X-ray emission found within the small interior shell and on the western rim of the large shell (Williams et al., 2004). From the *XMM-Newton* observation, this remnant was reproduced well with a single METAL model attenuated by the interstellar absorption with the hydrogen column density of $(1.1 \pm 0.9) \times 10^{21}$ cm^{-2}, the temperature of 0.28±0.04 keV, the abundances of 0.14±0.1 solar, and mission measure of $(2.4\pm1.2)\times10^{58}$ cm^{-3} (Williams et al., 2004). They estimated the relatively large age of $\sim 45,000$ yr.

J0453.2-6655 (N4)

This remnant was confirmed by Smith et al. (1994) with the X-ran and optical observation. The image taken with interference filters shows high [SII]/Hα ratios in the optical nebulae, which was confirming the presence of high velocity shocks commonly seen in SNRs. This remnant was reproduced by them well with a single temperature plasma in collisional ionization equilibrium attenuated by the interstellar absorption with the temperature of 0.2–0.32 keV and the hydrogen column density of (1.58–3.16)$\times 10^{20}$ cm^{-2} (Smith et al., 1994). The absorbed flux was also estimated to be 5.35×10^{-13} erg s^{-1} cm^{-3} in 0.11–2.4 keV. This X-ray morphology seems to have the relatively irregular morphology (Smith et al., 1994).

J0453.6-6829 (B0453-685)

This remnant are known to have a young energetic pulsar and its surrounding pulsar wind nebula, which are on of the "composite" SNRs. This pulsar and pulsar wind nebula were analyzed by Gaensler et al. (2003), which were reproduced well with a single component POWER LAW model attenuated by the interstellar absorption with the photon index of 1.5 (fixed) and the hydrogen column density of 1.3×10^{21} cm^{-2}. The unobserved X-ray luminosity was estimated by them to be $< 6 \times 10^{33}$ erg s^{-2}. The thermal emission was reproduced well with a single temperature component VNEI model attenuated by interstellar absorption with the temperature of $0.51^{+0.14}_{-0.14}$ keV, the ionization parameter of $(4.8\pm 0.5) \times 10^{10}$ cm^{-3}, the emission measure of 8.8×10^{58} cm^{-3} cm^{-3}, and the hydrogen column density of $< 1.1 \times 10^{21}$ cm^{-2} (Hughes et al., 1998).

J0453.9-7000 (B0454-7005)

This remnant seems to have the shell like morphology with the radio band 1.2, 2 and 4 mJy beam^{-1} Payne et al. (2008). The radio diameter was estimated by them to be $\sim 7'$, corresponded to the X-ray diameter. This remnant have been not also performed the detailed spectral analysis from past to present.

J0454.6-6713 (N9)

This remnant was notices by Smith et al. (1994) with the *ROSAT* observation, and confirmed through [SII]/Hα ratio and the non-thermal radio emission for the first time. This remnant has dimension 2'.3×3'.6 (33×52 pc) and is elongated in the north-south direction. The X-ray diffuse emission was reproduced well with a single component VPSHOCK model attenuated by the interstellar absorption with the temperature of $0.34^{+0.02}_{-0.02}$ keV, the emission measure of $2.99^{+0.90}_{-0.60} \times 10^{58}$ cm^{-4}, the ionization parameter of $8^{+3}_{-2} \times 10^{10}$ cm^{-3} s and the hydrogen column density of 2×10^{21} cm^{-2} (fixed). They estimated the relatively large age to be $\sim 3 \times 10^4$ yr, and detected the enhanced Fe abundance in the central region. This remnant was originated from Type Ia SNe.

J0454.8-6626 (N11L)

N11 L is the "L" component for the HII complex N11. The measured optical diameter for this remnant was estimated to be 1', corresponds to $\sim$ 15 pc. The Hα and [SII] morphologies for this remnant show a circular ring of filament with protruding "jet",

which is actually protection loop like filaments, to the northeast (Williams et al., 1999). Unfortunately, the detailed spectroscopy in the X-ray band has not been performed from past to present. The *ROSAT* PSPC count rates for this remnant were estimated to be 2.74×10^{-2} counts s^{-1}, correspond to 3.13×10^{-13} erg s^{-1} (absorbed flux) in the 0.5–10.0 keV band (Haberl & Pietsch, 1999). The absorbed flux can be converted to an estimated *ROSAT* PSPC count rate using PIMMS tool from HEASARC.

J0455.6-6839 (N86)

This remnant is one of the large SNRs (∼3' diameter) in the LMC, and seems to have a very nonuniform morphology. The X-ray emission for this remnant was analyzed by Williams et al. (1999). This remnant was reproduced well with a single temperature plasma in collisional ionization equilibrium attenuated by the interstellar absorption with the temperature of 0.15 keV, the emission measure of 2.61×10^{60} cm^{-3}, and the hydrogen column density of 6.3×10^{21} cm^{-2}. The absorbed flux was also derived by them to be 1.74×10^{-11} erg s^{-1} cm^{-2} in the 0.5–2.0 keV.

J0459.9-7008 (N186D)

This remnant was confused due to the superposed N186E region. As a result, this remnant had been difficult to observe. A velocity study can distinguish the expanding shell for this remnant (Laval et al., 1989). Rosado et al. (1990) indicated that this remnant was interacted with the N186E shell and that N186E was to be an older SNR. The detailed spectroscopy in the X-ray band had been performed from past to present. According to the *Chandra* online catalogue, the absorbed flux was estimated to be 2.03×10^{-13} erg s^{-1} in the 0.5-10.0 keV.

J0505.7-6753 (DEM L71)

This remnant belongs to a class of SNR that is dominated by the hydrogen emission in their optical spectra, which is indicated that this remnant is to be Type Ia SNe. Analysis of the optical spectrum for this remnant indicates a shock velocity of T_S =0.11–0.75 keV (Smith et al., 1994). To combine this information with a radius of ∼ 10 pc, this remnant was estimated to be the age of ∼ 10^4 yr. van der Heyden et al. (2003) discovered the enhanced Fe abundance in the central region, which was also indicated that this remnant was to be Type Ia SNe. They also revealed that this remnant exhibited both the shell-like X-ray emission and a centrally filled morphology. The detailed spectral analysis for the whole remnant was reported by van der Heyden et al. (2003). The entire X-ray emission was reproduced well with the two temperature components VNEI model attenuated by the interstellar absorption. One component had the temperature of 0.21±0.04 keV, the emission measure of $(3.0\pm1.0)\times10^{59}$ cm^{-3}, and the ionization parameter of $8.1^{+8.0}_{-3.0}\times10^{11}$ cm^{-3} s, while the other component had the temperature of $0.84^{+0.40}_{-0.21}$ keV, the emission measure of $(5.3\pm3.0)\times10^{58}$ cm^{-3} and the ionization parameter of $7.2^{+10.1}_{-4.2}\times10^{10}$ cm^{-3} s. The hydrogen column density was also derived to be $(1.2\pm0.6)\times10^{19}$ cm^{-2}.

J0505.9-6802 (N23)

J0505.9-6802 (N23) is identified as a SNR with the radio observation at 5 and 14.7 GHz (Milne et al., 1980). One part of the remnant were shown a evidence for enchanted O, Ne, and Mg abundances, which was suggested from core-collapse SNe (Hughes et al., 2006). In addition, there is a point source in this SNR (Hughes et al. 2006; Hayato et al. 2006), which the progenitor is suggested to be core-collapsed massive star. In the detailed analysis of whole remnant was presented by Someya et al. (2010). The spectrum was reproduced well with the two temperature components VNEI model attenuated by the interstellar absorption. One component had $0.218^{+0.012}_{-0.004}$ keV and the emission measure of $7.60^{+1.26}_{-1.83} \times 10^{59}$ cm^{-3}, while the other component had the temperature of $0.569^{+0.024}_{-0.013}$ keV and the emission measure of $2.48^{+0.51}_{-0.57} \times 10^{59}$ cm^{-3}. The ionization parameter common between the two temperature component VNEI model was derived to be $4.79^{+0.21}_{-0.08} \times 10^{13}$ cm^{-3} s. Finally, the hydrogen column density was derived to be $1.5^{+0.4}_{-0.9} \times 10^{21}$ cm^{-2}.

J0506.1-6541

This remnant was discovered in MCELS using reliable [SII]/Hα ratio, with SNRs typically having this ratio >0.4 (Fesen et al., 1985). In the recent *XMM-Newton* observation, the extended X-ray emission was reproduced well with a single component APEC model attenuated by the interstellar absorption with the temperature of 0.17 keV, the emission measure of $(1.20\pm0.60)\times10^{59}$ cm^{-3}, and the hydrogen column density 3.2×10^{21} cm^{-2}. This morphology seems to be interact between the hot interior (X-ray) and the cool shell (optical).

J0509.0-6844 (N103B)

This remnant is one of the bright radio and X-ray SNRs in the LMC. It was identified as SNR by the non-thermal spectrum in the radio observation for the first time (Mathewson et al., 1983). Its age was estimated to be 860 yr based on the light-echo (Rest et al., 2005), this remnant is one of the young SNRs in the LMC. This remanned was located at close to the HII region DEM L84 and the young rich cluster NGC 1850, which was indicated that this remnant was to be CC SNe (Chu & Kennicutt, 1988). In addition, van der Heyden et al. (2002) detected the strong line emissions from the fully ionized metals (O, Ne, and Mg produced by CC SNe) through the RGS observation, which they also concluded that this remnant this remnant was to be CC SNe. In contrast, Lewis et al. (2003) estimated the large amount Fe mass produced by Type Ia SNe. In the recent observation, the ejecta for Type Ia have the high symmetric morphology compared with those originated from CC SNe with the statical image analysis (Lopez et al., 2010). They concluded that this remnant was to be Type Ia SNe in their study. Its progenitor is still unclear, like this. In addition, its emission origin is also still unclear in spite of many observations (Lewis et al. 2003; van der Heyden et al. 2002). In this section, we introduce the *XMM-Newton* observation (Lewis et al., 2003). They reproduced well with the three temperature components VNEI model attenuated by the interstellar absorption ("H-dominated plasma"). The high, middle, and cool temperature component had the temperature of 3.5 ± 0.5 keV, 0.65 ± 0.05 keV, and $0.55^{+0.05}_{-0.32}$ keV, the emission measure of $(4.1\pm0.5)\times10^{58}$ cm^{-3}, $(6.5\pm0.1)\times10^{59}$ cm^{-3}, and $(2.6\pm0.1)\times10^{58}$ cm^{-3}, and the ionization

parameter of $(5.3 \pm 0.8) \times 10^{10}$ cm^{-3} s, $> 2.5 \times 10^{12}$ cm^{-3} s, and $(2.5 \pm 0.7) \times 10^{19}$ cm^{-2}, respectively. The hydrogen column density was derived to be $(2.5 \pm 0.7) \times 10^{19}$ cm^{-2}.

J0509.5-6731 (B0509-67.5)

This remnant has a spherical shape with the angular diameter of $\sim$ 25". Its age was estimated to be 400 yr based on the light-echo (Rest et al., 2005), which is indicated that this remnant was to be Type Ia SNe. The detailed spectroscopy in the X-ray band was performed by Warren & Hughes (2004) and Kosenko et al. (2008). Their study revealed that this remnant was rich in silicon, sulfur, and iron, that the bulk of the continuum emission has a non-thermal origin. The ambient density was estimated by them to be ~ 0.05 cm^{-3}, which was probably exploded in the relatively low density region. The overall spectrum for thermal emission was roughly reproduced with a single temperature VNEI component attenuated by the interstellar absorption with the temperature of $4.0^{+0.23}_{-0.18}$ keV, the emission measure of $(1.2 \pm 0.1) \times 10^{58}$, the ionization parameter of $(1.41 \pm 0.03) \times 10^{10}$, the hydrogen column density of (5–9)$\times 10^{20}$ cm^{-2}. On the other hand, the non-thermal emission had the photon index of 3.5 ± 0.1 and the normalization of $(2.3 \pm 0.3) \times 10^{-4}$ photons s^{-2} cm^{-2} (Kosenko et al., 2008).

J0518.7-6939 (N120)

This remnant was identified as an SNR by Mathewson & Clarke (1973) with the non-thermal radio spectrum and the high [SII]/Hα line ratio. The diameter was etimated to be $\sim$30 pc for an distance of 50 kpc (Feast, 1999). This remnant is located within the 9'$\times$7' (135$\times$105 pc) arc-shaped nebular complex N120 (Henize, 1956) or DEM 134 (Davies et al., 1976). The detailed X-ray spectroscopy was performed with *XMM-Newton* (Reyes-Iturbide et al., 2008). The spectrum was reproduced well with a single temperature component MEKAL model attenuated by the interstellar absorption with the temperature of 0.31 ± 0.06 keV, the hydrogen column density of $(1.21 \pm 0.06) \times 10^{20}$ cm^{-2}. The intrinsic X-ray luminosity was estimated to be 1.2×10^{35} erg s^{-1}.

J0519.6-6902 (B0519-690)

This remanned has an relatively patchy morphology. Its age was estimated to be 600$\pm$200 yr based on the light-echo (Rest et al., 2005), this remnant was also one of the young SNRs in the LMC. Hughes et al. (1995) discovered that this remnant was to be oxygen-poor and iron rich, and could be Type Ia SNe. The X-ray spectral analysis was performed by Kosenko et al. (2010), and they assumed the layer structure reflected by its explosion in their spectral analysis. The ISM component heated by the forward shock was reproduced well with a single temperature component VNEI model with the temperature of $0.64^{+0.02}_{-0.06}$ keV, the emission measure of $2.36^{+0.50}_{-0.11} \times 10^{59}$ cm^{-3}, and the ionization parameter of $> 6.7 \times 10^{11}$ cm^{-3} s. On the other hand, the ejecta component heated by the reverse shock was reproduced with the five temperature components VNEI model with the temperature of $\sim$1–7 keV, the emission measure of $\sim$1–9$\times 10^{54}$ cm^{-3} s, and the ionization parameter of $\sim 10^{10}$–10^{11} cm^{-3} s. The hydrogen column density was derived to be $2.64^{+0.07}_{-0.06} \times 10^{21}$ cm^{-2}. From the continuum component, they derived the ambient density of 2.4$\pm$0.2 cm^{-3}.

J0519.7-6926 (B0520-694)

SNR J0519.7-6926 (B0520-694) was identified as SNR based on the *Einstein* X-ray survey by Long et al. (1981). Payne et al. (2008) found an enhanced [SII]/Hα ratio of 0.8 typical for SNRs. Its X-ray emission extends $\sim 2'.6 \times 2'.2$ in the sky, showing a shell-like morphology (Williams et al., 1999). The detailed spectroscopy in the X-ray band has not been performed from past to present. The *ROSAT* PSPC count rates for this remnant were estimated to be 1.13×10^{-1} counts s^{-1}, corresponded to 1.25×10^{-12} erg s^{-1} in the 0.5–10.0 keV band (Haberl & Pietsch, 1999). The absorbed flux can be conveyed to be an estimated *ROSAT* PSPC count rate using PIMMS tool from HEASARC.

J0523.1-6753 (N44)

N44 is one of the HII regions in the LMC, consisting of three OB associations (e.g. Lucke & Hodge 1970). This remnant is close to these OB associations. Nakajima et al. (2006) observed this remnant, and reproduced well with a single temperature component VNEI component with the temperature of $0.40^{+0.3}_{-0.1}$ keV, the ionization parameter of $9.1^{+3.3}_{-2.3} \times 10^{11}$ cm^{-3}, the intrinsic flux of 0.35×10^{-12} ergs cm^{-2} s^{-1}, and the hydrogen column density of $2.40^{+0.63}_{-0.89} \times 10^{21}$.

J0525.1-6938 (N132D)

This remnant is one of the oxygen rich SNRs, and located in the bar of the LMC. In the X-ray morphology, this remnant seems to have an irregular sell with a break-out in the northeast. From the observation with grating spectrometers onboard *XMM-Newton*, the cool component estimated to be the temperature of 0.15 keV based on OVI/OV line ratio (Behar et al., 2001). The narrow band images seem to show the ambient medium heated by the forward shock. The shell region was reproduced well with the two temperature components VPSHOCK model attenuated by the interstellar absorption (Xiao & Chen, 2008). They performed the spatially resolved spectral analysis. The X-ray emission are derived to be the the temperature of $\sim$0.5 keV and $\sim$ 1.5 keV and the ionization parameter of $\sim 10^{12}$ cm^{-3} s and $\sim 10^{11}$ cm^{-3} s, respectively. The hydrogen column density was to be $\sim 1 \times 10^{21}$ cm^{-3}, respectively.

J0525.4-6559 (N49B)

This remnant is located $\sim 6'.5$ from northwest of N49, and one of the bright SNRs. In the optical band, this SNRs consists of two irregular-shaped knots, and separated by $\sim 1'.4$ (Mathewson et al., 1983). The *Einstein* and *ROSAT* data revealed a nearly circular X-ray morphology. The X-ray spectrum with *ASCA* was reproduced well with a single temperature component VNEI model attenuated by the interstellar absorption with the temperature of $\sim$0.4 keV, the ionization parameter of $\sim 10^{11}$ cm^{-3} s, and the hydrogen column density of $\sim 2.6 \times 10^{21}$ cm^{-2}. (Hughes et al., 1998). The derived metal abundances were compatible with the ISM average, although there was the evidence of the slightly enhanced Mg abundance. The superb angular resolution for *Chandra* resolved the complex structure from the X-ray emission (Park et al., 2003). The bright circumferential filaments are emission from the shocked dense ambient medium, and the X-ray spectrum was reproduced with a single component VNEI model attenuated by the

interstellar absorption with the temperature of $0.34^{+0.14}_{-0.10}$ keV, the ionization parameter of $11.2^{+4.7}_{-3.4} \times 10^{11}$ cm^{-3} s, and the hydrogen column density of $3.3^{+1.6}_{-1.3} \times 10^{21}$ cm^{-2}.On the other hand, the spatially resolved spectral analysis revealed the evidence of the enhanced Mg abundance, and the X-ray spectrum was reproduced well with a single temperature component VNEI model attenuated by the interstellar absorption with the temperature of $0.36^{+0.14}_{-0.09}$ keV, the ionization parameter of $4.5^{+4.1}_{-2.4} \times 10^{11}$ cm^{-3} s, and the hydrogen column density of $2.3^{+1.1}_{-2.0} \times 10^{21}$ cm^{-3}. The Mg and Si abundances have up to 1 solar, which corresponding to the ejecta heated by the reverse shock.

J0526.0-6605 (N49)

This remnant is one of the bright SNRs in the LMC. The most remarkable feature for this remnant is strong enhancements for the optical/X-ray surface brightness in the southeast. This asymmetric intensity distribution has been considered to be the interaction of the blast wave with the nearby molecular cloud located in the east of this remnant (Vancura et al. 1992; Banas et al. 1997). The X-ray spectrum from this remnant was obtained with *ASCA* (Hughes et al., 1998). They reproduced well with a single temperature component VNEI model attenuated by the interstellar absorption with the temperature of $\sim$0.6 keV , the ionization parameter of $\sim 10^{11}$ cm^{-3} s, and the hydrogen column density of 2.2×10^{21} cm^{-3}. Park et al. (2003) reported the spatially resolved spectral analysis. They also reproduced with a single temperature component VNEI component for each region attenuated by the interstellar absorption with the temperature of $\sim$0.5–1.0 keV, the ionization parameter of $\sim$ 10^{11}–10^{12} cm^{-3} s, and the hydrogen column density of $(1 - -3) \times 10^{21}$ cm^{-2}.

J0527.6-6912 (B0528-692)

The X-ray faintness and lack of celar definition for this remnant make classification difficult (Williams et al., 1999). Chu & Kennicutt (1988) suggested that this remnant was to be CC SNe, since this remnant is within the HII region DEM L210 and the density of nearly OB stars in very high. The detailed spectroscopy in the X-ray band has not been performed from past to present. The *ROSAT* PSPC count rates for this remnant were estimated to be 4.37×10^{-2} counts s^{-1}, corresponded to 4.26×10^{-13} erg s (absorbed flux) in the 0.5–10.0 keV (Haberl & Pietsch, 1999). The absorbed flux can be converted to an estimated *ROSAT* PSPC count rate using PIMMS tool from HEASARC.

J0531.9-7100 (N206)

J0531.9-7100 (N206) lies to the north and east of the HII region LHα 120-N206 in the LMC. This SNR was discovered in the radio by Mathewson & Clarke (1973). The X-ray emission from this remnant was analyzed by Williams et al. (2005). They reproduced well with a single temperature component VPSHOCK model attenuated by the interstellar absorption with the temperature of $0.453^{+0.005}_{-0.006}$ keV, the ionization parameter of $(3.5 \pm 0.2) \times 10^{11}$ cm^{-3}, the emission measure of $5.23^{+0.09}_{-0.06} \times 10^{58}$, and the hydrogen column density of $(2.2 \pm 0.1) \times 10^{21}$ cm^{-3}.

J0532.5-6732 (B0532-675)

SNR J0532.5-6732 (B0532-675) has the shell like morphology with the X-ray band in the our study. The detailed spectroscopy in the X-ray band has not been performed from past to present. The *ROSAT* PSPC count rates for this remnant were estimated to be 6.67×10^{-2} counts s^{-1}, corresponded to 6.87×10^{-13} erg s^{-1} in the 0.5–10.0 keV (Haberl & Pietsch, 1999). The absorbed flux can be converted to an estimated *ROSAT* PSPC count rate using PIMMS tool from HEASARC.

J0534.0-6955 (B0534-699)

The detailed spectral analysis for this remnant was performed by Hendrick et al. (2003) with *Chandra*. They reported that this remnant showed the bright central regions as well as the brightened limbs. The central region exhibited enhanced metal abundances, in contrast to limb, which showed the abundances consistent with the LMC average (Russell & Bessell, 1989). On the other hand, the central metal abundances is indicated to be Type Ia SNe. The relatively old age was to be ∼10,000 yr, which this remnant may be in the Sedov phase. According to their spectral analysis, the limb region was reproduced well with a single temperature component VPSHOCK shock model attenuated by the interstellar absorption with the temperature of $0.33^{+0.04}_{-0.13}$ keV, the ionization parameter of $2.43^{+1.71}_{-0.75}\times10^{11}$ cm^{-3} s, the emission measure of 1.05×10^{58} cm^{-3} in the south limb region. On the other hand, the central region was also reproduced with a single temperature component VPSHOCK model attenuated by the interstellar absorption with the temperature of $0.61^{+0.09}_{-0.10}$ keV, the ionization parameter of $1.46^{+1.64}_{-0.47}\times10^{11}$ cm^{-3} s, the emission measure of 5.2×10^{57} cm^{-3} in the south central region. The hydrogen column density was derived to be $1.90^{+1.6}_{-0.7}\times10^{21}$ cm^{-2}.

J0534.3-7033 (DEM L238)

This remnant has the bright central emission, and surrounding by a faint shell (Borkowski et al., 2006). The central emission had the X-ray thermal emission dominated by strong Fe-L shell lines, which were exceeded the solar value (Anders & Grevesse, 1989). This Fe overabundance leads to the conclusion that this remnant is to be Type Ia SNe (Borkowski et al., 2006). Under the assumption of the Sedov model, the age was estimated by them to be 10,000–15,000 yr. The shell emission was reproduced well with a single temperature component PSHOCK model attenuated by the interstellar absorption with the temperature of $0.11^{+0.23}_{-0.11}$ keV, ionization parameter of $9.4^{+2.0}_{-2.3}\times10^{11}$ cm^{-3} s, and the emission measure of 4.4×10^{57} cm^{-3}, while the central emission was also reproduced well with a single temperature component VPSHOCK model attenuated by the interstellar absorption with the temperature of $0.82^{+0.04}_{-0.02}$ keV, the ionization parameter of $0.83^{+0.38}_{-0.26}\times10^{12}$ cm^{-3} s, and the mission measure of 4.1×10^{57} cm^{-3} in the pn sector. The hydrogen column density was not presented in their paper.

J0535.5-6916 (SNR 1987A)

This remnant was discovered in February 23, 1987 for the first time. In the current stage for this remnant, the shock wave has reached the inner circumstellar ring, causing heating of the dense ring matter and brightening in the X-ray. In this section, we introduce the

Suzaku result observed on 2005 (Sturm et al., 2009). The X-ray spectrum for this remnant was reproduced well with two temperature components VPSHOCK model with attenuated by the interstellar absorption with the temperature of $0.45^{+0.07}_{-0.04}$ keV and $2.92^{+1.05}_{-0.54}$ keV, the ionization parameter of $8.1^{+2.6}_{-2.5} \times 10^{11}$ cm^{-3} s and $3.1^{+1.2}_{-1.5} \times 10^{11}$ cm^{-3} s, and the emission measure of $23.0^{+6.2}_{-7.5} \times 10^{58}$ cm^{-3} and $(2.0 \pm 0.4) \times 10^{58}$ cm^{-3}. The hydrogen column density was estimated to be $1.77^{+0.28}_{-0.40} \times 10^{21}$.

J0535.7-6602 (N63A)

This remnant is the second brightest SNR in the LMC. This remnant is located in a larger HII region (N63), and appears to be located within the OB association NGC 2030 (Chu & Kennicutt, 1988), which this remnant is believed to be the explosion of a massive star in the dense and complex environment (e.g. Hughes et al. 1998). The spectral analysis for an overall this remnant was performed by Hughes et al. (1998). The spectrum was reproduced with a single temperature component VNEI model attenuated by the interstellar absorption with the temperature of 0.62 ± 0.4 keV, the ionization parameter of 1.7×10^{11} cm^{-3}, and the X-ray luminosity in the 0.5–5.0 keV of 2.0×10^{37} erg s. The hydrogen column density was estimated to be $(1.4 \pm 0.1) \times 10^{21}$ cm^{-2}.

J0535.8-6918 (Honeycomb)

This remnant is located near SN 1987A and 30 Dor. The detailed analysis for this SNR was performed by Dennerl et al. (2001). The thermal emission was reproduced with a single temperature APEC model attenuated by the interstellar absorption with the temperature of 0.19 ± 0.02 keV and the hydrogen column density of $(2.2 \pm 0.9) \times 10^{21}$ cm^{-2}. The emission measure (e.g. flux) was not presented in their paper. According to the *Chandra* online catalogue, the absorbed flux was estimated to be $1.66 \sim 10^{-13}$ erg cm^{-2} s^{-1} in the 0.5–10.0 keV.

J0536.1-6735 (DEM L241)

This remnant was identified as SNR by Mathewson et al. (1985). They revealed that this remnant shoed the looped filamentary structure with the size of $\sim 2'$ in the optical image. Nishiuchi et al. (2001) observed this remnant with *ASCA*, and fount that the spectrum for this remnant requires not only thermal emission but also a power-law component with $\Gamma \sim 1.6$. This result indicated that this remnant had a pulsar and/or its wind nebula. In the recent observation, Bamba et al. (2006) analyzed the image with *XMM-Newton*, and fount the compact source in this remnant. The source spectrum was reproduced well by a single POWER LAW model attenuated by the interstellar absorption with the photon index of $1.57^{+0.05}_{-0.06}$ and the absorbed flux in the 0.5–10.0 keV of $(6.4 \pm 0.4) \times 10^{-13}$ erg s^{-1} cm^{-2}. The thermal component was reproduced well with a single temperature component VPSHOCK model attenuated by the interstellar absorption with the temperature of 0.39 ± 0.1 keV, the ionization parameter of $> 14.6 \times 10^{12}$ cm^{-3} s, and the emission measure of $4.4^{+0.4}_{-0.6} \times 10^{58}$ cm^{-3} in the head region. The X-ray emission in the tail region was roughly consistent with that in the head region. The hydrogen column density was estimated to be $5.6^{+0.8}_{-0.9} \times 10^{21}$ cm^{-2}. They indicated that this remnant was to be a very massive star (>20 M$_\odot$) based on the Fe/O ratio.

J0536.1-7039 (DEM L249)

This remnant has the bright central emission, and surrounding by the faint shell. The central X-ray emission has an entirely thermal emission dominated by strong Fe-L shell lines, which are exceeded the solar abundance (Anders & Grevesse, 1989). The Fe over-abundance leads to the conclusion that this remnant is to be Type Ia SNe (Borkowski et al., 2006). Under the assumption of the Sedov model, the age was estimated to be 10,000–15,000 yr. The shell emission was reproduced well with a single temperature component PSHOCK model attenuated by the interstellar absorption with the temperature of 0.36 keV, and the ionization parameter of 2.1×10^{11} cm^{-3}. On the other hand, the central emission was also reproduced with the same model with the temperature of $1.25^{+0.17}_{-0.50}$ keV, the ionization parameter of $0.88^{+5.30}_{-0.20}\times10^{11}$ cm^{-3} s, and the emission measure of 1.0×10^{58} cm^{-3}. The hydrogen column density was not presented in their paper.

J0536.2-6912 (30 Dor C)

This remnant is located in the southwestern region of the 30 Doradus complex, and one of the SBs in the LMC. A shell-like structure with a diameter of $\sim 6'$ was discovered by the radio observation (Mills & Turtle, 1984). In the recent observation, Bamba et al. (2004) discovered the synchrotron X-ray from the shell region with *Chandra* and *XMM-Newton*. Yamaguchi et al. (2009) also reported that the non-thermal spectrum was reproduced well with a single POWER LAW model attenuated by the interstellar absorption with the photon index of $2.17^{+0.4}_{-0.5}$ and the normalization of $(2.8\pm0.1)\times10^{-4}$ photons s^{-1} cm^{-2} keV^{-1} at 1 keV in the west region. On the other hand, the thermal emission was reproduced well with a single temperature component VAPEC model attenuated by the interstellar absorption with the temperature $0.66^{+0.10}_{-0.08}$ keV, the emission measure of $7.8^{+3.2}_{-4.6}\times10^{58}$ cm^{-3}, and the hydrogen column density of $6.2^{+3.5}_{-3.4}\times10^{20}$ cm^{-2} in the SE region.

J0537.4-6628 (DEM L256)

This remnant was discovered in MCELS using reliable [SII]/Hα ratio, with SNRs typically having this ratio >0.4. In recent *XMM-Newton* observation, Klimek et al. (2010) reported that the extended emission was reproduced with a single component APEC model with the temperature of 0.22 keV and the emission measure of $< 2.69\times10^{58}$ cm^{-3}. This morphology seems to interact between the hot interior (X-ray) and the cool shel (optical).

J0537.8-6910 (N157B)

J0537.8-6910 (N157B) has been classified as Crab-like and contains the fastest known young pulsar PSR J0537-6910, with a period of 16 ms (Marshall et al., 1998). In the recent spectroscopy in the X-ray band, Chen et al. (2006) reported that the pulsar (and/or its wind nebula) was reproduced with a single component POWER LAW model with the photon index of $2.29^{+0.05}_{-0.06}$, and the intrinsic flux of 1.4×10^{-11} erg s^{-1} cm^{-2} in the 0.5-10 keV. On the other hand, the thermal component for this remnant was reproduced well with a single temperature component VNEI model attenuated by the interstellar absorption with the temperature of $0.72^{+0.13}_{-0.10}$ keV, the ionization parameter of $2.39^{+3.05}_{-1.16}\times10^{10}$ cm^{-3} s, the emission measure of $5.22\times10^{+1.49}_{-1.95}\times10^{58}$ cm^{-3}, and the hydrogen column density of $(6.1\pm0.6)\times10^{21}$ cm^{-2}.

J0540.0-6944 (N159)

The center of this remanned was ∼2' east of the very bright X-ray source LMC X-1, thus X-ray measurement for the this remnant was difficult. The detailed X-ray spectroscopy for this remnant was performed by Seward et al. (2010) with *Chandra*, which has the superior angular resolution. This remnant (N Lobe in their paper) was reproduced well with a single VMEKAL model attenuated by the interstellar absorption with he temperature of 0.59 ± 0.02 keV and the hydrogen column density $(0.33 \pm 0.04) \times 10^{22}$ cm^{-3}. The X-ray luminosity was estimated to be 5.36×10^{35} erg $^{-1}$.

J0540.2-6920 (B0540-693)

B0540-69.3 is the 50 ms pulsar. This pulsar is surrounding by the shell of radius of ∼ 30", which is probably SNR. This remanned is a young oxygen-rich SNR. This pulsar was analyzed by Hirayama et al. (2002), and reproduced well with a single POWER LAW model with the photon index of 2.00 ± 0.02 and the X-ray flux of $(3.2 \pm 0.1) \times 10^{-11}$ erg s^{-1} cm^{-2} in the 1–10 keV. On the other hand, the thermal emission was reproduced well with a single component NEI model attenuated by the interstellar absorption with the temperature 0.58 ± 0.18 keV, the emission measure of $(9.2 \pm 0.7) \times 10^{58}$ cm^{-3}, the ionization parameter of $(2.5 \pm 0.5) \times 10^{10}$ cm^{-3} s, and the hydrogen column density of $(4 \pm 1) \times 10^{21}$ cm^{-2} (SW region; van der Heyden et al. 2001)

J0543.1-6858 (DEM L299)

This large SNR shows a central cavity of dimension 1'.8×2'.3. This remnant has the patchy morphology in the X-ray band (Williams et al., 1999). The detailed spectroscopy in the X-ray band has not been performed from past to present. The *ROSAT* PSPC count rates for this remnant were estimated to be 2.44×10^{-1} counts s, corresponded to 2.98×10^{-12} erg s^{-1} (absorbed flux) in the 0.5–10.0 keV band (Haberl & Pietsch, 1999). The absorbed flux can be converted to an estimated *ROSAT* PSPC count rate using PIMMS tool from HEASARC.

J0547.0-6943 & J0547.4-6941 (DEM L316 B & A)

This remnant was discovered by Mathewson & Clarke (1973) to have a high [SII]/Hα ratio. They designated the two lobes of this system shell A (DEM L316 A; the northeastern shell) and B (DEM L316 B to the southwest). The X-ray spectroscopy was performed by Williams & Chu (2005) with *Chandra*. The low abundance ratios for shell A (O/Fe of 1.5 and Ne/Fe of 0.2) and the high abundance ratios for shell B (O/Fe of 30–130 and Ne/Fe of 8–16) are consistent with Type Ia and Type II origins, respectively. The shell A was reproduced well with a single temperature component VPSHOCK model attenuated by the interstellar absorption with the temperature of $1.4^{+0.3}_{-0.2}$ keV, the ionization parameter of $1.7^{+1.2}_{-0.5} \times 10^{11}$ cm^{-3} s, the emission measure of $6.28^{+2.69}_{-2.09} \times 10^{57}$ cm^{-3} s, and the hydrogen column density of $3.6^{+0.6}_{-0.5} \times 10^{21}$ cm^{-2}. On the other hand, the shell B was reproduced well with two temperature components VPSHOCK model attenuated by the interstellar absorption with the temperature of 0.57 ± 0.4 keV and 5^{+5}_{-2} keV, the ionization parameter of $< 5 \times 10^{13}$ cm^{-3} s and $1.3^{+0.7}_{-0.4} \times 10^{11}$ cm^{-3} s, the emission measure of $2.4^{+0.1}_{-0.2} \times 10^{57}$ cm^{-3} and $(6.3 \pm 0.6) \times 10^{57}$ cm^{-3}, and the hydrogen column density of

$(2.1\pm0.2)\times10^{21}$ cm^{-2}, respectively. The high temperature component was also reproduced with a single POWER LAW model with the photon index of $1.7^{+0.4}_{-0.2}$ and the normalization of $5.3^{+0.6}_{-0.5} \times 10^{-4}$ photons s^{-1} cm^{-2} keV^{-1}.

J0547.8-7025 (B0548-704)

This remnant belongs to the class of Balmer-line dominated, which is probably to be Type Ia SNe. The detailed X-ray analysis for this remnant was performed by Hendrick et al. (2003) with *Chandra*. They reported that this remnant showed the bright central regions as well as brightened limbs. The central region exhibited enhanced metal abundances, in contrast to limb, which showed abundances consistent with the LMC average (Russell & Bessell, 1989). The central metal abundances would be Type Ia SNe origin. By considering the relatively old age (∼10,000 yr), this remnant may be in the Sedov phase, in which the X-ray spectrum would be dominated by the swept-up ambient medium. The east limb region was reproduced well with a single temperature component VPSHOCK model attenuated by the interstellar absorption with the temperature of $0.0^{+0.2}_{-0.0}$ keV, the ionization parameter of $1.89^{+0.95}_{-0.71} \times 10^{11}$ cm^{-3} s, the emission measure of 1.3×10^{58} cm^{-3}, and the hydrogen column density of $5.22^{+1.1}_{-1.2} \times 10^{21}$ cm^{-2}. On the other hand, the central emission was reproduced well with the same model with the temperature of $0.62^{+0.04}_{-0.03}$ keV, the ionization parameter of $4.15^{+1.99}_{-1.40}\times10^{11}$ cm^{-3} s, and the mission measure of 2.6×10^{55} cm^{-3}.

J0550.5-6823

This remnant exhibits a one side shell brightened morphology a dissipating in the southern region. This SNR is located on the eastern side of the LMC, far away from the main body of this dwarf galaxy. Bozzetto et al. (2011) point out the dissipating shell in the southern region remnant, and it is reasonable to assume that this SNR is expanding in a very low density environment. The detailed spectroscopy in the X-ray band have not been performed from past to present. According to the *Chandra* online catalogue, the absorbed flux was estimated to be 3.98×10^{-13} erg s^{-1} cm^{-2} in the 0.5–10.0 keV.

Bibliography

Allen, C. W. 1973, London: University of London, Athlone Press, —c1973, 3rd ed.,

Anders, E., & Grevesse, N. 1989, Geochim. Cosmochim. Acta, 53, 197

Arnett, W. D. 1969, Supernovae and Their Remnants, 89

Aschenbach, B. 1988, Appl. Opt., 27, 1404

Baade, W., & Zwicky, F. 1934, Proceedings of the National Academy of Science, 20,254

Badenes, C., Maoz, D., & Draine, B. T. 2010, MNRAS, 407, 1301

Bamba, A., et al. 2008, PASJ, 60, 153

Bamba, A., Ueno, M., Nakajima, H., Mori, K., & Koyama, K. 2006, A&A, 450, 585

Bamba, A., Ueno, M., Nakajima, H., & Koyama, K. 2004, ApJ, 602, 257

Banas, K. R., Hughes, J. P., Bronfman, L., & Nyman, L.-A. 1997, ApJ, 480, 607

Behar, E., Rasmussen, A. P., Griffiths, R. G., et al. 2001, A&A, 365, L242

Berkhuijsen, E. M. 1988, A&A, 192, 299

Berkhuijsen, E. M. 1987, A&A, 181, 398

Berkhuijsen, E. M. 1986, A&A, 166, 257

Borkowski, K. J., Hendrick, S. P., & Reynolds, S. P. 2007, ApJ. Lett., 671, L45

Borkowski, K. J., Hendrick, S. P., & Reynolds, S. P. 2006, ApJ, 652, 1259

Borkowski, K. J., Lyerly, W. J., & Reynolds, S. P. 2001, ApJ, 548, 820

Borkowski, K. J., Sarazin, C. L., & Blondin, J. M. 1994, ApJ, 429, 710

Bothun, G. D., & Thompson, I. B. 1988, AJ, 96, 877

Bozzetto, L. M., Filipović, M. D., Crawford, E. J., et al. 2011, arXiv:1109.3945

Broeils, A. H., & van Woerden, H. 1994, A&AS, 107, 129

Chen, Y., Wang, Q. D., Gotthelf, E. V., Jiang, B., Chu, Y.-H., & Gruendl, R. 2006, ApJ, 651, 237

Chevalier, R. A. 1974, ApJ, 188, 501

Chu, Y.-H., Kim, S., Points, S. D., Petre, R., & Snowden, S. L. 2000, AJ, 119, 2242

Chu, Y.-H., & Kennicutt, R. C., Jr. 1988, AJ, 96, 1874

Cox, D. P. 1972, ApJ, 178, 159

Davies, R. D., Elliott, K. H., & Meaburn, J. 1976, MmRAS, 81, 89

den Herder, J. W., et al. 2001, A&A, 365, L7

Dennerl, K., et al. 2001, A&A, 365, L202

Dickey, J. M., & Lockman, F. J. 1990, ARA&A, 28, 215

Dufour, R. J. 1984, Structure and Evolution of the Magellanic Clouds, 108, 353

Dunne, B. C., Points, S. D., & Chu, Y.-H. 2001, ApJS, 136, 119

Dwarkadas, V. V. 2005, ApJ, 630, 892

Falle, S. A. E. G. 1981, MNRAS, 195, 1011

Falle, S. A. E. G. 1988, IAU Colloq. 101: Supernova Remnants and the Interstellar Medium, 419

Feast, M. 1999, PASP, 111, 775

Fesen, R. A., Blair, W. P., & Kirshner, R. P. 1985, ApJ, 292, 29

Flanagan, K. A., Canizares, C. R., Dewey, D., et al. 2004, ApJ, 605, 230

Filippenko, A. V. 1997, ARA&A, 35, 309

Filipovic, M. D., Haynes, R. F., White, G. L., & Jones, P. A. 1998, A&AS, 130, 421

Fusco-Femiano, R., & Preite-Martinez, A. 1984, ApJ, 281, 593

Gaetz, T. J., & Salpeter, E. E. 1983, ApJS, 52, 155

Gaensler, B. M., Hendrick, S. P., Reynolds, S. P., & Borkowski, K. J. 2003, ApJ. Lett., 594, L111

Gardiner, L. T., Sawa, T., & Fujimoto, M. 1994, MNRAS, 266, 567

Gardiner, L. T., & Noguchi, M. 1996, MNRAS, 278, 191

Garmire, G. P., Bautz, M. W., Ford, P. G., Nousek, J. A., & Ricker, G. R., Jr. 2003, Proc. SPIE, 4851, 28

Gehrels, N., & Williams, E. D. 1993, ApJ. Lett., 418, L25

Girardi, L., Chiosi, C., Bertelli, G., & Bressan, A. 1995, A&A, 298, 87

Haberl, F., & Pietsch, W. 1999, A&AS, 139, 277

Hamilton, A. J. S., Chevalier, R. A., & Sarazin, C. L. 1983, ApJS, 51, 115

Hayashi, I. 1997, Ph.D. Thesis,

Hayato, A., et al. 2010, ApJ, 725, 894

Hayato, A., Bamba, A., Tamagawa, T., & Kawabata, K. 2006, ApJ, 653, 280

Hendrick, S. P., Borkowski, K. J., & Reynolds, S. P. 2003, ApJ, 593, 370

Henize, K. G. 1956, ApJS, 2, 315

Hirayama, M., Nagase, F., Endo, T., Kawai, N., & Itoh, M. 2002, MNRAS, 333, 603

Hodge, P. W., & Sexton, J. A. 1966, AJ, 71, 363

Hoyle, F., & Fowler, W. A. 1960, ApJ, 132, 565

Hughes, J. P., Rafelski, M., Warren, J. S., Rakowski, C., Slane, P., Burrows, D., & Nousek, J. 2006, ApJ. Lett., 645, L117

Hughes, J. P., Ghavamian, P., Rakowski, C. E., & Slane, P. O. 2003, ApJ. Lett., 582, L95

Hughes, J. P., Rakowski, C. E., & Decourchelle, A. 2000, ApJ. Lett., 543, L61

Hughes, J. P. 2000, ApJ. Lett., 545, L53

Hughes, J. P., Hayashi, I., & Koyama, K. 1998, ApJ, 505, 732

Hughes, J. P., et al. 1995, ApJ. Lett., 444, L81

Hughes, J. P., Rafelski, M., Warren, J. S., Rakowski, C., Slane, P., Burrows, D., & Nousek, J. 2006, ApJ. Lett., 645, L117

Hwang, U., Decourchelle, A., Holt, S. S., & Petre, R. 2002, ApJ, 581, 1101

Hwang, U., Petre, R., Holt, S. S., & Szymkowiak, A. E. 2001, ApJ, 560, 742

Hwang, U., Holt, S. S., & Petre, R. 2000, ApJ. Lett., 537, L119

Hwang, U., Hughes, J. P., & Petre, R. 1998, ApJ, 497, 833

Ishisaki, Y., et al. 2007, PASJ, 59, 113

Itoh, H. 1984, Physica Scripta Volume T, 7, 19

Iwamoto, K., Brachwitz, F., Nomoto, K., Kishimoto, N., Umeda, H., Hix, W. R., & Thielemann, F.-K. 1999, ApJS, 125, 439

Jansen, F., et al. 2001, A&A, 365, L1

Katayama, H., Takahashi, I., Ikebe, Y., Matsushita, K., & Freyberg, M. J. 2004, A&A, 414, 767

Kennicutt, R. C., Jr., Bresolin, F., Bomans, D. J., Bothun, G. D., & Thompson, I. B. 1995, AJ, 109, 594

Kinugasa, K., & Tsunemi, H. 1999, PASJ, 51, 239

Klimek, M. D., Points, S. D., Smith, R. C., Shelton, R. L., & Williams, R. 2010, ApJ, 725, 2281

Klimek, M., Points, S. D., & Smith, C. 2006, Bulletin of the American Astronomical Society, 38, #156.11

Kokubun, M., Makishima, K., Takahashi, T., et al. 2007, PASJ, 59, 53

Kosenko, D., Helder, E., & Vink, J. 2010, arXiv:1001.0983

Kosenko, D., Vink, J., Blinnikov, S., & Rasmussen, A. 2008, A&A, 490, 223

Koyama, K., et al. 2007, PASJ, 59, 23

Kroupa, P., & Bastian, U. 1997, Hipparcos - Venice '97, 402, 615

Landau, L. D., & Lifshitz, E. M. 1959, Course of theoretical physics, Oxford: Pergamon Press, 1959,

Laval, A., Rosado, M., Boulesteix, J., et al. 1989, A&A, 208, 230

Levenson, N. A., Kirshner, R. P., Blair, W. P., & Winkler, P. F. 1995, AJ, 110, 739

Lewis, K. T., Burrows, D. N., Hughes, J. P., Slane, P. O., Garmire, G. P., & Nousek, J. A. 2003, ApJ, 582, 770

Liedahl, D. A., Osterheld, A. L., & Goldstein, W. H. 1995, ApJ. Lett., 438, L115

Long, K. S. 1983, Supernova Remnants and their X-ray Emission, 101, 525

Long, K. S., Dopita, M. A., & Tuohy, I. R. 1982, ApJ, 260, 202

Long, K. S., Helfand, D. J., & Grabelsky, D. A. 1981, ApJ, 248, 925

Lopez, L. A., Ramirez-Ruiz, E., Huppenkothen, D., Badenes, C., & Pooley, D. A. 2011, ApJ, 732, 114

Lopez, L. A., Ramirez-Ruiz, E., Huppenkothen, D., Badenes, C., & Pooley, D. 2010, arXiv:1011.0731

Lozinskaya, T. A. 1992, New York: American Institute of Physics, 1992,

Lucke, P. B., & Hodge, P. W. 1970, AJ, 75, 171

Macri, L. M., Stanek, K. Z., Bersier, D., Greenhill, L. J., & Reid, M. J. 2006, ApJ, 652, 1133

Marshall, F. E., Gotthelf, E. V., Zhang, W., Middleditch, J., & Wang, Q. D. 1998, ApJ. Lett., 499, L179

Masai, K. 1994, ApJ, 437, 770

Mason, K. O., et al. 2001, A&A, 365, L36

Mathewson, D. S., Ford, V. L., Tuohy, I. R., Mills, B. Y., Turtle, A. J., & Helfand, D. J. 1985, ApJS, 58, 197

Mathewson, D. S., Ford, V. L., Dopita, M. A., Tuohy, I. R., Long, K. S., & Helfand, D. J. 1983, ApJS, 51, 345

Mathewson, D. S., Cleary, M. N., & Murray, J. D. 1974, ApJ, 190, 291

Mathewson, D. S., & Clarke, J. N. 1973, ApJ, 180, 725

Maoz, D., & Badenes, C. 2010, MNRAS, 407, 1314

McKee, C. F., & Ostriker, J. P. 1977, ApJ, 218, 148

Mewe, R., Lemen, J. R., & van den Oord, G. H. J. 1986, A&AS, 65, 511

Mewe, R., Gronenschild, E. H. B. M., & van den Oord, G. H. J. 1985, A&AS, 62, 197

Mills, B. Y., & Turtle, A. J. 1984, Structure and Evolution of the Magellanic Clouds, 108, 283

Milne, D. K., Caswell, J. L., & Haynes, R. F. 1980, MNRAS, 191, 469

Mitsuda, K., et al. 2007, PASJ, 59, 1

Misaki, K., et al. 2004, Proc. SPIE, 5168, 294

Moore, B., & Davis, M. 1994, MNRAS, 270, 209

Mori, H., et al. 2005, PASJ, 57, 245

Murai, T., & Fujimoto, M. 1980, PASJ, 32, 581

Murphy Williams, R. N., Dickel, J. R., Chu, Y., Points, S., Winkler, F., Johnson, M., & Lodder, K. 2010, Bulletin of the American Astronomical Society, 42, #454.16

Nakajima, H., Yamaguchi, H., Ueno, M., Bamba, A., & Koyama, K. 2006, The X-ray Universe 2005, 604, 341

Nishiuchi, M., Yokogawa, J., Koyama, K., & Hughes, J. P. 2001, PASJ, 53, 99

Nomoto, K., Hashimoto, M., Tsujimoto, T., Thielemann, F.-K., Kishimoto, N., Kubo, Y., & Nakasato, N. 1997, Nuclear Physics A, 616, 79

Nomoto, K., Thielemann, F.-K., & Wheeler, J. C. 1984, ApJ. Lett., 279, L23

Pagel, B. E. J., Edmunds, M. G., Fosbury, R. A. E., & Webster, B. L. 1978, MNRAS, 184, 569

Park, S., Hughes, J. P., Slane, P. O., Burrows, D. N., Warren, J. S., Garmire, G. P., & Nousek, J. A. 2003, ApJ. Lett., 592, L41

Parker, J. W., Hill, J. K., Cornett, R. H., et al. 1998, AJ, 116, 180

Park, S., Burrows, D. N., Garmire, G. P., Nousek, J. A., Hughes, J. P., & Williams, R. M. 2003, ApJ, 586, 210

Parker, E. N. 1963, New York, Interscience Publishers, 1963.,

Payne, J. L., White, G. L., & Filipović, M. D. 2008, MNRAS, 383, 1175

Pizzolato, N., Ventura, P., D'Antona, F., Maggio, A., Micela, G., & Sciortino, S. 2001, A&A, 373, 597

Possenti, A., Cerutti, R., Colpi, M., & Mereghetti, S. 2002, A&A, 387, 993

Putman, M. E., et al. 1998, arXiv:astro-ph/9808023

Putman, M. E., Staveley-Smith, L., Freeman, K. C., Gibson, B. K., & Barnes, D. G. 2003, ApJ, 586, 170

Rakowski, C. E. 2005, Advances in Space Research, 35, 1017

Rakowski, C. E., Ghavamian, P., & Hughes, J. P. 2003, ApJ, 590, 846

Read, A. M., & Ponman, T. J. 2003, A&A, 409, 395

Rest, A., et al. 2005, Nature, 438, 1132

Reyes-Iturbide, J., Rosado, M., & Velázquez, P. F. 2008, AJ, 136, 2011

Rho, J., & Petre, R. 1998, ApJ. Lett., 503, L167

Rosado, M., Laval, A., Boulesteix, J., et al. 1990, A&A, 238, 315

Rothschild, R. E., Kulkarni, S. R., & Lingenfelter, R. E. 1994, Nature, 368, 432

Russell, S. C., & Bessell, M. S. 1989, ApJS, 70, 865

Russell, S. C., & Dopita, M. A. 1990, ApJS, 74, 93

Russell, S. C., & Dopita, M. A. 1992, ApJ, 384, 508

Rybicki, G. B., & Lightman, A. P. 1986, Radiative Processes in Astrophysics, by George B. Rybicki, Alan P. Lightman, pp. 400. ISBN 0-471-82759-2. Wiley-VCH , June 1986.,

Sedov, L. I. 1959, Similarity and Dimensional Methods in Mechanics, New York: Academic Press, 1959,

Serlemitsos, P. J., et al. 2007, PASJ, 59, 9

Seward, F. D., Harnden, F. R., Jr., & Helfand, D. J. 1984, ApJ. Lett., 287, L19

Seward, F. D., Williams, R. M., Chu, Y.-H., Gruendl, R. A., & Dickel, J. R. 2010, AJ, 140, 177

Seward, F. D., Williams, R. M., Chu, Y.-H., Dickel, J. R., Smith, R. C., & Points, S. D. 2006, ApJ, 640, 327

Shimizu, T., Masai, K., & Koyama, K. 2011, arXiv:1110.4948

Smith, R. K., Brickhouse, N. S., Liedahl, D. A., & Raymond, J. C. 2001, ApJ. Lett., 556, L91

Smith, C., Leiton, R., & Pizarro, S. 2000, Stars, Gas and Dust in Galaxies: Exploring the Links, 221, 83

Smith, R. C., Raymond, J. C., & Laming, J. M. 1994, ApJ, 420, 286

Smith, R. C., Chu, Y.-H., Mac Low, M.-M., Oey, M. S., & Klein, U. 1994, AJ, 108, 1266

Sofue, Y. 1994, PASJ, 46, 431

Someya, K., Bamba, A., & Ishida, M. 2010, PASJ, 62, 1301

Spitzer, L. 1962, Physics of Fully Ionized Gases, New York: Interscience (2nd edition), 1962,

Strüder, L., et al. 2001, A&A, 365, L18

Sturm, R., Haberl, F., Hasinger, G., Kenzaki, K., & Itoh, M. 2009, PASJ, 61, 895

Takahashi, T., et al. 2007, PASJ, 59, 35

Tsujimoto, M., Guainazzi, M., Plucinsky, P. P., et al. 2011, A&A, 525, A25

Tuohy, I. R., Dopita, M. A., Mathewson, D. S., Long, K. S., & Helfand, D. J. 1982, ApJ, 261, 473

Turner, M. J. L., et al. 2001, A&A, 365, L27

Warren, J. S., & Hughes, J. P. 2004, ApJ, 608, 261

Warren, J. S., Hughes, J. P., & Slane, P. O. 2003, ApJ, 583, 260

Weaver, R., McCray, R., Castor, J., Shapiro, P., & Moore, R. 1977, ApJ, 218, 377

Weisskopf, M. C., Brinkman, B., Canizares, C., Garmire, G., Murray, S., & Van Speybroeck, L. P. 2002, PASP, 114, 1

Williams, R. M., Chu, Y.-H., & Gruendl, R. 2006, AJ, 132, 1877

Williams, R. M., Chu, Y.-H., Dickel, J. R., Gruendl, R. A., Seward, F. D., Guerrero, M. A., & Hobbs, G. 2005, ApJ, 628, 704

Williams, R. M., & Chu, Y.-H. 2005, ApJ, 635, 1077

Williams, R. M., Chu, Y.-H., Dickel, J. R., Gruendl, R. A., Shelton, R., Points, S. D., & Smith, R. C. 2004, ApJ, 613, 948

Williams, R. M., Chu, Y.-H., Dickel, J. R., Petre, R., Smith, R. C., & Tavarez, M. 1999, ApJS, 123, 467

Williams, R. M., Chu, Y.-H., Dickel, J. R., Smith, R. C., Milne, D. K., & Winkler, P. F. 1999, ApJ, 514, 798

Winkler, P. F., Gupta, G., & Long, K. S. 2003, ApJ, 585, 324

Vancura, O., Blair, W. P., Long, K. S., et al. 1992, ApJ, 401, 220

van der Heyden, K. J., Bleeker, J. A. M., Kaastra, J. S., & Vink, J. 2003, A&A, 406, 141

van der Heyden, K. J., Behar, E., Vink, J., Rasmussen, A. P., Kaastra, J. S., Bleeker, J. A. M., Kahn, S. M., & Mewe, R. 2002, A&A, 392, 955

van der Heyden, K. J., Paerels, F., Cottam, J., Kaastra, J. S., & Branduardi-Raymont, G. 2001, A&A, 365, L254

Vink, J. 2008, ApJ, 689, 231

Vink, J. 2004, Nuclear Physics B Proceedings Supplements, 132, 21

Vink, J., Kaastra, J. S., & Bleeker, J. A. M. 1997, A&A, 328, 628

Vink, J., Bloemen, H., Kaastra, J. S., & Bleeker, J. A. M. 1998, A&A, 339, 201

Vink, J., Kaastra, J. S., & Bleeker, J. A. M. 1996, A&A, 307, L41

Xiao, X., & Chen, Y. 2008, Advances in Space Research, 41, 416

Yamaguchi, H., Bamba, A., & Koyama, K. 2009, PASJ, 61, 175

Yamaguchi, H., et al. 2008, PASJ, 60, 141

Yun, M. S., Ho, P. T. P., & Lo, K. Y. 1994, Nature, 372, 530

Acknowledgments

Without the support from my collaborators, this thesis could not have been completed.

First of all, I am deeply grateful to Manabu Ishida in ISAS, who has given and shown me a pleasure to study astrophysics and very important thing to work in the society. I have learned a lot from him, not only the basis of X-ray astronomy, but also prospective for the research and science.

I greatly appreciate Aya Bamba in Aoyama Gakuin University for giving a chance to study about supernova remnant. I have learned a lot on supernovae and their physics from her. I was very happy to study with her.

I am deeply grateful for my supervisor Tadayasu Dotani in ISAS for providing an opportunity to study X-ray astronomy in ISAS. I was encouraged by him countless times.

I express my thanks to Yoshitomo Maeda in ISAS and Hideyuki Mori in Nagoya University for giving many advice from observational studies.

And I would like to thank all the members in ISAS. I am grateful to Ikuyuki Mitsuishi, Takayuki Hayashi, Hiroshi Yoshitake, Kumiko Morihana whose meticulous comments were of enormous help.

This research has made use of data obtained from the Data Archive and Transmission System (DARTS) at ISAS/JAXA, the High Energy Astrophysics Science Archive Research Center at the NASA/Goddard Space Flight Center. I also thank to all members of *Suzaku*, *XMM-Newton*, and *Chandra* for their contributions to the instrument preparation, spacecraft operation, software development, and in-orbit instrumental calibration. This study was supported by the 21st Century COE program of the Tokyo Institute of Technology.

Finally, I would like to thank to may family for their supports, encouragements, and understandings.